

**NUMERICAL SIMULATIONS OF GRANULAR ASSEMBLIES
WITH THREE-DIMENSIONAL ELLIPSOID-SHAPED PARTICLES**

by

Hamza Ouadfel

A thesis

presented to the University of Waterloo

in fulfillment of the

thesis requirement for the degree of

Doctor of Philosophy

in

Civil Engineering

Waterloo, Ontario, Canada, 1998

©Hamza Ouadfel 1998



National Library
of Canada

Acquisitions and
Bibliographic Services

395 Wellington Street
Ottawa ON K1A 0N4
Canada

Bibliothèque nationale
du Canada

Acquisitions et
services bibliographiques

395, rue Wellington
Ottawa ON K1A 0N4
Canada

Your file Votre référence

Our file Notre référence

The author has granted a non-exclusive licence allowing the National Library of Canada to reproduce, loan, distribute or sell copies of this thesis in microform, paper or electronic formats.

The author retains ownership of the copyright in this thesis. Neither the thesis nor substantial extracts from it may be printed or otherwise reproduced without the author's permission.

L'auteur a accordé une licence non exclusive permettant à la Bibliothèque nationale du Canada de reproduire, prêter, distribuer ou vendre des copies de cette thèse sous la forme de microfiche/film, de reproduction sur papier ou sur format électronique.

L'auteur conserve la propriété du droit d'auteur qui protège cette thèse. Ni la thèse ni des extraits substantiels de celle-ci ne doivent être imprimés ou autrement reproduits sans son autorisation.

0-612-32850-3

The University of Waterloo requires the signatures of all persons using or photocopying this thesis. Please sign below, and give address and date.

ABSTRACT

A numerical model to simulate the behaviour of idealized rounded granular materials in conditions of static equilibrium using assemblies of ellipsoid-shaped particles is developed. The model is based on the discrete element method (DEM) which simulates the state of an assembly of particles through tracing the motion of constitutive particles and their interactions at contact points.

The development of the model for ellipsoids consisted mainly of implementing an inter-ellipsoid contact detection algorithm to detect and calculate characteristics of contacts between ellipsoids. The algorithm was implemented in an existing discrete element program for spheres (TRUBAL).

A modified program TRUBAL was utilized to perform constant pressure deviatoric compression tests on a 1000 ellipsoids' assembly. The results of these tests showed that the characterization of anisotropy by symmetric and deviatoric second-order tensors applies to assemblies of ellipsoids. However, the provision for an additional fourth-order anisotropy tensor can become necessary in some cases (for example, to describe anisotropy in average tangential contact forces).

A Stress-Force-Fabric relationship between the macroscopic stress tensor and anisotropies in contact forces and in fabric was derived for ellipsoids. Particle shape has an increasingly higher effect on the relationship as deformation progresses. A form of force-fabric joint anisotropy contribution, usually negligibly small in two dimensions, was found to play an important role in shaping the stress behaviour.

Rotations of ellipsoids were analyzed from a statistico-geometrical perspective and found to influence the (contact formation/disintegration)-related anisotropy. Ellipsoids have a tendency to create more contacts around their flat areas than any other area. They use their rotational ability to maintain a near-constant distribution of contacts around their surfaces irrespective of the stress and deformation levels.

ACKNOWLEDGEMENTS

The author would like to thank his supervisor Dr. L. Rothenburg who introduced the author to the general problem and was generous with his time and advice to see the project through to completion. He also sincerely acknowledges Dr. Rothenburg's moral, technical, and financial support.

Appreciation is extended to my past and present colleagues, Dr. R. Lashkaripour, Dr. A. A. Heidari, Dr. M. Palassi, Dr. A. A. Mirghasemi, and C. Flaman, for their enthusiastic company.

I would also like to thank the graduate secretary of Civil Engineering, C. Jones, for her help and kind character.

The financial support provided by Elf-Aquitaine is gratefully acknowledged.

Finally, heartfelt thanks to my wife Ouafae and daughter Lamiss, for providing me with moral support, encouragement, and an enjoyable family life.

To the memory of my father

To my mother

To my wife and daughter

To my brother Ali

To all my Family and Friends

TABLE OF CONTENTS

TITLE PAGE	i
ABSTRACT	iv
ACKNOWLEDGEMENTS	vi
DEDICATION	vii
TABLE OF CONTENTS	viii
LIST OF TABLES	xix
LIST OF FIGURES	xx
NOMENCLATURE	xxxi

CHAPTER I: INTRODUCTION.....	1
1.1 General Background	1
1.2 Research Topic	4
1.3 Objectives	8
1.4 Organization of the Thesis.....	9
 CHAPTER II: MICROSCOPIC CHARACTERIZATION OF GRANU-	
 LAR MATERIAL BEHAVIOUR	12
2.1 Load Transfer in Granular Materials.....	12
2.2 Static Equilibrium and the Average Stress Tensor	15
2.2.1 Symmetry of the Average Stress Tensor.....	17
2.3 Microscopic Characteristics of Granular Assemblies	19
2.3. The Coordination Number.....	19
The Average Contact Density	21
2.3.2 Contact Normal Orientations.....	22
Spherical Partitioning of the Orientation Space.....	23
Near Uniform Partitioning of the Orientation Space	25
Contact Normal Orientation Distribution Function	28
The Fabric Tensor	31
Measurement of Anisotropy in Contact Normal Orientations.....	33

2.4 Distribution of Average Contact Forces	34
2.4.1 The Average Normal Contact Force Tensor	37
2.4.2 The Average Tangential Contact Force Tensor	38
Symmetry of the Tangential Stress Tensor	40
2.5 Influence of Fourth-Order Terms on the Quality of Approximation by Fourier Series	42
2.5.1 Fourth-Order Fourier Series Approximation of Contact Normal Orientation Distribution	42
2.5.2 Fourth-Order Fourier Series Approximation of Average Normal Contact Force Distribution	44
2.5.3 Fourth-Order Fourier Series Approximation of Average Tangential Contact Force Distribution	46
2.5.4 The Average Radial Tangential Contact Force Distribution	50
Approximation of the Average Radial Tangential Contact Force Distribution	50
2.6 Average Stress Tensor for Infinite Systems	53
2.7 Conclusions	55

CHAPTER III: THE DISCRETE ELEMENT METHOD AND THE MODIFIED PROGRAM TRUBAL	57
3.1 Introduction	57
3.2 The Discrete Element Method for Ellipsoids	59
3.2.1 Contact Force Calculation	61
3.3 Motion Update	67
3.3.1 Damping	71
3.3.2 Numerical Stability	73
3.3.3 Numerical Integration	74
3.4 Modified Program TRUBAL	75
3.4.1 Pre-Processing	77
3.4.2 Processing	78
3.4.3 Post-Processing	80
3.4.4 Data Structures	80
Group of Particle Data	82
Group of Contact Data	82
3.4.5 Identification of Neighbours	82
Boxing Scheme	83
Envelope Space	83
3.4.6 Periodic Space Algorithm	85
3.4.7 Stress Servo-Control	86

3.4.8 Deviatoric Compression at Constant Mean Pressure	87
3.4.9 Particle “Growth” and Assembly Generation	87
“Growth” Scheme with Constant Particle Volume	88

CHAPTER IV: INTER-ELLIPSOID CONTACT DETECTION ALGO-

RITHM.	91
4.1 Introduction	91
4.2 Test for Overlap	94
4.2.1 Quadric Surface Equation	95
4.2.2 Classification of a Quadric Surface	96
4.2.3 Basic Concept	96
Principle of the Overlap Test	98
4.2.4 Scan of Quadrics C_f	99
4.3 Calculation of Contact Parameters	100
4.3.1 Principle.	100
4.3.2 First Approximation of the Contact.	102
4.3.3 Refinement of First Approximation	104
4.3.4 Efficiency	107
4.3.5 Calculation of Contact Characteristics	107
Contact Normal Vector	107
Interpenetration	107

Reference Contact Point.	109
4.4 Tests of the Contact Detection Scheme.	109
4.4.1 Simple Tests	109
4.4.2 Comparison with a Contact Detection Algorithm for Ellipses	113
4.5 Conclusions	115

CHAPTER V: RESULTS OF SIMULATION WITH ASSEMBLIES OF ELLIPSOIDS. 117

5.1 Introduction	117
5.1.1 Generated Samples of Ellipsoids.	117
5.1.2 Test Program	118
5.1.3 Physical and Numerical Units	120
5.2 Compaction	120
5.3 Particle Shape Transformation	121
5.3.1 System of Smooth Non-Spherical Particles in Static Equilibrium ..	122
5.3.2 Evolution of the Average Coordination Number	125
Effect of the Mean Pressure on the Coordination Number	127
5.3.3 Evolution of the Packing Fraction.	127
5.3.4 Evolution of the Average Normal Contact Force Magnitude	128
5.3.5 Shear Strength	128
5.3.6 Evolution of Fabric And Contact Forces.	128

5.3.7 Evolution of the Distribution of Particle Coordination Number	130
5.3.8 Evolution of Anisotropy	132
5.3.9 Summary of Particle Shape Transformation Results.	134
5.4 Constant Mean Stress Compression Tests	135
5.4.1 Stress-Strain Behaviour.	135
5.4.2 Volumetric Strain Behaviour.	140
5.4.3 Packing Density Behaviour.	141
5.4.4 Average Coordination Number Behaviour	144
Effect of Confining Pressure	146
5.4.5 Average Normal Contact Force Behaviour	147
5.4.6 Effect of Assembly Size	149
5.4.7 Evolution of Microstructure and Contact Forces	151
Development of Contact Normal Orientations Anisotropy	151
Development of Average Contact Force Anisotropy.	154
5.4.8 Anisotropy Behaviour	155
Anisotropy in Contact Normal Orientations	155
Anisotropy in Average Normal Contact Forces.	158
Anisotropy in Average Tangential Contact Forces	160
Comparison of Anisotropies at their Peak States and the Influence of Confining Pressure.	162
Anisotropy in Average Branch Lengths.	164
5.5 Conclusions	168

CHAPTER VI: THE STRESS-FORCE-FABRIC RELATIONSHIP FOR ELLIPSOIDS.....	170
6.1 Introduction	170
6.2 The Average Stress Tensor	171
6.3 Distribution of Average Branch Vectors.....	173
6.3.1 Distribution of Average Normal Branch Vectors	175
6.3.2 Distribution of Average Tangential Branch Vectors.....	175
6.4 The S-F-F Relationship for Infinite Systems of Ellipsoids	178
6.4.1 Verification of the S-F-F Relationship	183
6.4.2 Analysis of Microscopic Contributions to the Average Stress Tensor	188
6.4.3 Specific Effects Related to Particle Shape	194
6.5 Microscopic Anisotropy and its Relation to Shear Strength	195
6.5.1 Shear Stress Ratio Equation	197
Normal Stress.....	197
Shear Stress	198
6.5.2 Anisotropy Contributions to the Material Shear Strength.....	206
Another Illustration of the direct effect of particle shape	211
6.5.3 Sense of Anisotropy Contributions to the Material Shear Strength ..	211
Individual Contributions of α_{ij}^n and α_{ij}^t	211
Individual Contributions of α_{ij}^v and α_{ij}^s	214

Sense of Coaxiality of the Differential Anisotropy Tensor $a_{ij}^{\Delta z}$	214
Joint Contribution of a_{ij}^r and a_{ij}^z	216
Joint Contribution of a_{ij}^r and a_{ij}^f	216
Joint Contribution of a_{ij}^z and a_{ij}^f	216
Shear Stress Ratio Equation at Large Strains.	216
6.6 Conclusions	217

CHAPTER VII: STATISTICAL AND GEOMETRICAL ANALYSIS OF CONTACTS 222

7.1 Introduction	222
7.2 Distribution of Local Contact Vector Orientations	223
7.2.1 Density and Distribution Functions of Local Contact Probability . .	226
7.2.2 Probability Distribution of Contact Vector Lengths	230
7.2.3 Application to Predicting Proportions of Contact Vector Lengths . .	231
Grouping of Contacts	232
7.2.4 Relationship Between Local Contact Probabilities and Particle Surface Areas	236
Calculation of the Distribution of Normalized Particle Surface Areas	238
7.3 Distribution of Particle Orientations	238

7.3.1 Evolution of Anisotropy in Particle Orientations During Shear Deformation	239
7.4 Relationship Between Anisotropies in Contact Normal Orientation and Particle Orientation	242
7.4.1 Relationship in Two Dimensions	242
Assemblies of Ellipses in the Biaxial Test.	251
7.4.2 Relationship in Three Dimensions	257
7.5 Conclusions	260
 CHAPTER VIII: CONCLUSIONS AND RECOMMENDATIONS...	262
8.1 General.	262
8.2 Microscopic Description of Granular Material Behaviour	265
8.3 Inter-Ellipsoid Contact Detection Algorithm	268
8.4 Results of Particle Growth.	268
8.5 Behaviour of Assemblies of Ellipsoids in the Deviatoric Compression Test at Constant Mean Pressure	269
8.5.1 Macroscopic Behaviour.	269
8.5.2 Microscopic Behaviour	271
8.6 Average Stress Tensor Decomposition	273
8.7 Effect of Particle Shape on Fabric Anisotropy	277

8.8 Recommendations for Future Research	279
8.8.1 The Average Strain Tensor	279
APPENDIX A: Nearly-Uniform Partitioning of the Orientation Space	283
APPENDIX B: Intersection of Two Ellipsoids	289
APPENDIX C: Calculation of Integrals $\int_{\mathbf{n}} n_{i_1} n_{i_2} \dots n_{i_{2m}} d\mathbf{n}$	292
REFERENCES	295

LIST OF TABLES

Table 5•1: Parameters of particle shape transformation	
.....	122
Table 5•2: Initial conditions and parameters of “ p =constant” tests with ellipsoids	
.....	136
Table 6•1: Percent contributions of microscopic anisotropies to the mobilized material shear strength	
.....	221

LIST OF FIGURES

Figure 2•1: Biaxial compression test on an assembly of photo-elastic disks <i>(after De Josselin De Jong and Verruijt, 1969)</i>	
(a) Distribution of contact forces	
(b) Vertical contacts	
(c) Horizontal contacts	
.....	14
Figure 2•2: Elements of definition of the stress tensor for a granular system	
.....	16
Figure 2•3: Definition of the particle coordination number, the contact normal vector, and the contact vector	
.....	20

Figure 2•4: Spherical partitioning of the unit sphere	
(a) Spherical coordinates	
(b) Distribution of patches	
(c) Variation of patch area with position	
.....	24
Figure 2•5: Nearly uniform partitioning of the unit sphere	
(a) Partitioning of the basic region	
(b) Distribution of patches	
(c) Variation of patch area with position	
.....	26
Figure 2•6: Typical shapes of the contact normal orientation distribution	
.....	29
Figure 2•7: Normal and tangential contact force components	
.....	35
Figure 2•8: Measured and approximated distributions	
(a) Contact normal orientation	
(b) Average normal contact force	
.....	45
Figure 2•9: Measured and approximated distributions of average tangential contact force	
.....	49
Figure 2•10: 2-D Average radial tangential contact force distribution	
(a) Definition of the radial force	
(b) Measured and approximated distributions (in separate graphs)	
(c) Illustration of the change in maximum direction	
.....	51

Figure 3•1: Cycle of mechanical calculations used in DEM	60
Figure 3•2: Two ellipsoids in contact	62
Figure 3•3: Linear contact model	
(a) Particle-to-particle interaction	
(b) Normal and shear contact force-displacement laws	64
Figure 3•4: Incremental rotation of the shear contact force	66
Figure 3•5: Orientation of an ellipsoid	70
Figure 3•6: Organization of program TRUBAL	76
Figure 3•7: Flow chart of DEM routine in the modified program TRUBAL	79
Figure 3•8: Data structures of original program TRUBAL	
(a) Partition of A(I) array	
(b) Link list scheme	81
Figure 3•9: Mapping scheme for ellipsoids	
(a) Envelope space	
(b) Boxing scheme (2-D view)	84

Figure 4•1: A pair of overlapping particles	
(a) Spheres	
(b) Ellipsoids	
.....	93
Figure 4•2: Classification of quadric surfaces and conic sections <i>(after Levin, 1979)</i>	
.....	97
Figure 4•3: (θ, ϕ) parametrization of the surface of an ellipsoid	
.....	101
Figure 4•4: Surface intersections	
(a) Sphere-sphere intersection	
(b) Cone-ellipsoid intersection	
.....	103
Figure 4•5: Contact approximation by curves with one constant parameter	
.....	105
Figure 4•6: Flow chart of the inter-ellipsoid contact detection algorithm	
.....	106
Figure 4•7: Determination of characteristics of contact	
(a) Contact normal direction	
(b) Normal overlap distance and reference contact point	
.....	108
Figure 4•8: Effect of relative particle displacement on normal overlap distance	
(a) Rotation	
(b) Normal displacement	
(c) Tangential displacement	
.....	111

Figure 4•9: Evolution of the normal overlap distance with relative particle displacement	112
Figure 4•10: Illustration of a comparison of results between the 3D-inter-ellipsoid contact algorithm and a reference 2D-inter-ellipse contact scheme	114
Figure 5•1: Structure of assemblies of spheres used in particle shape transformation	119
Figure 5•2: Illustration of contact force orientation for a smooth and a frictional contact	123
Figure 5•3: Behaviour of assemblies of ellipsoids during particle shape transformation	
(a) Average inertial force fraction; (b) Average coordination number	
(c) Packing fraction; (d) Average overlap distance fraction	
(e) Angle of shearing resistance	
	126
Figure 5•4: Evolution of fabric and average normal contact forces during particle shape transformation	129
Figure 5•5: Particle coordination number vs. eccentricity during particle shape transformation (1000 ellipsoids)	
(a) Standard deviation	
(b) Relative standard deviation	
	131

Figure 5•6: Evolution of anisotropy during particle shape transformation	133
Figure 5•7: Illustration of macro-behaviour during shear deformation	
(a) Shear stress ratio vs. axial strain	
(b) Volumetric strain vs. axial strain	
	137
Figure 5•8: Effect of confining pressure on peak shear stress ratio and peak dilation rate	139
Figure 5•9: Peak friction angle vs. peak dilation rate for simulated assemblies of plane ellipses, 3-D ellipsoids, and a Ham River Sand	142
Figure 5•10: Evolution of packing density during shear deformation	143
Figure 5•11: Evolution of average coordination number and its rate of change during shear deformation	145
Figure 5•12: Evolution of the mean average normal contact force during shear deformation	148
Figure 5•13: Effect of assembly size	150
Figure 5•14: Induced anisotropy in contact normal orientations and normal contact forces (Test 4d)	152

Figure 5•15: Vertical and horizontal contacts (Test 4d)	
(a) Number of contacts versus axial strain	
(b) Fraction of contacts versus axial strain	
(c) Fraction of normal contact force magnitude versus axial strain	
.....	153
Figure 5•16: Evolution of anisotropy in contact normal orientations during shear deformation (Test 4d)	
.....	156
Figure 5•17: Evolution of anisotropy in average normal contact forces during shear deformation (Test 4d)	
.....	159
Figure 5•18: Evolution of anisotropy in average tangential contact forces during shear deformation (Test 4d)	
.....	161
Figure 5•19: Comparison between anisotropies at their peak values and the influence of applied confining pressure	
.....	163
Figure 5•20: Evolution of anisotropy in average branch vector lengths during shear deformation (Test 4d)	
.....	165
Figure 5•21: Evolution of the average branch vector length during shear deformation	
.....	167
Figure 6•1: Contact vectors, branch vectors, and contact normal vectors	
(a) Spheres	
(b) Ellipsoids	
.....	172

Figure 6•2: Measured and approximated distributions of average normal and tangential branch vectors	176
Figure 6•3: Verification of the S-F-F relationship (major principal stress)	184
Figure 6•4: Verification of the S-F-F relationship (intermediate principal stress)	185
Figure 6•5: Verification of the S-F-F relationship (minor principal stress)	186
Figure 6•6: Verification of the S-F-F relationship (shear stress ratio)	187
Figure 6•7: Major principal stress decomposition	190
Figure 6•8: Intermediate principal stress decomposition	191
Figure 6•9: Minor principal stress decomposition	192
Figure 6•10: Mean stress decomposition	193
Figure 6•11: Direct effect of particle shape on the S-F-F relationship	196
Figure 6•12: Verification of coaxiality and axisymmetry of anisotropy tensors	205
Figure 6•13: Verification of the shear stress ratio equation	207

Figure 6•14: Shear stress ratio decomposition	209
Figure 6•15: Percent contributions of microscopic anisotropies to the mobilized shear strength	210
Figure 6•16: Percent contribution of particle shape-related anisotropies to the mobilized shear strength	212
Figure 6•17: Sense of coaxiality of basic anisotropy tensors	213
Figure 6•18: Effect of confining pressure on the difference between anisotropies in normal and tangential average branch vectors	215
 Figure 7•1: Anisotropy in local contact vector orientations	
(a) Measured and approximated distributions (4 states)	
(b) variation with applied strain, and confining pressure	
(c) Variation with particle shape	
	225
 Figure 7•2: Contact probability calculations	
(a) Density of probability function	
(b) Cumulative probabilities	
	229
 Figure 7•3: Contact groups of given vector lengths	
(a) Definition	
(b) Illustration	
	233

Figure 7•4: Measured and estimated fractions of contact vectors and contact types for well-defined groups of contacts	235
Figure 7•5: Illustration of a comparison between calculated distributions of local contact probabilities and ellipsoid surface areas	237
Figure 7•6: Geometry of a strained assembly (initially and at a large strain)	240
Figure 7•7: Illustration of induced anisotropy in ellipsoids' orientations	
(a) Histogram distributions (initially and at a large strain)	
(b) Magnitude of anisotropy vs. applied axial strain	241
Figure 7•8: Relationship between orientations of the contact normal vector, the local contact vector, and the particle's long-axis	
(a) Disk	
(b) Ellipse	244
Figure 7•9: Variations of the deviation angle (between contact normal and contact vector) with varying contact position	245
Figure 7•10: Illustration of coefficients, c_1 , c_2 , s_1 , and s_2 , and their variation with particle shape	253
Figure 7•11: Contribution of rotations to the anisotropy in contact normal orientations	255
Figure 7•12: Definition of an ellipsoid's orientation in terms of Euler's angles	259

Figure 8•1: Elements of definition of the strain tensor for a plane granular system

..... 281

NOMENCLATURE

a	= Ellipsoid major semi-axis
a_{rot}^r	= Contribution of ellipse rotations to the magnitude of contact normal orientation anisotropy
a_{ij}^r	= Second-order tensor of contact normal orientation anisotropy
a_{ij}^n	= Second-order tensor of average normal contact force anisotropy
a_{ij}^t	= Second-order tensor of average tangential contact force anisotropy
a_{ij}^z	= Second-order tensor of average branch vector length anisotropy
a_{ij}^v	= Second-order tensor of average normal branch vector anisotropy
a_{ij}^{τ}	= Second-order tensor of average tangential branch vector anisotropy
a_{ij}^E	= Second-order tensor of ellipsoid long-axis orientation anisotropy
$a_{ij}^{c\vee L}$	= Second-order tensor of local contact vector orientation anisotropy

a_σ	= Shear stress ratio
a_σ^r	= Contribution of contact normal anisotropy to the shear stress ratio
a_σ^z	= Contribution of average branch vector anisotropy to the shear stress ratio
a_σ^f	= Contribution of average contact force anisotropy to shear stress ratio
a_σ^{rz}	= Joint contribution of contact normal and average branch vector anisotropies to the shear stress ratio
a_σ^{rf}	= Joint contribution of contact normal and average contact force anisotropies to the shear stress ratio
a_σ^{zf}	= Joint contribution of average branch vector and average contact force anisotropies to the shear stress ratio
a_σ^{rzf}	= Joint contribution of contact normal, average branch vector, and average contact force anisotropies to the shear stress ratio
$A_l(\beta)$	= Prolate spheroid surface area (comprised between azimuth angles 0 and β)
$A_l^*(\beta)$	= Normalized prolate spheroid surface areas = $A_l(\beta) / A_l(\pi)$
b	= Ellipsoid intermediate semi-axis
b_{ijkl}	= Fourth-order anisotropy tensor
c	= Contact point
	= Cohesion (Chapter 3)
	= Ellipsoid minor semi-axis
C_E	= Ellipse circumference
C_f	= Pencil of two ellipsoid surfaces
D_1, D_2	= Constants (Chapter 2)

$D_{i, (i = 2, 4)}$	= Invariants of the discriminant matrix Q (Chapter 4)
D_σ	= Ratio of mean stress to spherical stress
ds	= Elemental length
e	= Eccentricity = $(a-b)/(a+b)$
	= Void ratio
\tilde{e}	= Eccentricity = $\sqrt{a^2 - b^2} / a$
e^s	= Unit vector along ellipsoid minor-axis (short)
e^I	= Unit vector along ellipsoid intermediate-axis
e^L	= Unit vector along ellipsoid major-axis (long)
elr	= Ellipsoid elongation ratio = (intermediate-axis/long-axis)
Err	= Average relative error
$E(n)$	= Contact normal orientation distribution function
$E^*(n)$	= Deviatoric part of $E(n)$ function
f^c	= Force vector at a contact point c
$f^{c,k}$	= Force vector at a contact point c on the surface of a particle k
f_i^β	= Force vector component at a boundary contact point β
\bar{f}_i	= Average contact force component
\bar{f}_i^*	= Average contact force deviator component
\bar{f}^n	= Average normal contact force
\bar{f}_i^t	= Average tangential contact force component
$f_r^t(\alpha, \beta)$	= Radial component of the tangential contact force
$\bar{f}_r^t(\beta)$	= Average radial tangential contact force

\bar{f}_n^p	= Average normal contact force over all individual contacts
\bar{f}^p	= Average normal contact force over all groups of contacts
F_i	= Resultant force vector component
F^n	= Normal contact force
F_i^s	= Shear contact force vector component
ΔF^n	= Normal contact force increment
ΔF_i^s	= Shear contact force increment vector component
F_{ij}^n	= Average normal contact force tensor
F_{ij}^t	= Average tangential contact force tensor
$F_i(\alpha, \beta)$	= Local contact probability distribution function
$f_{(x)}$	= Fraction of (x)-type contact vectors
$f_{(x-y)}$	= Fraction of (x-y)-type contact vector pairs
flr	= Ellipsoid flatness ratio (=short-axis/intermediate-axis)
g_i	= Gravity acceleration vector component
$G_i(\beta)$	= Local contact vector probability distribution function (prolate spheroids)
$H_i(\beta)$	= Local contact vector length probability distribution function = $2G_i(\beta)$
h^c	= Components of the contact vector between polygonal units
\hat{h}^c	= Counter-clockwise rotated polygon contact vector
I	= Intersection of two ellipsoid surfaces
I_A	= Trace of inter-ellipsoid surface intersection (on one of them (A))
I_{ij}	= Ellipsoid inertia tensor in global coordinates
I_{ij}^p	= Ellipsoid principal inertia tensor

K^n	= Normal contact stiffness coefficient
K^s	= Shear contact stiffness coefficient
l^c	= Contact vector length
l^o	= Assembly average contact vector length
l_j^c	= Contact vector component
\bar{l}_j	= Average contact vector component
M	= Total number of assembly contacts
\tilde{M}	= Total number of assembly physical contacts = $M/2$
$M_{(x)}$	= Number of (x)-type contact vectors
$M_{(x-y)}$	= Number of (x-y)-type contact vector pairs
M_i	= Resultant moment vector component
ΔM^g	= Number of contacts in a group/class of orientation g .
m	= Particle mass
m_v	= Assembly average contact density
N	= Total number of assembly particles
N	= Number of class intervals in $[0, \pi/4]$ (Chapter 2)
\mathbf{n}	= Unit vector
$[\mathbf{n}]^G$	= Unit vector in global coordinates
$[\mathbf{n}]^L$	= Unit vector in local coordinates
\mathbf{n}^c	= Unit vector normal to a contact plane at a location c
\mathbf{n}^g	= Unit vector normal representative of an orientation group g
\mathbf{n}^r	= Radial unit vector

\mathbf{n}^l	= Unit local contact vector
\mathbf{n}^E	= Unit vector along an ellipsoid long-axis
$ \Delta \mathbf{n}^s $	= Orientation class magnitude
Q	= Ellipsoid discriminant matrix
Q_u	= Ellipsoid sub-discriminant matrix
$\mathbf{r}^{c,k}$	= Position vector of a contact point c on the surface of a particle k
r	= Ellipsoid geometric mean radius = Sphere's radius of equal ellipsoid volume
\bar{r}	= Ellipse arithmetic mean radius = (minor semi-axis + major semi-axis)/2
R_{ij}	= Fabric tensor (Chapter 2)
	= Ellipsoid orientation matrix (Chapter 3)
R_{Θ^E}	= Rotation matrix associated with Euler angle Θ^E
R_{Φ^E}	= Rotation matrix associated with Euler angle Φ^E
R_{Ψ^E}	= Rotation matrix associated with Euler angle Ψ^E
s_γ	= Standard deviation of the particle coordination number histogram
s_γ^r	= Relative standard deviation = (standard deviation) / (mean value)
s_x^y	= Sign of anisotropy tensor scalar products
S_l	= Ellipsoid/Ellipse local contact vector orientation probability density function
S_E	= Ellipsoid/Ellipse long-axis orientation probability density function
$S_{\theta_L^E}$	= Probability density function of the random variable θ_L^E
$S_{\theta_L^E, E}$	= Joint probability density function of the pair of random variables (θ_L^E, θ^E)
t	= Time
Δt	= Time-step

t_j^c	= Component of the unit vector along the tangential branch vector
T^{β}	= Boundary vector traction
$T_i, (i = 1, 3)$	= Invariants of the sub-discriminant matrix Q_u
$\Delta U_b, \Delta U_i^c$	= Increment of displacement vector component
ΔU^n	= Increment of normal displacement
ΔU_i^s	= Increment of shear displacement vector component
V	= Assembly volume
V_s	= Volume of solid
V_i	= Relative velocity at inter-particle contact
\bar{v}_p	= Average particle volume
x_i	= Particle centre position vector component
\dot{x}_i	= Particle centre velocity vector component
\ddot{x}_i	= Particle centre acceleration vector component
Δx_i	= Increment of particle centre position vector component
x_j^{β}	= Position vector component at a boundary contact point β
\underline{X}	= Uni-line vector position
\underline{X}^T	= Transposed uni-column vector position.
z^c	= Branch vector at a contact c
z^n	= Normal branch vector
z_j^t	= Tangential branch vector component
\bar{z}_i	= Average branch vector component
\bar{z}_i^*	= Component of the average branch vector deviator

\mathbf{z}^n	= Average normal branch vector
$\overline{\mathbf{z}}_i^t$	= Average tangential branch vector component
\overline{z}^o	= Assembly average branch vector length
α_L	= Damping coefficient (linear motion)
α_R	= Damping coefficient (rotational motion)
α	= Polar angle in spherical coordinates
α^l	= Polar angle of local contact vector in spherical coordinates
β	= Azimuth angle in spherical coordinates
β^l	= Azimuth angle of local contact vector in spherical coordinates
$\beta_{i_1 i_2 \dots i_m}^{(m)}$	= Constant tensor of order (m) (Chapter 6, Appendix B)
$\gamma, \gamma_i, \gamma_{ss}$	= Average coordination number (current, initial, and steady-state, respectively)
δ_{ij}	= Kronecker delta tensor
δ^n	= Inter-particle normal overlap distance
ϵ_{ij}	= Strain tensor
$\dot{\epsilon}_{ij}$	= Strain rate tensor
ϵ_{ijk}	= Alternating tensor (to calculate vector cross products)
$\epsilon_a, \epsilon_a^i, \epsilon_a^{ss}$	= Axial strain (current, initial, and steady-state, respectively)
ϵ_v	= Volumetric strain
$\dot{\epsilon}_v$	= Volumetric strain rate
ϕ	= Angle of internal friction
	= Parametric curve variable (Chapter 4)
Φ^E	= Euler angle (Chapter 7)

ϕ_μ	= Angle of inter-particle friction
μ	= Coefficient of interparticle friction
ρ, ρ_0, ρ_{ss}	= Packing density (current, initial, and steady-state, respectively)
σ_{ij}	= Assembly stress tensor
σ_{ij}^o	= Spherical stress tensor
σ_{ij}^r	= Contribution of contact normal anisotropy to the stress tensor
σ_{ij}^x	= Contribution of average branch vector anisotropy to the stress tensor
σ_{ij}^f	= Contribution of average contact force anisotropy to the stress tensor
σ_{ij}^{rf}	= Joint contribution of contact normal and average branch vector anisotropies to the stress tensor
σ_{ij}^{rf}	= Joint contribution of contact normal and average contact force anisotropies to the stress tensor
σ_{ij}^{xf}	= Joint contribution of average branch vector and average contact force anisotropies to the stress tensor
σ_{ij}^{rxf}	= Joint contribution of contact normal, average branch vector, and average contact force anisotropies to the stress tensor
σ_{ij}^β	= Boundary stress tensor
σ^n	= Mean stress
$\sigma_n^{\varepsilon=0}$	= Initial mean stress
σ'	= Shear stress
σ^c	= Confining stress
π	= Permutation of indices (Chapter 2, Chapter 8)

ω	= Particle angular velocity
θ	= Particle rotation (Chapter 3)
	= Parametric curve variable (Chapter 4)
Θ^E	= Euler angle
θ^E	= Ellipse major-axis orientation angle
θ_G^n	= Contact normal orientation angle in global coordinates (Ellipses)
θ_L^n	= Contact normal orientation angle in local coordinates (Ellipses)
$\Delta\theta'$	= Deviation angle between contact normal and contact vector directions
$\Delta\theta_{ij}$	= Increment of rotation matrix
Ψ^E	= Euler angle (Chapter 7)
ψ^c	= Angle between the contact normal and branch vectors
λ	= Constant used in the definition of shear stress
η_{ij}	= Constant second-order tensor
ξ	= A non-dimensional variable

CHAPTER I: INTRODUCTION

1.1 General Background

This study relates to numerical simulations of the mechanical behaviour of rounded granular materials.

From a phenomenological point of view, granular materials exhibit a complex mechanical behaviour which involves dilation and/or contraction, and sensitivity of strength and deformation properties to applied confining stress. These characteristics are the result of the discontinuous structure possessed by these materials; therefore, a microscopic description of granular materials is the fundamental one. Considered from the microscopic viewpoint, granular materials consist of mutually contacting solid particles contained within the liquid and/or gaseous phase.

CHAPTER I: INTRODUCTION

The complex mechanical behaviour of granular materials is a reflection of their structure, *i.e.*, essentially that of the state of motion of the individual particles and their mutual interaction. The existence of contacts between neighbouring particles restricts their freedom of motion, thereby determining the strength and deformation properties of a granular material.

Several microscopic factors contribute to the macroscopic behaviour of granular materials. In the case of cohesionless granular materials such as sands, these factors are: the size, shape, texture (smoothness/roughness) and strength of individual particles; the nature of the interaction between the various phases; the state of the geometrical arrangement of the assemblage of grains, called fabric; and the nature of the applied external load. In the case of bonded systems, the number and strength of the contact bonds (themselves a consequence of the previous factors) must be added to the list. All of these factors are incorporated into the concept of microstructure.

In order to model and to understand the behaviour of granular materials from a microscopic point of view, it is necessary to account for all of these factors. It is sometimes difficult, if not impossible, to distinguish between their effects, as they usually influence each other.

It is important to distinguish between two types of properties reflecting: (1) microscopic composition, *i.e.*, grain size, shape, texture, hardness of the solid phase as well as content of other phases such as gas and/or water; (2) macroscopic state parameters such as stress, strain, average number of contacts per particle and other volume averages that are needed for the description of constitutive behaviour from a microscopic point of view.

CHAPTER I: INTRODUCTION

While the determination of microscopic composition is relatively easy to perform in the laboratory, the determination of state quantities is virtually impossible. It would necessitate sample destruction and tedious microscopic measurements at contact points between particles. It also must take into account the state of the granular material being studied, and this prerequisite calls for experiments on undisturbed samples. This has been an obstacle that has slowed the progress of development of micromechanics theories of granular materials, up until the time that numerical simulations were introduced. Simulations are typically based on the discrete element method (DEM).

The discrete element method is a numerical procedure that was developed for the simulation of dynamic systems containing discontinuous solid elements in interaction with each other through inter-element contact forces. The method was successfully applied to model the mechanical behaviour of soils idealized by assemblies of particles having well-defined geometrical shapes and certain assigned physical properties.

Since the pioneering work by Cundall and Strack (1979a, b), the method became progressively a standard tool in the research area of micromechanics of soils, replacing older popular methods based on physical experiments (such as those using photo-elastic materials). The wide success of DEM relates mainly to its ability to observe in great detail the micromechanical aspects of granular assemblies and to allow for the examination of microscopic mechanisms that are not easily accessible in physical experiments.

Numerical simulations solve the problem of having to disturb the original state of a sample in the laboratory by reconstructing numerically the original assumed state of the sample before disturbance. Numerical simulations also provide complete information

about the sample without having to interrupt the test. Moreover, numerical simulations present the advantage of being very flexible; for example, successive states can be saved and tests repeated from any of these states. Completely different new paths of loading/unloading can be applied to these saved states. Very critical and sensitive parameters can be isolated and studied easily, which is sometimes impossible to do using physical experiments. The most important feature of numerical simulations is that the mechanisms of deformation and all macro-descriptions of the mechanical behaviour of granular systems can be determined with precision. This offers a unique opportunity to investigate macroscopic to microscopic relationships during the micromechanical constitutive modeling of granular materials.

1.2 Research Topic

The most significant feature of granular materials is that their deformation is brought about by mutual sliding of interlocked regions comprised of several particles. Each region moves and behaves as one rigid block. This behaviour contrasts very much with the description of materials as continuous media, where the deformation involves the contribution of each and every material point in the continuum. For this reason, the state of granular materials may vary within comparatively narrow limits, so that a number of deformation mechanisms (including various changes of the nature, shape and size of these interlocked conglomerates or clusters) can progressively come into play within the conventional engineering range of stresses. Another structural effect is rotation of particles which is typical of discontinuous media and especially of granular materials. The effect of

CHAPTER I: INTRODUCTION

rotation on the mechanical behaviour of a strained system of particles increases proportionally to the degree of elongation of particle shapes. For ideally spherical particles however, rotation is not a factor that affects the overall behaviour of the system of particles. One must often, therefore, expect a difference between the behaviour of granular materials with isometric grains (whose dimensions in three mutually perpendicular directions are approximately the same) and that of granular materials with elongated particles.

In the past, most of the work in micromechanics of granular materials was related to numerical simulations of plane assemblies of disks. This choice was dictated by the relative simplicity of the model, because the objectives at that time were to comprehend the complex mechanisms of deformation of granular materials from a microscopic point of view (*e.g.*, Cundall, Drescher and Strack, 1982; Cundall and Strack, 1983). Assemblies of circular particles were satisfactory for this purpose, as they exhibit most of the qualitative properties of granular materials (such as strain softening, volume increase, transition to a steady state at large strains). On the other hand, their strength is low and their deformation properties are quantitatively far too different from real sands. Simulations of three-dimensional assemblies of spheres were the next step in the development of numerical simulations. These assemblies gave more realistic, but still not entirely satisfactory, results regarding strength.

The primary reason for the discrepancies between simulated assemblies of circular particles in two and three dimensions and real materials can be attributed to the simplistic representation of particle shape. Indeed, numerical simulations performed with plane assemblies of polygons and ellipses have shown more realistic trends in relation to the me-

chanical behaviour of real sands (*e.g.*, Rothenburg and Bathurst, 1992, 1993; Ting *et al.*, 1993; Mirghasemi, 1994).

Not only is the mobilized strength comparable with that of a typical sand, but also the initial conditions of particle packing for a dense sand can be more easily replicated with non-circular-shaped particles than with circular particles. It is well known that the behaviour of an assembly of particles greatly depends on the initial conditions of packing and contact density. Usually, the more densely packed the assembly volume is, and the higher the number of contacts present within it, the stronger its material resistance to an applied deviatoric stress tensor.

All previous research studies conducted with non-circular shaped particles pointed out clearly the ability of non-circular particles to be compacted in highly dense structures, and to rotate rather than simply roll as spheres tend to do. Because of particle rotation, assemblies of non-spherical particles will resist deviatoric loads without softening over a larger strain range as compared to assemblies of spherical particles. This is the result of the mobilization of a specific form of anisotropy in particle orientation.

In relation to the state of contacts that can be observed inside assemblies of non-spherical particles, several studies using numerical simulations of polygon-shaped particles (*e.g.*, Mirghasemi, 1994) showed that the average number of contacts per particle is usually comparable to that of disks; however, higher densities can be achieved with polygons than with disks. The difficulty of working with polygons in two dimensions and polyhedra in three dimensions resides in having to deal with several types of contacts between particles: face-to-face, face-to-edge, face-to-corner, edge-to-edge, and edge-to-cor-

ner. For some of these contact types, the contact normal vector is not uniquely defined, and this limits the use of such models to a special class of problems characterized by small deformations and a predictable evolution of the contact normal direction. An example is the simulation of joints between blocks of rock. Large-scale deformations, however, are more difficult to simulate with these shapes.

An alternative to the polyhedra is the triaxial ellipsoid shape. The triaxial ellipsoid is characterized by a unique continuous outward normal vector on its surface. In the general case, it is a quadric surface which can be fully defined by three angles of orientation, two aspect ratios, and an average length measure.

Several early studies in the field of sedimentary petrology, concerning methods of characterizing the shape of granules that make up soils, suggested that the triaxial ellipsoid can approximate fairly well the gross shape of rounded granules (*e.g.*, Krumbein, 1941; Aschenbrenner, 1956). Next to spheres, the triaxial ellipsoid is also the simplest geometrical shape, and is also flexible enough to model a wide range of shapes that can vary from rod-like, to equi-dimensional, to blade, and disk-like geometries.

These considerations, added to the fact that planar systems of non-circular particles do not replicate well the volumetric behaviour of real three-dimensional systems, motivated the work with ellipsoidal particles to study the behaviour of dense rounded granular systems.

An existing three-dimensional discrete element model of spheres called TRUBAL, originally developed by Cundall and Strack (1979c), Strack and Cundall (1984), was modified to accommodate the new particle shape. The modified version of the program was

used to produce the results reported in this study.

1.3 Objectives

The objectives of this study are multi-fold:

1. Develop a three-dimensional discrete element model to simulate the behaviour of assemblies of ellipsoids by modifying the existing discrete model TRUBAL for spheres. This task consisted mainly of implementing and validating an inter-ellipsoid contact detection scheme and modifying the equations of the mechanics of rigid spheres to rigid ellipsoids, as well as implementing new procedures of data extraction to interpret the results within the framework of the objectives set for this study.
2. Conduct a series of constant mean pressure deviatoric compression tests on assemblies of ellipsoids of different sizes (27, 125, and 1000 particles) and different confining pressures, with an optimal shape of particles (corresponding to optimal initial conditions of particle packing and contact densities) and an inherent anisotropy. These tests were intended to study the effects of assembly size, particle shape, inherent anisotropy, and confining pressure on the macro-mechanical and micro-mechanical behaviour of assemblies of ellipsoids.
3. Derive a Stress-Force-Fabric relationship for ellipsoids by including the direct effect of shape into the equations of the average stress tensor for particulate systems, and to validate the derived equation using results of the above numerical tests on the larger-sized sample of ellipsoids.

4. Interpret the derived relationship from the perspective of expressing the mobilized material shear strength in terms of contributions due to microscopic development of anisotropy throughout the course of deformation, and also to evaluate the effects of inherent anisotropy and particle shape on the mobilized shear strength.
5. Conduct statistics on contacts and particles using parameters describing specific shape-related anisotropies in particle orientation and contact occurrence around the surface of an ellipsoid, and to use these statistics to examine the hypothesis that the creation of contacts around a particle is mainly controlled by its shape.
6. Develop a model for estimating the effect of shape on the magnitude of anisotropy in contact normal orientations, in two and three dimensions.

1.4 Organization of the Thesis

The thesis is organized as follows:

In Chapter 1, a general background on granular materials and numerical simulations by the discrete element method is given. An outline of the topic and objectives of research is also presented.

In Chapter 2, the approach of microscopic characterization of the behaviour of a granular material is discussed. A new method of space partitioning for the grouping of contacts according to the direction of their contact normals is established and compared to the classical partitioning of the space by a single set of spherical coordinates. Finally, a study of

CHAPTER 1: INTRODUCTION

the influence of fourth order terms of Fourier series approximations of microscopic distributions is presented, based on results of numerical simulations with assemblies of ellipsoids.

In Chapter 3, the discrete element method for ellipsoids and its implementation in the modified program TRUBAL are presented. The data structures and features of the modified program are listed and discussed. The algorithm to generate samples of ellipsoids from assemblies of spheres is also discussed.

In Chapter 4, the inter-ellipsoid contact detection scheme and the flow chart of the algorithm of contact calculation are presented. A validation of the program by simple tests and a comparison with a well established, two-dimensional, inter-ellipse contact detection algorithm on a sample of nearly 3000 contacts are reported.

In Chapter 5, results of particle growth tests and (p =constant) deviatoric compression tests with ellipsoids are presented and analyzed from the microscopic and macroscopic points of view. Influences of assembly size, particle shape, and applied confining pressure are emphasized during the discussion of results.

In Chapter 6, the Stress-Force-Fabric relationship for ellipsoids is derived and verified numerically. Based on the Stress-Force-Fabric relationship, an explicit equation relating the mobilized material shear strength to microscopic contributions (due to development in anisotropy) is also derived. This relationship is used to measure the impact of particle shape, inherent anisotropy, and the different aspects of load-induced microstructural anisotropies on the shearing capacity of assemblies of ellipsoids.

In Chapter 7, an attempt is undertaken to interrelate different fabric anisotropies,

CHAPTER I: INTRODUCTION

namely, anisotropies in contact normal orientations, particles orientations, and local contact vector orientations. Predictions of the two-dimensional model are discussed.

In Chapter 8, a summary of the objectives and achievements of this study are listed. Recommendations for future research are also suggested.

The references are listed in alphabetical order of author's name.

Three Appendices are added as follows:

In Appendix A, the method of partitioning the space of orientations (unit sphere) by near uniform class sizes is presented.

In Appendix B, the method implemented in the modified program TRUBAL to solve the inter-ellipsoid intersection equation is presented.

Finally, in Appendix C, a method of deriving analytical expressions of useful 3D-integrals involving any arbitrary number of products of unit vector components in spherical coordinates is suggested.

CHAPTER II: MICROSCOPIC CHARACTERIZATION OF GRANULAR MATERIAL BEHAVIOUR

2.1 Load Transfer in Granular Materials

The first experiments involving collections of particles under external load attempted to observe the transfer of forces from the boundaries of the sample to chains of contacts responsible for keeping the assembly stable. The early physical experiments used the photoelasticity technique to visualize and measure the magnitude of the forces transmitted at contact points (*e.g.*, Dantu, 1957; De Josselin De Jong and Verruijt, 1969).

The results of these studies showed that under anisotropic load conditions (unequal forces applied at the boundaries of the sample) the response of the assembly was anisotropic.

The contacts with an orientation sub-parallel to the major direction of load carried the

largest proportion of the transferred load while the contacts with an orientation sub-parallel to the minor direction of load carried the smallest proportion. In the same effort to oppose the anisotropic applied load, the contacts with normal vectors sub-parallel to the major direction of load (load-carrying contacts) were mainly preserved in number while the number of lateral contacts facing the minor load-direction steadily decreased with strain.

The described qualitative features of load transfer in granular materials can be well illustrated by reference to an experiment on an assembly of photo-elastic disks by De Josselin De Jong and Verruijt (1969), shown in Figure 2•1a. The pattern of line segments in the figure represents orientations and magnitudes of interparticle forces in an assembly of disks confined by rectangular platens.

The assembly is under a deviatoric boundary load. The thickness of lines is proportional to the magnitude of contact forces. Higher forces can be identified by contacts oriented towards the direction of maximum boundary load. To emphasize this bias, Figure 2•1b and Figure 2•1c illustrate groups of vertical and horizontal load-bearing contacts represented by lines connecting the centroids of particles. The difference between the numbers of vertical and horizontal contacts is a measure of geometrical anisotropy.

The fact that vertical and horizontal contacts also carry forces of distinctly different magnitudes illustrates an important link between microscopic geometry and characteristics of load transfer.

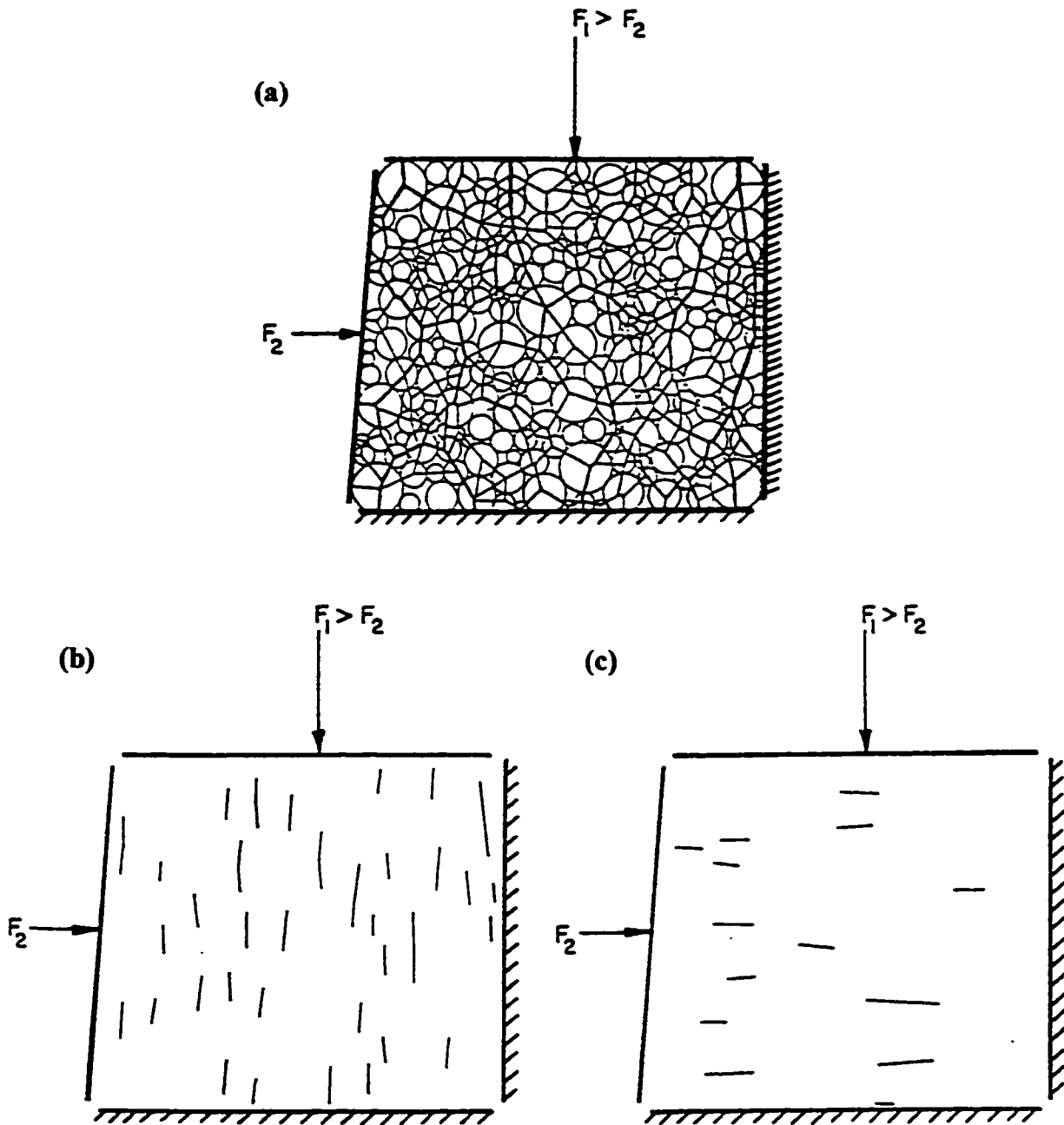


Figure 2-1 Biaxial compression test on an assembly of photo-elastic disks (after De Josselin De Jong and Verruijt, 1969)
(a) Distribution of contact forces
(b) Vertical contacts
(c) Horizontal contacts

Although the forces acting at contacts with similar orientations vary in a seemingly random manner, average forces over such groups are constrained by conditions of static equilibrium and fabric characteristics. As such, the parameters describing the anisotropy in the average contact forces and contact orientations can be related to the boundary loads.

2.2 Static Equilibrium and the Average Stress Tensor

An average stress tensor for particulate systems can be defined from considerations of static equilibrium of an assembly of randomly shaped particles subjected to a uniform set of boundary tractions T^p on its surface as shown in Figure 2•2. The tractions are assumed to apply to a continuous membrane and therefore derivable from a continuous boundary stress tensor σ_{ij}^p .

From equations of static equilibrium of the interface between the applied external load and the recipient boundary particles of this load, it can be shown that the boundary stress tensor σ_{ij}^p can be related to the forces and vectors at contact points β between the boundary and adjacent particles of the assembly (Figure 2•2).

The relationship proposed by Rothenburg (1980), based on the average stress tensor of continuum mechanics can, be written as:

$$\sigma_{ij}^p = \frac{1}{V} \sum_{\beta \in S} f_i^p x_j^p \quad (2•1)$$

where x_j^p and f_i^p are the position and force vectors at boundary contact points β , respectively; and V is the assembly volume.

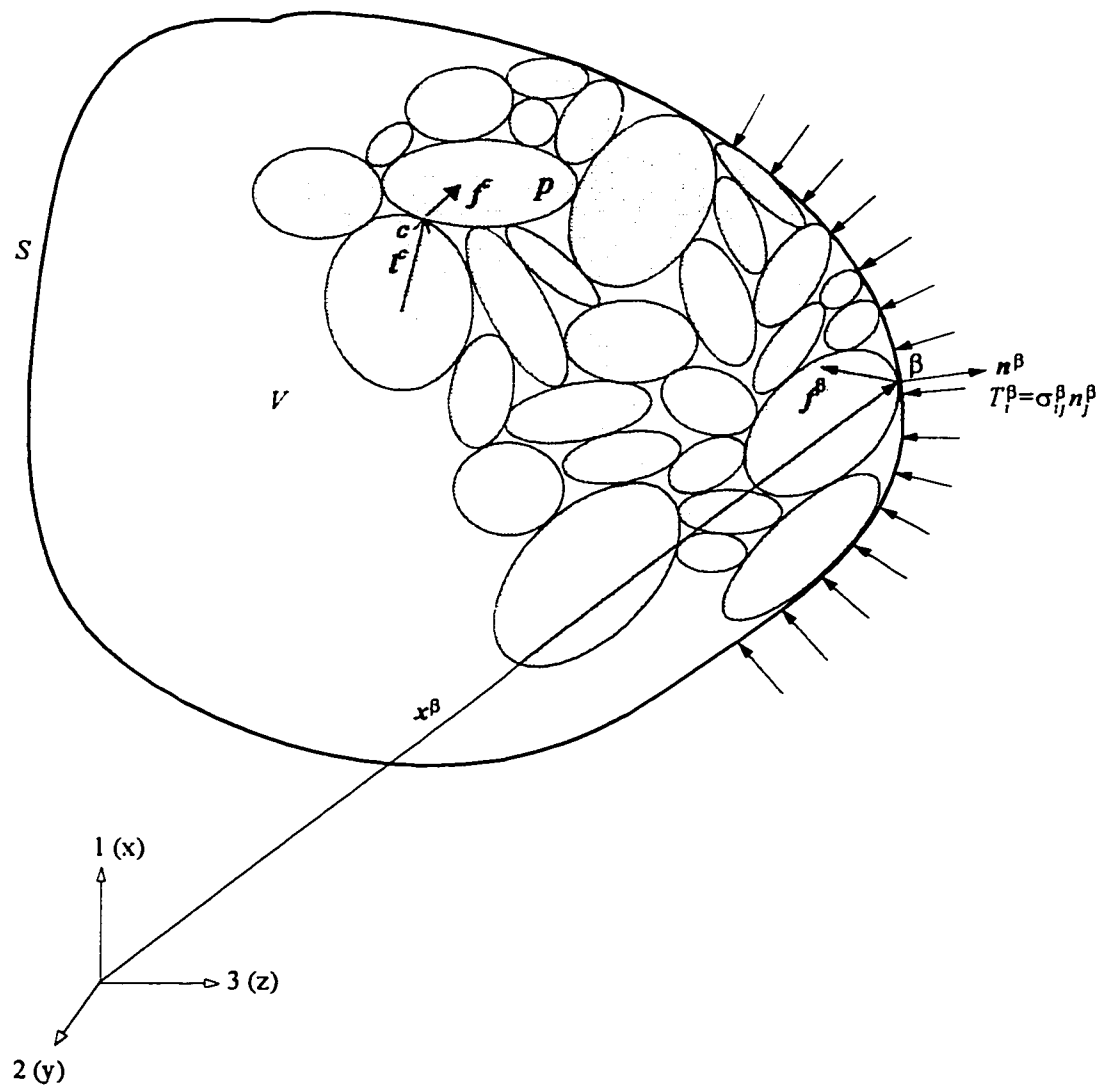


Figure 2.2 Elements of definition of the stress tensor for a granular system

A more convenient form of this relationship which makes no explicit reference to the shape of the studied volume can be obtained by noting that for an assembly in static equilibrium, the following relationship is satisfied between boundary and internal forces:

$$\sum_{\beta \in S} f_i^\beta x_j^\beta = \sum_{c \in V} f_i^c l_j^c \quad (2 \cdot 2)$$

where l_j^c and f_i^c are the position and force vectors at particle-to-particle contact points (c), respectively; therefore:

$$\sigma_{ij}^\beta = \frac{1}{V} \sum_{c \in V} f_i^c l_j^c \quad (2 \cdot 3)$$

The relationship (2• 3) was derived under different forms many times by researchers using different approaches (*e.g.*, Weber, 1966; Dantu, 1968; Rothenburg, 1980; Christoffersen *et al.*, 1981; amongst others).

It can be shown that (2• 3) holds inside the assembly as well, and as such could be used to define the average stress tensor for granular materials in static equilibrium.

2.2.1 Symmetry of the Average Stress Tensor

For an arbitrary particle, p , shown in Figure 2•2, static equilibrium translates into the following system of vectorial equations:

$$\left\{ \begin{array}{l} \sum_{c \in p} f^c = 0 \\ \sum_{c \in p} l^c \otimes f^c = 0 \end{array} \right. \quad (2 \cdot 4)$$

where the moment equation is written with respect to the center of the particle. The moment equations about any two arbitrary distinct points, O_1 and O_2 , are equivalent be-

cause:

$$\sum_{c \in p} (O_2 c - O_1 c) \otimes f^c = O_1 O_2 \otimes \sum_{c \in p} f^c = 0 \quad (2\bullet 5)$$

Written in a component form, the moment equilibrium equations become:

$$\sum_{c \in p} \varepsilon_{ijk} l_j^c f_k^c = 0 \quad i=1, 3 \quad (2\bullet 6)$$

where ε_{ijk} is the 3rd order alternating tensor for calculating cross products of vectors as:

$$\varepsilon_{ijk} = \begin{cases} 1 & \text{if } (ijk) \text{ even} \\ -1 & \text{if } (ijk) \text{ odd} \\ 0 & \text{if repeated indices occur} \end{cases} \quad (2\bullet 7)$$

Even permutations of the triplet (ijk) are (123) , (231) , and (312) . Odd permutations are (132) , (213) and (321) .

Summing up the relationships in (2• 6) over all particles p in the system:

$$\sum_{c \in V} \varepsilon_{ijk} l_j^c f_k^c = 0 \quad i=1, 3 \quad (2\bullet 8)$$

Elimination of ε_{ijk} from the above equation results in the first component moment equation being re-expressed as:

$$\sum_{c \in V} f_2^c l_3^c = \sum_{c \in V} f_3^c l_2^c \quad (2\bullet 9)$$

Similarly, for any pair of indices (i, j) :

$$\frac{1}{V} \sum_{c \in V} f_i^c l_j^c = \frac{1}{V} \sum_{c \in V} f_j^c l_i^c \quad (2\bullet 10)$$

Or:

$$\sigma_{ij} = \sigma_{ji} \quad (2\bullet 11)$$

The defined stress tensor has all of the properties of the Cauchy stress tensor defined for continua, for statistically homogeneous infinite systems of particles (Rothenburg and Selvadurai, 1981).

2.3 Microscopic Characteristics of Granular Assemblies

During shear deformations, cohesionless granular materials exhibit continuous changes in the evolution of interparticle forces and internal geometry. In particular, shear deformations lead to changes in magnitudes and distribution of interparticle forces. Simultaneously, there are changes in the number of load-carrying contacts and the distribution of their normal orientations.

Both the number of contacts and their orientations are essential indicators of the state of the fabric and should be monitored to measure their evolution during deformation. This is done by determining some characteristic parameters.

2.3.1 The Coordination Number

The *particle coordination number* refers to the number of contacts a particle shares with neighbouring particles. In the example shown in Figure 2•3, the central particle *A* has a coordination number, $\gamma_A = 4$.

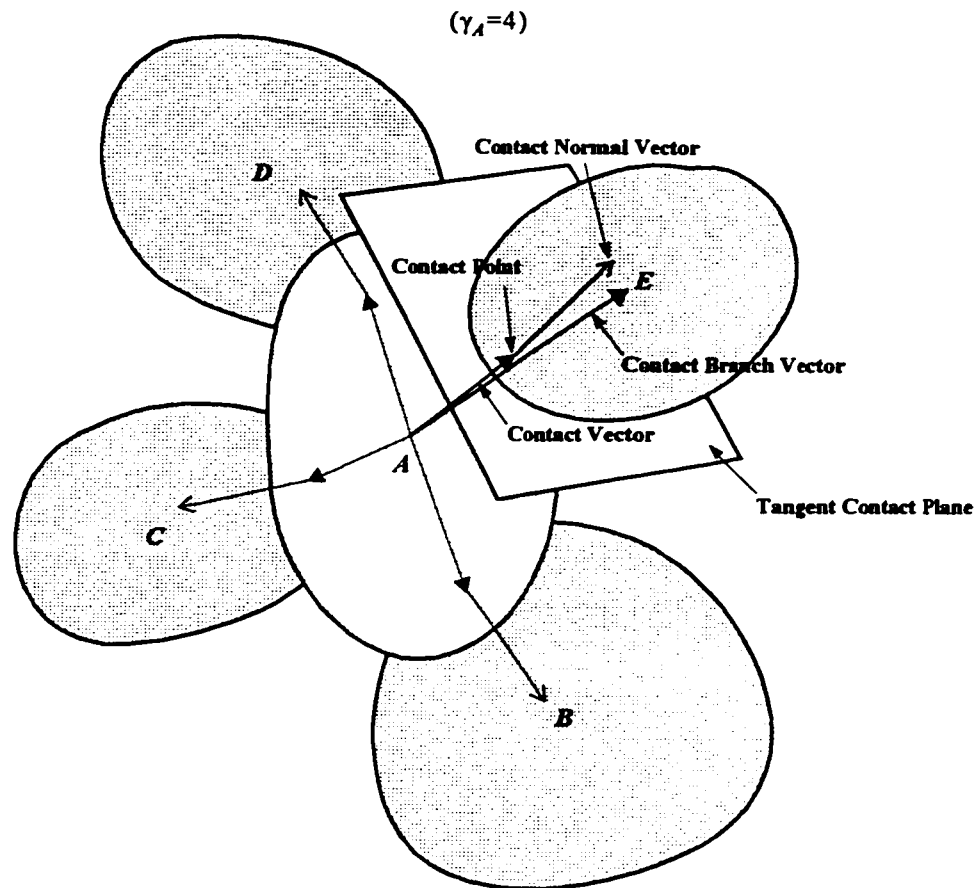


Figure 2-3 Definition of the particle coordination number, the contact normal vector, and the contact vector

The *assembly coordination number* is the average number of contacts per particle, it is therefore equal to the ratio:

$$\gamma = \frac{M}{N} \quad (2\bullet 12)$$

M is the total number of contacts in the assembly (twice the number of physical contacts); N is the total number of particles in the assembly.

Results from numerous investigations show that the assembly coordination number is strongly correlated to common measures of particle packing such as the assembly density or void ratio (Smith *et al.*, 1929; Oda, 1977).

The mechanical behaviour of an assembly of particles largely depends on the initial number of contacts in the assembly. In general, an assembly with a high coordination number is more stable and less mobile than an assembly with a low average coordination number.

2.3.1.1 The Average Contact Density

The *average contact density* is defined by the ratio of the total number of contacts, M , to the volume, V , of the assembly of particles:

$$m_v = \frac{M}{V} \quad (2\bullet 13)$$

Parameters m_v and γ are related through the packing density $\rho = V_s/V$ and the average particle volume $\bar{v}_p = V_s/N$ as:

$$m_v = \frac{\rho\gamma}{\bar{v}_p} \quad (2\bullet 14)$$

where V_s is the volume of solids in the assembly.

The packing density ρ and the void ratio e are related by $\rho = 1/(1 + e)$. Therefore, the average contact density can be expressed in terms of the void ratio as:

$$m_v = \frac{\gamma}{\bar{v}_p(1 + e)} \quad (2.16)$$

The contact density or the coordination number are limited descriptors of the state of packing as they carry no information on orientation of interparticle contacts, shape or size of particles.

Considering that intergranular forces are strongly dependent upon the orientation of contacts, a complete description of load transfer in granular assemblies requires information on the distribution of contact orientations. The unit vector normal to the tangent contact plane at the contact point characterizes the contact orientation (Figure 2.3).

Another important fabric element used to characterize the particle size and shape at a particular contact point is the contact vector or the contact branch vector (Figure 2.3).

2.3.2 Contact Normal Orientations

The load-induced anisotropy in contact normal orientations is not confined to the maximum and minimum load directions, but affects all directions of the space.

A convenient means of illustrating a possible bias in the contact normal orientation distribution is by plotting the histogram of the proportion of contacts with normals falling inside a series of adjacent orientation classes that partition the full orientation space (represented by the unit sphere).

2.3.2.1 Spherical Partitioning of the Orientation Space

The unit sphere is partitioned into a *finite* number of group orientations to accommodate the *finite* number of contacts in the assembly. The most-common partitioning of the orientation space utilizes meridian and polar curves in spherical coordinates with reference to a single coordinate system. Spherical coordinates provide the easiest way to perform the partition and the classification of contacts into their parent classes. A group of orientations (g) in this system of coordinates is characterized by an average orientation in terms of a unit vector n^g , and a class amplitude $|\Delta n^g|$.

Since the unit vector n^g is defined by the pair of angles (α^g, β^g) , the partition is often made with respect to these angles, and constant angle intervals are selected; for example, $\Delta\alpha = \Delta\beta = 10^\circ$ (Figure 2•4a). This simple choice of angle intervals results in the partition pattern displayed in Figure 2•4b.

This simple and convenient partitioning, however, suffers from a serious drawback. The overall class amplitude (solid angles) of the partition class $|\Delta n^g|$ is not constant, but varies with the position of the group. Therefore, during the grouping process, the large classes are likely to contain more contacts than they would if the partition was spatially uniform.

On the other hand, the smaller classes will contain fewer contacts. Since the averaging of contact force and contact vector components over a class of orientation is affected by the number of contacts, the importance of having equal size classes before grouping contacts in classes is appreciated.

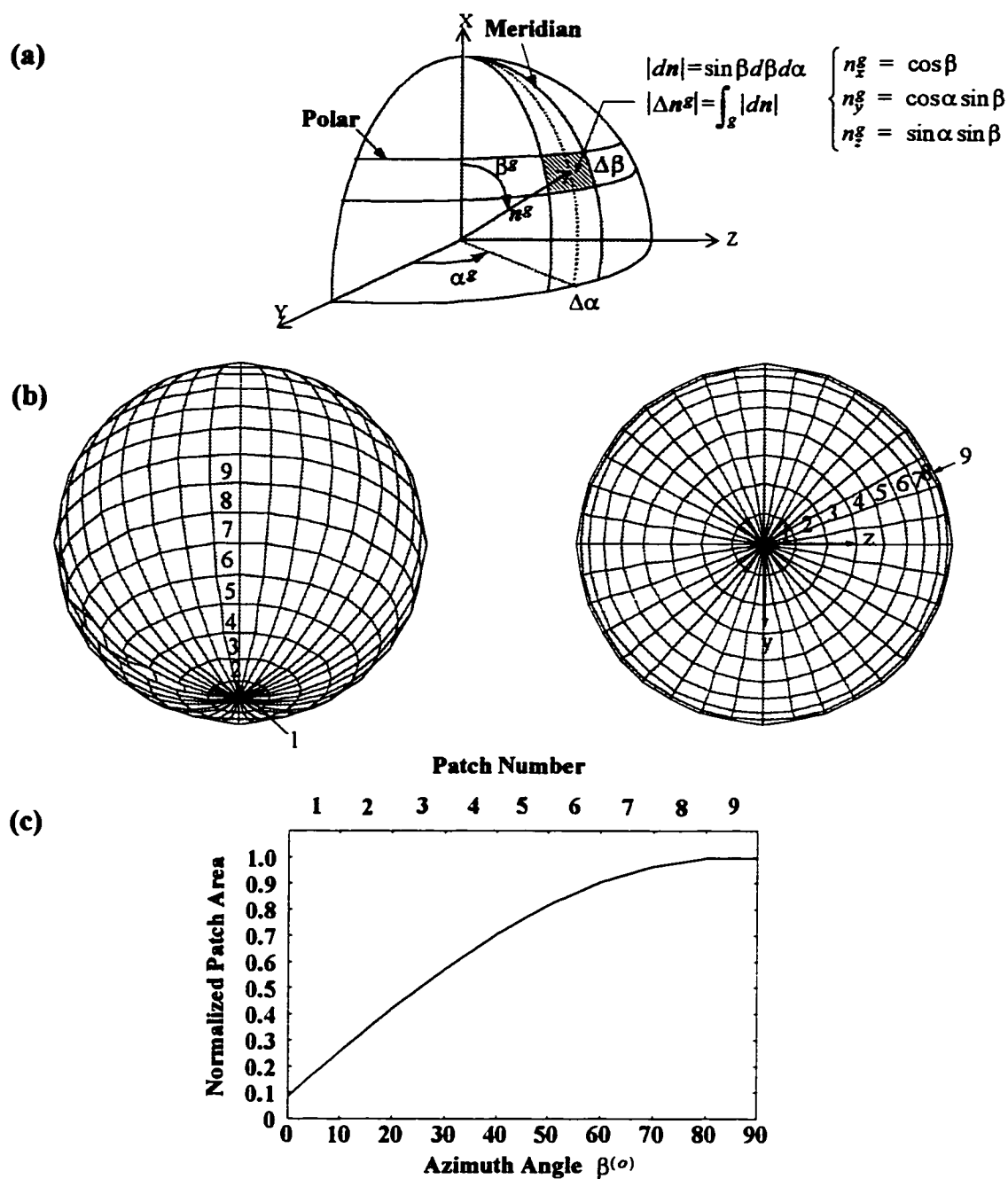


Figure 2-4 Spherical partitioning of the unit sphere
(a) Spherical coordinates
(b) Distribution of patches
(c) Variation of patch area with position

The spherical partitioning with constant $\Delta\alpha$ and $\Delta\beta$ is definitely not a good choice since the range of variation of the class amplitudes is too large to allow an equitable contact grouping process. The plot of $|\Delta n^s|/\Delta\alpha\Delta\beta$ versus β in Figure 2•4c illustrates this variation.

Analytically, $|\Delta n^s|$ is expressed as:

$$|\Delta n^s| = \int_s \sin \beta d\beta d\alpha = \left[\cos(\beta^s - \frac{\Delta\beta}{2}) - \cos(\beta^s + \frac{\Delta\beta}{2}) \right] \Delta\alpha \quad (2\bullet 16)$$

If $\Delta\beta$ is small, then:

$$|\Delta n^s|/(\Delta\alpha\Delta\beta) \equiv \sin(\beta^s). \quad (2\bullet 17)$$

The spherical partitioning is therefore characterized by large class amplitudes near $\beta^s = 90^\circ$, and very small class amplitudes towards $\beta^s = 0^\circ$.

2.3.2.2 Near Uniform Partitioning of the Orientation Space

In order to reduce the large scatter of orientation class sizes, a special partitioning was developed which gives nearly constant class amplitudes throughout the orientation space. The technique uses the classical partitioning of the unit sphere with polars and meridians, but combines all three sets of spherical coordinates (xyz), (yzx) and (zxy) at once.

The method of partitioning is illustrated with reference to a region extending over 1/8 of the unit sphere, as shown in Figure 2•5a. The partition of this region is performed three times. At each time, the meridians originating from one pole intersect the meridians from another pole, generating, in the process, the partition of one third of the region with rectangular patches.

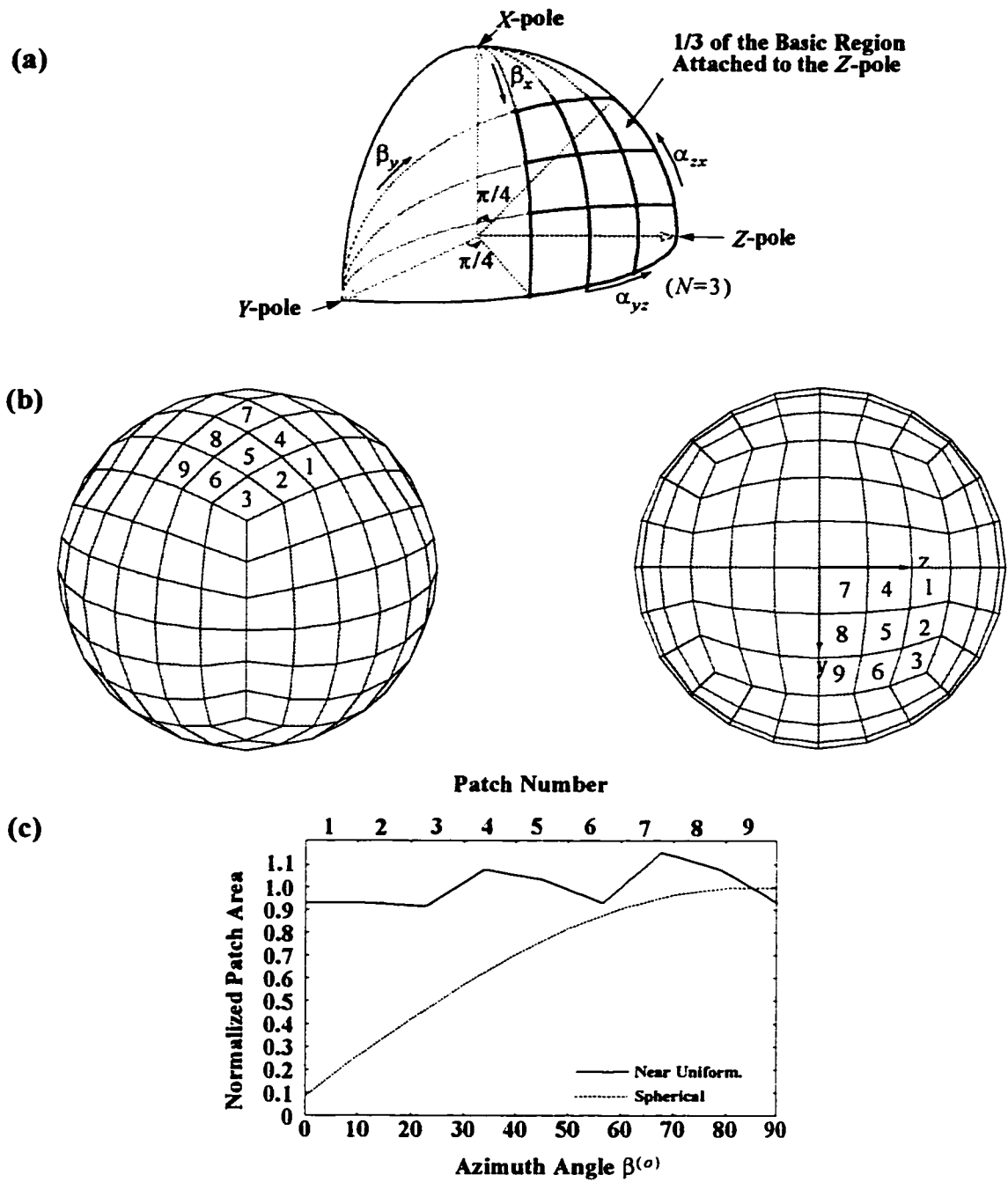


Figure 2-5 Nearly uniform partitioning of the unit sphere
 (a) Partitioning of the basic region
 (b) Distribution of patches
 (c) Variation of patch area with position

The third of the region (equal to $1/24$ of the total surface area) is called “*basic region*”. It is partitioned into $N \times N$ patches, where N is the number of class intervals in $[0, \pi/4]$. In the example shown in Figure 2•5a, the partitioning is performed with $N = 3$.

The remaining sphere’s partition is executed in a manner similar to that of the basic region and can be obtained using the symmetries of the sphere. Therefore, by using this method, only $1/24$ of the total sphere surface is effectively partitioned. The final result is shown in Figure 2•5b.

The distribution of patch areas in the basic region was computed for several values of the interval subdivision number N . Values of $N = 3$ and $N = 4$ provided the best partitions with regard to uniformity of class sizes.

The plot in Figure 2•5c illustrates the variation in the normalized patch area for a 3×3 basic region. As can be seen, the distribution is nearly uniform.

The near uniform partitioning obtained for $N = 4$ is used for histogram generation throughout this thesis. With this choice, the three-dimensional space is covered by $24 \times (4 \times 4) = 384$ classes of orientation.

Considering that the number of physical contacts in a dense 1000 ellipsoid assembly ranges between 3000 (near steady-state of deformation) and 6000 (densest possible state), the average number of contacts per class will vary between 15 and 30. This range of numbers of contacts per class is low; however, it is still satisfactory for calculating meaningful averages over groups of contacts.

The details of the technique and the method of locating and calculating class sizes, as well as assigning contact normals to their parent classes, are described in Appendix A.

The procedure of contact normal assignment in the near uniform partitioning was implemented in the modified computer simulator TRUBAL to produce the plots of spatial histograms presented throughout the study.

2.3.2.3 Contact Normal Orientation Distribution Function

Once the grouping is performed, the proportion of contacts in each group, $\Delta M^g/M$, is calculated.

In order to eliminate the effect of class amplitude, a density of a probability type function is defined as:

$$E(n^g) = \frac{\Delta M^g}{M|\Delta n^g|} \quad (2 \cdot 18)$$

If there is any bias in contact normal proportions, it will show on the plot of the function $E(n)$. The idea of representing the fabric of large systems of particles with a continuous density of probability type function was first introduced by Horne (1965).

Figure 2•6 illustrates three typical profiles of $E(n)$ showing isotropic, moderately anisotropic, and strongly anisotropic distributions. If the distribution is isotropic, its shape is close to spherical. With increasing anisotropy, the shape mutates to a “peanut” shape.

For a very large system of particles, the number of contacts is very large, and the partitioning of the orientation space in classes can be made finer and finer. The refinement can extend up to a limit where the number of contacts per class is still reasonably large for performing adequate averaging over contacts in the class.

As the classes of orientation become smaller, the class representatives become closer, and $E(n)$ tends to be continuous.

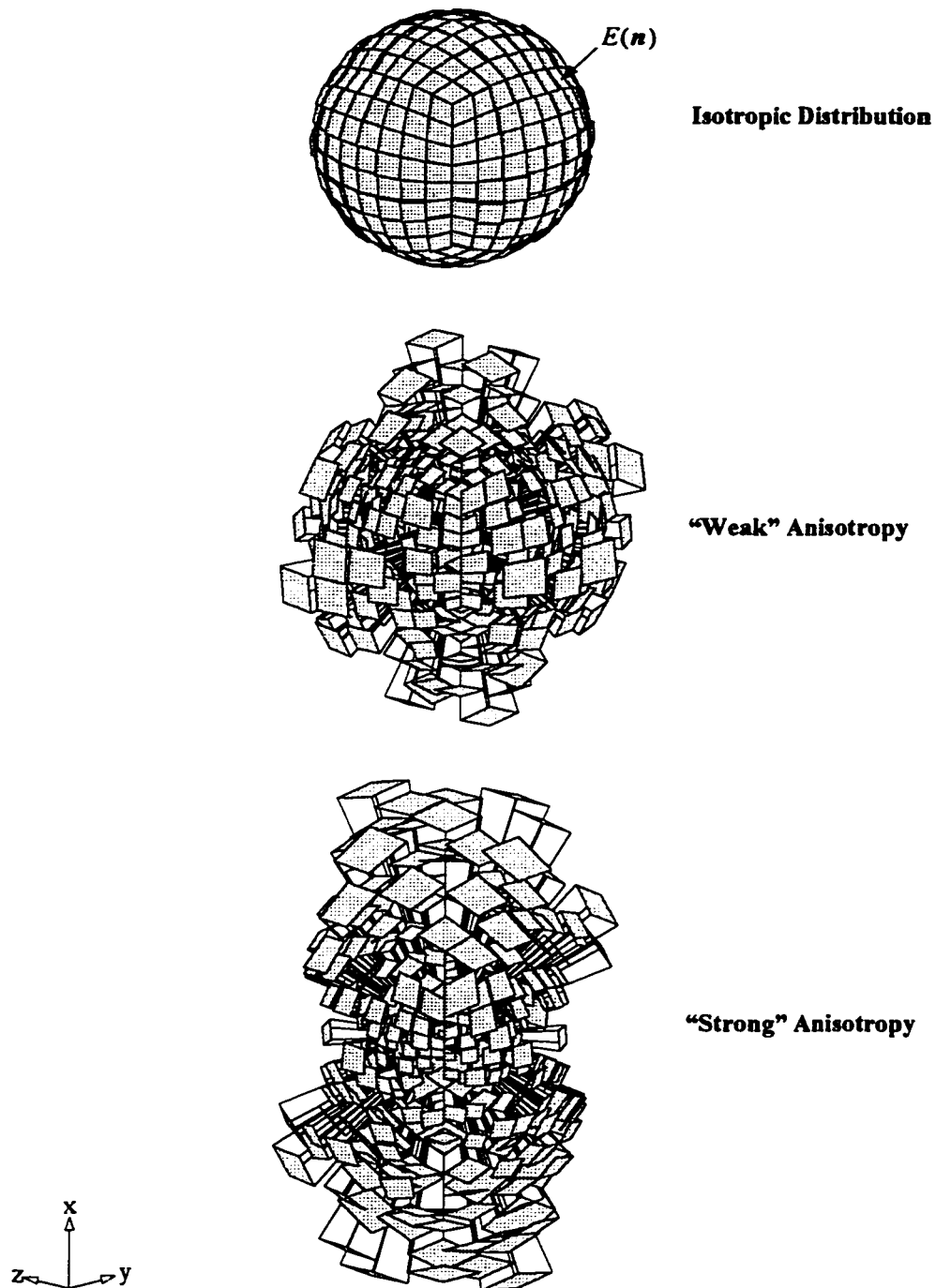


Figure 2-6 Typical shapes of the contact normal orientation distribution

In the limiting case of an infinitely large number of particles, any orientation in the space will be shared by many contacts and $E(\mathbf{n})$ is continuous. However, actual systems are finite and moderately large, so that only a continuous approximation of the actual discrete $E(\mathbf{n})$ can be calculated to model the true distribution of contact normal orientations. The modeling of complex distributions with simple continuous models helps eliminate secondary effects, and emphasizes major trends in these distributions.

Equation (2• 18) can be written as:

$$\Delta M^g = ME(\mathbf{n}^g)|\Delta \mathbf{n}^g| \quad (2• 19)$$

By summing up the above expression over all groups of contact normals, the following identity is obtained:

$$\sum_g E(\mathbf{n}^g)|\Delta \mathbf{n}^g| = 1 \quad (2• 20)$$

For an infinite system $E(\mathbf{n})$ is continuous and the discrete sum is an integral over the unit sphere:

$$\int_{\mathbf{n}} E(\mathbf{n}) d\mathbf{n} = 1 \quad (2• 21)$$

$E(\mathbf{n})$ can be represented by an infinite Fourier series of even order terms because of its symmetry ($E(-\mathbf{n}) = E(\mathbf{n})$). It is generally sufficient to limit the expansion to the second-order terms to obtain a good approximation of numerically observed distributions. But, there are cases where a fourth-order term is not totally negligible and must be taken into account.

For most of the of physical experiments and numerical simulations performed with moderately large specimens, including those reported in this study, a good approximation

of the contact orientation distribution is provided by the second-order Fourier series:

$$\begin{cases} E(\mathbf{n}) = \frac{1}{4\pi}(1 + a'_{ij}n_i n_j) \\ a'_{ij} = a'_{ji} \quad a'_{ii} = 0 \end{cases} \quad (2\bullet 22)$$

If all orientations of the space are filled by the same number of contacts, the distribution is uniform and isotropic. In this case, $E(\mathbf{n}) = 1/4\pi$ and $a'_{ij} = 0$. If on the other hand, the classes are disproportional and exhibit favored contact normal orientations, the distribution is anisotropic, and $a'_{ij} \neq 0$. For this reason, a'_{ij} is called *tensor of anisotropy*.

Isotropic distributions are usually encountered in assemblies under isotropic load conditions. Anisotropic distributions characterize either a state of initially anisotropic assemblies, due, for instance, to some depositional history (*inherent anisotropy*), or initially isotropic materials which became anisotropic to accommodate an applied anisotropic load (*induced anisotropy*).

2.3.2.4 The Fabric Tensor

Information about the principal directions and magnitude of anisotropy in contact normal orientations are obtained from the tensor of anisotropy a'_{ij} . This tensor must be deviatoric, *i.e.*, $a'_{kk} = 0$, because by writing $E(\mathbf{n})$ in the form expressed in (2• 22), the term $a'_{ij}n_i n_j$ represents a deviation from the isotropic state.

The tensor a'_{ij} is symmetric, *i.e.*, $a'_{ij} = a'_{ji}$. This is a consequence of the symmetry of another second-order tensor called the *fabric* tensor; defined by the following discrete sum:

$$R_{ij} = \frac{1}{M} \sum_{c \in V} n_i^c n_j^c \quad (2 \bullet 23)$$

The fabric tensor was first introduced by Satake (1978) as a measure of changes in the fabric of granular materials. This parameter emerges naturally as a measure of stress in an assembly of particles characterized only by an induced anisotropy in contact normal orientations.

For simplicity, all contact forces are assumed to be constant in magnitude (this happens for example if the system of particles undergoes an isotropic hydrostatic pressure). They are assumed to act on smooth mono-size spheres of radius l^o (no shear components). In this case, contact vectors and contact normal vectors are colinear:

$$\begin{cases} f_i^c = f^o n_i^c \\ l_j^c = l^o n_j^c \end{cases} \quad (2 \bullet 24)$$

The stress tensor in (2• 3) simplifies to:

$$\sigma_{ij} = \frac{l^o f^o}{V} \sum_{c \in V} n_i^c n_j^c \quad (2 \bullet 25)$$

Or:

$$\sigma_{ij} = m_v l^o f^o R_{ij} \quad (2 \bullet 26)$$

Note that, in the general case, the stress tensor is not directly proportional to R_{ij} but depends on other tensorial quantities representing anisotropies in contact forces and in contact vectors.

2.3.2.5 Measurement of Anisotropy in Contact Normal Orientations

The model of $E(\mathbf{n})$ in (2• 22) is strictly valid for infinite systems of particles, but it can be used to approximate finite systems.

By multiplying the left and right hand sides of (2• 18) by $n_i^g n_j^g$ (for the nine possible combinations of pair of indices (i, j)), nine new equations for the group (g) are obtained as:

$$\Delta M^g n_i^g n_j^g = M E(\mathbf{n}^g) n_i^g n_j^g |\Delta \mathbf{n}^g| \quad (2• 27)$$

By summing the last expression over all groups in the assembly:

$$\sum_g \Delta M^g n_i^g n_j^g = M \sum_g E(\mathbf{n}^g) n_i^g n_j^g |\Delta \mathbf{n}^g| \quad (2• 28)$$

By definition of an orientation group:

$$\Delta M^g n_i^g n_j^g = \sum_{c \in g} n_i^c n_j^c \quad (2• 29)$$

Therefore:

$$\sum_g \Delta M^g n_i^g n_j^g = \sum_g \sum_{c \in g} n_i^c n_j^c = \sum_{c \in V} n_i^c n_j^c \quad (2• 30)$$

The comparison of equations (2• 23), (2• 28), and (2• 30) yields:

$$R_{ij} = \sum_g E(\mathbf{n}^g) n_i^g n_j^g |\Delta \mathbf{n}^g| \quad (2• 31)$$

For an infinite assembly of particles, the discrete sum in (2• 31) is replaced by a continuous integral over the unit sphere, thus:

$$R_{ij} = \int_{\mathbf{n}} E(\mathbf{n}) n_i n_j d\mathbf{n} \quad (2• 32)$$

Finally, by substituting the model expression of $E(\mathbf{n})$ in (2• 22) and integration:

$$a'_{ij} = \frac{15}{2} R'_{ij} \quad (2\bullet 33)$$

where $R'_{ij} = R_{ij} - \delta_{ij}/3$ stands for the deviator of the fabric tensor.

Based on the above relationship, the symmetry of a'_{ij} is a consequence of the symmetry of R_{ij} . The relationship is also valuable for estimating the components of the tensor of anisotropy a'_{ij} for finite systems such as those used in numerical simulations, where R_{ij} can be measured by knowing the full state of contacts.

A similar relationship was used by Bathurst (1985) for model estimation of contact normal orientation distribution for numerically simulated plane systems of disks.

2.4 Distribution of Average Contact Forces

Two rigid particles, A and B , in contact at some point, c , are shown in Figure 2•7. Two forces with equal magnitudes and opposite directions are generated at the contact point. If \mathbf{n} is the contact normal unit vector exterior to particle A , and \mathbf{f} is the vector force representing the action of particle A on particle B , then $-\mathbf{n}$ is the unit vector exterior to particle B and $-\mathbf{f}$ represents the action of particle B on particle A . To the pair of contact normals $(\mathbf{n}, -\mathbf{n})$ is associated the pair of contact forces $(\mathbf{f}, -\mathbf{f})$.

The following symmetries can be derived from the above association:

$$\begin{cases} f(-\mathbf{n}) = -f(\mathbf{n}) \\ f^i(-\mathbf{n}) = (-f_i)(-n_i) = f^i(\mathbf{n}) \\ f_i(-\mathbf{n}) = -f_i - f^i(-n_i) = -(f_i - f^i n_i) = -f_i(\mathbf{n}) \end{cases} \quad i=1, 3 \quad (2\bullet 34)$$

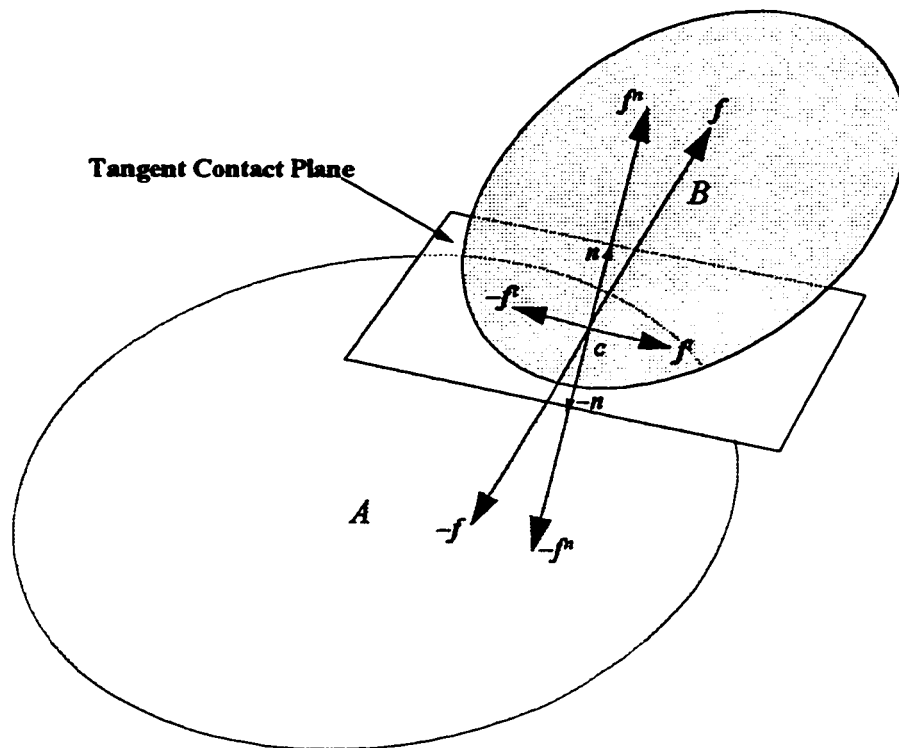


Figure 2-7 Normal and tangential contact force components

where $f^n n_i$ and f_i^t ($i=1, 3$) are the normal and tangential components of the contact force vector, respectively:

$$\begin{cases} f^n = f_k n_k \\ f_i^t = f_i - f^n n_i \end{cases} \quad i=1, 3 \quad (2\cdot 35)$$

The above symmetries at individual contacts are transmitted to averages over groups of contacts of similar orientation.

The distribution of average normal contact forces $\bar{f}^n(\mathbf{n})$ must be symmetric, thus it can be described by a truncated Fourier series of even orders. The expansion up to the second-order term can be written as:

$$\begin{cases} \bar{f}^n(\mathbf{n}) = \bar{f}^0 (1 + a_{ij}^n n_i n_j) \\ a_{ij}^n = a_{ji}^n, \quad a_{ii}^n = 0 \end{cases} \quad (2\cdot 36)$$

The distribution of average tangential force components $\bar{f}_i^t(\mathbf{n})$ (odd) can be approached by a truncated Fourier series of odd orders such as:

$$\begin{cases} \bar{f}_i^t(\mathbf{n}) = \bar{f}^0 (a_{ij}^t n_i - a_{kl}^t n_k n_l n_i) \\ a_{ij}^t = a_{ji}^t, \quad a_{ii}^t = 0 \end{cases} \quad i=1, 3 \quad (2\cdot 37)$$

These models were first formulated based on purely physical considerations by Rothenburg (1980). They have been validated later by means of numerical simulations (Bathurst and Rothenburg, 1988; Rothenburg and Bathurst, 1993; Chantawarangul, 1993).

The meaning of \bar{f}^0 stems from its expression as:

$$\bar{f}^0 = \frac{1}{4\pi} \int_{\pi} \bar{f}^n(\mathbf{n}) d\mathbf{n} \quad (2\cdot 38)$$

\bar{f}^o represents the normal contact force average over groups of orientation when these groups are given an equal weight. \bar{f}^o is different from the genuine assembly average normal contact force $\bar{f}_n^o = (\sum f_n^c) / V$. They become equal if the contact normal orientation distribution is isotropic.

2.4.1 The Average Normal Contact Force Tensor

By analogy to the fabric tensor, an *average normal contact force tensor*, F_{ij}^n , can be defined as:

$$F_{ij}^n = \frac{1}{4\pi} \sum_g \bar{f}^n(n^g) n_i^g n_j^g |\Delta n^g| \quad (2 \cdot 39)$$

The average normal contact force tensor can be related to the micromechanical definition of the stress tensor itself.

Consider an ideal assembly of mono-size smooth spheres of radius l^o . The assembly is loaded by a homogeneous applied stress in such a way not to disturb the distribution of contact normals existing in the assembly before loading. Another possibility is that contacts in the assembly be cemented (case of bonded particles). If initially the fabric is isotropic, then the average stress tensor reduces to:

$$\sigma_{ij} = \frac{l^o}{V} \sum_{c \in V} f_n^c n_i^c n_j^c \quad (2 \cdot 40)$$

After grouping in contact classes, the following expression is obtained:

$$\sigma_{ij} = \frac{m_v l^o}{4\pi} \sum_g \bar{f}^n(n^g) n_i^g n_j^g |\Delta n^g| \quad (2 \cdot 41)$$

Or:

$$\sigma_{ij} = m_v \bar{f}^n F_{ij}^n \quad (2\bullet 42)$$

The relationship in (2• 42) reveals the physical meaning of the average normal contact force tensor as a measure of the contribution of the anisotropy in average normal contact forces to the stress tensor.

The continuous expression of F_{ij}^n for large systems is:

$$F_{ij}^n = \frac{1}{4\pi} \int_n \bar{f}^n(n) n_i n_j dn \quad (2\bullet 43)$$

By substituting (2• 36) into (2• 43) and integrating, the following expression is obtained:

$$a_{ij}^n = \frac{15 F_{ij}^{n'}}{2 \bar{f}^n} \quad (2\bullet 44)$$

where $F_{ij}^{n'} = F_{ij}^n - (\bar{f}^n / 3) \delta_{ij}$.

By virtue of its definition as a discrete sum, F_{ij}^n can be calculated for finite assemblies of particles and used to approximate the normal force anisotropy tensor a_{ij}^n through the relationship in (2• 44). The same relationship proves the symmetry and the deviatoric nature of a_{ij}^n .

2.4.2 The Average Tangential Contact Force Tensor

The same ideal assembly of spheres used before is considered again. The particle surfaces are assumed to be rough enough to develop shear forces at contact points with other particles. The contact force vector is decomposed as the sum of a normal and tangential components as:

$$\vec{f}_i = f_n^c \vec{n}_i + \vec{f}_{t,i} \quad (2\bullet 45)$$

Consequently, the stress tensor is decomposed as:

$$\sigma_{ij} = \frac{l^o}{V} \sum_{c \in V} f_n^c n_i^c n_j^c + \frac{l^o}{V} \sum_{c \in V} f_t^c n_j^c \quad (2 \bullet 46)$$

The contribution of tangential contact forces to the stress tensor is:

$$\sigma_{ij}^t = \frac{l^o}{V} \sum_{c \in V} f_t^c n_j^c \quad (2 \bullet 47)$$

Or, after grouping into classes of orientation:

$$\sigma_{ij}^t = \frac{m_v l^o}{4\pi} \sum_g \bar{f}_i(n^g) n_j^g |\Delta n^g| \quad (2 \bullet 48)$$

Thus:

$$\sigma_{ij}^t = m_v l^o F_{ij}^t \quad (2 \bullet 49)$$

where:

$$F_{ij}^t = \frac{1}{4\pi} \sum_g \bar{f}_i(n^g) n_j^g |\Delta n^g| \quad (2 \bullet 50)$$

F_{ij}^t is called the *average tangential contact force tensor*. The expression in (2• 49) illustrates well its physical meaning.

For large systems of particles, F_{ij}^t can be calculated by a continuous integral over the unit sphere as:

$$F_{ij}^t = \frac{1}{4\pi} \int_n \bar{f}_i(n) n_j dn \quad (2 \bullet 51)$$

Substituting of the expression in (2• 37) into (2• 51) and integrating yields the average tangential contact force anisotropy tensor a_{ij}^t in terms of F_{ij}^t as:

$$a_{ij}^t = s \frac{F_{ij}^t}{\bar{f}^o} \quad (2\bullet 52)$$

This relationship is the basis for extracting components of the anisotropy tensor a_{ij}^t from simulated data.

F_{ij}^t is deviatoric because of the orthogonality between the tangential force and the corresponding normal vector, expressed as:

$$F_{ii}^t = \frac{1}{4\pi} \int_n \bar{f}_i^t(n) n_i dn = 0 \quad (2\bullet 53)$$

2.4.2.1 Symmetry of the Tangential Stress Tensor

If the symmetry of the tangential part of the stress tensor in (2• 47) is proven, then the symmetry of F_{ij}^t will be implied by the relationship in (2• 49).

By referring to equations (2• 46) and (2• 47), the tangential component of the stress tensor is:

$$\sigma_{ij}^t = \sigma_{ij} - \sigma_{ij}^n \quad (2\bullet 54)$$

where:

$$\sigma_{ij}^n = \frac{l^o}{V} \sum_{c \in V} f_n^c n_i^c n_j^c \quad (2\bullet 55)$$

σ_{ij}^n is symmetric, therefore, σ_{ij}^t , being the difference of two symmetric tensors, is symmetric.

In the general case of non-spherical particles, the expression of the normal part of the stress tensor cannot be reduced to the simple symmetric form in (2• 55) because the contact vector and contact normal vector are not colinear. It is possible to decompose the con-

tact vector l_j^c into a normal component $l_n^c n_j$ and a tangential component $l_{t,j}^c$, and write the normal part of the stress tensor as:

$$\sigma_{ij}^n = \frac{1}{V} \sum_{c \in V} f_n^c l_n^c n_i n_j + \frac{1}{V} \sum_{c \in V} f_n^c n_i l_{t,j}^c \quad (2 \cdot 56)$$

The skew symmetric part of the tensor σ_{ij}^n can be simplified as follows:

$$\sigma_{ij}^n - \sigma_{ji}^n = \frac{1}{V} \sum_{c \in V} f_n^c (n_i l_{t,j}^c - n_j l_{t,i}^c) \quad (2 \cdot 57)$$

The quantities $(n_i l_{t,j}^c - n_j l_{t,i}^c)$ (for $i \neq j$) represent the components of the cross product of the contact normal vector and the contact vector. If the two vectors are colinear, the cross product is zero and the normal stress tensor is symmetric. If they are not colinear, the overall sum might not vanish. However, in the case of the tested assemblies of ellipsoids used as a model for this study, the angle between the contact vector and contact normal vector remain very small in average, throughout the test. The overall sum is also expected to remain negligible. The normal stress tensor in this case is practically symmetric, and so are the tangential stress tensor and the average tangential contact force tensor F_{ij}^t .

Finally, because of the relationship in (2 \cdot 52), the symmetry and the deviatoric properties of the average tangential contact force tensor F_{ij}^t are passed on to the average tangential contact force anisotropy tensor a_{ij}^t . The latter is also calculated from the former (directly measurable from simulation data)

2.5 Influence of Fourth-Order Terms on the Quality of Approximation by Fourier Series

The study of the influence of higher order terms on the quality of the approximation was motivated by the observed differences between measured and approximated distributions using second-order Fourier series from results of simulation using ellipsoids. These differences can be major ones, especially for the particular case of average tangential contact force distributions. Improved approximations can be achieved by adding fourth-order terms to the expansion by Fourier series.

The effects of higher order terms on the approximation of the various observed distributions are illustrated for a simulated assembly comprising a 1000 ellipsoids. The assembly was tested from an initial hydrostatic state of stress by increasing the applied vertical stress while maintaining the mean pressure constant. All illustrations on subsequent figures correspond to a state of the assembly at about 20% axial deformation.

2.5.1 Fourth-Order Fourier Series Approximation of Contact Normal Orientation Distribution

The fourth-order model for the contact normal orientation distribution is as follows:

$$\begin{cases} E(\mathbf{n}) = \frac{1}{4\pi}(1 + a'_{ij}n_i n_j + b'_{ijkl}n_i n_j n_k n_l) \\ a'_{ij} = a'_{ji} \quad b'_{ijkl} = b'_{\pi(ijkl)} \end{cases} \quad (2 \cdot 58)$$

The fourth-order anisotropy tensor b'_{ijkl} is assumed to be symmetric with respect to all permutations π of indices $(ijkl)$.

The procedure to extract the components of this fourth-order tensor from observed

data on simulated samples of particles resembles the one used to extract second-order anisotropy tensors.

First, the difference between the actual density of probability function $E(\mathbf{n})$ and the second-order approximation is evaluated over all groups of contact normal orientation. The difference can be modeled by the purely deviatoric fourth-order term as follows:

$$\begin{cases} \Delta E(\mathbf{n}) = \frac{1}{4\pi} (b'_{ijkl} n_i n_j n_k n_l) \\ b'_{ijkl} = b'_{\pi(ijkl)} \end{cases} \quad (2 \cdot 59)$$

The second and fourth-order fabric tensors are defined as:

$$\begin{cases} \Delta R_{ij} = \sum_{\mathbf{g}} \Delta E(\mathbf{n}^{\mathbf{g}}) n_i^{\mathbf{g}} n_j^{\mathbf{g}} \\ \Delta R_{ijkl} = \sum_{\mathbf{g}} \Delta E(\mathbf{n}^{\mathbf{g}}) n_i^{\mathbf{g}} n_j^{\mathbf{g}} n_k^{\mathbf{g}} n_l^{\mathbf{g}} \end{cases} \quad (2 \cdot 60)$$

and for infinite systems:

$$\begin{cases} \Delta R_{ij} = \int_{\mathbf{n}} \Delta E(\mathbf{n}) n_i n_j d\mathbf{n} \\ \Delta R_{ijkl} = \int_{\mathbf{n}} \Delta E(\mathbf{n}) n_i n_j n_k n_l d\mathbf{n} \end{cases} \quad (2 \cdot 61)$$

Substituting of $\Delta E(\mathbf{n})$ in (2• 59) into (2• 61), integrating and rearranging, lead to the following expression of the fourth-order anisotropy tensor:

$$b'_{ijkl} = \frac{9}{2} \Delta R'_{ijkl} - (\delta \cdot \Delta R')_{[ijkl]} \quad (2 \cdot 62)$$

where $(\delta \cdot \Delta R')_{[ijkl]}$ is the symmetric part of the fourth-order tensor obtained as the dual product of second-order tensors, δ_{ij} and $\Delta R'_{ij}$, *i.e.*,

$$\begin{aligned} (\delta \cdot \Delta R')_{[ijkl]} = \frac{1}{2} \{ & \delta_{ij} \Delta R'_{kl} + \delta_{kl} \Delta R'_{ij} + \delta_{ik} \Delta R'_{jl} + \delta_{jl} \Delta R'_{ik} \\ & + \delta_{il} \Delta R'_{jk} + \delta_{jk} \Delta R'_{il} \} \end{aligned} \quad (2 \cdot 63)$$

where $\Delta R'_{ij}$ and $\Delta R'_{ijkl}$ are deviatoric tensors defined by:

$$\begin{cases} \Delta R'_{ij} = \Delta R_{ij} - \frac{1}{3}\delta_{ij} \\ \Delta R'_{ijkl} = \Delta R_{ijkl} - \frac{1}{15}(\delta_{ij}\delta_{kl} + \delta_{ik}\delta_{jl} + \delta_{il}\delta_{jk}) \end{cases} \quad (2\cdot 64)$$

The procedure was applied to produce the fourth-order approximation of the contact normal orientation distribution for the 1000 ellipsoid assembly as described earlier (Figure 2•8a).

The plots show a noticeable improvement of the approximation from the second-order model to the fourth one. In addition to the change in shape of the calculated distributions, a slight rotation of the major principal direction of anisotropy is introduced by the fourth term.

2.5.2 Fourth-Order Fourier Series Approximation of Average Normal Contact Force Distribution

Similarly to the contact normal orientation distribution, the average normal contact force distribution can be represented by a fourth-order truncated Fourier expansion of even order terms. The difference between the actual distribution and the second-order model can be described by a fully symmetric fourth-order anisotropy tensor as:

$$\begin{cases} \Delta \bar{f}(\mathbf{n}) = \bar{f}(b_{ijkl}^n n_i n_j n_k n_l) \\ b_{ijkl}^n = b_{\pi(ijkl)}^n \end{cases} \quad (2\cdot 65)$$

where π can be any permutation of indices $(ijkl)$.

The extraction of the fourth-order tensor components from simulation data follows the same procedure described for contact normals.

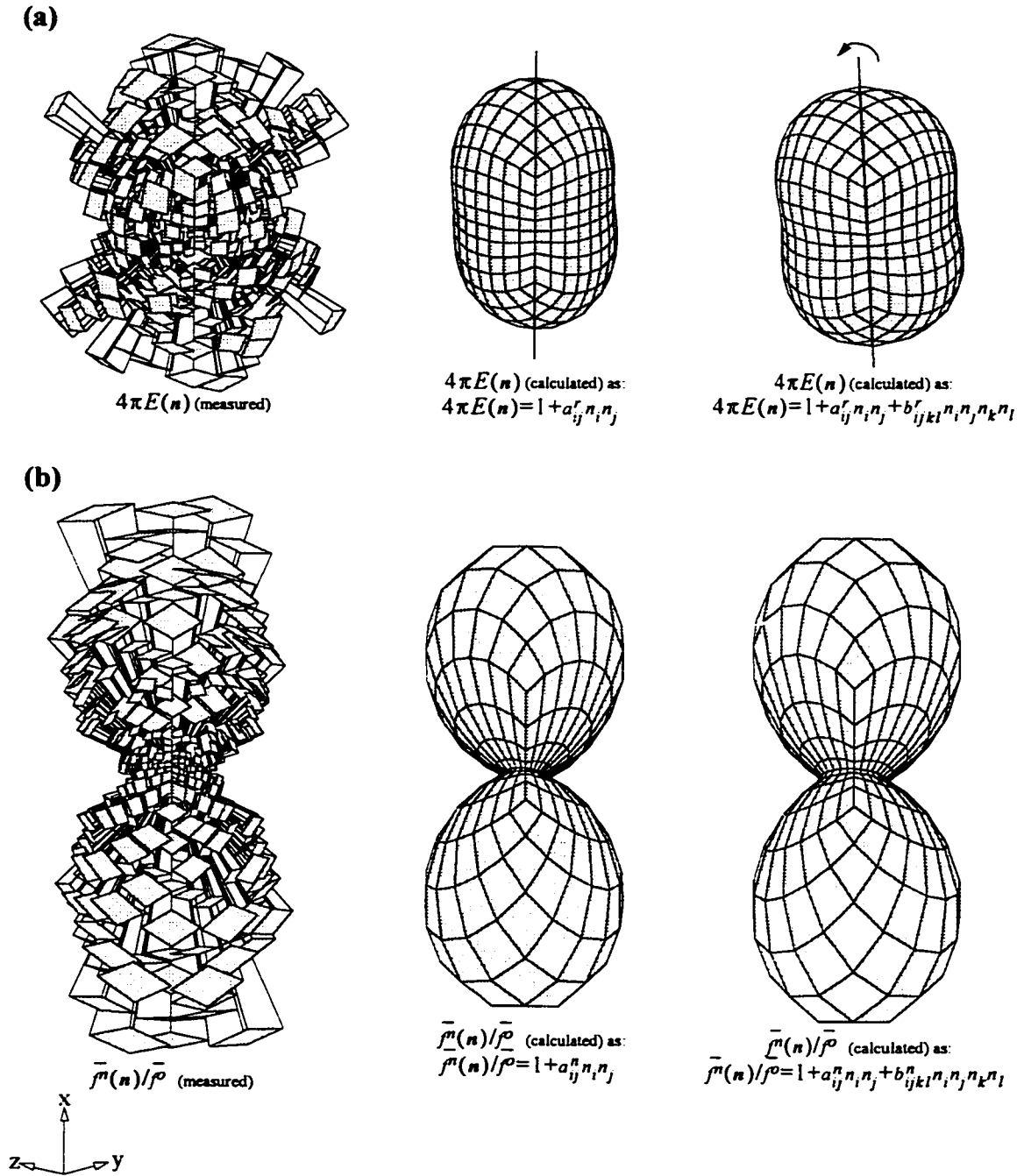


Figure 2-8 Measured and approximated distributions
 (a) Contact normal orientation
 (b) Average normal contact force

Measurable second and fourth-order normal contact force tensors are defined and related to the components of the fourth-order anisotropy tensor. They are defined by:

$$\begin{cases} \Delta F_{ij}^n = \frac{1}{4\pi} \sum_g \Delta \bar{f}^n(n^g) n_i^g n_j^g \\ \Delta F_{ijkl}^n = \frac{1}{4\pi} \sum_g \Delta \bar{f}^n(n^g) n_i^g n_j^g n_k^g n_l^g \end{cases} \quad (2 \bullet 66)$$

For large systems, they are continuous integrals:

$$\begin{cases} \Delta F_{ij}^n = \frac{1}{4\pi} \int_n \Delta \bar{f}^n(n) n_i n_j dn \\ \Delta F_{ijkl}^n = \frac{1}{4\pi} \int_n \Delta \bar{f}^n(n) n_i n_j n_k n_l dn \end{cases} \quad (2 \bullet 67)$$

The result of the substitution of the model approximation of $\Delta \bar{f}^n(n)$ in (2• 65) into (2• 67), integration and rearrangement, is an expression of the fourth-order tensor similar in form to (2• 62) for the contact normal orientation distribution, where $\Delta R'_{ij}$ is replaced by $\Delta F'_{ij}/\bar{f}^0$, $\Delta R'_{ijkl}$ by $\Delta F'_{ijkl}/\bar{f}^0$, and, b'_{ijkl} by b^n_{ijkl} .

Figure 2•8b shows the two approximations of the average normal contact force distribution by second and fourth-order series. The improvement is noticeable but not dramatic.

2.5.3 Fourth-Order Fourier Series Approximation of Average Tangential Contact Force Distribution

The extension of the second-order model for tangential forces is not as straightforward as in the case of contact normals and average normal contact forces. The reason is that the second-order approximation for tangential forces is not merely due to any truncated Fourier series expansion, but one that has special geometrical and physical properties. Nevertheless, a possible extension of the model could be:

$$\begin{cases} \bar{f}_i(\mathbf{n}) = \bar{f}^0(a_{ij}^t n_j - a_{ki}^t n_k n_i) + \Delta \bar{f}_i^t(\mathbf{n}) & i=1, 3 \\ a_{ij}^t = a_{ji}^t & a_{kk}^t = 0 \end{cases} \quad (2\bullet 68)$$

where:

$$\begin{cases} \Delta \bar{f}_i^t(\mathbf{n}) = \bar{f}^0(b_{ijkl}^t n_j n_k n_l - b_{jklm}^t n_j n_k n_l n_m n_i) & i=1, 3 \\ b_{ijkl}^t = b_{klij}^t \end{cases} \quad (2\bullet 69)$$

The extended model complies with the geometrical properties of tangential forces: skew-symmetry, $\bar{f}_i(-\mathbf{n}) = -\bar{f}_i(\mathbf{n})$; orthogonality with the normal contact vector, $\bar{f}_i n_i = 0$; and a zero average value over groups of orientation, $\int_{\mathbf{n}} \bar{f}_i^t(\mathbf{n}) = 0$.

The anisotropy tensor b_{ijkl}^t can be calculated from simulation data as follows:

First, average tangential contact force tensors are defined for finite systems as:

$$\begin{cases} \Delta F_{ij}^t = \frac{1}{4\pi} \sum_{\mathbf{g}} \Delta \bar{f}_i^t(\mathbf{n}^g) n_j^g \\ \Delta F_{ijkl}^t = \frac{1}{4\pi} \sum_{\mathbf{g}} \Delta \bar{f}_i^t(\mathbf{n}^g) n_j^g n_k^g n_l^g \end{cases} \quad (2\bullet 70)$$

They are extended to infinite systems as:

$$\begin{cases} \Delta F_{ij}^t = \frac{1}{4\pi} \int_{\mathbf{n}} \Delta \bar{f}_i^t(\mathbf{n}) n_j d\mathbf{n} \\ \Delta F_{ijkl}^t = \frac{1}{4\pi} \int_{\mathbf{n}} \Delta \bar{f}_i^t(\mathbf{n}) n_j n_k n_l d\mathbf{n} \end{cases} \quad (2\bullet 71)$$

After substituting of the model approximation in (2• 69) into (2• 71) and integrating, the following expression of the fourth-order anisotropy tensor b_{ijkl}^t is obtained:

$$b_{ijkl}^t = \frac{63}{2} \frac{\Delta F_{ijkl}^t}{\bar{f}^3} + \frac{14}{3} \left(\delta_{ij} \frac{\Delta F_{kl}^t}{\bar{f}^3} + \delta_{ik} \frac{\Delta F_{jl}^t}{\bar{f}^3} + \delta_{il} \frac{\Delta F_{jk}^t}{\bar{f}^3} \right) - \frac{35}{6} \left(\delta_{jk} \frac{\Delta F_{il}^t}{\bar{f}^3} + \delta_{jl} \frac{\Delta F_{ik}^t}{\bar{f}^3} + \delta_{kl} \frac{\Delta F_{ij}^t}{\bar{f}^3} \right) \quad (2 \cdot 72)$$

The application of the method to the state of tangential forces in the numerical sample of ellipsoids produced the fourth-order model approximation shown in Figure 2•9.

As can be seen, a dramatic correction is provided by the fourth term; this must be better understood and interpreted physically.

Tangential forces play a major role in failure mechanisms that take place in granular materials. Phenomenological models predicts that failure propagates along a certain plane of maximum shear. From the micromechanical point of view, the failure plane(s) should be parallel to the orientation of space characterized by the highest average tangential contact force.

The three-dimensional plots of the average tangential contact force distribution are not suited to recognize some of the changes introduced by higher order terms. For this reason it was decided to transfer the plots into the plane.

By integrating the average tangential contact force radially over the full range of polar angles α , *i.e.*, $[0, 2\pi]$, a plane distribution can be obtained which is more suitable to illustrate the changes introduced by the fourth term.

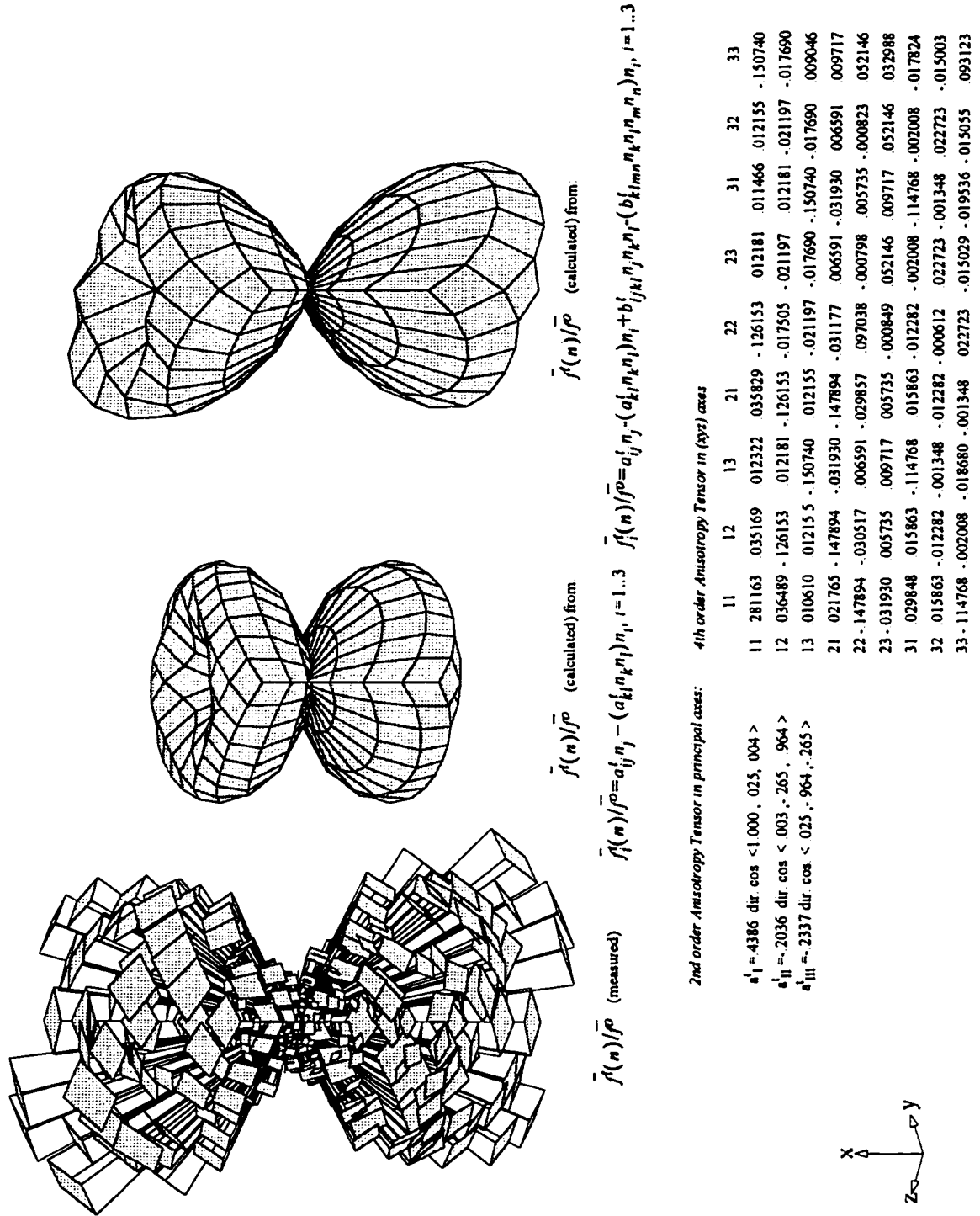


Figure 2-9 Measured and approximated distributions of average tangential contact force

2.5.4 The Average Radial Tangential Contact Force Distribution

The radial tangential force at an individual contact is defined as shown in Figure 2•10a. For an arbitrary group of contacts of normal vector \mathbf{n}^s , the radial component of the average tangential contact force is given by the following dot product:

$$f_r(\mathbf{n}^s) = \bar{f}_i n_i^r = \bar{f}_2' \cos \alpha^s + \bar{f}_3' \sin \alpha^s \quad (2\bullet 73)$$

where the radial unit vector \mathbf{n}^r has components: $(0, \cos \alpha^s, \sin \alpha^s)$.

The average radial tangential contact force for a finite system is defined by:

$$\bar{f}_r'(\beta^s) = \frac{1}{2\pi} \sum_{\alpha^s} f_r(\alpha^s, \beta^s) \Delta \alpha \quad (2\bullet 74)$$

For an infinite system, it is defined by a continuous integral as:

$$\bar{f}_r'(\beta) = \frac{1}{2\pi} \int_0^{2\pi} f_r(\alpha, \beta) d\alpha \quad (2\bullet 75)$$

To measure the impact of the second and fourth-order 3D-models for average tangential contact forces on the 2D-distribution of average radial tangential contact forces, these are calculated in the two cases and compared to numerically measured distributions inside simulated assemblies of ellipsoids.

2.5.4.1 Approximation of the Average Radial Tangential Contact Force Distribution

Substitution of (2• 73) into (2• 75) results in the average radial tangential contact force becoming approximated (in the case of a finite system) by a continuous integral as:

$$\bar{f}_r'(\beta) \cong \frac{1}{2\pi} \int_0^{2\pi} (\bar{f}_2'(\alpha, \beta) \cos \alpha + \bar{f}_3'(\alpha, \beta) \sin \alpha) d\alpha \quad (2\bullet 76)$$

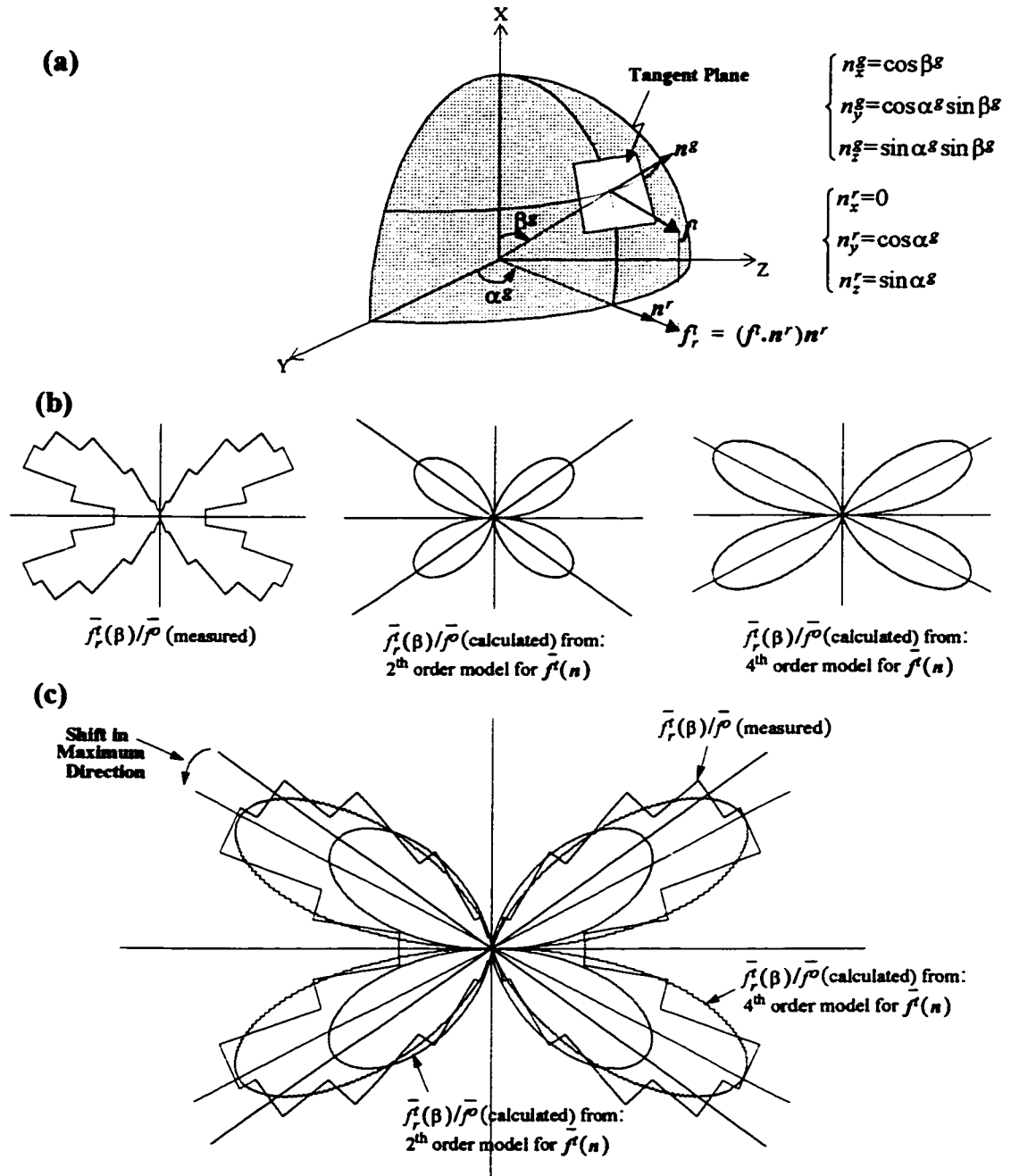


Figure 2•10 2-D Average radial tangential contact force distribution
 (a) Definition of the radial force
 (b) Measured and calculated distributions (in separate graphs)
 (c) Illustration of the change in maximum direction

Substitution of the second-order approximation model in (2• 68) into the above integral and integration yields:

$$\frac{\bar{f}_r'(\beta)}{\bar{f}^0} = -\frac{3}{8}a_{11}'(\sin\beta + \sin 3\beta) \quad (2• 77)$$

The fourth-order approximation model in (2• 68) and (2• 69), yields:

$$\begin{aligned} \frac{\bar{f}_r'(\beta)}{\bar{f}^0} = & -\frac{3}{8}a_{11}'(\sin\beta + \sin 3\beta) \\ & + \frac{1}{8}(D_1 - D_2)\sin\beta + \frac{1}{16}(3D_1 - D_2)\sin 3\beta + \frac{1}{8}(D_1 + D_2)\sin 5\beta \end{aligned} \quad (2• 78)$$

where:

$$\begin{cases} D_1 = b_{3113}' + b_{3311}' + b_{3131}' - b_{1111}' \\ D_2 = b_{1122}' + b_{1212}' + b_{1221}' - b_{2222}' \end{cases} \quad (2• 79)$$

The validity of the obtained expressions is limited to the case of an axisymmetric load pattern (e.g., $\sigma_1 > \sigma_2 = \sigma_3$) such that the generated contact force distributions are also axisymmetric.

The results are illustrated by plots of the different distributions (measured and calculated) in polar coordinates in Figure 2•10b and Figure 2•10c.

The fourth-order term seems to affect both the size of the distribution and the direction of the maximum average radial tangential contact force. Note that the shift in the maximum direction could hardly be identified by comparison of the 3D-histograms in Figure 2•9.

The expression in (2• 78) shows that the fourth-order term is not a mere higher order term involving $(\sin 5\beta)$ alone, as would be expected at first, but it also includes lower or-

der terms such as $(\sin \beta)$ and $(\sin 3\beta)$.

The correction affecting the coefficients of the lower order terms $(\sin \beta)$ and $(\sin 3\beta)$ is responsible for the adjustment of the distribution size to the actual size of the measured distribution (Figure 2•10b). On the other hand, the shift in the direction of the maximum average radial tangential contact force is due to the higher order term $(\sin 5\beta)$ (Figure 2•10c).

2.6 Average Stress Tensor for Infinite Systems

The definition of the stress tensor as a discrete sum over individual contacts in a large system of particles does not exhibit the biases in contact force and contact normal distributions. These will naturally emerge once spacial variables in the stress equation are averaged over contacts in a same group of orientation (g) as:

$$\sigma_{ij} = \sum_g \sum_{c \in g} f_i^c l_j^c / V \quad (2\bullet 80)$$

If \bar{f}_i^g , \bar{l}_j^g , and $\overline{f_i l_j^g}$ define averages over contacts in an arbitrary group (g) of: the contact force, the average contact vector, and the average dual product of the two, respectively; then:

$$\begin{cases} \bar{f}_i^g = (\sum_{c \in g} f_i^c) / \Delta M^g \\ \bar{l}_j^g = (\sum_{c \in g} l_j^c) / \Delta M^g \\ \overline{f_i l_j^g} = (\sum_{c \in g} f_i^c l_j^c) / \Delta M^g \end{cases} \quad (2\bullet 81)$$

where ΔM^g is the number of contacts within the group.

Therefore:

$$\sigma_{ij} = \sum_g \Delta M^g (\bar{f}_i \bar{l}_j^g / V) \quad (2 \bullet 82)$$

Now by assuming that the distribution of average contact forces \bar{f}_i^g and the distribution of average contact vectors \bar{l}_j^g are statistically independent, *i.e.*, $\overline{(\bar{f}_i \bar{l}_j)^g} = \bar{f}_i^g \bar{l}_j^g$, then the stress equation can be re-written as:

$$\sigma_{ij} = \sum_g \Delta M^g (\bar{f}_i^g \bar{l}_j^g / V) \quad (2 \bullet 83)$$

The assumption of independence of the average contact force and the average contact vector distributions has always been supported by simulations in two dimensions, using various particle shapes (such as disks, ellipses, polygons), and in three dimensions (using spheres). The simulations with ellipsoids also support the assumption.

Substituting of the expression of ΔM^g in terms of the density function $E(n^g)$ in (2•19) into the above equation gives:

$$\sigma_{ij} = m_v \sum_g \bar{f}_i^g \bar{l}_j^g E(n^g) |\Delta n^g| \quad (2 \bullet 84)$$

As the assembly of particles increases in size and the distribution of contact normals becomes denser, smaller size orientation classes are considered for the conceptual grouping. At the limiting case of an infinite assembly of particles, any unit vector n is a class representative.

Rothenburg (1980) shows that the sum defining the stress tensor can then be extended to a continuous integral over the unit sphere as.

$$\sigma_{ij} = m_v \int \bar{f}_i(n) \bar{l}_j(n) E(n) dn \quad (2 \bullet 85)$$

where m_v is the contact density for an infinite system, *i.e.*,

$$m_v = \lim_{V \rightarrow \infty} \frac{M}{V} \quad (2 \cdot 86)$$

To develop further the obtained stress equation, the models for the distributions of the average contact force $\bar{f}_i(\mathbf{n})$, contact vector $\bar{l}_j(\mathbf{n})$, and contact normal orientation $E(\mathbf{n})$, must be substituted into (2• 85) and the result integrated. The shape of the average contact vector distribution has not been determined yet. Its determination and approximation is discussed in Chapter 6 when analyzing the stress-anisotropy relationship for simulated assemblies of ellipsoids.

2.7 Conclusions

In this chapter, the general microscopic approach to characterize the mechanical behaviour of assemblies of cohesionless particles, based on the pioneering work of Rothenburg (1980), was reviewed. Several additional elements in relation to assemblies of ellipsoids were introduced:

1. A new method of space partitioning was utilized for classifying contacts with regard to their contact normal orientation. The method is based on a more uniform size of orientation classes instead of the disproportionate class sizes generated by the regular partitioning with a single set of spherical coordinates.
2. The second-order approximation of spatial distributions with truncated Fourier series was extended to include a fourth-order component represented by a fourth-order fully symmetric tensor of anisotropy.

3. The application of the fourth-order Fourier series expansion to approximate distributions of the contact normal orientation and average normal contact force showed a slight improvement in comparison with the second-order approximation. A significant improvement, however, was obtained for the distribution of average tangential contact force. This improvement was transferred into the plane by comparison between measured and calculated average radial tangential contact forces (by second and fourth-order approximations). It appeared that both the size of the distribution and orientation of maximum average tangential contact force are corrected by the fourth-order term.

CHAPTER III: THE DISCRETE ELEMENT METHOD AND THE MODIFIED PROGRAM TRUBAL

3.1 Introduction

Discrete Element Models is a term describing the family of models that simulate the behaviour of a collection of dynamic solid elements interacting with each other through inter-element forces. The Discrete Element Method (DEM) is one of the various numerical techniques used to update the position of elements when displaced as a response to some applied external stress or strain increment.

The method was first applied in the field of Rock Mechanics under the name of Discrete/Distinct Block Method (DBM) to simulate the progressive failure of rock slopes consisting of two-dimensional rigid blocks (Cundall, 1971). It was then modified to simulate the mechanical behaviour of granular materials using two-dimensional assemblies of

disks (Strack and Cundall, 1978, Cundall and Strack, 1979a, b, c). The method was coded in a Fortran program called BALL.

A three-dimensional version of BALL, named TRUBAL, was developed by the authors of BALL (Cundall and Strack, 1979c; Strack and Cundall, 1984). The 3-D program TRUBAL models the mechanical behaviour of assemblies of spheres.

The structure of TRUBAL resembles that of BALL. However, the program TRUBAL substitutes the original rigid boundaries used in BALL with periodic boundaries, where opposite faces of a sample are numerically connected. Linear and Hertzian contact laws are available to model contact interactions. A stress servo-mechanism is implemented in the program, allowing a variety of stress loading paths to be applied, such as, a true triaxial test with a constant Lode parameter, a conventional triaxial test at constant mean pressure, and many more; a 2-D mode is available to test planar assemblies of disks, for example, to replicate a plane stress or strain condition. Details and discussion of these various features can be found in Cundall (1987, 1988).

The program TRUBAL was extended to allow micromechanical data to be extracted (Chantawarangul, 1993), and was modified again here to be used for an ellipsoidal shape of particles. The major challenge encountered in the latter task was the implementation of a robust scheme for inter-particle contact detection. Since the mechanics of solid non-spherical objects are different from ideal spheres, the mechanical routine that performs motion and force calculations was also re-written for the new shape of particles.

In its current state, all features of the original TRUBAL can be used with the new shape except the Hertzian-contact law and the 2-D mode. The Hertzian contact law was

studied before and showed to yield results which are similar to those obtained using the linear contact law (*e.g.*, Chantawarangul, 1993; Mirghasemi 1994). For the 2-D mode, two-dimensional codes with elliptical particles exist and were extensively and successfully used to analyze the peculiar behaviour of plane systems (*e.g.*, Rothenburg and Bathurst, 1992).

3.2 The Discrete Element Method for Ellipsoids

As mentioned earlier, DEM updates the state of an assemblage of dynamic solid particles undergoing an external deformation. In TRUBAL it is simulated by applying to the volume of the sample a homogeneous strain rate tensor. Since the process is dynamic, TRUBAL uses a time domain algorithm to perform the repositioning of the particles at each increment of time. First, the equations of motion of each particle are solved. TRUBAL employs an explicit time, finite-difference technique to discretize and integrate Newton's equations of motion. The contact displacements are obtained by integrating the relative velocity vectors between pairs of contacting particles, and are used to compute the new contact forces according to the adopted law of contact force-displacement. Finally, the new contact forces are input into the equations of motion to reposition the particles for the next time step. The procedure is called "mechanical cycle", or "cycle", and is repeated at each increment of time until the end of the simulation. The loop of mechanical calculations (cycle) is illustrated in Figure 3•1.

The implementation of DEM in the modified version of TRUBAL for ellipsoids differs in a number of aspects from the one originally used for spheres (Cundal and Strack, 1979c). A degree of complexity is added due to the difference in shape from ideal spheres for which some simplifications exist. The motion and force calculations are particularly changed as a consequence of the change in shape (*e.g.*, Hart *et al.* 1988).

3.2.1 Contact Force Calculation

Let A and B denote two ellipsoids in contact with each other at some location point C . Let n be the normal vector to the tangent contact plane as illustrated in Figure 3•2.

If both the translational and the rotational velocities of the two particles are known from integration of equations of motion at a previous time-step, the contact velocity, defined as the velocity of particle B relative to particle A at the contact location C , is calculated as:

$$V_i = [\dot{x}_i^B + \epsilon_{ijk} \omega_j^B (C_k - B_k)] - [\dot{x}_i^A + \epsilon_{ijk} \omega_j^A (C_k - A_k)] \quad (3•1)$$

where A and B are the position vectors, and, \dot{x}^A and \dot{x}^B are the translation velocity vectors of the centroids of particles A and B , respectively; ω_j^A and ω_j^B are the corresponding angular velocity vectors; and ϵ_{ijk} is a third rank permutation tensor used to express the cross product of spatial vectors.

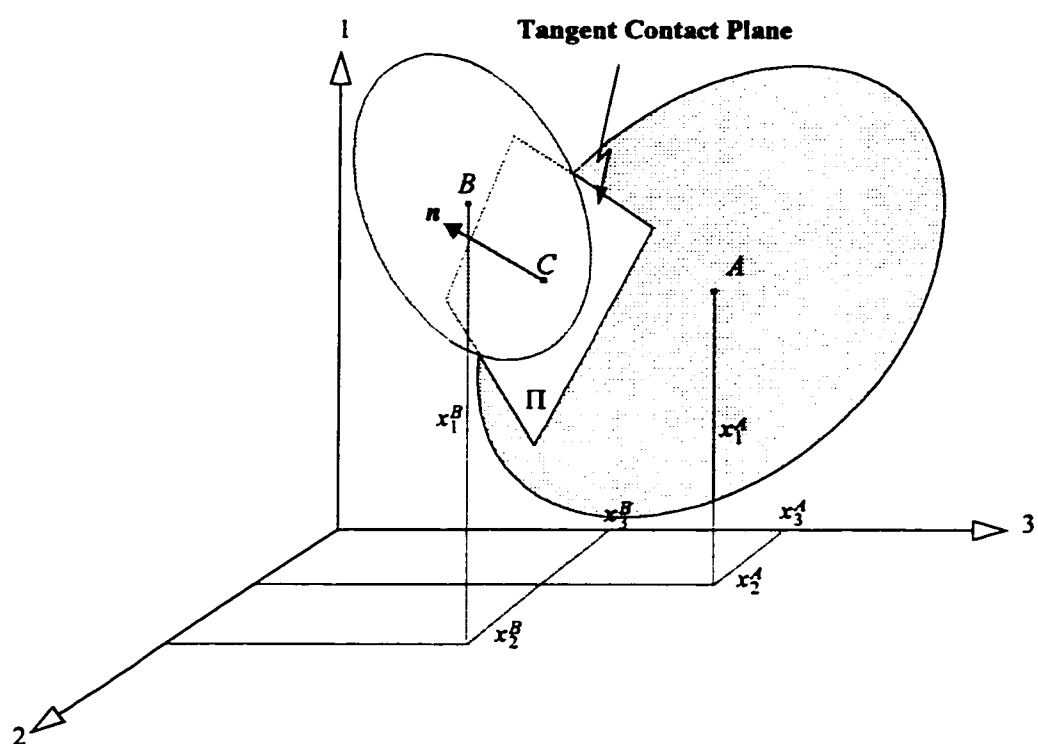


Figure 3-2 Two ellipsoids in contact

The contact displacement increment vector is calculated as:

$$\Delta U_i = V_i \Delta t \quad (3\cdot 2)$$

It can be resolved into normal and shear components along the plane of contact. The normal displacement is given by:

$$\Delta U^n = \Delta U_i n_i \quad (3\cdot 3)$$

The shear displacement increment vector is calculated as:

$$\Delta U_i^s = \Delta U_i - \Delta U^n n_i \quad (3\cdot 4)$$

The contact displacement increments are used to calculate the elastic contact force increments through a linear contact force-displacement model as illustrated in Figure 3•3a.

The normal contact force increment, taking compressive forces to be positive, is given by:

$$\Delta F^n = -K_n \Delta U^n \quad (3\cdot 5)$$

The shear contact force increment is given by:

$$\Delta F_i^s = -K_s \Delta U_i^s \quad (3\cdot 6)$$

where K_n and K_s are the normal and shear contact stiffnesses, respectively.

The total normal and shear contact force vectors are updated as:

$$\begin{cases} F^n \leftarrow F^n + \Delta F^n \\ F_i^s \leftarrow F_i^s + \Delta F_i^s \end{cases} \quad (3\cdot 7)$$

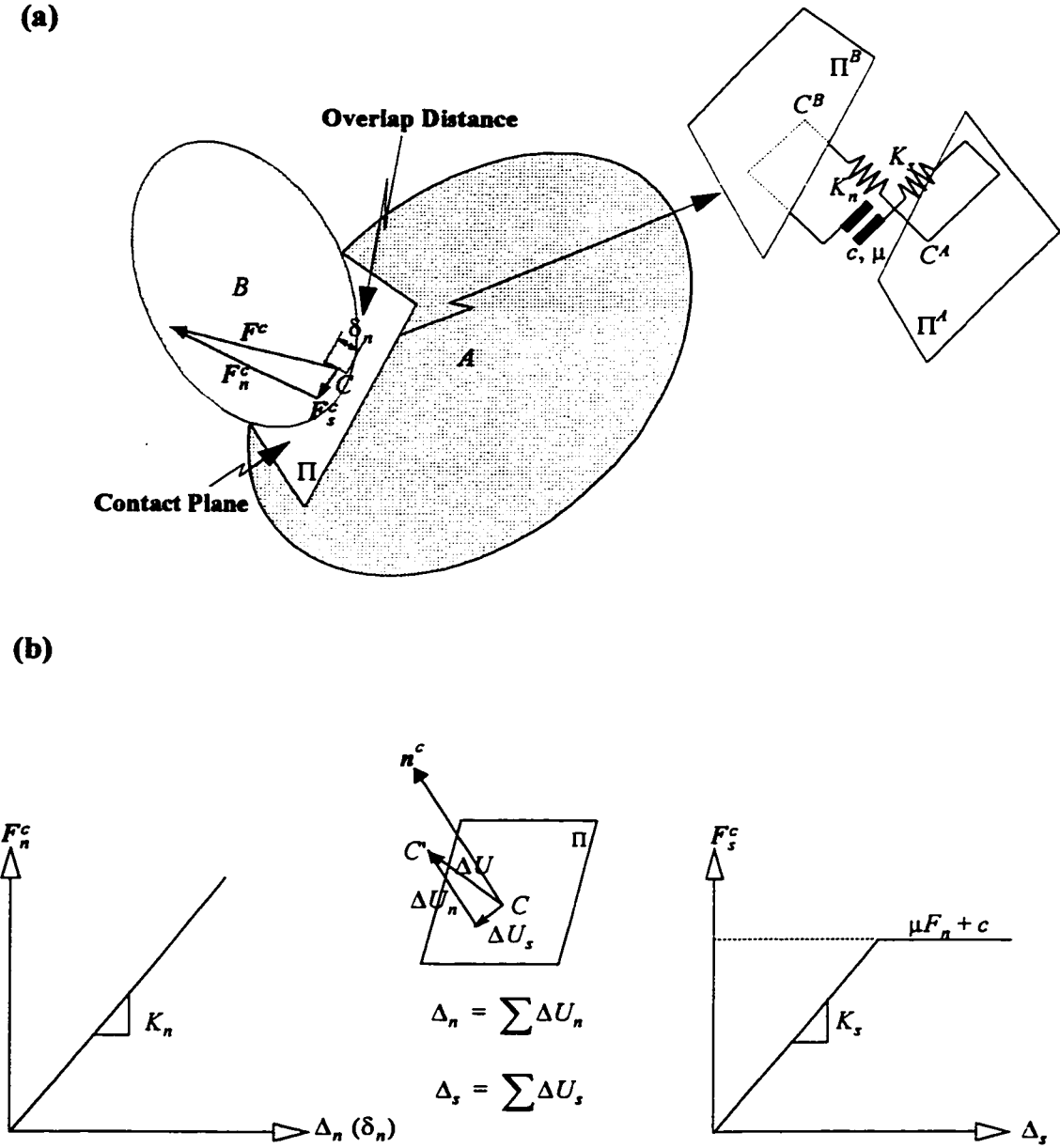


Figure 3-3 Linear contact model
 (a) Particle-to-particle interaction
 (b) Normal and shear contact force-displacement laws

The normal contact force can be calculated directly from the value of the normal overlap distance at a contact point between numerical particles, δ_n , (Figure 3•3a). This method is easier to implement for ellipsoids and was used in preference to the incremental method. The linear contact model can be expressed as:

$$F^n = K_n \delta_n \quad (3• 8)$$

Once the normal and shear contact forces are updated, they are adjusted according to the contact constitutive relations plotted in Figure 3•3b.

At present, TRUBAL employs a Coulomb friction law with no tensile strength. The maximum shear force is calculated by:

$$F_{max}^s = c + F^n \tan \phi_\mu \quad (3• 9)$$

where c is the contact cohesion, and ϕ_μ is the inter-particle friction angle.

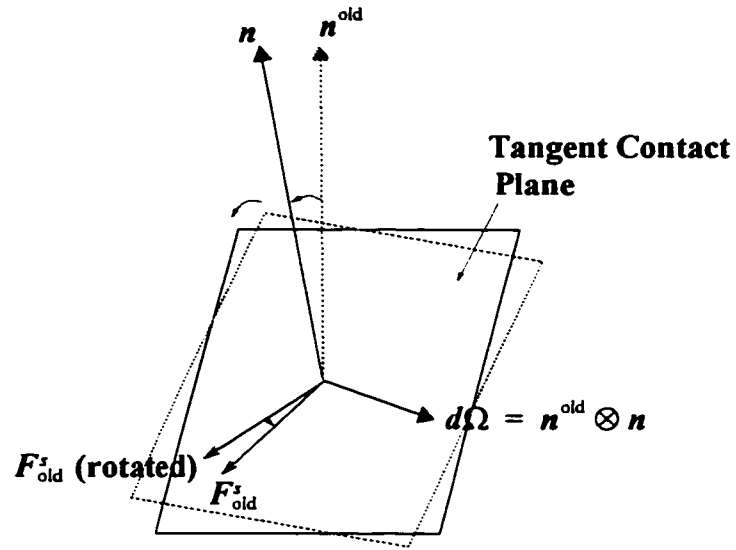
When updating the shear contact force vector, the incremental rotation of the contact normal vector \mathbf{n} must be taken into account. The vector representing the existing shear force in global coordinates \mathbf{F}^s must be rotated prior to adding to it the increment of shear contact force. The following correction applies:

$$\mathbf{F}_i^s \leftarrow (\mathbf{F}_i^s - \epsilon_{ijk} \epsilon_{kmn} \mathbf{F}_j^s \mathbf{n}_m^{\text{old}} \mathbf{n}_n) \quad (3• 10)$$

where \mathbf{n}^{old} is the contact normal vector at the previous time-step (Figure 3•4). The symbol, \leftarrow , means “replaced by”.

If the absolute value of the shear force $F^s = (F_i^s F_i^s)^{1/2}$ is greater than F_{max}^s , the shear force is reduced to this maximum value:

$$\mathbf{F}_i^s \leftarrow \mathbf{F}_i^s \left(\frac{F_{max}^s}{F^s} \right) \quad (3• 11)$$



$$\begin{aligned} F_{old}^s (rotated) &= F_{old}^s + d\Omega \otimes F_{old}^s \\ &= F_{old}^s + n^{old} \otimes n \otimes F_{old}^s \end{aligned}$$

Or:

$$[F_{old}^s]_i (rotated) = [F_{old}^s]_i - \epsilon_{ijk} \epsilon_{kmn} [F_{old}^s]_j n_m^{old} n_n$$

Figure 3-4 Incremental rotation of the shear contact force

The total contact force vector representing the action of particle A on particle B can be calculated, in global coordinates, as:

$$F_i^c = F^n n_i^c + F_t^s \quad (3 \cdot 12)$$

where n^c is the unit contact normal vector exterior to particle A .

The body force of a particle is equal to the vectorial sum of the contact forces acting at the surface of the particle. The body moment vector is the vectorial sum of the moments of contact forces calculated with respect to the particle's centroid; therefore,

For A :

$$\begin{cases} F_i^A \leftarrow F_i^A - F_i^c \\ M_i^A \leftarrow M_i^A - \varepsilon_{ijk}(C_j - A_j)F_k^c \end{cases} \quad (3 \cdot 13)$$

For B :

$$\begin{cases} F_i^B \leftarrow F_i^B + F_i^c \\ M_i^B \leftarrow M_i^B + \varepsilon_{ijk}(C_j - B_j)F_k^c \end{cases} \quad (3 \cdot 14)$$

3.3 Motion Update

Newton's equations of a rigid body motion are used to describe the motion of particles inside a strained assembly. They consist of a set of equations representing the translational particle centroid and rotational motion.

The centroid translational motion is described in the global coordinates by:

$$\ddot{x}_i + \alpha_L \dot{x}_i = \frac{F_i}{m} + g_i \quad (3 \cdot 15)$$

where \ddot{x} denotes the acceleration vector of the particle centroid; α_L is a viscous (mass-

proportional) damping constant for translational motion; F is the total force acting on the particle's centroid (*i.e.*, the sum of all contact forces acting on the particle); m is the particle's mass; and g is the gravity acceleration vector.

The undamped rigid body rotation is described by:

$$\begin{cases} I_1 \dot{\omega}_1 + (I_3 - I_2) \omega_3 \omega_2 = M_1 \\ I_2 \dot{\omega}_2 + (I_1 - I_3) \omega_1 \omega_3 = M_2 \\ I_3 \dot{\omega}_3 + (I_2 - I_1) \omega_2 \omega_1 = M_3 \end{cases} \quad (3 \cdot 16)$$

The above equations are known as Euler's equations of rigid body rotation. They are referred to the principal axes of inertia of the particle; $\dot{\omega}_j$ is the angular acceleration vector; ω_j is the angular velocity vector; M is the torque vector or the body moment vector; and I_i are the principal moments of inertia of the rigid body.

For an assembly of particles evolving between quasi-static states, the particle rotational velocities are such that the quadratic terms $\omega_i \omega_j$ can be neglected and therefore eliminated from the expression of Euler's equations in (3• 16). The simplified system of equations becomes linear and can be referred to the global coordinates by a simple matrix transformation from the local particle principal axes to the global coordinate axes.

Without this simplification, the system of equations can still be treated by using an elaborated explicit finite-difference discretization, but the numerical integration takes more calculation steps to update particle positions. A comparison between the results of solving the simplified and full equations showed that no substantial gain in the quality of the results is obtained by solving the full equations. Therefore, in order to save in calculation time, the simplified equations are solved by the modified program TRUBAL.

Relative to the global axes, the simplified Euler's equations can be written in the following tensorial form:

$$I_{ij}\dot{\omega}_j = M_i \quad (3\cdot 17)$$

The inertia tensor I_{ij} is calculated from its expression in the principal axes of inertia I_{ij}^P as:

$$I_{ij} = R_{ik}I_{kl}^P R_{jl} \quad (3\cdot 18)$$

where I_{ij}^P for an ellipsoid of mass m and principal radii ($a \geq b \geq c$) is given by:

$$I_{ij}^P = \frac{2}{5}m \begin{bmatrix} b^2 + c^2 & 0 & 0 \\ 0 & a^2 + c^2 & 0 \\ 0 & 0 & a^2 + b^2 \end{bmatrix} \quad (3\cdot 19)$$

and where R_{ij} is the orientation matrix of the ellipsoid defined in global coordinates by:

$$R_{ij} = \begin{bmatrix} e_1^L & e_2^L & e_3^L \\ e_1^I & e_2^I & e_3^I \\ e_1^S & e_2^S & e_3^S \end{bmatrix} \quad (3\cdot 20)$$

Here, e^L , e^I , and e^S are unit vectors in the direction of the long, intermediate, and short axes of the ellipsoid, respectively. The set of vectors (e^L , e^I , e^S) with the centre of the ellipsoid define the local coordinate system (Figure 3•5).

To complete the formulation of the equations of rotational motion solved by the program, a viscous damping term, similar to that considered for translational motion, is added to the simplified Euler's equations in global coordinates:

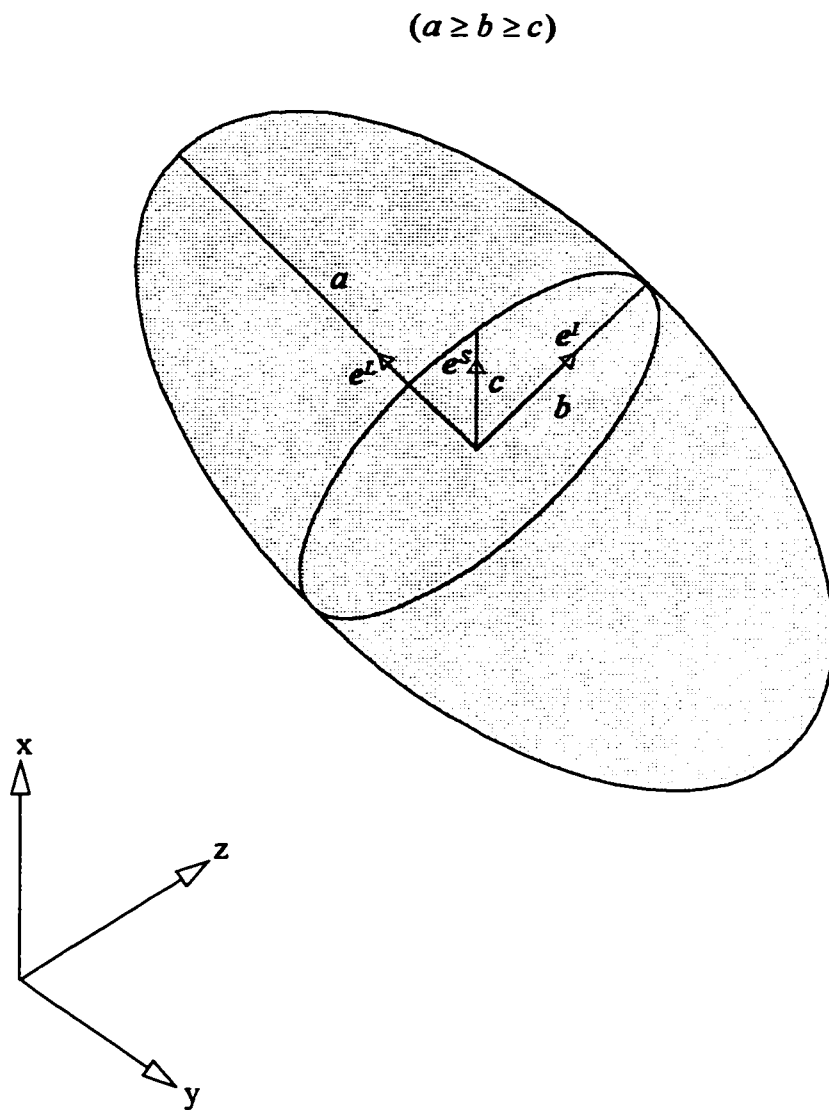


Figure 3-5 Orientation of an ellipsoid

$$\dot{\omega}_i + \alpha_R \omega_i = I_{ij}^{-1} M_j \quad (3 \cdot 21)$$

where I_{ij}^{-1} denote the inverse of the inertia tensor in global coordinates, and α_R is a rotational damping constant coefficient.

3.3.1 Damping

In order to model a quasi-static process using a dynamic method such as DEM, it is necessary to provide some means to absorb the excess kinetic energy within the system.

A viscous damping (represented by the pair (α_L, α_R)) is added into the equations of motion to achieve convergence to a steady-state equilibrium in the system.

The type of viscous damping used can be physically represented by a dashpot connecting the particle's center mass to a fixed frame of reference. It acts on the absolute velocity of the particle through an artificial body force which resists its motion. The combined effect of individual particle dampings on the system is similar to that of an assembly fully immersed in a viscous fluid.

Damping in granular materials is a real phenomenon. It is the global response of the combined effect of all mechanisms of energy dissipation present in the system. These mechanisms are complex and difficult to model, especially for discontinuous systems. Therefore, instead of representing the phenomenon in its complexity, simplified methods are used to account for the global damping response. Artificial damping is used for this purpose.

The program TRUBAL uses a “mass-proportional” damping, called “Rayleigh” damping. The damping coefficients (multipliers of velocities) for the translational and ro-

tational motions are proportional to the mass, m , and moment of inertia, $[I]$, of the particle, respectively:

$$\begin{cases} c_L = \alpha_L m \\ [C_R] = \alpha_R [I] \end{cases} \quad (3 \cdot 22)$$

The choice of the proportionality coefficients α_L and α_R is a source of difficulty because the optimum damping depends on the dominant modes of oscillation of the system. The latter are dependent on the size and shape of the particles and on instantaneous material properties. Another difficulty comes from the discontinuous nature of the system. In fact there is no unique way of choosing α_L and α_R for a complex system of several hundreds of particles in the general case. However, the uncertainty in the range of values can be minimized by a category of damping calculations methods called “adaptive damping schemes”. They are algorithms which allow selection of the damping coefficients to satisfy some criteria set in advance. The latter could be, for example, to enforce a constant dissipation rate of kinetic energy by damping at all times (Cundall, 1982), or to enforce an optimum condition of convergence and a stable finite-difference integration (Bardet and Proubet, 1991). In the latter case, the scheme was applied to a biaxial test performed with planar disks and the damping coefficient was plotted versus the simulation time. The curve of variation shows very pronounced oscillations from the beginning to the end of the test, indicating that there is no unique value of the damping coefficient for the entire test.

Unfortunately, the current version of program TRUBAL is not provided with an adaptive damping scheme. The damping coefficients are set in advance as constant input parameters.

3.3.2 Numerical Stability

Numerical instability is a potential problem in the explicit time, finite-difference procedure used in TRUBAL. The source of instability is the integration time-step; if it is greater than a *critical time-step*, the scheme is unstable and the results of the simulation are unreliable.

Methods of analysis of numerical instability exist and can be used to assess the critical time-step in cases where the discretized differential equation is simple.

The method can be applied, for example, to analyze the translational motion of a particle having a single contact with another particle. Each component of the system of differential equations describing the particle motion represents the motion of an equivalent single-degree-of-freedom mass-spring system.

The numerical stability analysis of such an equation shows that the critical time-step is related to the mass m and the stiffness k of the spring as follows:

$$\Delta t_c = 2 \sqrt{\frac{m}{k}} \quad (3\cdot 23)$$

A particle usually has more than a single contact, and there are many particles in the assemblage, therefore a global critical time-step for the entire assemblage should combine the lightest particle with the stiffest contact in the system:

$$\Delta t_c = 2 \sqrt{\frac{m_{min}}{k_{max}}} \quad (3\cdot 24)$$

Further reduction of the critical time-step is necessary to take into account the fact that the apparent stiffness acting on a particle increases as it becomes surrounded by other

particles. The critical time-step is multiplied in the program by a factor between 0.01 and 0.5, depending on the problem and shape of particles. For ellipsoids, values of the multiplying factor as low as 0.01 are commonly used to avoid instability.

3.3.3 Numerical Integration

A finite-difference procedure is used to integrate the equations of motion. To numerically discretize the equations, the velocity and acceleration vectors at time t are functions of the velocity vectors at mid-time intervals, $t-\Delta t/2$, and, $t+\Delta t/2$.

For the velocities:

$$\begin{cases} \dot{\mathbf{x}}_i^t = \frac{1}{2}(\dot{\mathbf{x}}_i^{t-\Delta t/2} + \dot{\mathbf{x}}_i^{t+\Delta t/2}) \\ \dot{\boldsymbol{\omega}}_i^t = \frac{1}{2}(\dot{\boldsymbol{\omega}}_i^{t-\Delta t/2} + \dot{\boldsymbol{\omega}}_i^{t+\Delta t/2}) \end{cases} \quad (3 \cdot 25)$$

For the accelerations:

$$\begin{cases} \ddot{\mathbf{x}}_i^t = \frac{1}{\Delta t}(\dot{\mathbf{x}}_i^{t+\Delta t/2} - \dot{\mathbf{x}}_i^{t-\Delta t/2}) \\ \ddot{\boldsymbol{\omega}}_i^t = \frac{1}{\Delta t}(\dot{\boldsymbol{\omega}}_i^{t+\Delta t/2} - \dot{\boldsymbol{\omega}}_i^{t-\Delta t/2}) \end{cases} \quad (3 \cdot 26)$$

Substituting these expressions into the equations of motion and solving for the velocities at time $t+\Delta t/2$ results in the following expressions:

$$\begin{cases} \dot{\mathbf{x}}_i^{t+\Delta t/2} = (A_L \dot{\mathbf{x}}_i^{t-\Delta t/2} + (F_i^{(t)}/m + g_i)\Delta t)B_L \\ \dot{\boldsymbol{\omega}}_i^{t+\Delta t/2} = (A_R \dot{\boldsymbol{\omega}}_i^{t-\Delta t/2} + I_{ij}^{-1(t)} M_j^{(t)}\Delta t)B_R \end{cases} \quad (3 \cdot 27)$$

where:

$$\begin{bmatrix} A_L & B_L \\ A_R & B_R \end{bmatrix} = \begin{bmatrix} 1 - \alpha_L \Delta t/2 & (1 + \alpha_L \Delta t/2)^{-1} \\ 1 - \alpha_R \Delta t/2 & (1 + \alpha_R \Delta t/2)^{-1} \end{bmatrix} \quad (3 \cdot 28)$$

The increments of translation and rotation are obtained as:

$$\begin{cases} \Delta x_i = \dot{x}_i^{t+\Delta t/2} \Delta t \\ \Delta \theta_i = \omega_i^{t+\Delta t/2} \Delta t \end{cases} \quad (3 \cdot 29)$$

The position and orientation of a particle are updated as:

$$\begin{cases} x_i^{t+\Delta t} = x_i^t + \Delta x_i \\ R_{ij}^{t+\Delta t} = R_{ij}^t + \Delta R_{ij} \end{cases} \quad (3 \cdot 30)$$

where:

$$\Delta R_{ij} = \Delta \theta_{ik} R_{kj}^t \quad (3 \cdot 31)$$

and:

$$\Delta \theta_{ij} = \begin{bmatrix} 0 & \Delta \theta_3 & -\Delta \theta_2 \\ -\Delta \theta_3 & 0 & \Delta \theta_1 \\ \Delta \theta_2 & -\Delta \theta_1 & 0 \end{bmatrix} \quad (3 \cdot 32)$$

ΔR_{ij} is the change in the orientation matrix that follows the increment of rotation represented by the skew-matrix $\Delta \theta_{ij}$.

After the motion update is completed, the force sum, F , and the moment sum, M , of each particle are reset to zero at the end of each cycle.

3.4 Modified Program TRUBAL

TRUBAL is organized as shown in Figure 3•6. A set-up routine is executed at the beginning to open all files and initialize all parameters. The program reads the execution commands from an instruction file called “trb.dat”. The commands are ordered in a sequential manner and interpreted through the central input routine.

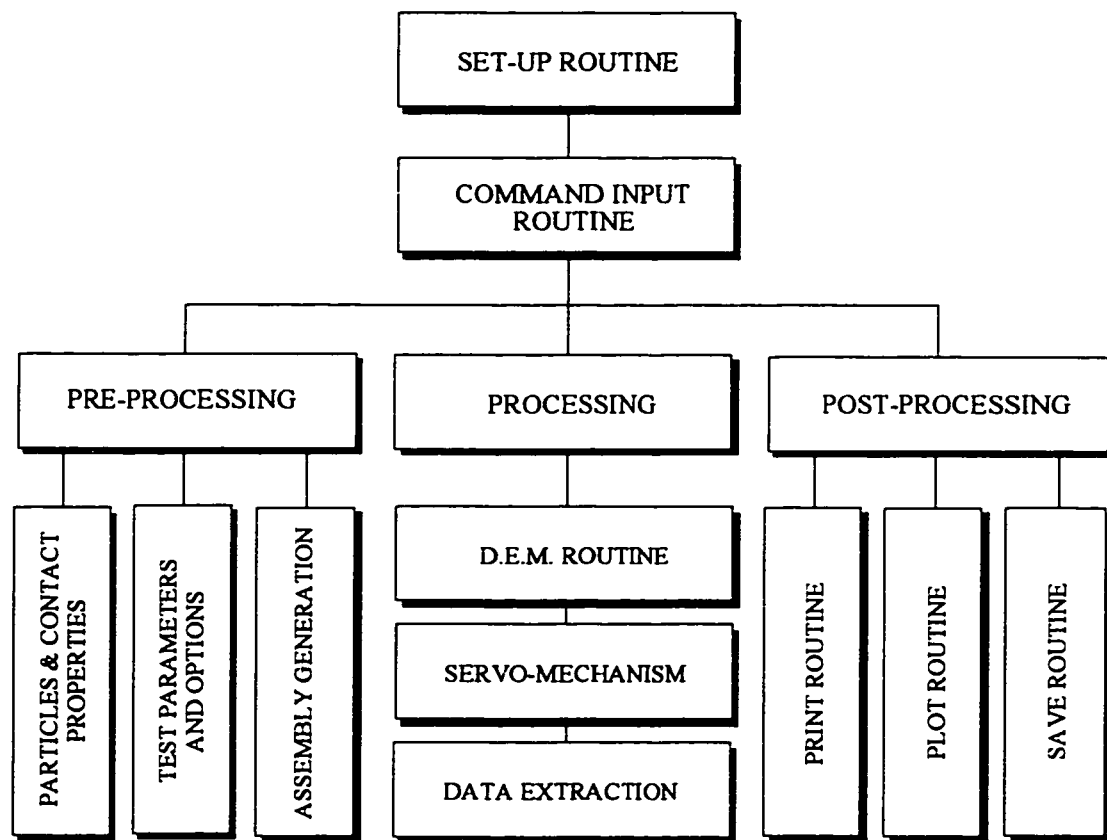


Figure 3-6 Organization of program TRUBAL

The program ends if all instructions are executed or an error is detected that causes the program to stop. The execution commands are of three types: Pre-processing, Processing, and Post-processing.

3.4.1 Pre-Processing

The pre-processing consists of the following tasks:

1. Input particle and contact properties. A particle's type identifies a group of particles having the same size and density. A contact type identifies the physical properties of contacts between particles' types. Examples of contact properties are the normal and shear stiffnesses, the coefficient of inter-particle friction and cohesion. TRUBAL accommodates up to 25 particle types and 25 contact types.

Input test parameters and options. Test parameters are: viscous damping, fraction of critical time-step, grid strain rate, servo-mechanism and shape transformation parameters (to generate ellipsoids from spheres).

Test options are: 2-D mode (spheres only), Hertzian contact law (spheres only), servo-mechanism mode, and particle shape.

2. Generate an initial assembly of particles within a rectangular cell of a specified size. Two methods are possible:
 - a. Use the random generator facility available to generate an initial assembly of non-overlapping spheres; then, invoke a "growth"

scheme to transform the assembly of spheres into an assembly of ellipsoids.

- b. Use the “create” command to place the particles in specific locations in the cell. The command can be equally used to create spheres or ellipsoids.

3.4.2 Processing

The processing consists of repeating the cycle of mechanical calculations according to the instructions in the input data file. As shown in Figure 3•7, the calculation of particle motions and particle-to-particle interactions is processed through the subroutine “CYCLE” which invokes two main subroutines: “MOTION”, which updates particle position and orientation, and “FORD”, which computes interparticle contact forces.

The extraction of micromechanical parameters is processed in the subroutine “CYCLE” through a series of subroutines which initialize the micro-parameters (subroutine “MICROINT”), accumulate groups of contact normals and micro-variables (subroutine “MICROEXT”), and calculate group averages for micro-variable histograms (subroutine “MICROAVG”).

Finally, extract model approximations of measured distributions of the average microscopic variables (subroutine “MICROPAR”). The servo-control is processed in subroutine “RUNSRV”, called from the main subroutine “CYCLE”.

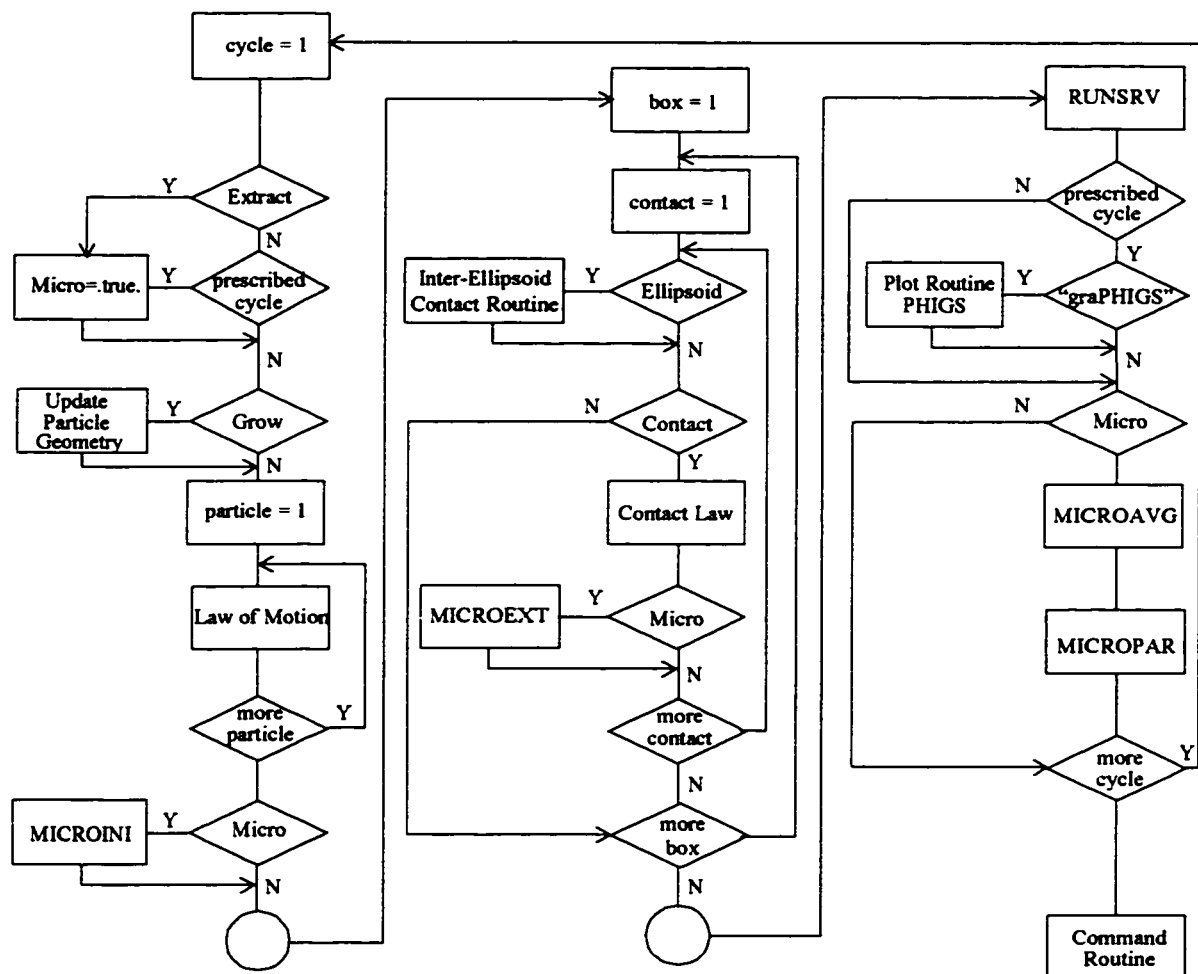


Figure 3-7 Flow chart of DEM routine in the modified program TRUBAL

The subroutines to extract data for histogram plots (originally using a single spherical partitioning of the orientation space) can now accommodate the near-uniform partitioning algorithm described in Appendix A. Additional data are extracted such as the fourth-order Fourier's approximations of measured distributions and numerous other statistics on contacts and particles.

3.4.3 Post-Processing

The post-processing includes the printout of results and saving of particular states of the assembly for further processing.

3.4.4 Data Structures

The data structures of the original TRUBAL are shown in Figure 3•8. The data structures of the modified TRUBAL are almost the same ones used in the original version.

Minor changes involve modifying the main array to allocate additional space for new variables necessary to update ellipsoid motion as well as detecting and calculating inter-ellipsoid contacts.

All data are stored in a single array $A(I)$ which is partitioned into sub-arrays containing information about the particles, boxes, and the linked list for box entries and contacts. This partition is shown in Figure 3•8a.

The variables M_1 , M_3 , and M_5 are set to fixed values at the start of a new problem, after the user has declared how many particles and boxes are required. Variables M_1^* and M_4 are also set at the beginning of a test run, but they can change as the user creates more particles or as the requirements for box entries and contacts change during the test.

(b) Link list scheme



3.4.4.1 Group of Particle Data

A group of 38 words is allocated to describe a single ellipsoid within the partition, M_1 to M_{38} , as shown in Figure 3•8b. This group consists of data, in a global Cartesian coordinate system, for centroid position and velocity vectors, rotation vector, angular velocity vector, vector force sums, vector moment sums, and a pointer to the particle properties arrays. Originally, a sphere required only 29 words to describe it. Nine additional words are allocated in the modified data structures to store the nine components of the ellipsoid orientation matrix.

3.4.4.2 Group of Contact Data

A group of seven words is used to describe a contact between two spheres. It consists of data for the tangential contact force vector, the normal contact force, the addresses of the two particles forming the contact, and the pointer to the next contact in the linked list of contacts that map into a given box (Figure 3•8b). The contact normal and contact vectors are stored for ellipsoids in nine additional words.

3.4.5 Identification of Neighbours

In DEM, particles are allowed complete freedom to interact with each other. An efficient scheme is needed to identify possible candidates for contact with a given particle. It is computationally prohibitive to check all possible pairs of particles. The method devised in TRUBAL confines the search to pairs that are in contact or close enough to be in contact in a later time during the simulation.

3.4.5.1 Boxing Scheme

The rectangular cell containing the assembly of particles is divided into smaller 3-D cells (boxes). A rectangular “envelope space” is assigned to each particle and mapped into the box or boxes it occupies (Figure 3•9a). Two particles are considered to be neighbours and checked for contact if they are both mapped into at least one common box (Figure 3•9b).

3.4.5.2 Envelope Space

The envelope space around a particle is defined by a rectangular box containing the particle with sides parallel to the directions of the frame of reference. For a sphere, it is a cube of a length equal to the sum of the sphere’s diameter and a fixed length *TOL* (as tolerance) to ensure that all potential candidates are examined for possible contact.

For an ellipsoid, the envelope space is taken around a fictitious sphere at the ellipsoid’s centre with a radius equal to the ellipsoid’s major semi-axis (Figure 3•9a). The envelope space defined as such is larger than the optimal envelope (containing the ellipsoid in the closest possible geometry) but the choice made is convenient because:

1. The existing mapping scheme used for spheres is not altered.
2. The mapping scheme might generate more neighbours to be checked for contact, compared to a mapping scheme based on the choice of the optimal envelope of ellipsoids. However, the inter-particle detection scheme discussed in the next chapter is provided with an algorithm that eliminates empty contacts before processing the contact detection routine.

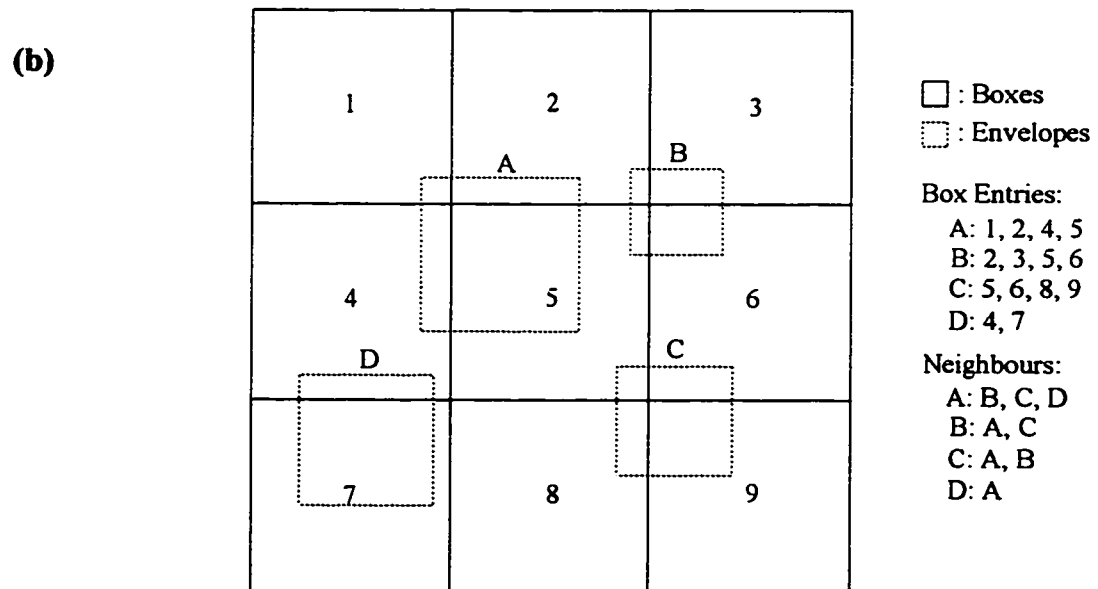
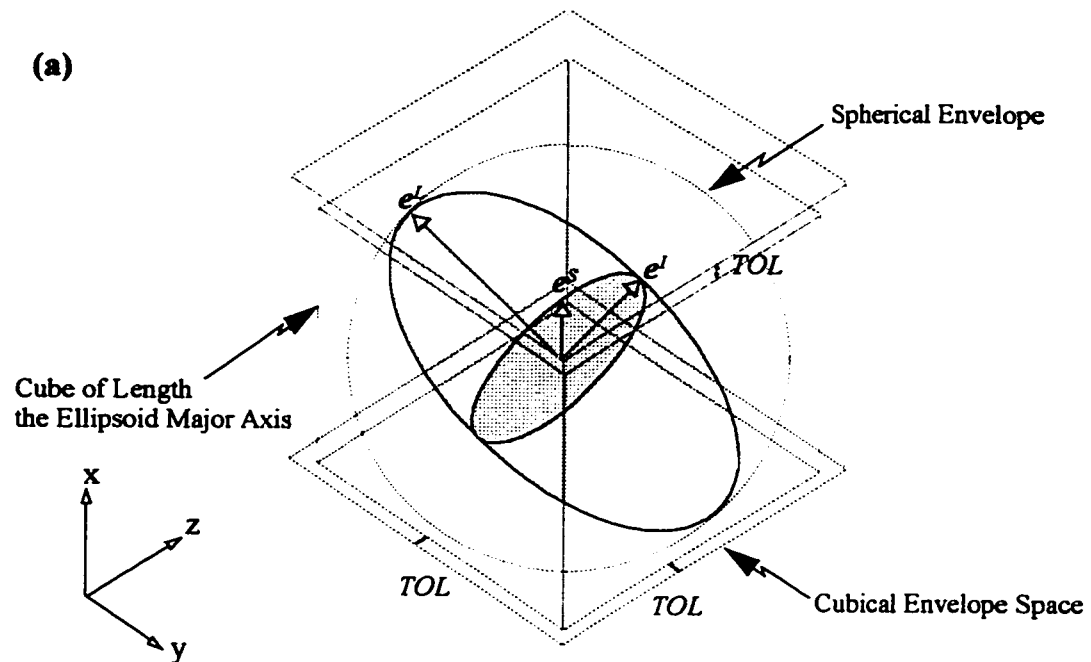


Figure 3-9 Mapping scheme for ellipsoids
 (a) Envelope space
 (b) Boxing scheme (2-D view)

3. The determination of the optimal envelope vertices necessitate a relatively expensive computational effort by comparison to the first choice.

3.4.6 Periodic Space Algorithm

A generated assembly is automatically confined within parallelepipedic boundaries with a numerical connection between their opposite faces. Two aspects define this numerical connection (periodicity) of the space solution:

Geometrically:

1. The particles that move out of the cell through a particular face re-enter the cell from the opposite face. A particle that “protrudes” a boundary face is considered to be outside the cell if its centroid is located outside the cell.
2. If a particle “protrudes” the sample boundaries through one or several faces but remains inside the cell, then the program creates “virtual images”, identical to the original particle, at the opposite faces. These images can physically interact with other particles as if the original particle was present in several locations at the same time.

Numerically:

1. The height x_1^b , the length x_2^b , and the width x_3^b of the cell are updated after each increment of strain as:

$$x_i^b \leftarrow (x_i^b + \dot{\epsilon}_{ij} x_j^b \Delta t) \quad (3-33)$$

2. For every particle, an increment of displacement due to the strain rate of the periodic space is added to the increment of displacement due to the velocity of the particle as:

$$\Delta x_i^{(tot.)} = \Delta x_i^{(vel.)} + \dot{\epsilon}_{ij} x_j \Delta t \quad (3-34)$$

where x is the particle's position vector.

3. The relative velocity of two particles in contact (used to calculate the contact force) is the sum of the real relative velocity and a component due to the periodic deformation:

$$\dot{x}_i^{r(tot.)} = \dot{x}_i^{r(real)} + \dot{\epsilon}_{ij} z_j \quad (3-35)$$

where z is the vector joining the centroids of particles in contact (branch vector).

By virtue of this type of numerical connection, the effect of physical boundaries on the final solution is eliminated.

3.4.7 Stress Servo-Control

The program TRUBAL accommodates simple stress loading paths including constant stress components, constant 3-D mean stress $(\sigma_{11} + \sigma_{22} + \sigma_{33})/3$, constant 2-D mean stress $(\sigma_{11} + \sigma_{22})/2$, constant angle of major principal stress in a ring shear test, and any physically reasonable combination of these.

A stress variable is controlled and maintained to a certain level through the control of the applied strain increment.

The stress control model is the same for all stress paths. It is explained in the follow-

ing section for the particular category of tests used in this study where the samples are strained to simulate a deviatoric compression with a constant 3D-mean stress.

3.4.8 Deviatoric Compression at Constant Mean Pressure

The compression is obtained by imposing an initial negative strain rate in the direction of the compression (axial), and smaller positive strain rates on lateral faces.

The servo-mechanism controls the mean pressure by adjusting the strain rate components in such a way as to keep the value of the difference between the specified and measured mean stresses as close to zero as possible. The following model is implemented to control the mean pressure:

$$\dot{\epsilon}_{ij} \leftarrow \dot{\epsilon}_{ij} + \frac{gain}{3} (p^{(target)} - p^{(measured)}) \quad (3-36)$$

where $\dot{\epsilon}_{ij}$ is the applied strain rate tensor, and *gain* is a user-defined parameter representing the “gain” of the servo-mechanism. The mean pressure is calculated from the components of the measured stress tensor, σ_{ij} , as: $p = \sigma_{kk}/3$.

3.4.9 Particle “Growth” and Assembly Generation

The option of generating an initial “gas” of non-overlapping ellipsoids and compacting it to a desired packing density before testing was dismissed for two reasons: (1) It necessitates a special procedure to place the ellipsoids in non-overlapping locations within the cell; (2) The results of the compaction are not easy to control.

Controlling the initial packing density is not as important as controlling the initial coordination number. Through the compaction of a “gas” of particles, it is only possible to

control the pressure, and perhaps the packing density, but not the coordination number.

An alternative to this procedure of assembly generation is to create the assembly of ellipsoids from a compacted assembly of spheres by changing the shape of spheres incrementally over many calculation cycles. This method was successfully employed to generate very dense assemblies of plane ellipses (Rothenburg and Bathurst, 1992).

At each cycle, the dimensions of the particle radii in three mutually perpendicular directions are incremented, some positively and some negatively, to preserve the volume of the particle constant. The process continues until the targeted shape is reached. The rate and direction of “growth” are set by the user. The rate of “growth” is specified in terms of a number of calculation cycles to achieve a certain particle eccentricity. The following options are executed in parallel: (1) maintain the mean pressure constant, (2) set the inter-particle friction to zero in order to ease particles’ interlocking, (3) “relax” the system between successive increments of particle shape transformations to control inertia forces and regain static equilibrium.

3.4.9.1 “Growth” Scheme with Constant Particle Volume

The size and shape of an ellipsoid are fully determined by its principal radii, $a \geq b \geq c$.

To emphasize the shape in particular, two aspect ratios representing the *elongation* and *flatness* of the ellipsoid can be defined as:

$$\begin{cases} \text{elr} = a/b \\ \text{flr} = b/c \end{cases} \quad (3-37)$$

where, elr , is the elongation ratio, and, flr , is the flatness ratio.

A suitable parameter to describe the size of an ellipsoid is the *geometric mean radius* equal to the radius of a sphere of equal volume to that of the ellipsoid, *i.e.*:

$$r = \sqrt[3]{abc} \quad (3 \cdot 38)$$

The set of variables (elr, flr, r) is equivalent to the set of principal semi-axes (a, b, c) . The two sets are related through the following identities:

$$\begin{cases} a = r flr^{-1/3} elr^{-2/3} \\ b = a elr \\ c = b flr \end{cases} \quad (3 \cdot 39)$$

The set of variables (elr, flr, r) is more convenient for implementing the constant volume shape transformation algorithm.

Initially, the aspect ratios are set to $elr = 1$ and $flr = 1$ (spheres). Between two successive cycles of the particle shape transformation, n and $n + 1$, the particle shape is modified only by incrementing the elongation and flatness ratios.

In order to preserve the volume of the particle constant, the geometric mean radius must be kept unchanged (equal to the radius of the initial spherical shape); therefore:

$$\begin{cases} elr^{(n+1)} = elr^{(n)} + \delta elr \\ flr^{(n+1)} = flr^{(n)} + \delta flr \\ r^{(n)} = r^{(0)} \end{cases} \quad (3 \cdot 40)$$

where $(\delta elr, \delta flr)$ are the increments of elongation and flatness ratios, respectively.

For the simulations performed for the study, only the elongation ratio is changed during the shape transformation to generate the simplest shape (oblate spheroids) instead of a

more-general ellipsoid shape. One reason for this choice is that the effect of particle shape on the mechanical behaviour of granular systems is still a new subject of study for numerical simulations of granular materials. Starting with simple ellipsoid shapes is a first step that should precede the investigation of more-complex shapes. Another reason is that prolate spheroids are three-dimensional analogues of plane-ellipses, for which some micro-mechanical studies have been already published, and can be used for comparison between the two-dimensional and three-dimensional cases.

With this choice, the size and shape of ellipsoids are fully determined by the pair of parameters (elr, r) .

Similar equivalent parameters to define ellipsoids with a single aspect ratio are:

$$\begin{cases} e = (a - b) / (a + b) \\ \bar{r} = (a + b) / 2 \end{cases} \quad (3.41)$$

CHAPTER IV: INTER-ELLIPSOID CONTACT DETECTION ALGORITHM

4.1 Introduction

Real particles of sand are nearly rigid except at the compliant contact points with other particles where they can deform under the action of contact forces. The numerical particles also deform at contact locations but without changing shape. The particle deformation is taken into account by allowing the contacting particles to cross each other near the contact points. The amount of overlap is a measure of contact deformation. It is usually a very small fraction of the average particle diameter.

In order to calculate the overlap distance at the contact between two arbitrary ellipsoids, the region of overlap shared by the two ellipsoids must be determined. The equation of such a region is the equation of intersection of the ellipsoid surfaces. The approximated

region of overlap is used not only to calculate the extent of overlap but also to calculate some basic characteristics of a contact such as the normal vector and the contact vectors.

The problem of intersection of two spheres is straightforward (Figure 4•1). Two spheres are in contact if the distance between their centroids, S_1 and S_2 , is less than the sum of their respective radii, r_1 and r_2 , i.e., $S_1S_2 \leq r_1 + r_2$.

The contact normal and contact vectors are parallel to the segment joining the centroids $[S_1S_2]$, and the normal overlap distance is equal to $\delta^n = r_1 + r_2 - S_1S_2$. The solution is simple because the radius of curvature at any point of the surface of a sphere is equal to the radius of the sphere.

However, an arbitrary ellipsoid is characterized at each point on its surface by a pair of radii of curvatures depending on the location of the point. Also, the contacts inside an assembly of particles can involve two ellipsoids of arbitrary sizes, orientations and positions in the space. These two aspects of the problem enhance the relative complexity of solving the intersection equation in the general case.

The method developed to solve the problem of intersection for ellipsoids aims at only calculating the contact characteristics that are required to implement the contact force-displacement law. The knowledge of the exact shape of the overlap area is not necessary and an accurate approximation is sufficient for this purpose.

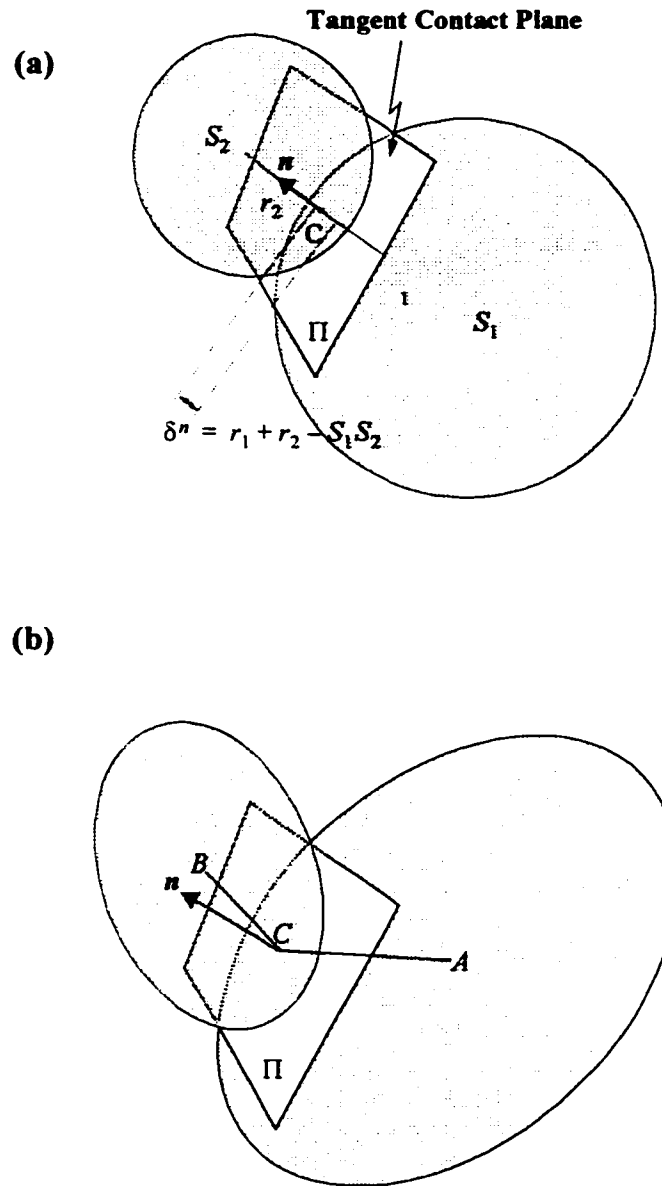


Figure 4-1 A pair of overlapping particles
 (a) Spheres
 (b) Ellipsoids

The inter-ellipsoid contact detection problem is divided into two sub-problems.

1. To test for overlap between the considered ellipsoids for contact. Knowing in advance whether or not two ellipsoids intersect each other determines if the second step should be undertaken. Considering that most of the contact list consists of pairs of particles that have relatively close positions but have empty intersections, the savings in computational effort provided by the test for overlap can be appreciable.
2. To calculate the contact characteristics if the test for overlap is positive. The determination of the contact characteristics is based on solving the intersection equation.

4.2 Test for Overlap

An intersection between two ellipsoid surfaces is an intersection between two quadric surfaces. In addition to these two surfaces, there is an infinite set of quadrics which also contains that intersection. If only one member of this infinite set is empty, then the intersection is empty. Otherwise, it can be assumed that the intersection is full. This summarizes the principle used to test for overlap between ellipsoids. Subsequent developments are concerned with explaining the principle in more detail and showing how this principle can be implemented in a computer code.

4.2.1 Quadric Surface Equation

The surface of an ellipsoid is a special quadric surface. The general equation of a quadric surface in Cartesian coordinates is:

$$Ax^2+By^2+Cz^2+2Dxy+2Eyz+2Fzx+2Gx+2Hy+2Jz+K = 0 \quad (4.1)$$

A matrix form of the same equation known as the *discriminant* form of the quadric surface is:

$$\underline{X}Q\underline{X}^T = 0 \quad (4.2)$$

where:

$$Q = \begin{bmatrix} A & D & F & G \\ D & B & E & H \\ F & E & C & J \\ G & H & J & K \end{bmatrix} \quad (4.3)$$

Q is called the discriminant matrix of the quadric surface. $\underline{X} = [x \ y \ z \ 1]$ is the uni-line vector position. \underline{X}^T is the transposed uni-column vector position.

Another important parameter used to classify quadric surfaces is the *sub-discriminant*, Q_u , defined as the upper-left (3x3) sub-matrix of the discriminant matrix Q :

$$Q_u = \begin{bmatrix} A & D & F \\ D & B & E \\ F & E & C \end{bmatrix} \quad (4.4)$$

4.2.2 Classification of a Quadric Surface

As shown in the diagram of Figure 4•2, a quadric surface whose generic equation in an arbitrary set of axes is known can automatically be classified as a particular surface type (e.g., ellipsoid, hyperboloid, etc.).

It is sufficient for recognizing a quadric surface type that the signs taken by a few of the invariants of its discriminant and/or sub-discriminant matrices be known. These invariants are referred to in the diagram of Figure 4•2 as $D_{i, (i = 2, 4)}$ for the discriminant matrix Q , and $T_{i, (i = 1, 3)}$ for the sub-discriminant matrix Q_u .

Each combination of these signs characterizes a particular surface type. It does not matter in which set of axes the generic equation is expressed since the classification is only based on frame invariant quantities.

For example, a quadric surface which satisfies the series of inequalities: $T_3 > 0$, $T_2 < 0$, $T_1 T_3 > 0$ and $D_4 < 0$ is an ellipsoid. Here, T_1 , T_2 and T_3 are the first, the second, and the third invariants of the sub-discriminant Q_u , respectively, and D_4 is the determinant of the discriminant Q .

There also exist three particular combinations of the signs of invariants $T_{i, (i = 1, 3)}$ and $D_{i, (i = 2, 4)}$ characterizing *empty* surfaces. They are termed “INVALID” in the diagram of Figure 4•2.

4.2.3 Basic Concept

Let A and B denote two ellipsoids with a non-empty intersection: $I = A \cap B \neq \emptyset$, and let Q_A and Q_B be their respective discriminant matrices.

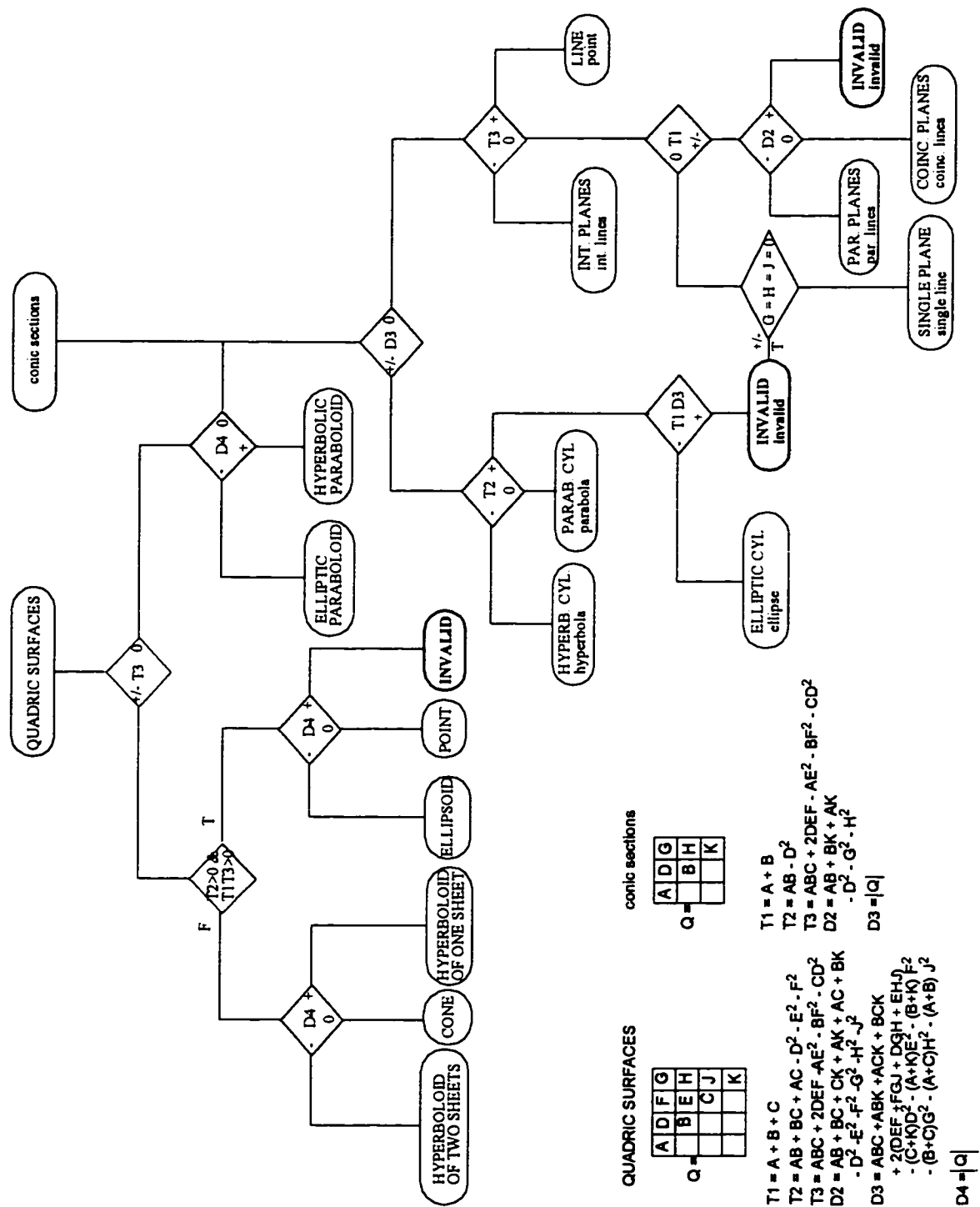


Figure 4.2 Classification of quadric surfaces and conic sections (after Levin, 1979)

By definition, a point \underline{X} in the intersection satisfies the generic equations of both A and B , therefore:

$$\begin{cases} \underline{X}Q_A\underline{X}^T = 0 \\ \underline{X}Q_B\underline{X}^T = 0 \end{cases} \quad (4\bullet 5)$$

The following equation (obtained by linear combination of the above equations) is also satisfied for any point in the intersection, I , and any arbitrary number, f :

$$\underline{X}(Q_A + fQ_B)\underline{X}^T = 0 \quad (4\bullet 6)$$

Equation (4• 6) defines a family of new quadric surface C_f having $Q_A + fQ_B$ as a discriminant matrix. All points in the intersection satisfy the generic equation of C_f , therefore:

$$I \subset C_f \quad (4\bullet 7)$$

4.2.3.1 Principle of the Overlap Test

If it is possible to classify all C_f according to their types as given by the diagram in Figure 4•2, then:

- i. If a particular value of f is found for which the quadric surface C_f is empty, then, according to (4• 7) the intersection, I , is empty and the ellipsoids, A and B , do not overlap one another.
- ii. If no such a quadric is found, it will be assumed that the ellipsoids share a common non-empty intersection.

An apparent difficulty arises when the following question is posed: How can an infinite family of quadric surfaces (C_f) be scanned in search for a particular value of f which

may or may not exist? The answer to this problem is briefly described in the following section.

4.2.4 Scan of Quadrics C_f

The type of a quadric C_f depends only on the signs taken by its invariants $T_i(f)$ and $D_i(f)$. These are *polynomial* expressions of the variable, f , with the highest degree of four obtained for $D_4(f)$. It is well known that the number of real roots of a polynomial never exceeds its degree; therefore, the total number of real roots of all invariants combined never exceeds:

$$1_{(T_1)} + 2_{(T_2)} + 3_{(T_3)} + 2_{(D_2)} + 3_{(D_3)} + 4_{(D_4)} = 14 \quad (4.8)$$

It is also known that polynomials do not change signs between real roots. This means that for example, $T_1(f)$ will change the sign two times at the most, $T_2(f)$ three times, etc. Therefore, it is sufficient to search for an “INVALID” case for values of f at the middle between two successive roots after these have been sorted in order of increasing values. In the worst case, $14+2$ (one before the first root and one after the last root)=16 checks are necessary. Practically, there are many fewer distinct real roots and not all invariants are involved in the classification, so that the number of checks is much less than sixteen. Generally, these are exhausted only if the intersection is not empty. Empty intersections on the other hand, are quickly detected.

4.3 Calculation of Contact Parameters

The calculation of the contact parameters is based on the solution of the intersection between two ellipsoids' surfaces. Only the trace of the intersection on the surface of one of the two ellipsoids is required. Let it be ellipsoid A ; then, the following notations will be used:

- The surface-to-surface (A - B) intersection is denoted by I
- The trace of the intersection, I , on the surface of ellipsoid, A , is denoted by I_A .

4.3.1 Principle

As shown in Figure 4•3, the parametric representation of an ellipsoid by the pair of variables (θ, ϕ) can be interpreted geometrically as follows:

The curves corresponding to $\theta = \text{constant}$ (called θ -curves) scan the surface of the ellipsoid longitudinally from one pole to the opposite one, similar to meridians for spheres. On the other hand, the ϕ -curves are mutually parallel and cross the θ -curves.

Any pair of θ -curves and any pair of ϕ -curves intersect in four points, thereby delimiting a curvilinear parallelogram on the surface of an ellipsoid. Any region of the surface of the ellipsoid can be geometrically bounded by two pairs of appropriately chosen θ -curves and ϕ -curves. Using this concept, the trace of the contact of two ellipsoids on the surface of one of them can be approximated by such curves.

In order to calculate these curves, it is necessary to represent one of the ellipsoids' surfaces by a system of parametric equations using the pair of variables (θ, ϕ) ; for example, ellipsoid A and ellipsoid B may be represented by a regular algebraic equation.

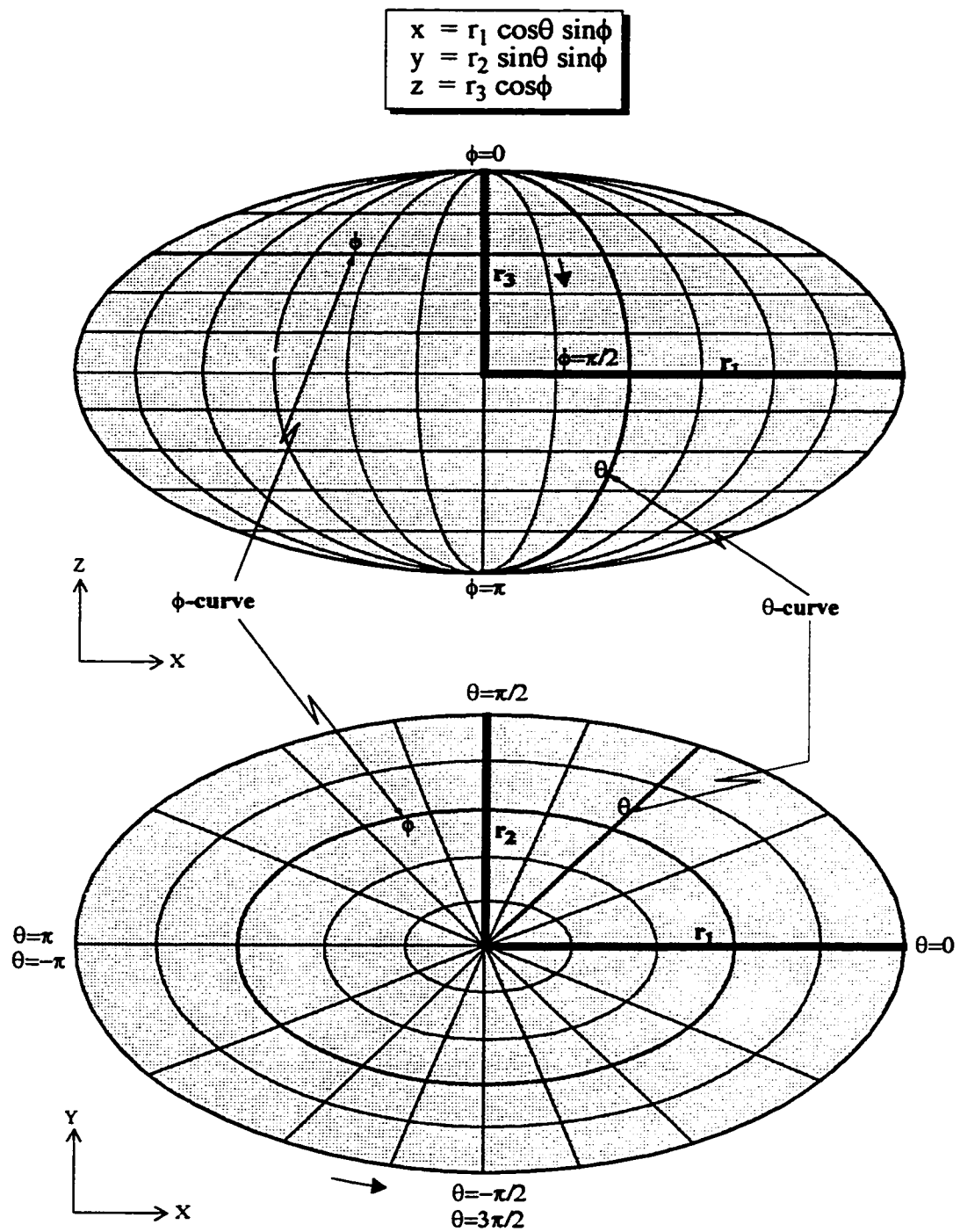


Figure 4-3 (θ, ϕ) parametrization of the surface of an ellipsoid

The ellipsoid-to-ellipsoid intersection can be decomposed into two types of curve-to-surface intersections: (θ -curve)-to-surface and (ϕ -curve)-to-surface intersections. These are simpler to determine than the original surface-to-surface intersection because they only involve one varying parameter.

The basic idea of the contact detection algorithm is to approximate the contact by solving a minimum number of curve-to-surface intersections, and then to use the obtained approximation to determine the characteristics of the contact.

The solution of curve-to-surface type equations is explained in Appendix B.

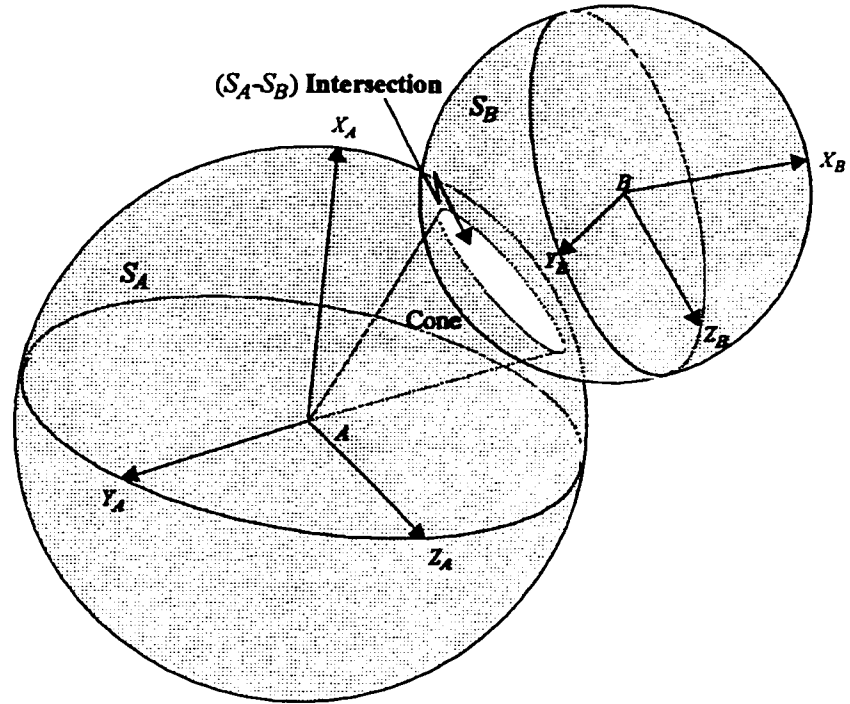
4.3.2 First Approximation of the Contact

A first region containing the trace of the contact on the surface of ellipsoid A , *i.e.*, I_A , is obtained analytically from the solution of the intersection of a circular cone originating from the centroid of ellipsoid A with the surface of ellipsoid A . The cone is chosen so that its intersection with A contains I_A .

To find the first set of parametric curves, a circular cone, C , is intersected with ellipsoid, A , as shown in Figure 4•4b. The intersection C - A contains the trace I_A .

The base of the cone is selected to be the intersection of the smallest spheres circumscribing the ellipsoids S_A and S_B (Figure 4•4a). As such, the cone must contain the trace I_A since I is part of the S_A - S_B intersection. Now, I_A , being inside the cone, C , and on the surface of, A , must belong to their intersection, *i.e.*, $I_A \subset C \cap A$.

(a)



(b)

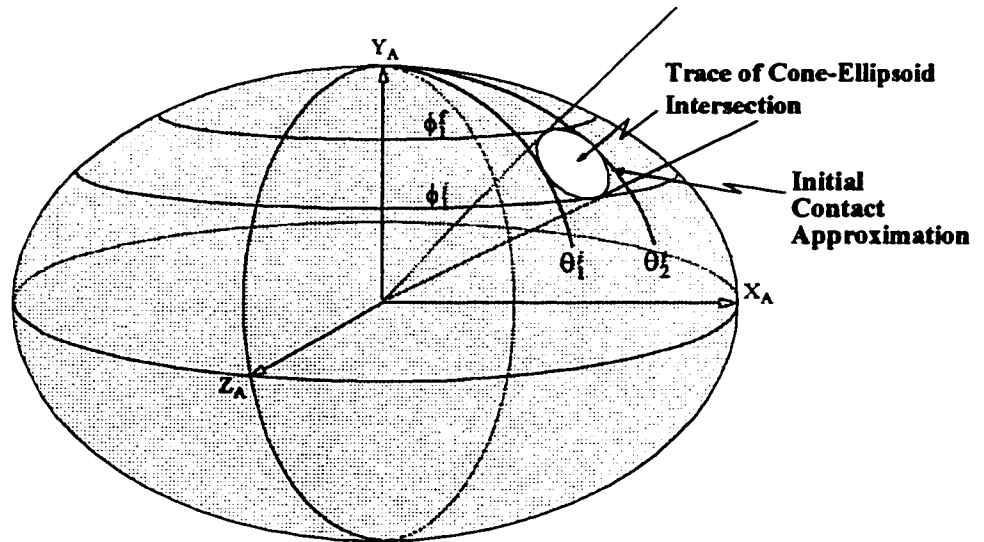


Figure 4-4 Surface intersections
 (a) Sphere-sphere intersection
 (b) Cone-ellipsoid intersection

If a set of four parametric curves can be determined which circumscribes the trace of (ellipsoid A -cone C) intersection, this same set also circumscribes the trace I_A . In this manner a first approximation to the solution is found.

4.3.3 Refinement of First Approximation

The direct way to improve this first approximation is by refining it. If the refinement is to be done incrementally, then the procedure would be practically useless since it would take an unacceptable amount of time to execute. A quick alternative is used as follows:

Let, θ_1^i , θ_2^i , ϕ_1^i , and ϕ_2^i , be the set of parameters characterizing the first region of contact, and let $\bar{\theta}$ be the middle value between θ_1^i and θ_2^i . By solving the ($\bar{\theta}$ -curve) -to-ellipsoid, B , intersection, a new pair of ϕ 's is obtained. This pair is closer to the real intersection boundary (Figure 4•5).

Note that the ($\bar{\theta}$ -curve) -to-ellipsoid, B , intersection is almost always full because the initial region happens to be centered about the contact. Exceptions can be encountered for excessively small contacts between very eccentric and randomly oriented ellipsoids. In simulations the particle eccentricities are moderate and this situation is never encountered.

However, if this is the case, another middle value between θ_1^i and $\bar{\theta}$, or between $\bar{\theta}$ and θ_2^i , is tried, and so on, until a full intersection is found.

Let ϕ_1^f and ϕ_2^f be the new pair and $\bar{\phi}$ their arithmetic mean. Once more by solving the ($\bar{\phi}$ -curve) -to- B intersection, the final pair (θ_1^f, θ_2^f) is obtained (Figure 4•5). This last intersection is always full.

The flow chart of the algorithm is given in Figure 4•6.

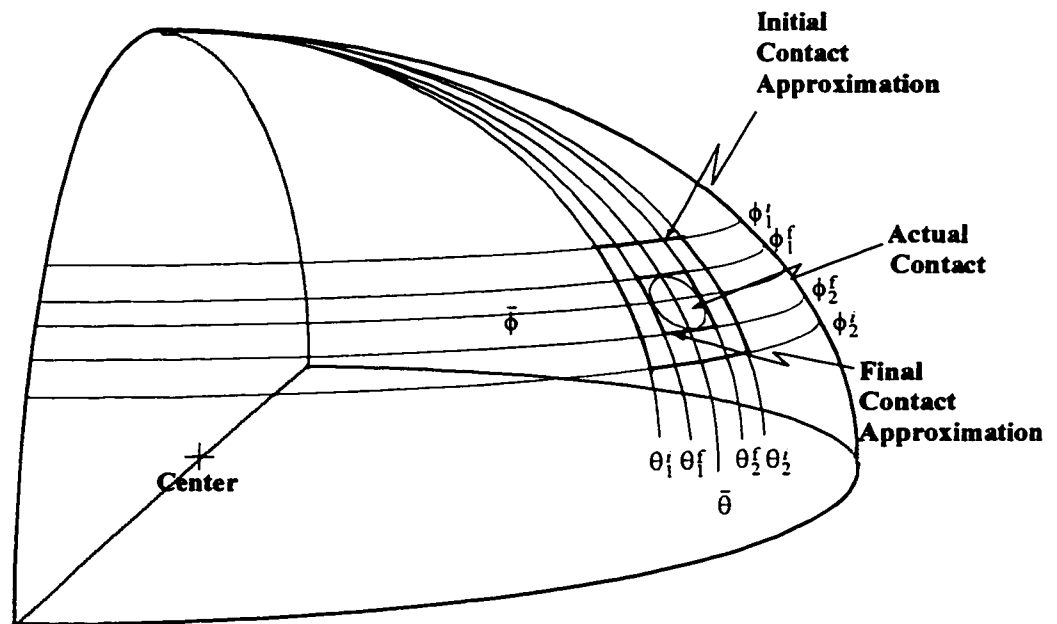


Figure 4-5 Contact approximation by curves with one constant parameter

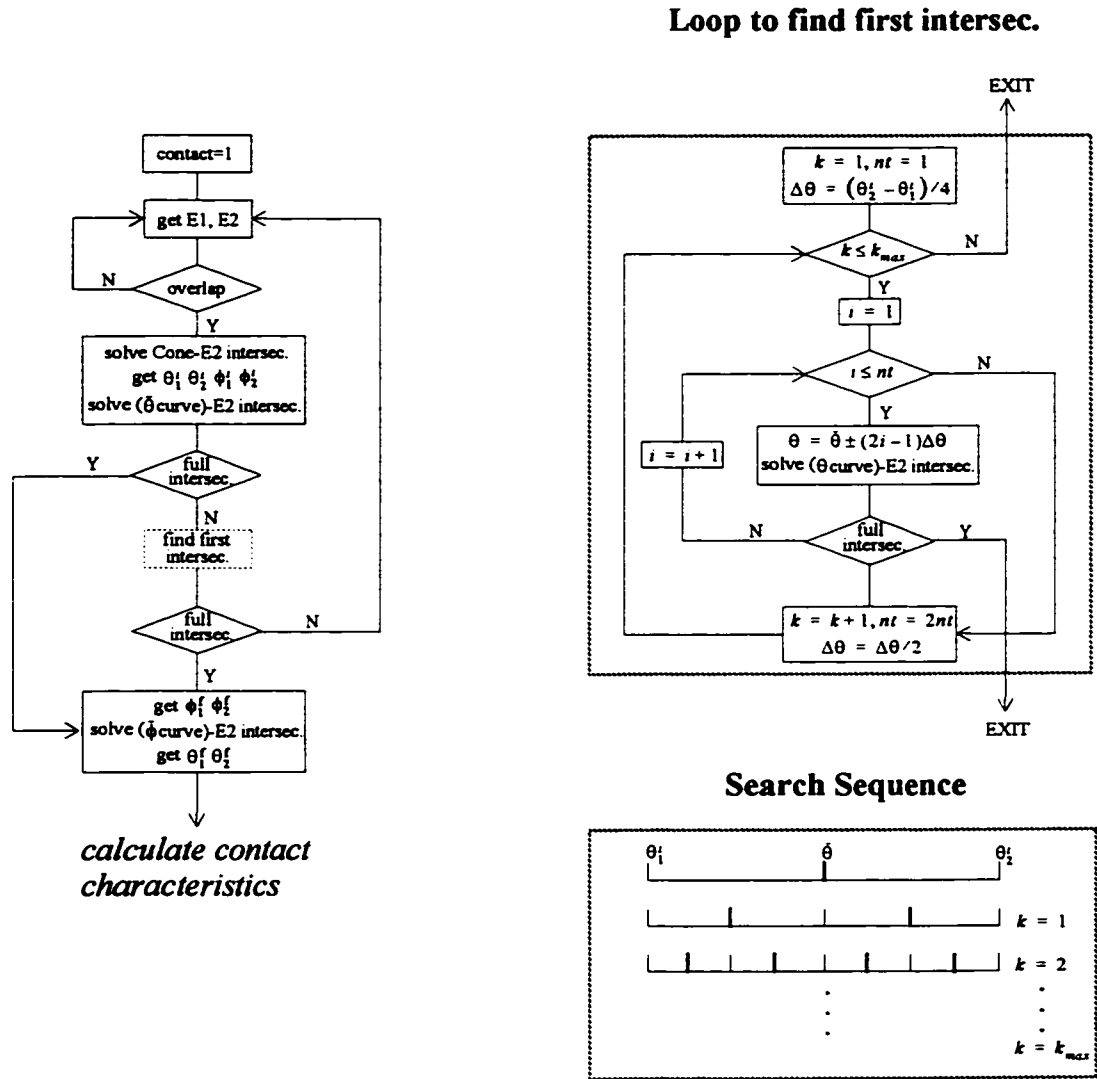


Figure 4-6 Flow chart of the inter-ellipsoid contact detection algorithm

4.3.4 Efficiency

As seen, the contact is calculated by solving only two curves-to-surface intersections, which is the minimum possible number to characterize a contact by the method of curves.

The initial set of curves is obtained from an analytical solution developed for the ellipsoid-cone intersection problem and does not involve any curve-to-surface equation.

4.3.5 Calculation of Contact Characteristics

The final set of curves is used to calculate the contact normal vector, the interpenetration in the contact normal direction, the reference contact point, and the contact vectors.

4.3.5.1 Contact Normal Vector

The θ_1^f , θ_2^f , ϕ_1^f and ϕ_2^f , curves intersect at four points C_i , ($i = 1, 4$) on the surface of ellipsoid, A , as illustrated in Figure 4•7a. It can be shown that these points are *co-planar*.

Points C_i , ($i = 1, 4$) define a unique plane interpreted as the tangent plane of contact. The normal to this plane defines the contact normal direction.

4.3.5.2 Interpenetration

Let C_G denote the centroid of the four points C_i , ($i = 1, 4$). The line passing through C_G and parallel to the direction of the contact normal intersects the ellipsoids in two points each, P_1 and P_2 , for ellipsoid A , and, Q_1 and Q_2 , for ellipsoid B (Figure 4•7b).

The interpenetration δ^n (calculated in the direction of the contact normal) is defined by the shortest distance between, $P_{i, (i=1,2)}$ and $Q_{i, (i=1,2)}$, as:

$$\delta^n = \min_{i,j=1,2} |P_i Q_j| \quad (4•9)$$

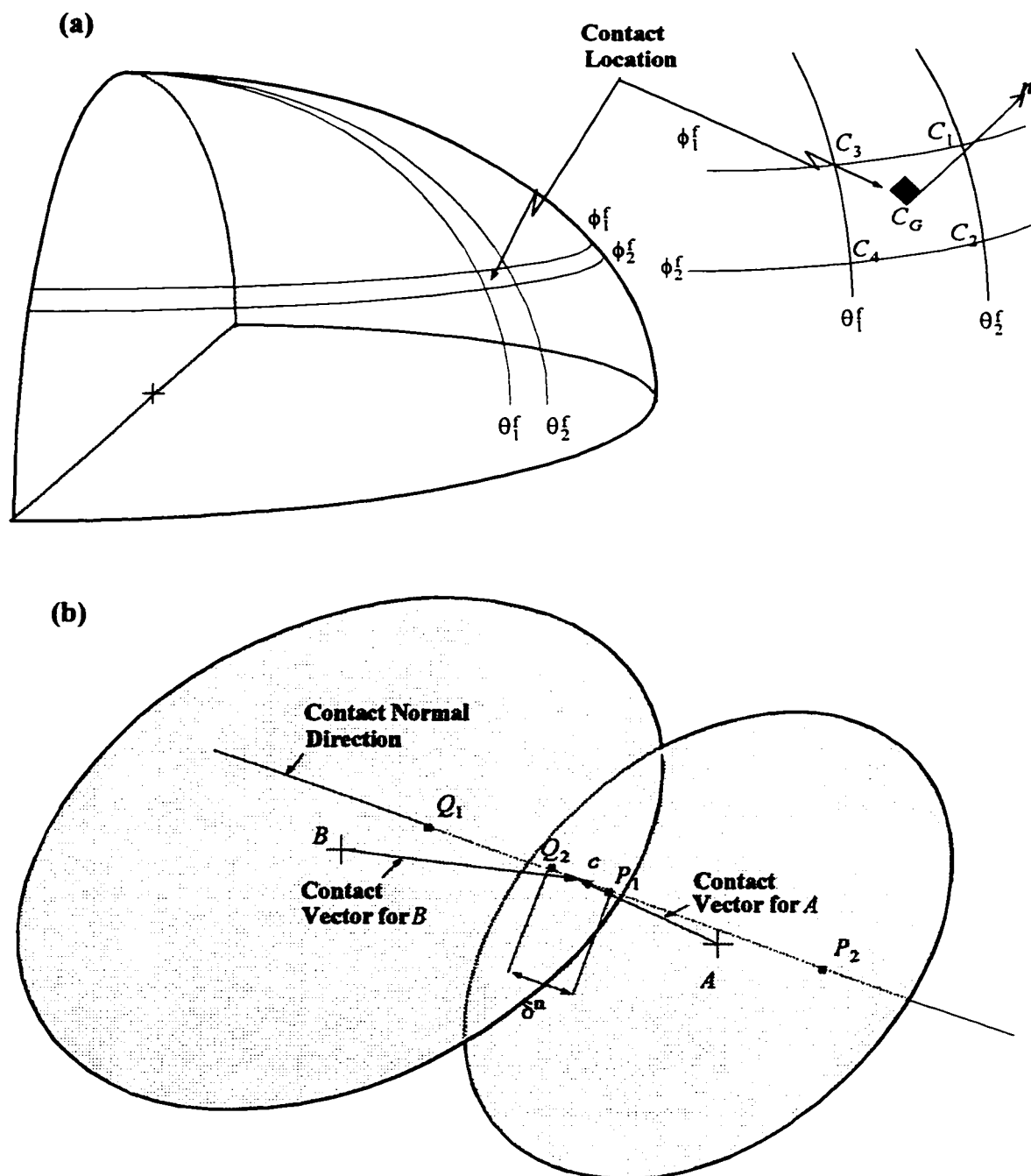


Figure 4-7 Determination of characteristics of contact
 (a) Contact normal direction
 (b) Normal overlap distance and reference contact point

4.3.5.3 Reference Contact Point

A reference contact point, denoted by c , is calculated as the midpoint between the closest pair of points, (P_i, Q_j) . In Figure 4-7b, the reference contact point is at half the distance between P_1 and Q_1 .

4.4 Tests of the Contact Detection Scheme

The performance of the numerical simulator depends on the performance of the inter-particle contact detection algorithm. Therefore, the results of numerical simulations are the real test of the performance of the inter-particle contact detection scheme. However, the results of numerical simulations only indirectly attest to the quality of the contact-detection algorithm. For a direct illustration, simple and direct contact situations are analyzed and a comparison with a two-dimensional scheme for ellipses is presented.

4.4.1 Simple Tests

The tests consist of displacing two particles, initially in contact, apart from each other and tracing the evolution of the contact overlap distance during the separation. Also, the two particles, initially separated, can be brought into contact, and the evolution of the particle overlap distance or any other parameter can be observed. A first indicator of a consistent contact detection scheme is that if the separation is “smooth” (incremental), similar to the way it takes place in simulations of large assemblies, the curve of variation of any contact parameter should also be “smooth”. The second indicator relates to the shape of the curve of variation when special relative displacements are applied. If the particles are ini-

tially in contact, they can be separated by displacing the particles in three special directions:

1. Parallel to the direction of the initial contact normal (normal displacement),
2. Parallel to the contact plane (tangential displacement),
3. Relative rotation of the particles.

In the three displacement cases, the normal overlap distance is a specific type of function of the relative displacement as illustrated in Figure 4•8.

The curve profiles should be:

- i. Linear for rotation and normal displacement (Figure 4•8a, b) and,
- ii. Parabolic for tangential displacement (Figure 4•8c).

The contact detection was tested on three types of contacts (1, 2 and 3) where the particles were displaced relative to each other following the above special directions. The results of inter-particle normal overlap distance versus the magnitude of displacement are shown in Figure 4•9.

As seen, the theoretical profiles are replicated numerically. Moreover, in the case of “contact 2”, the theoretical slope of the linear profile is shown to be “ -45° ”. This value is also obtained numerically.

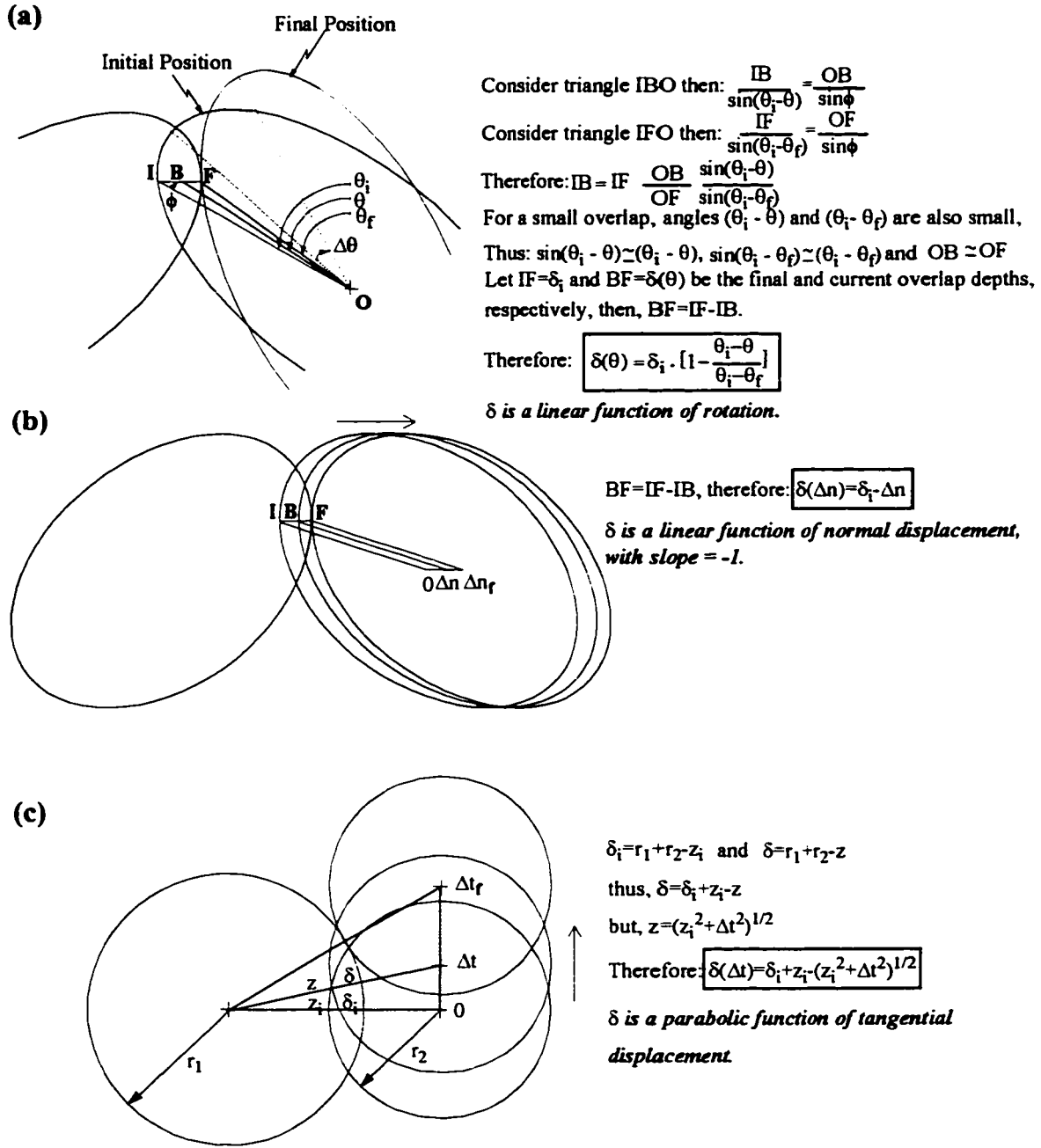


Figure 4-8 Effect of relative particle displacement on normal overlap distance
 (a) Rotation
 (b) Normal displacement
 (c) Tangential displacement

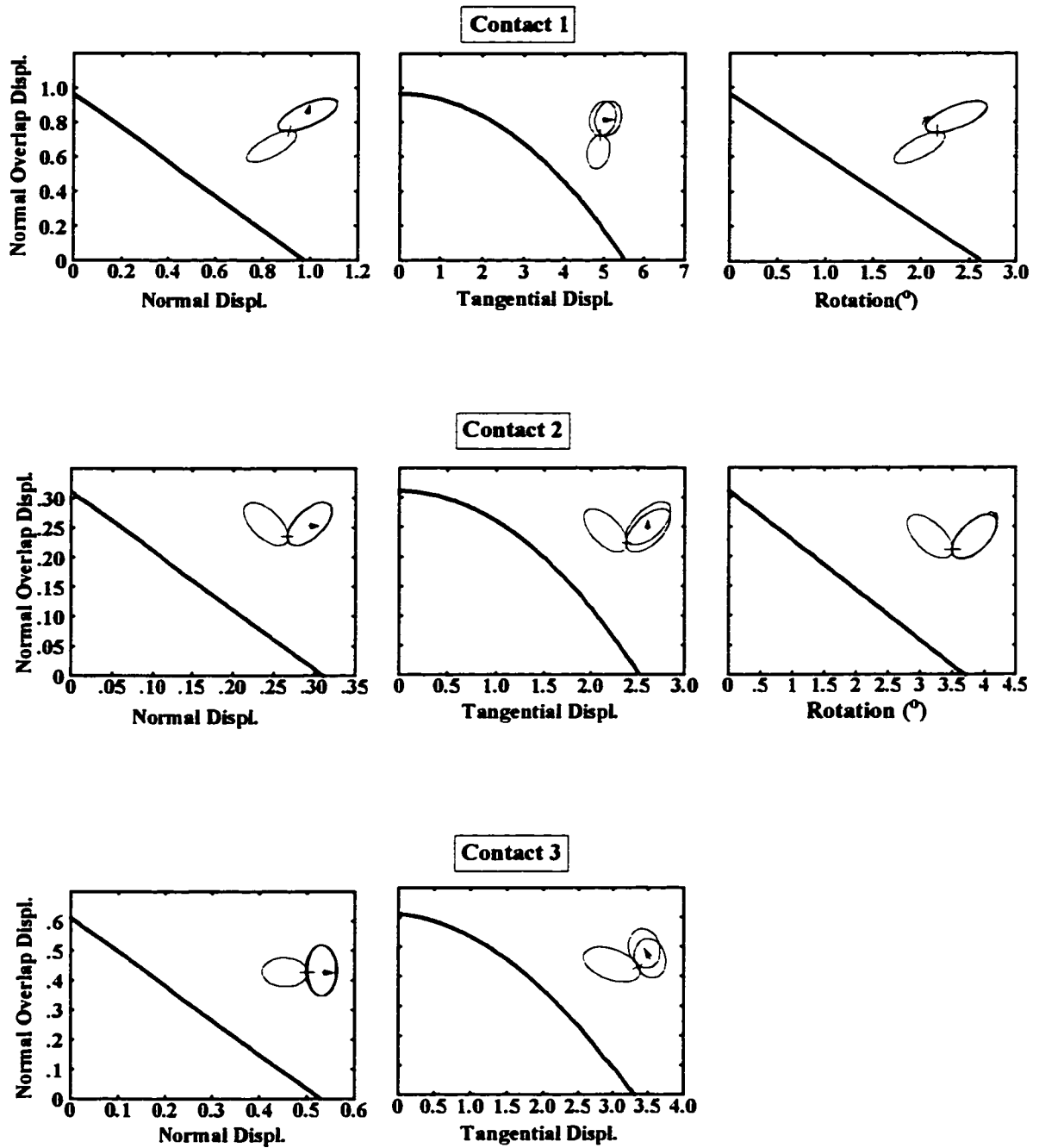


Figure 4-9 Evolution of the normal overlap distance with relative particle displacement

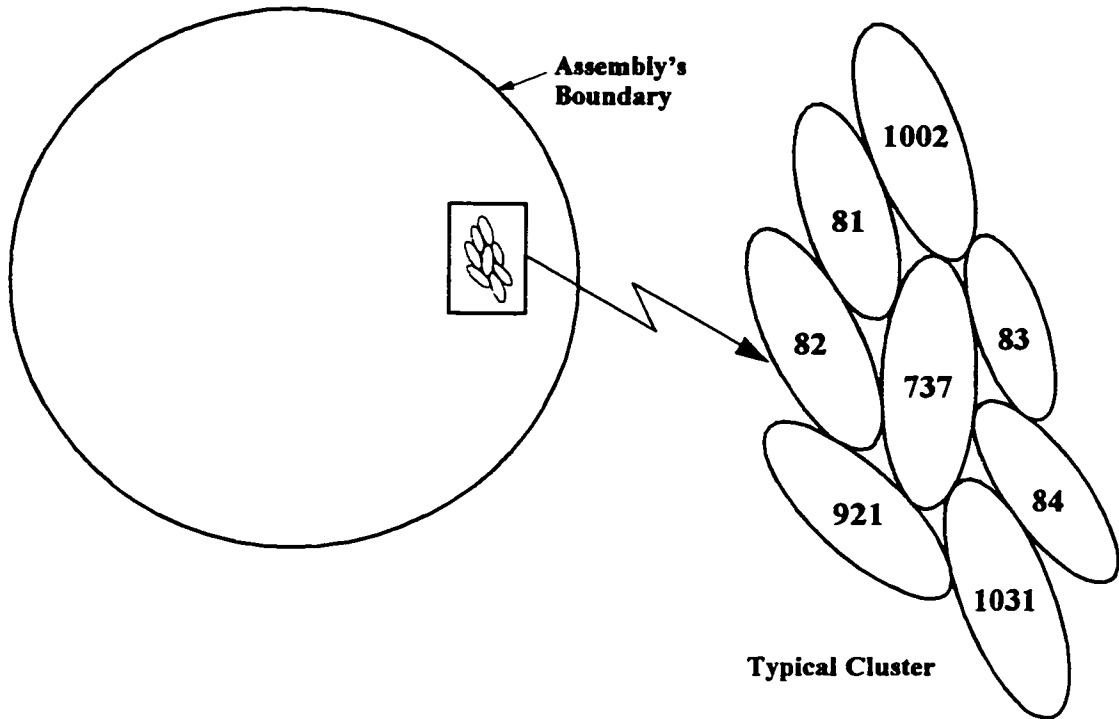
4.4.2 Comparison with a Contact Detection Algorithm for Ellipses

Another test of the ellipsoid contact detection algorithm is to compare its results with those of a completely different, well established scheme, on a given contact situation. The reference scheme used for comparison is a 2-D scheme developed for ellipses (Rothenburg and Bathurst, 1991). A list of 2794 contacts inside a sample comprised of 1000 ellipses, was input to the ellipsoid contact detection routine and the results compared with what the 2-D scheme originally produced. The comparison between the two schemes is illustrated on an arbitrary selected cluster of particles as shown in Figure 4•10.

It should be mentioned that the chosen sample was in its densest state before shearing where the average coordination number is the highest, and the likelihood of having the widest range of contact situations is a maximum.

It is also important to know that in 2-D, the contact problem between two ellipses is represented by a single fourth degree algebraic equation. Therefore, no approximation is involved in computing the inter-ellipse depth of overlap. The only error made is inherent to the numerical method used to solve the fourth degree algebraic equation representing the intersection equation and the use of floating points operations. The latter was minimized by using double precision variables.

It can therefore be stated that the reference to such a scheme is close to a reference to an exact method of calculation.



Contact List Inside the Cluster

Ellipse1	Ellipse2	Original Overlap (Reference 2D-scheme)	Calculated Overlap (Ellipsoid 3D-scheme)
82	737	.4900774360E-01	.4901578000E-01
81	737	.2741995268E-01	.2744216500E-01
737	921	.7798041403E-01	.7811386000E-01
737	1002	.7038669288E-01	.7030864000E-01
83	737	.5845873966E-03	.5249049300E-03
84	737	.7066919655E-01	.7070573000E-01
737	1031	.2205942385E-01	.2211644100E-01
81	82	.1070524007E+00	.1070834900E+00
81	1002	.5603915453E-01	.5612176000E-01
82	921	.8908383548E-01	.8918934000E-01
83	84	.1386999488E+00	.1388084900E+00
83	1002	.7853911817E-01	.7885681000E-01
84	1031	.9451217204E-01	.9477636000E-01
921	1031	.8038467169E-01	.8045673000E-01

Figure 4-10 Illustration of a comparison of results between the 3D-inter-ellipsoids contact algorithm and a reference 2D-inter-ellipse contact scheme

A comparison based on the overlap distance shows that both schemes give very similar results. To quantify the difference between the two methods, an average relative error was calculated over all contacts as:

$$Err = \frac{1}{M} \sum_c |(\delta_n^{(calc.)} - \delta_n^{(orig.)}) / \delta_n^{(orig.)}| \quad (4\bullet 10)$$

where $M=2794$ is the total number of contacts; $\delta_n^{(calc.)}$, and $\delta_n^{(orig.)}$ denote the calculated and the original overlap distances, respectively.

The average relative error Err was found to be less than 0.41%, which means that overlap distances are identical up to the third decimal place.

4.5 Conclusions

The series of direct tests conducted with the developed three-dimensional inter-ellipsoid contact detection scheme illustrate well the reliability of the algorithm in calculating contacts. However, the results of numerical tests with large samples of ellipsoids are the final real test of the scheme. A test with an assembly comprised of thousand ellipsoids usually takes several million cycles to bring the assembly to the beginning of the steady state. In each cycle, a minimum of three thousand and a maximum of six thousand effective contacts are detected. The contact list is much larger due to the close vicinity of some particles that are not in contact but are still examined for contact. Therefore, the scheme is confronted with a large, almost continuous, spectrum of contact situations.

As shown in Chapter 5, coordination numbers of twelve and more are computed for very dense assemblies of ellipsoids. These coordination numbers are obtained from a pro-

gressive particle shape transformation where the assembly is kept in static equilibrium at constant mean pressure, and where the geometry of particles and contact situations are continuously changing.

CHAPTER V: RESULTS OF SIMULATION WITH ASSEMBLIES OF ELLIPSOIDS

5.1 Introduction

A complete test with ellipsoids comprises two separate phases: (1) generation of the ellipsoid sample; (2) an appropriate mechanical test.

5.1.1 Generated Samples of Ellipsoids

As mentioned before, the generated ellipsoids are prolate spheroids. They are useful for comparison between results in two and three dimensions. The following common parameter is used to define the eccentricity for both cases:

$$e = \frac{(\text{major-axis}) - (\text{minor-axis})}{(\text{major-axis}) + (\text{minor-axis})} \quad (5-1)$$

A special method was used to generate the assemblies of ellipsoids for the “p=con-

stant” tests described in this chapter:

- i. Before compaction, an assembly of spheres was generated inside a box at specified locations such that no two spheres touched each other. The spheres had equal sizes and were placed in the nodes of a simple cubic packing structure. In this manner a slight isotropic compaction should create six contacts for each sphere.
- ii. The particle shape transformation started from this state of the assembly of spheres (Figure 5•1). At the same time that the particle shape was progressively changed from spherical to ellipsoidal, isotropic compression was maintained. This situation lasted for only 1% of particle eccentricity increase. The compression was then stopped and the assembly of changing ellipsoids evolved at constant mean pressure. The inter-particle friction was initially set to zero so that the contact density could increase by a mechanism of particle interlocking.

Three sample sizes (27, 125 and 1000 ellipsoids) and values of ellipsoid eccentricity varying between $e = 0$ and $e = 0.22$, were generated by this procedure.

5.1.2 Test Program

The small and medium assemblies were useful for preliminary testing of the simulator. They were quicker to test than the 1000 ellipsoid assembly, and provided important indications about the selection of the test parameters and results that might be expected for large assemblies.

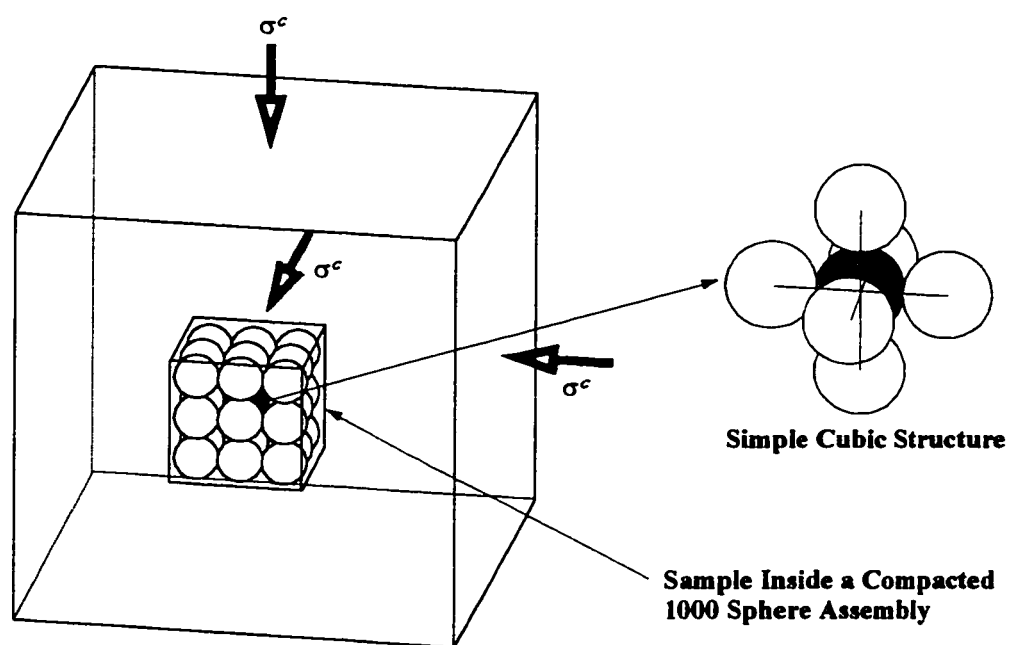


Figure 5-1 Structure of assemblies of spheres used in particle shape transformation

They were also employed to observe the assembly size effect on the mechanical behaviour by comparison with large assemblies.

The 1000 ellipsoid assembly has an acceptable size for examining its microscopic behaviour during shear deformation.

One aspect of interest to the study is the effect of confining pressure on the mechanical behaviour of assemblies of ellipsoids. Five large samples were generated with five different confining pressures (from 10×10^6 to 100×10^6 units) to study this parameter.

5.1.3 Physical and Numerical Units

The program TRUBAL can accommodate any consistent set of physical units, but these must be converted to numerical units in such a way that the particle sizes are between 10 and 50 numerical units. It is essential for the efficiency of computations that the particle sizes be in this range of values (Cundall, 1978). Subsequently, all dimensional variables are given in TRUBAL numerical units.

Prior to presenting and discussing the results of ($p=\text{constant}$) tests, a few aspects of the compaction and particle shape transformation simulations are examined in the following two sections.

5.2 Compaction

During compaction, the periodic space (a box enclosing the particles) is homogeneously and isotropically strained. The particles move with the outer boundaries until collision between particles occur. Then, the particles acquire velocities relative to each other.

The motion of a particle becomes dependent not only on the imposed external strain but also on the sum of contact forces acting on its surface.

Soon after the sample is pressured, the average coordination number rises from zero to six. The structure of the assembly of spheres and the type of compaction (hydrostatic compression) allow this significant change in the value of the coordination number. The structure of the assembly becomes more rigid as all particles approach a stable equilibrium state. Any further increase in the assembly coordination number can only be the result of increased elastic deformation at the compliant contact points between particles.

5.3 Particle Shape Transformation

The particle shape transformation is performed over many calculation cycles. The required number of cycles to increase the eccentricity by one per cent defines the rate of transformation. If it is too fast, the quasi-static equilibrium condition is quickly lost due to difficulty in controlling the velocity of smooth particles. It is essential to keep the assembly in static equilibrium in order to create a dense packing of ellipsoids with a high contact density at all stages of the transformation. For this reason, intermittent periods of assembly “relaxation” are set where the excess kinetic energy can be dissipated.

The assembly is “relaxed” after each percent of particle eccentricity increase. Table 5.1 shows the applied “growth” rates and the “relaxation time” shares for the different transformations carried out with the three sample sizes. As can be seen, the ‘relaxation” of the assembly consumes the major part of the transformation. This indicates the difficulty of controlling inertial forces for smooth particles, even at constant mean pressure.

Assembly size	27	125	1000
"Growth" rate No. cycles per (%) of ecc.	1000	1000	1000
"Relaxation" Time	83%	93%	95%
Mean pressure (σ^c)	7e+6	47e+6	100e+6

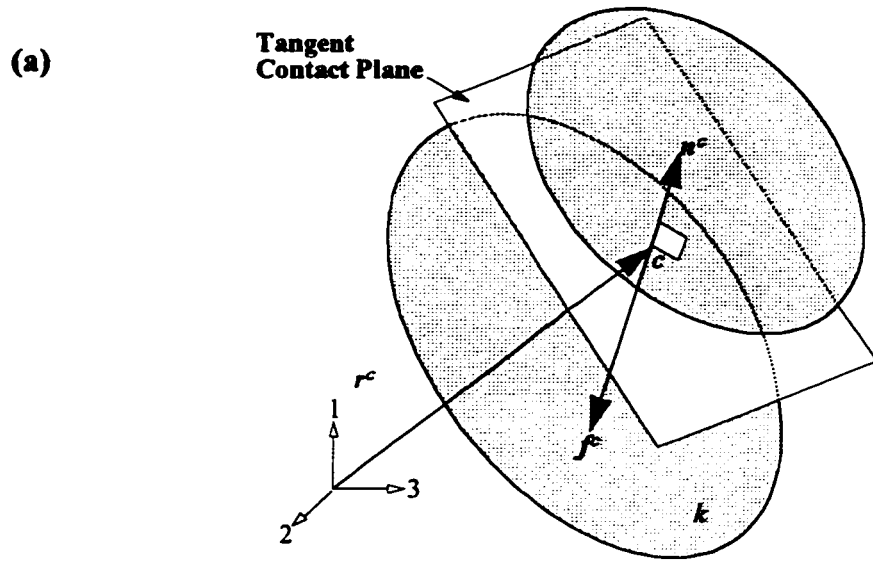
Table 5-1 Parameters of particle shape transformation

5.3.1 System of Smooth Non-Spherical Particles in Static Equilibrium

The particle shape transformation is performed with the objective of generating the densest possible packing before the deviatoric compression tests. This is achieved by setting the friction angle to zero and controlling the static equilibrium of the changing assembly. Then, the particles are stimulated to create more contacts in order to preserve their static equilibrium condition. Theoretically, the average coordination number of such an assembly must be equal to twelve.

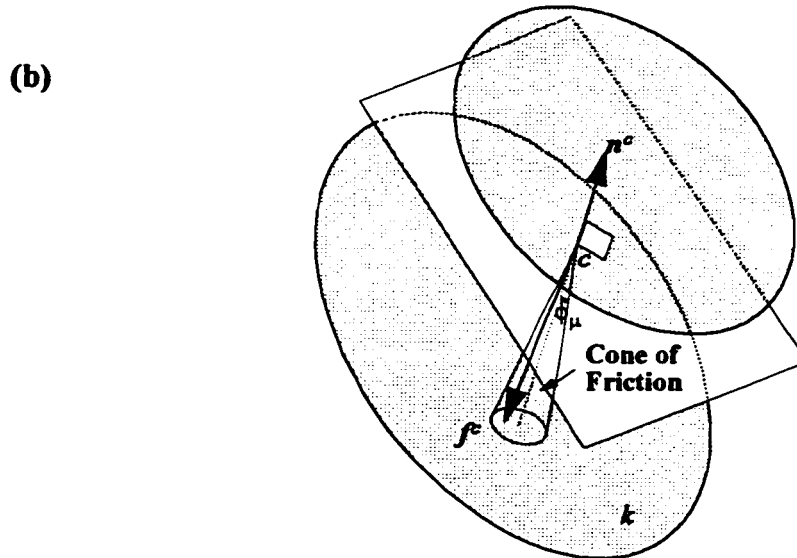
A contact force vector acting upon a smooth particle must be normal to the surface of that particle (Figure 5•2a). On the other hand, a contact force vector acting upon a frictional particle can be oriented anywhere within the cone of friction delimited by the inter-particle friction angle (Figure 5•2b).

More contacts on the surface of a particle are required to satisfy the former constraint by comparison to the latter one, because the range of possibilities for the contact force orientation are infinite if the particle is frictional, while the contact force vector acting upon a smooth particle can only be normal to the particle surface (a single possibility).



Smooth Contact

$$(\phi_\mu = 0) \Rightarrow f^c = f^c n^c$$



Frictional Contact

$$(\phi_\mu \neq 0) \Rightarrow \begin{cases} f^c = (f_i^c n_i^c) n^c + f_i^c \\ |f_i^c| \leq \tan \phi_\mu |f_i^c n_i^c| \end{cases}$$

Figure 5-2 Illustration of contact force orientation for a smooth and a frictional contact

If a system comprising N smooth particles in static equilibrium is considered, then the force and moment equilibrium equations must be satisfied simultaneously for each particle:

$$\begin{cases} \sum_{c \in k} f_j^{c,k} = 0 & j = 1, 3 \\ \sum_{c \in k} (f_j^{c,k} \otimes r^{c,k})_j = 0 & j = 1, 3 \end{cases} \quad (5.2)$$

where $f^{c,k}$ and $r^{c,k}$ are the force and position vectors at a contact point c on the surface of a particle k , respectively.

This means that for the entire assembly a total of $6N$ equations must be satisfied.

If the particles are perfectly smooth, the contact force f^c and the contact normal vector n^c must be colinear and this translates into three constraints on contact forces as follows:

$$(f^c \otimes n^c)_j = 0 \quad j = 1, 3 \quad (5.3)$$

It can be shown that only two of the three constraints are independent; therefore, if M is the total number of contacts (twice the number of physical contacts), the number of constraints is equal to $2(M/2) = M$. Thus, the total number of equations to be satisfied sums up to $6N + M$.

On another hand, there are $3(M/2)$ contact force components f_j^c to solve for, assuming that the contact location position and orientation vectors, r^c and n^c are known.

The principle of static determinancy states that the number of equations must be at least equal to the number of unknowns for the system to be in static equilibrium, *i.e.*, $6N + M = 3M/2$.

If the condition of static equilibrium is approached for each particle, the expected coordination number should tend to the theoretical value, $\gamma = M/N = 12$. A coordination number of this order belongs only to dense systems of particles.

5.3.2 Evolution of the Average Coordination Number

The major difficulty encountered during particle shape transformation was to enforce a quasi-static equilibrium condition for all levels of the changing ellipsoid eccentricity. In spite of devoting more than 93% of the total time to sample relaxation (case of the 1000 ellipsoid assembly) the quasi-static equilibrium still could not be maintained beyond a certain level of eccentricity, that is $e \cong 0.2$.

Figure 5•3a shows the variation of the ratio of the average inertial force to the average contact force with varying eccentricity. The inertial force fraction, initially relatively low for this type of process where particles are perfectly smooth, rapidly increases after an eccentricity of about 0.15 (1000 ellipsoid assembly).

The assembly coordination number begins decaying at that same eccentricity as shown in Figure 5•3b. The “optimum eccentricity” is defined as the eccentricity at which the assembly coordination number is maximum. It is $e_{\text{opt}(3D)} = 0.15$ for 3D-ellipsoids. Rothenburg and Bathurst (1991) generated assemblies of plane ellipses by the method of particle shape growth. The obtained optimum eccentricity for 2D-ellipses was $e_{\text{opt}(2D)} = 0.2$.

It has also been observed that the trend of evolution of the coordination number for 3D-ellipsoids bears some similarities with the two-dimensional case.

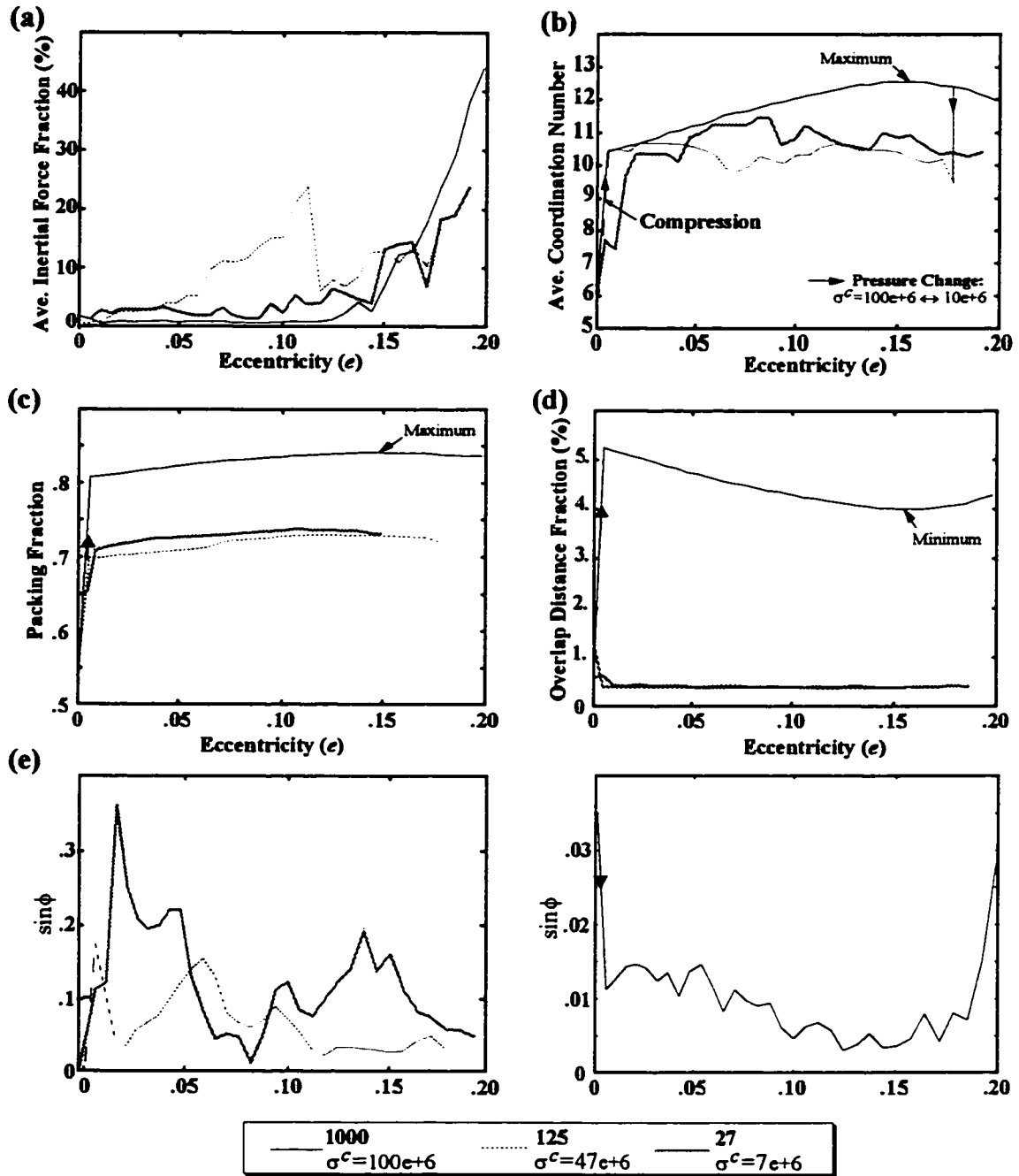


Figure 5-3 Behaviour of assemblies of ellipsoids during particle shape transformation
 (a) Average inertial force fraction; (b) Average coordination number
 (c) Packing fraction; (d) Average overlap distance fraction
 (e) Angle of shearing resistance

The maximum coordination number reached exceeds the theoretical limit of twelve ($\gamma_{\max} \cong 12.5$). This is due to the applied compression during the first percent of eccentricity increase where the confining pressure was increased by an order of magnitude from $\sigma^c = 10\text{e}+6$ to $\sigma^c = 100\text{e}+6$ units. The coordination number increased under both the effect of particle shape change and increased linear elastic compression at the compliant contact points between particles.

5.3.2.1 Effect of the Mean Pressure on the Coordination Number

In order to generate samples with lower mean pressures, the value $\sigma^c = 100\text{e}+6$ was decreased gradually to the initial lower value $\sigma^c = 10\text{e}+6$, for the sample of ellipsoids at eccentricity $e = 0.175$. As a result, the value of the average coordination number dropped from $\gamma_{\max} \cong 12.5$ to $\gamma = 9.5$ (Figure 5•3b).

5.3.3 Evolution of the Packing Fraction

Due to the applied compression and the change in particle shape, the packing fraction increased from 0.55 up to 0.81 during the first percent of eccentricity increase (Figure 5•3c). The change in shape that followed only slightly improved the state of packing where the maximum value reached was 0.84. The maximum value corresponds to the optimum eccentricity defined earlier. The comparison with the two-dimensional case reveals large differences in packing fractions between the two cases (0.84 for 3D-ellipsoids versus 0.90 for 2D-ellipses). Plane ellipses seem to pack more closely than 3D-ellipsoids.

5.3.4 Evolution of the Average Normal Contact Force Magnitude

The average normal contact force is similar to the interparticle overlap fraction plotted in Figure 5•3d. These two parameters are proportional. This is implied by the assumed linear contact force-displacement law implemented in the program TRUBAL for ellipsoids.

After a linear rise explained by the applied compression, an unpredictable moderate decline takes place for varying particle eccentricity at constant mean pressure. A minimum value is reached around the optimum eccentricity before the average normal force increases again.

5.3.5 Shear Strength

The plot of $\sin \phi = (\sigma_1 - \sigma_3) / (\sigma_1 + \sigma_3)$ with varying eccentricity is shown in Figure 5•3e where σ_1 , σ_3 are the major and minor principal stresses, respectively. The values taken by the sine of the shearing resistance angle are very low (less than 0.04). This is consistent with the conditions of the test where the boundary normal stresses were kept constant and equal and the inter-particle friction set to zero.

5.3.6 Evolution of Fabric And Contact Forces

The change in fabric and in the contact force distribution is illustrated for the 1000 ellipsoid assembly in Figure 5•4.

Four items are represented: (1) the sample's geometric configuration; (2) the histogram of the particle coordination number; (3) the histogram of the contact normal orientation distribution; and (4) the histogram of the average normal contact force distribution.

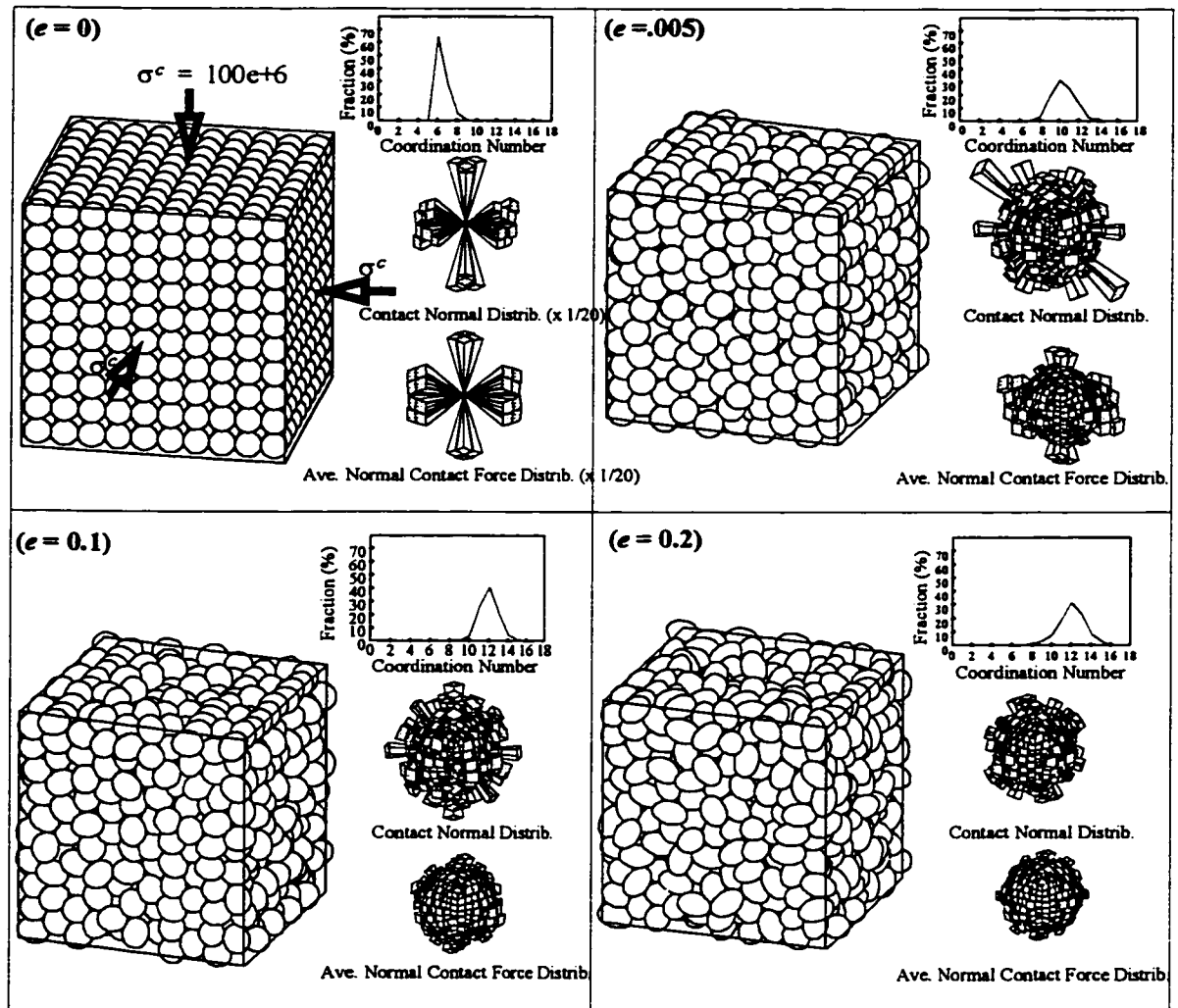


Figure 5-4 Evolution of fabric and average normal contact forces during particle shape transformation

The average tangential contact force distribution is zero for assemblies of smooth particles (absence of shear contact forces).

As can be seen, the initial distribution of contact normals is highly anisotropic and is characterized by contacts which are concentrated exclusively in to the three principal directions of strain (simple cubic structure).

The organized structure rapidly breaks (within the first half percent of eccentricity increase) and contacts are formed in all directions of the space. The obtained contact normal orientation and average normal contact force distributions become almost isotropic.

5.3.7 Evolution of the Distribution of Particle Coordination Number

As can be observed from Figure 5•4, the histograms of particle coordination number are all of Gaussian type. A measure of the scatter around the mean value of a Gaussian type distribution is provided by the standard deviation s_γ .

The relative standard deviation, $s'_\gamma = s_\gamma/\bar{\gamma}$, expresses the scatter of the distribution relative to the arithmetic mean. Figure 5•5a displays the curve of variation of the standard deviation with varying eccentricity for the changing 1000 ellipsoid assembly. During the initial compression the scatter around the mean coordination number increases linearly. It then decreases once the particle shape is changed at constant mean pressure. A minimum value is reached around the optimal eccentricity.

Up to an eccentricity of about $e = 0.2$, the standard deviation does not exceed 1.5. This value must be compared with the initial value of 0.67 characterizing a structured fabric where the coordination number is distributed almost uniformly among particles.

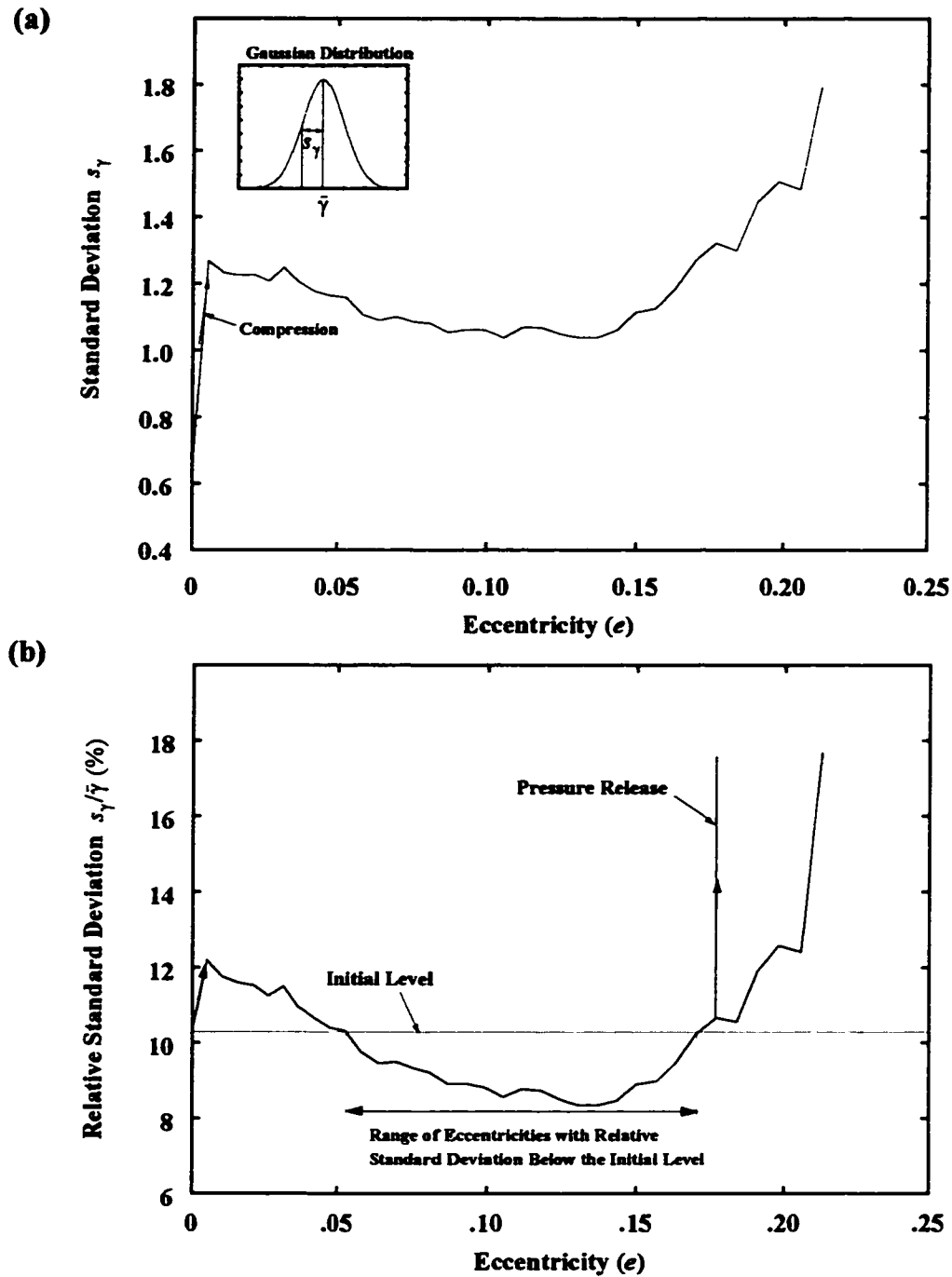


Figure 5-5 Particle coordination number vs. eccentricity during particle shape transformation (1000 ellipsoids)
 (a) Standard deviation
 (b) Relative standard deviation

To take into account the increasing character of the average coordination number, the relative standard deviation gives a better picture of how the distribution of particle coordination numbers evolves around its increasing mean value. The relative standard deviation is plotted in Figure 5•5b. The values range between 10% and 18% of the mean value. This indicates that the generated samples at all shapes are fairly relatively uniform. Samples characterized by eccentricities between $e = .05$ and $e = .17$, are even relatively more uniform than the initial sample.

The release in mean pressure is a factor of fabric disruption much higher than the progressive change in particle shape; but the effect it produces on the particle coordination number distribution remains limited. The relative standard deviation is only increased by less than 8% from its initial value.

5.3.8 Evolution of Anisotropy

In order to assess quantitatively the evolution of anisotropy during particle shape transformation, the variation of some global measure of anisotropy is plotted with varying eccentricity. The average normal contact force anisotropy and three aspects of fabric anisotropy (*i.e.*, particle orientation, contact normal orientation, and branch vector length) are plotted with varying eccentricity, shown in Figure 5•5b.

For each measure of anisotropy, a dramatic drop is observed in the initial high anisotropy (due to the simple cubic structure of initial sample of spheres) to different levels, depending on the particular type of anisotropy.

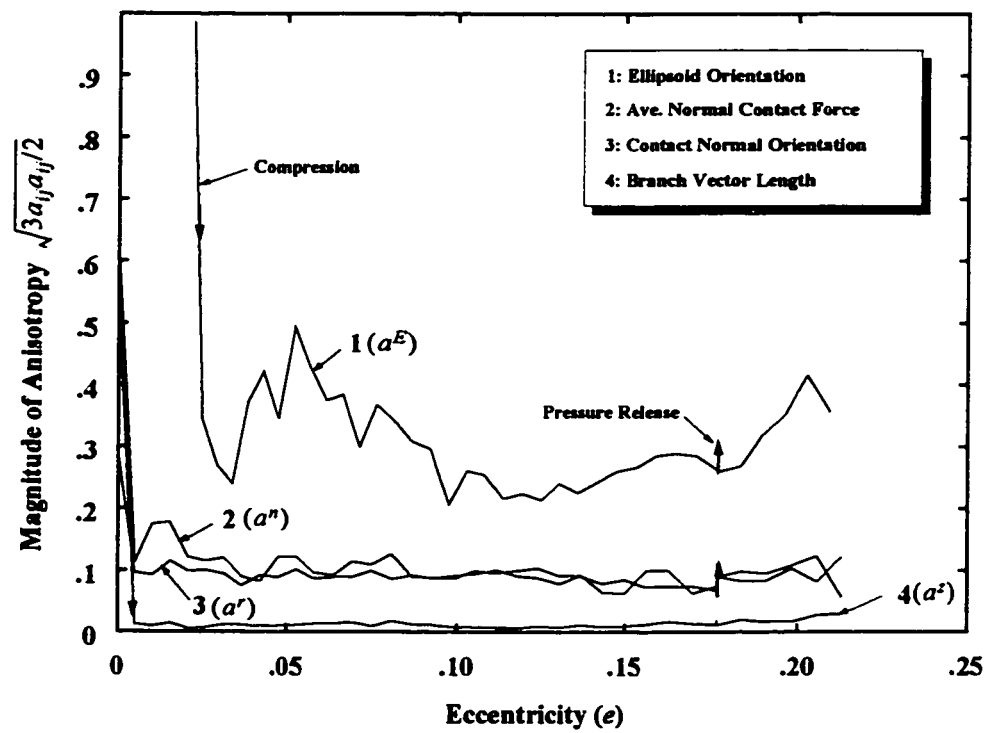


Figure 5-6 Evolution of anisotropy during particle shape transformation

For instance, while the anisotropy in the contact vector distribution seems totally overcome, a small residual anisotropy persists for the remaining aspects of fabric and also in average normal contact force anisotropy. This residual anisotropy results from initially setting the direction of ellipsoids' major axis growth to be horizontal. The rotation of ellipsoids that took place after could not totally eliminate this trend, and this explains the remaining residual anisotropy. This also indicates that by setting the initial direction of growth to different constant angles, it is possible to simulate inherent anisotropy in particles' orientation, such as the one occurring due to the natural phenomenon of gravitational deposition of sediments (or particles pouring in the laboratory).

5.3.9 Summary of Shape Transformation Results

From the results of particle "growth" simulations, the following observations can be made:

- i. The range of obtained assembly coordination numbers by the "particle growth" model are in agreement with theoretical values. This indicates that the simulation program, in general, behaved as expected, and that the contact detection scheme, in particular, detected and calculated all contacts (3000 to 6000 at every cycle).
- ii. The shape transformation method is effective in generating relatively dense systems of ellipsoids at relatively low eccentricities. The difficulty in maintaining the condition of quasi-static equilibrium of smooth particles at high eccentricities limit the applicability of the method to only low eccentricities.

- iii. The generated assemblies of ellipsoids are fairly isotropic with respect to the fabric and contact forces. Considering that the initial simple cubic structure was highly anisotropic, the residual anisotropies that persisted throughout the simulation are relatively minor.

5.4 Constant Mean Stress Compression Tests

Deviatoric compression may be started from any arbitrarily saved state of the sample during the course of particle shape transformation.

For the series of tests performed with the simulator and presented here, the initial conditions and parameters of the tests are shown in Table 5•2.

The smaller samples (27, 125) were sheared mainly to test the simulator. They were also used to compare their behaviour with the behaviour of larger samples to assess the influence of assembly size.

The 1000 ellipsoid sample has a reasonable size that allows the use of averaging techniques to study micromechanical aspects, as well as the macroscopic behaviour of these assemblies. The effect of particle shape and applied confining pressure on either behaviour are subsequently emphasized.

5.4.1 Stress-Strain Behaviour

The macroscopic behaviour is commonly represented by plots of the stress-strain and volume change curves. These are shown in Figure 5•7 for the 1000 ellipsoid sample under different confining pressures.

CHAPTER V: RESULTS OF SIMULATION WITH ASSEMBLIES OF ELLIPSOIDS


Test No.		1	3	4a	4b	4c	4d	4e
Gradation	No. Particles	27	125	1000	1000	1000	1000	1000
	Mean Radius (r)	10.0	10.0	10.0	10.0	10.0	10.0	10.0
	Ecc. ($e = \frac{a-b}{a+b}$) Elong. Ratio ($elr = \frac{b}{a}$)	.176 .7	.176 .7	.11 .8	.176 .7	.176 .7	.176 .7	.176 .7
Material Properties	Contact Normal Stiffness (k_n)	5e+10	5e+10	5e+10	5e+10	5e+10	5e+10	5e+10
	Ratio of Tang. to Norm. Contact Stiffnesses ($\kappa = k_t/k_n$)	1.0	1.0	1.0	1.0	1.0	1.0	1.0
	Inter-Particle Friction ($\mu = \tan \phi_\mu$)	.5	.5	.5	.5	.5	.5	.5
Test Parameters	Strain Rate $\dot{\epsilon}_{11} \dot{\gamma}_{12}$  $\dot{\epsilon}_{22} \dot{\gamma}_{23}$ $\dot{\epsilon}_{33} \dot{\gamma}_{31}$	-1e-3 0 .5e-3 0 .5e-3 0	-1e-4 0 .5e-4 0 .5e-4 0	-1e-4 0 .5e-4 0 .5e-4 0	-1e-4 0 .5e-4 0 .5e-4 0	-1e-4 0 .5e-4 0 .5e-4 0	-1e-4 0 .5e-4 0 .5e-4 0	-1e-4 0 .5e-4 0 .5e-4 0
	Time-Step (Δt)	4.73e-4	4.73e-4	4.73e-4	4.73e-4	4.73e-4	4.73e-4	4.73e-4
	Servo-Gain	1e-5	1e-5	1e-5	1e-5	1e-5	1e-5	1e-5
	Damping Coeff. ($\frac{\alpha}{\kappa}$)	60	60	60	60	60	60	60
	Mean Pressure (σ^c)	7e+6	47e+6	100e+6	70e+6	50e+6	30e+6	10e+6
	Initial Ave. Normal Contact Force (\bar{f}^0)	1.15e+9	7.15e+9	1.3e+10	9.91e+9	7.39e+9	4.81e+9	1.93e+9
Assembly's Initial State	Initial Ave. Coordination No. ($\bar{\gamma}$)	10.52	11.21	12.44	11.70	11.46	10.92	9.50
	Initial Porosity	.262	.218	.144	.180	.205	.235	.268

Table 5-2 Initial conditions and parameters of “p=constant” tests with ellipsoids

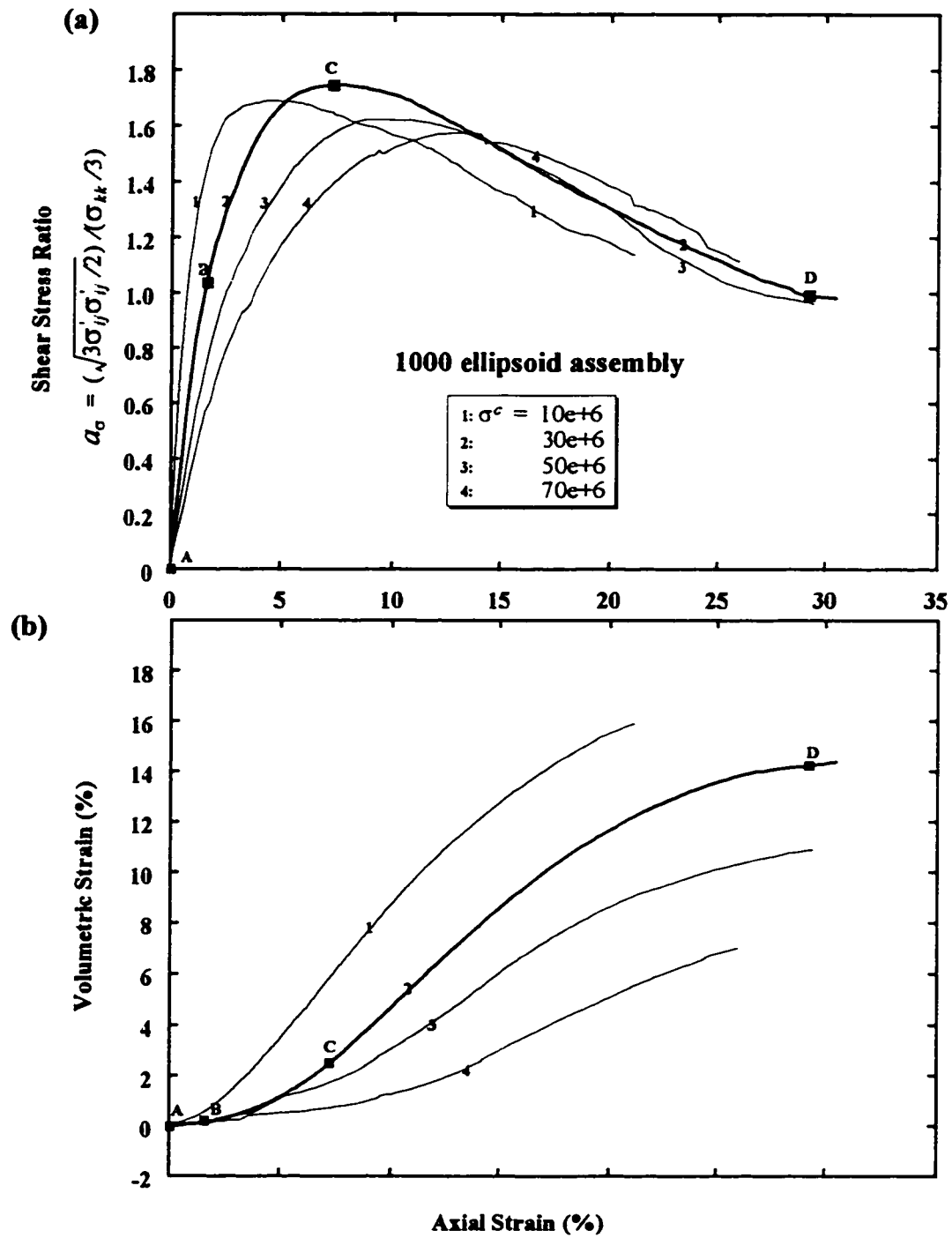


Figure 5-7 Illustration of macro-behaviour during shear deformation

(a) Shear stress ratio vs. axial strain

(b) Volumetric strain vs. axial strain

The shear stress ratio-axial strain curves show all aspects that can be observed experimentally on densely packed samples of sand (Figure 5•7a). These include the transition to a maximum value of the internal friction angle and strain softening. Four particular states are singled out on the plots of test 4d:

- A. Before deviatoric loading,
- B. at the start of plastic yielding,
- C. at the peak friction angle, and,
- D. at the start of constant volume deformation (steady state).

The last three states mark transitions between macroscopically distinct types of behaviour, and are used later as reference states when describing the evolution of microscopic parameters.

The effect of confining pressure is also faithfully replicated, where the mobilization of the maximum friction angle is delayed with increasing confining stress (Figure 5•8c). Globally, the shear strength decreases with the confining stress, and at large strain the curves seem to converge towards a single curve (steady state).

The similarity between the numerical and experimental curves includes also the range of values of shear capacity of these materials. The measured maximum angles of shearing resistance are plotted in Figure 5•8a for different confining pressures. Values between 39 and 43.5 degrees were obtained, which are considered to be typical friction angles for dense sands.

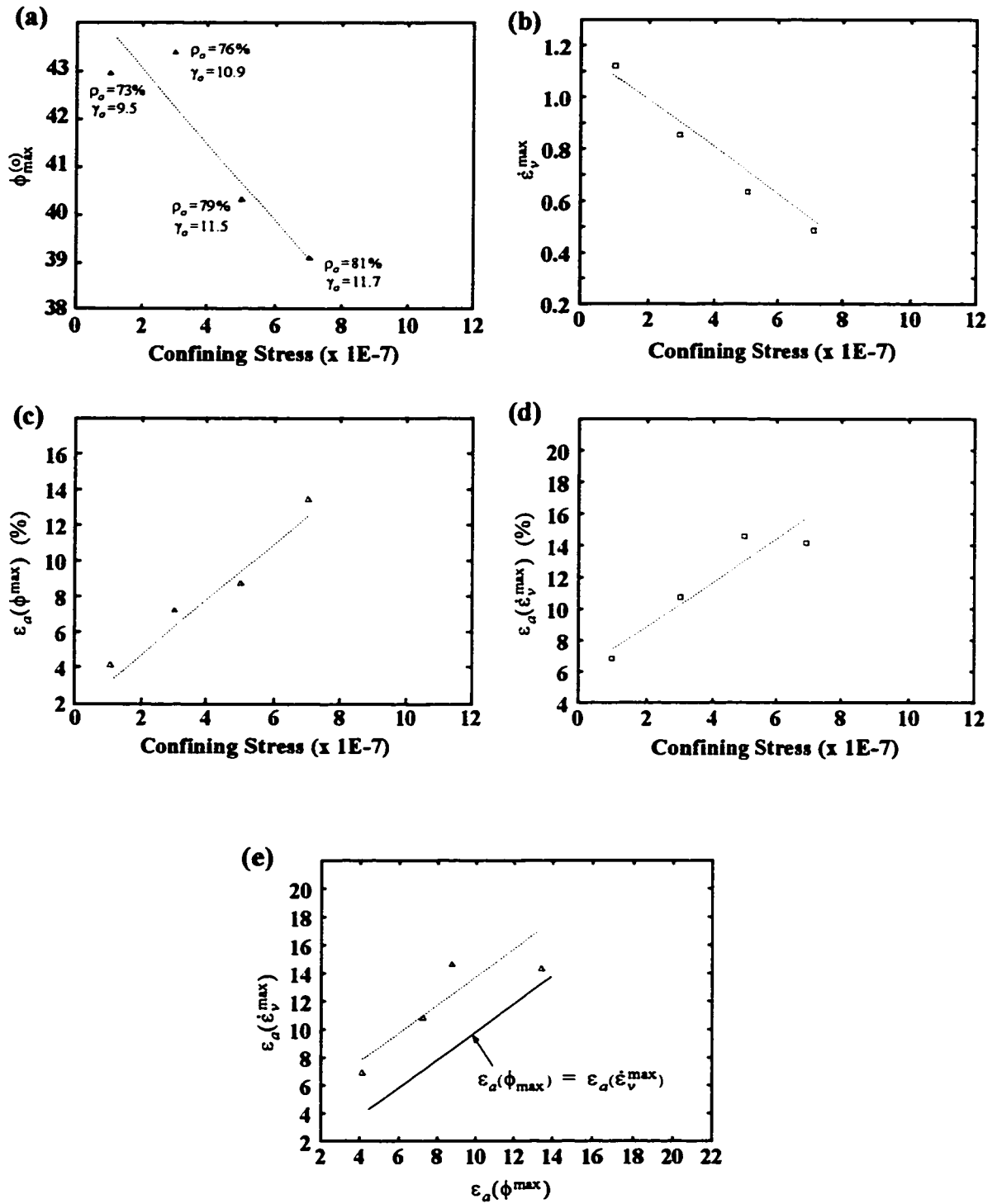


Figure 5-8 Effect of confining pressure on peak shear stress ratio and peak dilation rate

5.4.2 Volumetric Strain Behaviour

The dilatancy behaviour is represented in Figure 5•7b. For the type of tests carried out, where the confining pressure is kept constant, no contraction takes place. The characteristics of the behaviour of a densely packed sand are also clearly replicated. A typical trend of evolution characteristic of a slow increase to a maximum dilation rate, followed by a regular decrease in dilation rates towards a stationary value (state of constant volume), can be observed.

The curves corresponding to different confining pressures show that at any state of applied deformation, the volumetric strain decreases with increasing confining stress. This supports the intuitive idea that the higher the confining pressure, the more restricted is the motion of the particles and the assembly volume expands less.

It can also be remarked that the curves seem to preserve different levels of global volume change and do not converge towards a single curve, as was the case for friction angles. This is consistent with the well established fact that the limiting void ratio depends on the confining pressure (Been and Jefferies, 1985). Eliadorani (1992) obtained similar results with numerically simulated assemblies of plane ellipses.

The measured maximum dilation rates are plotted in Figure 5•8b. They seem to decrease with increasing confining pressure. This applies not only to the state of maximum dilation rate but includes all states of deformation as described in Figure 5•7b.

The axial strain at the state of maximum dilation rate is plotted against the confining pressure in Figure 5•7d. Similarly to the maximum friction angle, the occurrence of the maximum dilation rate is delayed by the increasing confining stress.

From the comparison of states of occurrence of maximum friction angle and dilation rate in Figure 5•8e, it was observed that the peak of the shear stress ratio is attained well before the peak dilation rate, except for the highest confining stress value where there is coincidence.

Finally, a comparison between results of the current simulations and those conducted with plane ellipses at different eccentricities (Rothenburg and Bathurst, 1992) and data for Ham River sand presented by Bishop (1971) is shown in Figure 5•9. The figure displays the results in a diagram of peak friction angle versus the peak dilation rate.

As can be seen, both plane ellipses and 3-D ellipsoids give peak friction angles comparable to the Ham River Sand, but only assemblies of ellipsoids replicate peak dilation rates of the same order as those of the Ham River sand.

Plane systems produced maximum rates of dilation between 0.8 and 1.9, depending on the particle shape. Three-dimensional systems of ellipsoids at a single eccentricity $e = 0.176$ and several confining pressures had peak dilation rates between 0.35 and 1.1, while the Ham River sand is characterized by values ranging between 0 and 0.78.

5.4.3 Packing Density Behaviour

The plot of this parameter for different confining pressures is shown in Figure 5•10a. As expected, the initial value as well as the steady state value are all dependent on the confining stress. Note that the packing density ρ and void ratio e are related by $\rho = 1/(1 + e)$.

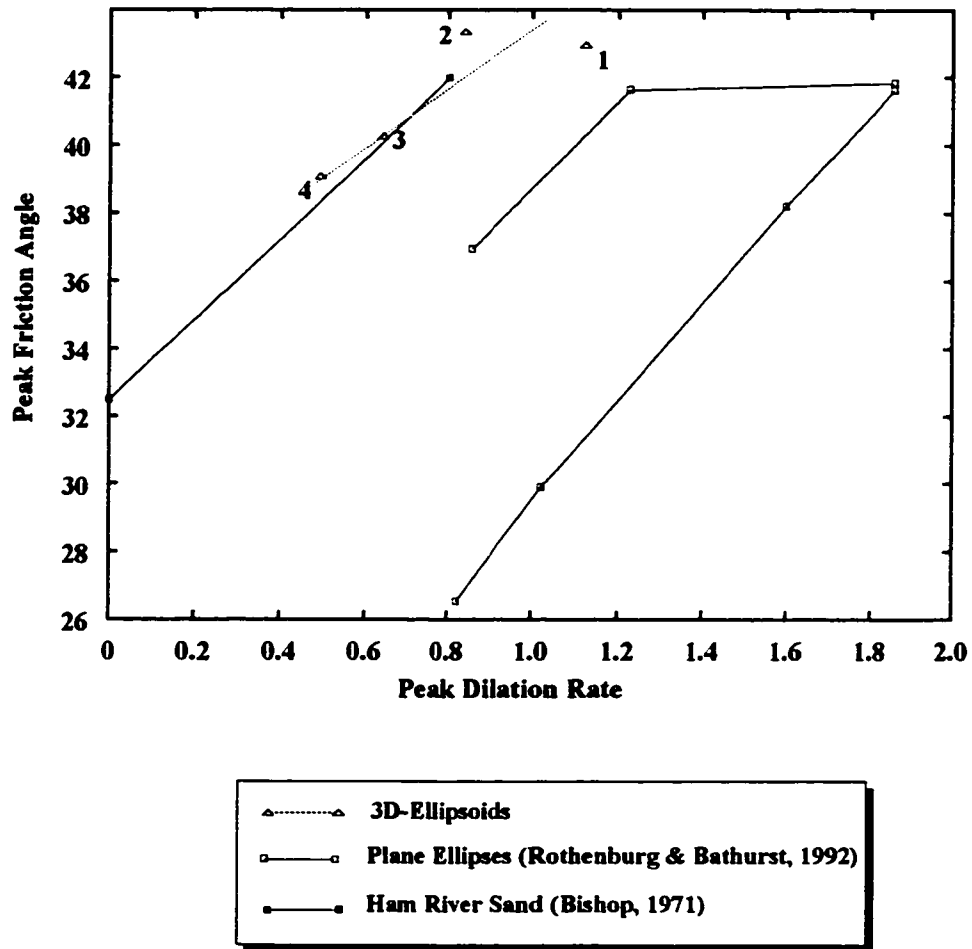


Figure 5-9 Peak friction angle vs. peak dilation rate for simulated assemblies of plane ellipses, 3-D ellipsoids, and a Ham River Sand

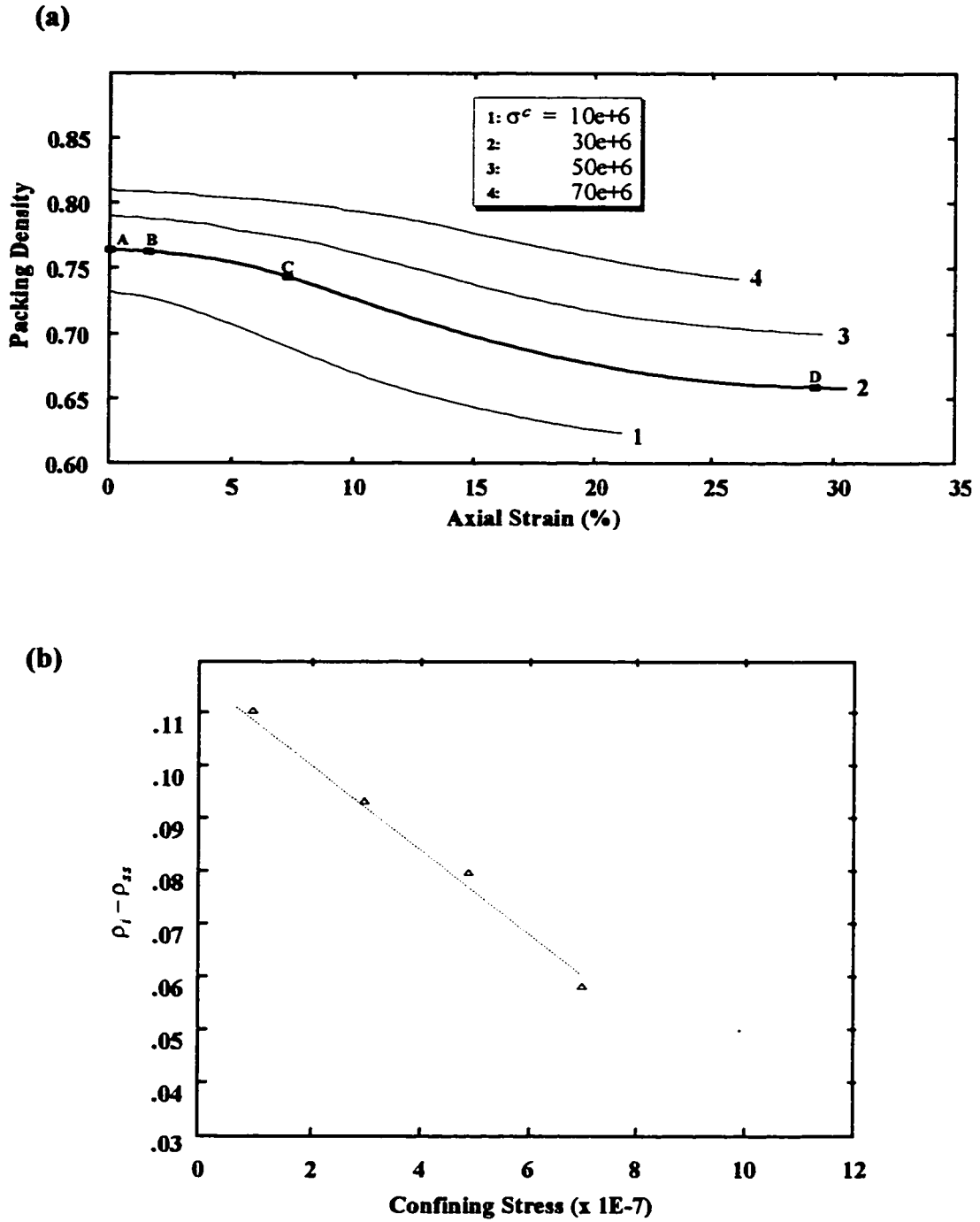


Figure 5-10 Evolution of packing density during shear deformation

The global effect of the confining pressure on the rate of change of the packing density can be measured by the average rate of change $\overline{\frac{d\rho}{d\varepsilon_a}}$ over the full range of applied axial deformation. The quantity $\overline{\frac{d\rho}{d\varepsilon_a}}$ can be related to the difference $(\rho_i - \rho_{ss})$ between the initial state and the steady state as:

$$\overline{\frac{d\rho}{d\varepsilon_a}} = \frac{1}{\varepsilon_a^{ss} - \varepsilon_a^i} \int_{\varepsilon_a^i}^{\varepsilon_a^{ss}} \left[\frac{d\rho}{d\varepsilon_a} \right] d\varepsilon_a = \frac{\rho_i - \rho_{ss}}{\varepsilon_a^i - \varepsilon_a^{ss}} \quad (5.4)$$

The plot in Figure 5.10b displays the variation of $(\rho_i - \rho_{ss})$ with varying confining pressure. The steep regression line indicates that a strong correlation exists between these two parameters.

Note that steady state was taken to be at 20.5% axial deformation. This is the largest axial deformation shared by all tests, but it is understood that the start of steady state depends on the confining pressure and is not the same for all tests.

5.4.4 Average Coordination Number Behaviour

The average coordination number in Figure 5.11a displays a trend of evolution which is typical of deviatoric tests. The steady decrease of this parameter is due to the overall loss of contacts (mainly in the lateral directions).

The number of contacts that are lost are only partially replaced by new contacts, so that the rate of creation is well below the rate of contact loss, at least until the strain softening begins; then the two rates start getting closer and become balanced at the steady-state. At the beginning of the steady-state the net number of contacts in the assembly tends to a constant value.

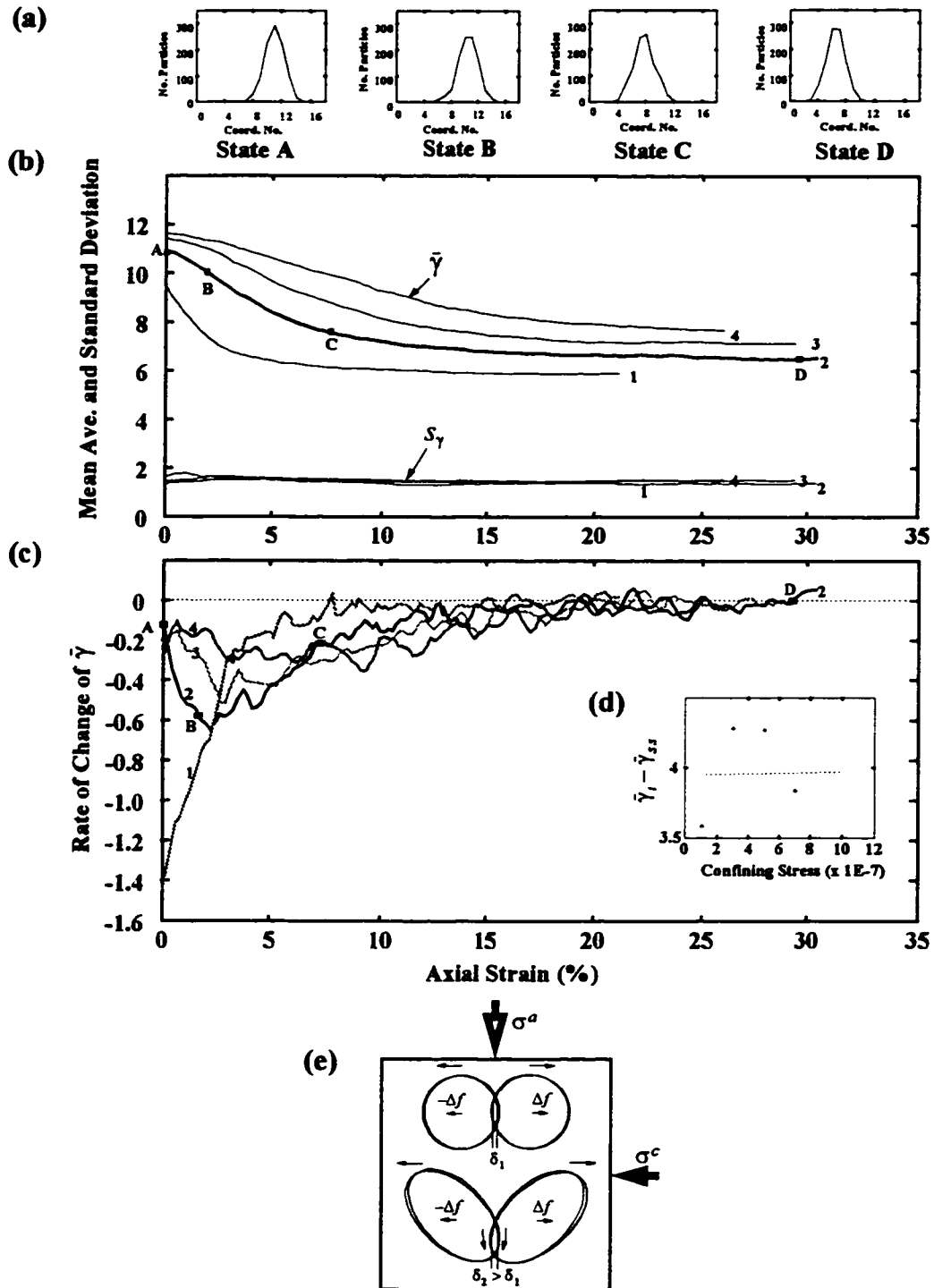


Figure 5-11 Evolution of average coordination number and its rate of change during shear deformation

From the histogram plots of the particle coordination number in Figure 5•11a, it is observed that the contacts at the post-peak states remain distributed in similar or at least close proportions around their arithmetic means, compared to those after the peak state. This trend is confirmed by the plot of the standard deviation of average coordination number in Figure 5•11b. This parameter experiences no significant change during shear deformation. It is also not sensitive to changes in applied confining stress.

An initial delay in contact loss is observed for large confining pressures (Figure 5•11b). The effect of shape is believed to be responsible for this phenomenon. It acts on the component of displacement contributed by rotations to oppose the effort of separation of two particles in contact. The schematics in Figure 5•11e illustrate this idea. Under the same separation effort, Δf , a pair of spheres in contact will separate before a pair of ellipsoids initially having the same overlap distance. In reality and in simulations, each particle is in contact with many particles. The contacts have different orientations and the breaking of contacts involves many factors at the same time, but, for lateral contacts, which constitute the major proportion of lost contacts, the effort of separation is lateral and the simple model shown is an acceptable approximation of the simulated reality.

5.4.4.1 Effect of Confining Pressure

It is observed that the initial delay in contact loss is not present for the smallest confining pressure (curves 1) in Figure 5•11b.

The rate of change of the coordination number, plotted in Figure 5•11c, shows a sensitivity to the applied confining pressure within the first 5% axial deformation. For the

large part of the deformation process, however, the curves of variations of these rates are hardly distinguishable. This means that the influence of the confining pressure is observable for the range of deformation before strain softening begins. Beyond this state, the sample would have dilated enough to allow its particles to move freely within their immediate surrounding without major restriction imposed by the overall mean pressure (especially in the lateral directions to the applied maximum-load).

The difference $(\bar{\gamma}_i - \bar{\gamma}_{ss})$ is plotted against the confining pressure as shown in Figure 5•11d. The regression line to fit the data shows a very poor correlation between these two parameters (very low slope angle). This result indicate that the influence of the confining pressure on the coordination number rate is globally insignificant, although its influence on the pre-peak states is recognized.

5.4.5 Average Normal Contact Force Behaviour

The average state of normal contact forces can be described by the average normal contact force magnitude, \bar{f}^p , over groups of contact normal orientations, as shown by plots in Figure 5•12a. The influence of confining pressure on initial and steady state values of \bar{f}^p is clearly observable on these plots. Moreover, Figure 5•12b shows a strong correlation between the average rate of change of \bar{f}^p and the applied confining stress.

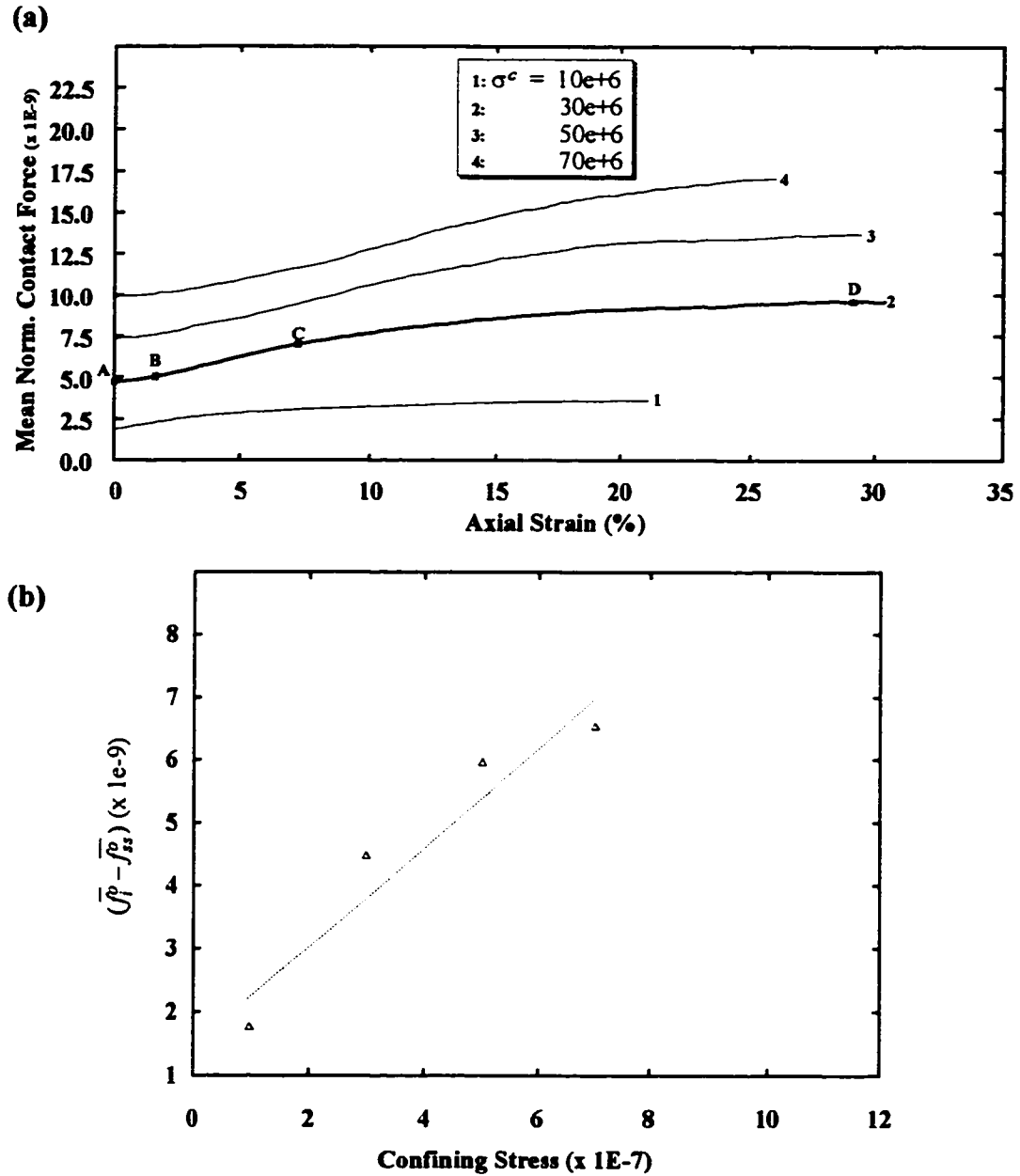


Figure 5-12 Evolution of the mean average normal contact force during shear deformation

5.4.6 Effect of Assembly Size

The effect of assembly size on the macro-mechanical behaviour can be visualized by comparison between samples of different sizes but initially having properties that are similar or at least close enough to be comparable. Two pairs of samples are considered:

- i. The 125 ellipsoid assembly tested at a confining pressure of $47\text{E}+6$ units (Test 3) and the 1000 ellipsoid assembly tested at a confining pressure of $50\text{E}+6$ units (Test 4c). These two tests are characterized by initial coordinations numbers of 11.21 and 11.46, initial porosities of 21.8% and 20.5%, and initial magnitudes of average intergranular normal forces of $7.15\text{e}+09$ and $7.39\text{e}+9$ units, respectively.
- ii. The 27 ellipsoid sample tested at a confining pressure of $7\text{E}+6$ units (Test 1), and the 1000 ellipsoid sample tested at a confining pressure of $10\text{E}+7$ (Test 4e). In this case, the samples have initial coordination numbers of 10.52 and 9.50, initial porosities of 26.2% and 26.8%, and initial magnitudes of average intergranular normal forces of $1.15\text{e}+9$ and $1.93\text{e}+9$, respectively.

The comparison between the first pair of samples is illustrated in Figure 5•13a. The striking closeness of the stress-strain curves, the dilatancy curves, and the evolution of the average coordination numbers and packing densities of the two samples indicates that the assembly size has a minor effect on the behaviour of the assemblies.

The comparison between the second pair of samples is illustrated in Figure 5•13b. In this case the difference in behaviour is relatively significant. The initial coordination numbers are different by more than one unit, which is substantial for this kind of parameter.

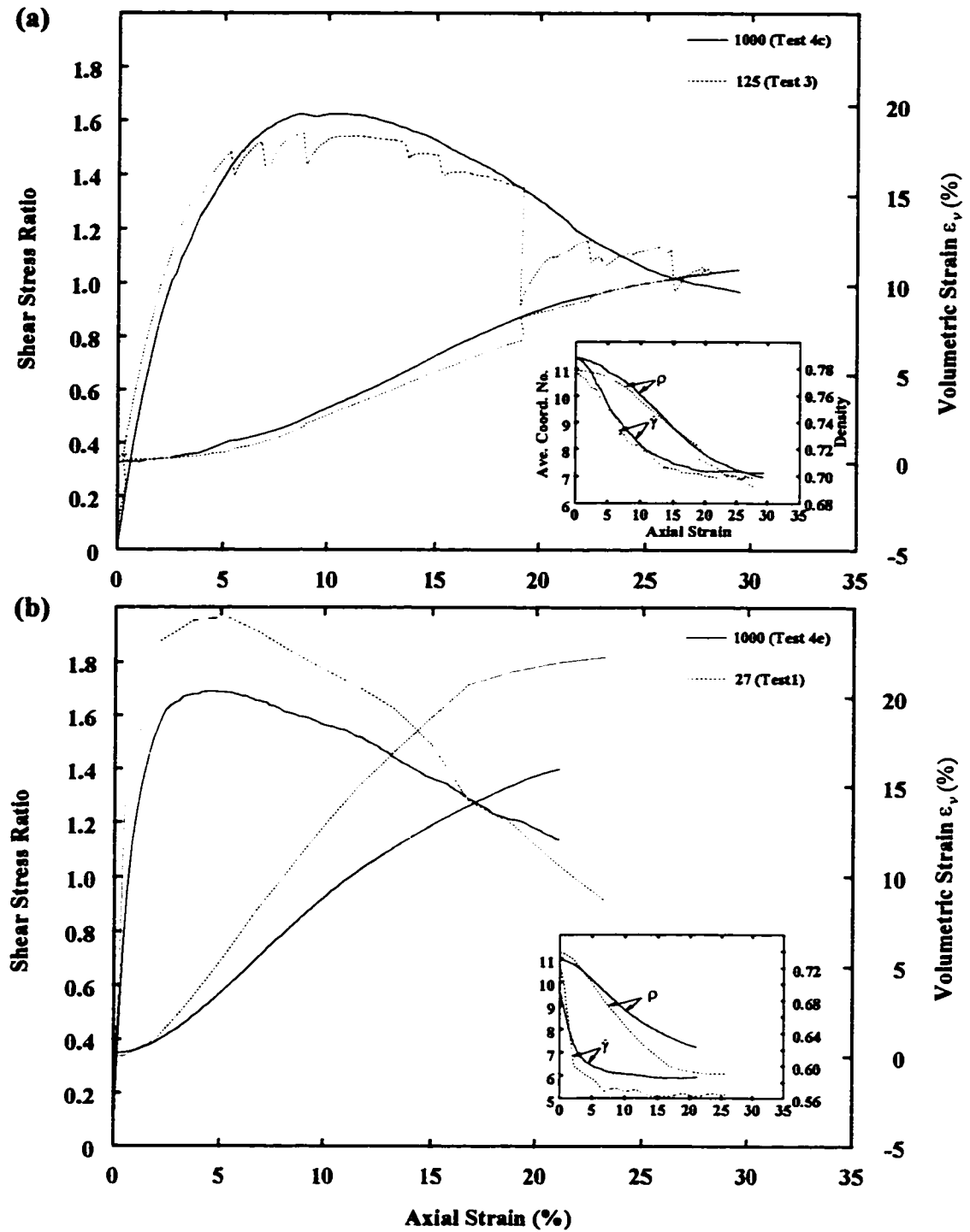


Figure 5-13 Effect of assembly size

This comparison reinforces the idea that the assembly size has no effect on the macro-mechanical behaviour and that the coordination number is a major factor in pre-determining the behaviour of sheared assemblies of particles.

5.4.7 Evolution of Microstructure and Contact Forces

A qualitative illustration of the load transfer in simulated assemblies of ellipsoids is provided in Figure 5•14. The plots are shown for the assembly of particles tested at a confining pressure $\sigma^c = 30\text{e}+6$ (Test 4d) which is in the medium lower range of used values.

The contact force magnitudes are proportional to the thickness of the lines connecting particles in contact. Three groups of contact orientations are represented (*i.e.*, in x, y and z-directions) at four particular states of deformations (A, B, C and D) as defined earlier and shown on the figure. Anisotropy will be most apparent on the chosen contact orientations (which are also principal directions of stress) because of the co-axiality of the stress and most of the induced anisotropy tensors.

Initially, the magnitudes of contact forces are mainly uniformly distributed among the three groups of contacts. These groups are also comprised of close but unequal numbers of contacts due to the existing initial anisotropy in contact orientations (Figure 5•15a).

5.4.7.1 Development of Contact Normal Orientations Anisotropy

As the test progresses, however, the number of contacts in the three directions decreases following the overall decline in the number of contacts. The rate of change is much slower for (x)-contacts than (y) and (z)-contacts (Figure 5•15a).

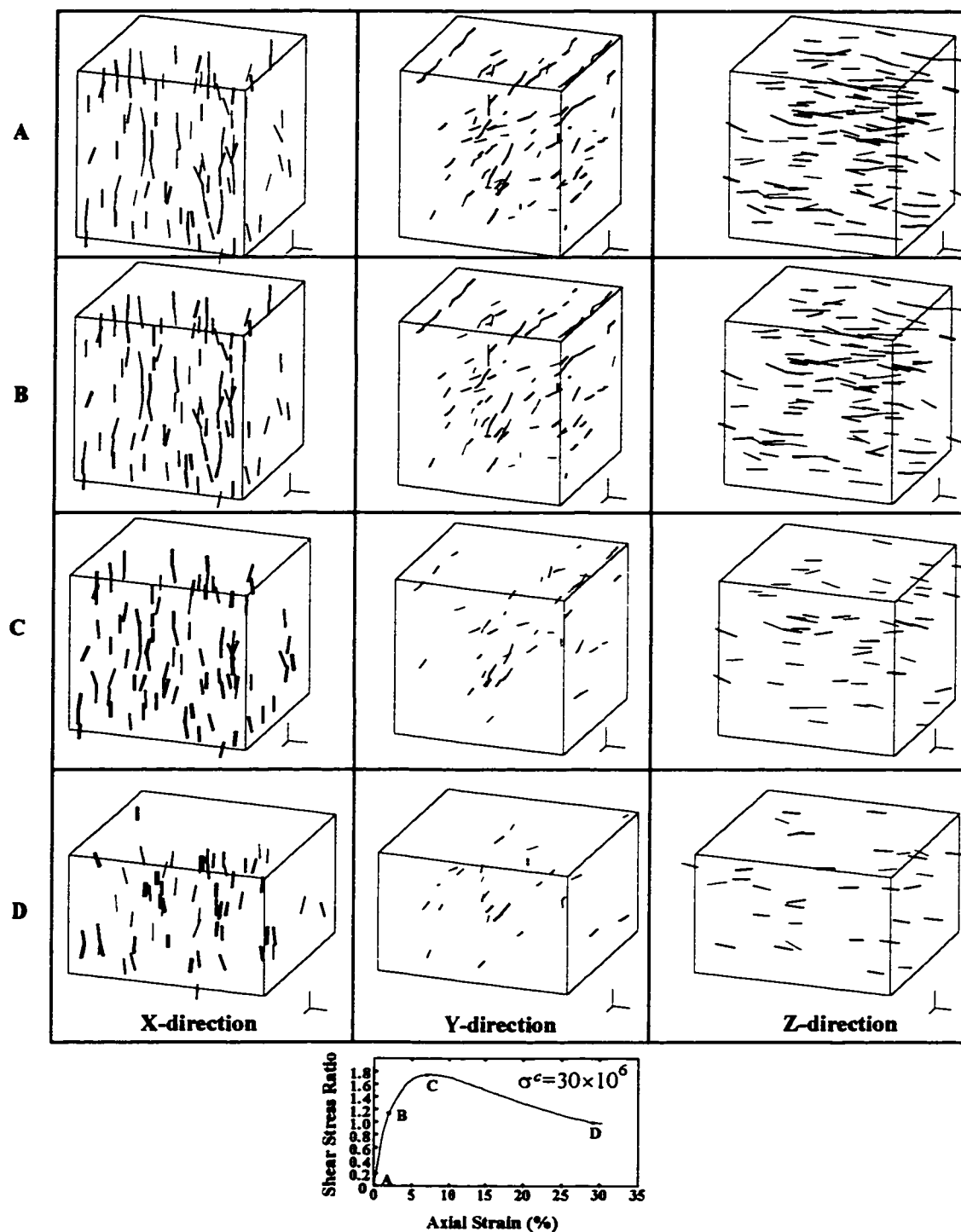


Figure 5-14 Induced anisotropy in contact normal orientations and normal contact forces (Test 4d)

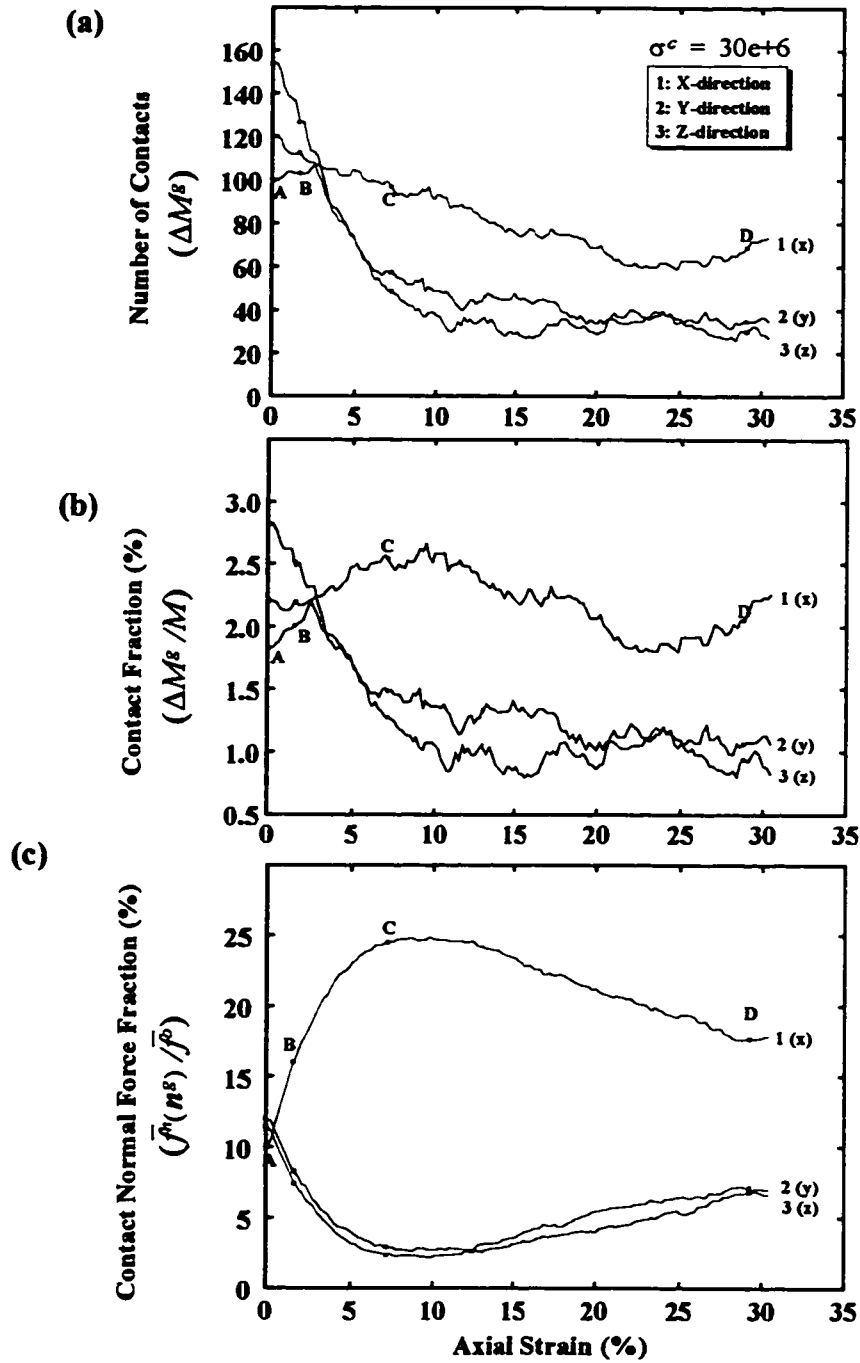


Figure 5-15 Vertical and horizontal contacts (Test 4d)
 (a) Number of contacts versus axial strain
 (b) Fraction of contacts versus axial strain
 (c) Fraction of normal contact force magnitude versus axial strain

The bias that is created as a result, initially relatively small, increases with shear deformation to a maximum value before gradually decreasing to a stable value. It is seen on Figure 5•15a that the decrease in the degree of induced anisotropy (calculated as a difference between the number of (x)-contacts and (y) or (z)-contacts) takes place after the peak of shearing resistance (state C).

Figure 5•15b shows the variation of the fraction of contacts oriented in the principal directions of stress during shear deformation. The contact fraction is defined by the ratio of the number of contacts in the particular orientation group to the total number of contacts in the assembly. Here, the contact fraction in the maximum load direction never drops below its initial level while the contact fractions in lateral directions steadily decrease and stabilize at large strain.

5.4.7.2 Development of Average Contact Force Anisotropy

The other visible form of anisotropy is related to the magnitude of contact forces. The maximum-load oriented contacts carry forces that are increasingly higher, as shown in Figure 5•15c. This is also noticeable from the increase in the thickness of the lines representing the contact force magnitudes up to the state of peak friction angle (state C). At the same time, the contact forces carried by lateral contacts (once at the same level of magnitude as the contact forces in the maximum-load direction) decrease dramatically, creating a major bias in the spatial distribution of contact force magnitudes.

The increase in contact force magnitudes carried by sub-axial contacts observed up to the peak state (state C) is caused by the overall decline in the number of contacts and the

need for the system to accommodate the excess load (once carried by contacts which are now lost). The excess load is distributed to the fewer remaining and newly formed contacts in the direction of compressive strain.

5.4.8 Anisotropy Behaviour

The induced anisotropy in fabric and in contact force magnitudes is the micromechanical response of the system of particles to the applied load. In Chapter 2, tensorial quantities were defined to measure this anisotropy by approximating the directional variations of the corresponding microscopic parameter (*e.g.*, contact normal orientation/contact vector length/contact force vector components) using truncated Fourier series expansions.

It has been seen that in some cases the approximation of these spacial distributions by second-order Fourier series was sufficient. In some other cases (the average tangential force, for example) fourth-order terms in the series were required to achieve a reasonable approximation.

Because of the mathematical difficulty in handling the fourth-order tensors used to express the fourth-order terms in the series expansion, the second-order anisotropy tensors alone are considered for quantifying anisotropy. They are subsequently used to trace quantitatively the above described development of anisotropy in simulated assemblies of ellipsoids during shear deformation.

5.4.8.1 Anisotropy in Contact Normal Orientations

The measured and calculated histograms of the contact normal orientation distributions are plotted at the four states, A, B, C and D, of the test 4d as shown in Figure 5•16a.

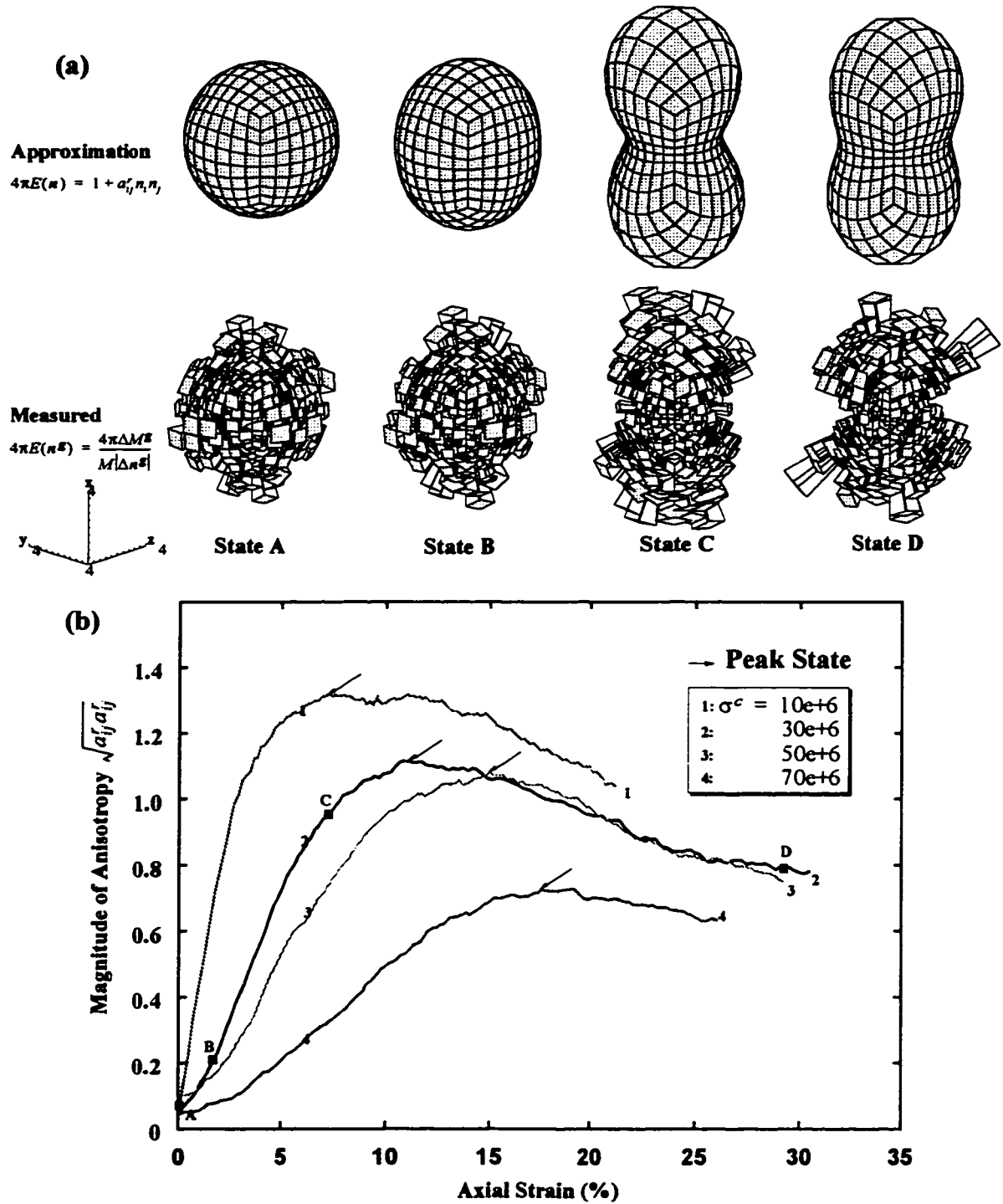


Figure 5-16 Evolution of anisotropy in contact normal orientations during shear deformation (Test 4d)

The development of anisotropy is indicated by the change in the shape of these distributions: From spherical (isotropic state A) to ellipsoidal (moderately anisotropic state B) to a “peanut” shape (states C and D). The degree of anisotropy of a “peanut” shape can be judged by reference to an isotropic distribution (unit sphere) in the principal directions of anisotropy where anisotropy is most apparent. Hence, it can be seen that the distribution of the state C is more anisotropic than that of state D. One possible measure of magnitude of anisotropy is $(a'_I - a'_{III}) / (a'_I + a'_{III})$ (Biarez and Wiendieck, 1963). A more-accurate measure that integrates all directions at once is by means of the second invariant of the anisotropy tensor $a' = \sqrt{a'_{ij}a'_{ij}}$.

The evolution of the magnitude of anisotropy in contact normal orientations, a' , is plotted in Figure 5•16b. The observed profiles show the same type of variation recorded by other simulation results, in two dimensions using disks and ellipses, and three dimensions using spheres. For instance, the curve of variation for disks and spheres was shown to be well approximated by a hyperbola or an exponential function. The hyperbolic trend is replicated in the case of ellipsoids, with few differences from the spherical case. A delay in the anisotropy increase takes place at the very beginning of the test for relatively large confining stresses.

In the case of assemblies of spheres, the contact disruption is not delayed by rotations of the particles, as in the case of ellipsoids. A similar delay was observed on the profiles of the average coordination number. The second difference is a strain softening phenomenon that takes place after the peak value.

The evolution trends of a' are microscopically related to the process of creation and

destruction of contacts during shear deformation. The increase of α' to a peak value then the decreasing convergence towards a steady value at large strain shows that the potential of anisotropy development is constrained by deformation.

When the applied deformation can be accommodated with a zero net number of created and disintegrated contacts, the value of the parameter α' stays constant (steady state of deformation). The steady state value seems to be sensitive to the level of applied confining pressure. Similar trends were observed in two-dimensional systems of numerical ellipses (Eliadorani, 1992).

5.4.8.2 Anisotropy in Average Normal Contact Forces

The magnitude of anisotropy in the average normal contact force, α'' , is plotted in Figure 5•17. It has characteristics of behaviour similar to the macroscopic stress-strain behaviour: for example, an initial increase to a maximum value, followed by strain softening and a transition to a constant value at large strain. The steady state value of α'' appears to be independent of the confining stress, this is similar to the angle of shearing resistance at steady state. The state of deformation at the peak value of α'' is also relatively close to that of the peak of angle of shearing resistance (curve 2).

The initial development of α'' obeys the tendency of the system of particles to distribute the transferred load in the form of high magnitude forces at contacts oriented in the maximum load direction along sub-vertical chains of particles, while minor load directions sustain lower magnitude forces. The magnitude of contact forces in the assembly keeps accumulating until inter-particle slip occurs.

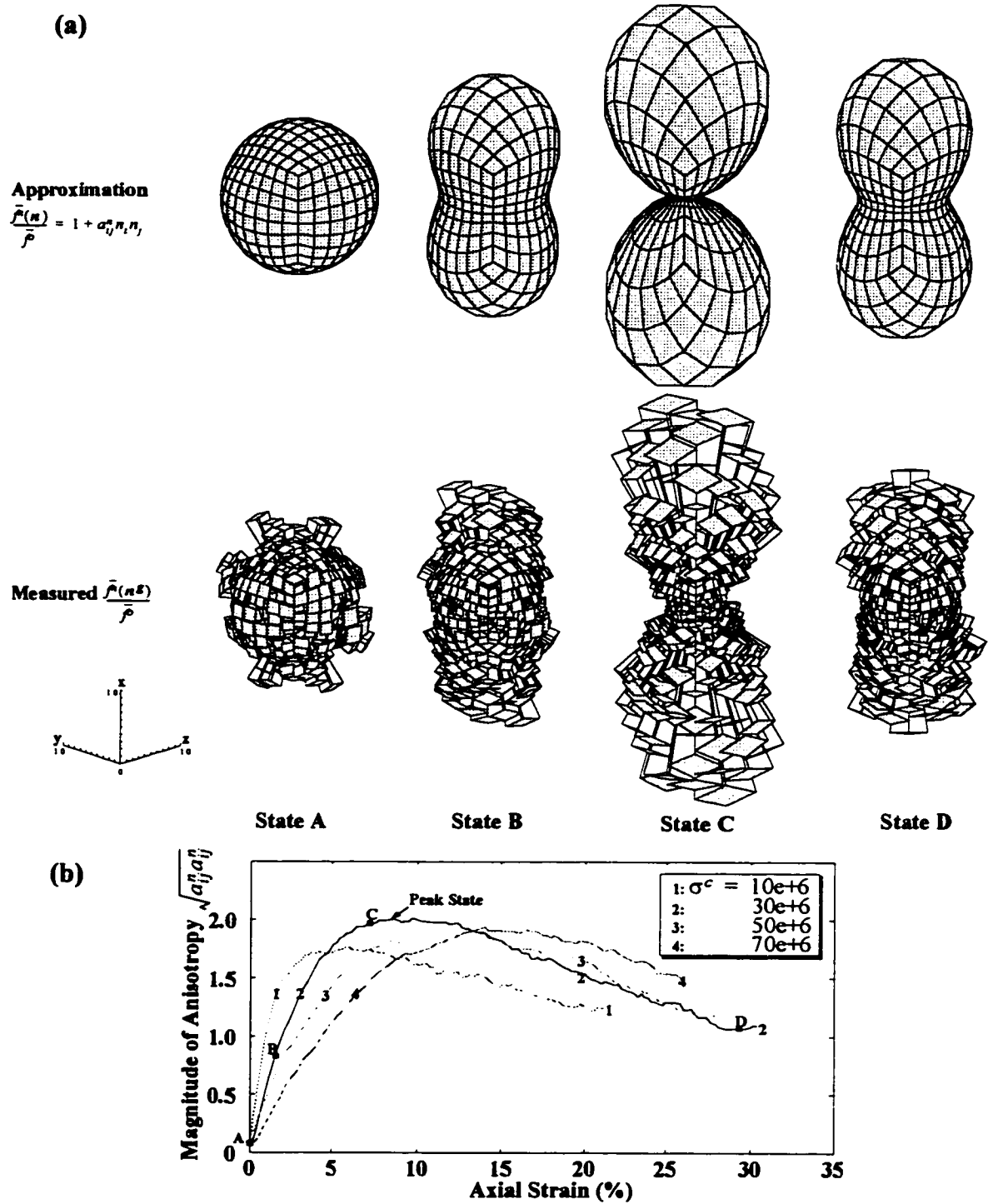


Figure 5-17 Evolution of anisotropy in average normal contact forces during shear deformation (Test 4d)

The slip leads to re-adjustments of the structure (increase in α') and the formation of interlocked regions in the form of compact clusters of particles which can move as rigid blocks in the direction of interlock (maximum compressive strain direction). Initially and up to the peak of internal friction angle, these regions will sustain high magnitude forces (increase in α'').

Under the effect of dilation and the lack of sufficient lateral support, the number of interlocked regions start diminishing gradually (decrease in α'') and stabilizes when the induced deformation can be accommodated by simple relative movement of the remaining blocks at a few slip contacts.

5.4.8.3 Anisotropy in Average Tangential Contact Forces

The magnitude of anisotropy in the average tangential contact force, α' features a relatively rapid rise (depending on the applied confining stress) to a maximum value, followed by a slow decline and convergence to a constant value, which seems to be unique for all applied confining pressures (Figure 5•18). The general behaviour is related to the number of contacts where slip occurs. It was observed that slip takes place primarily at contacts that represent end points of interlocked regions. As the number of contacts decreases, particles' rotational freedom is increased and tangential forces are slowly released.

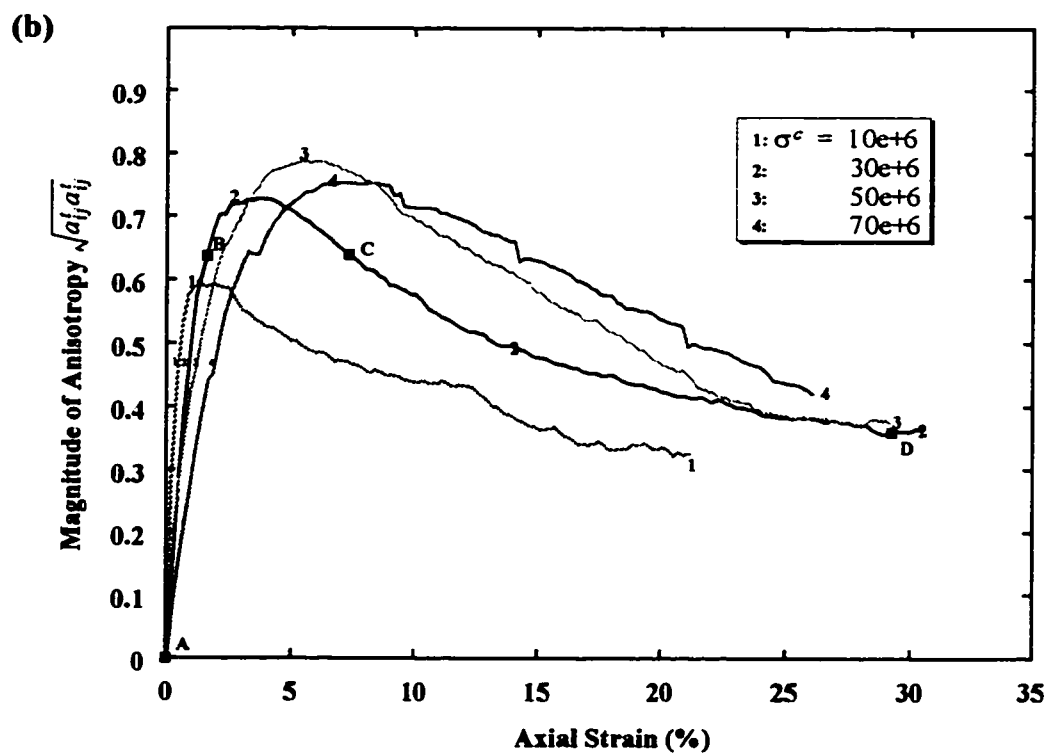
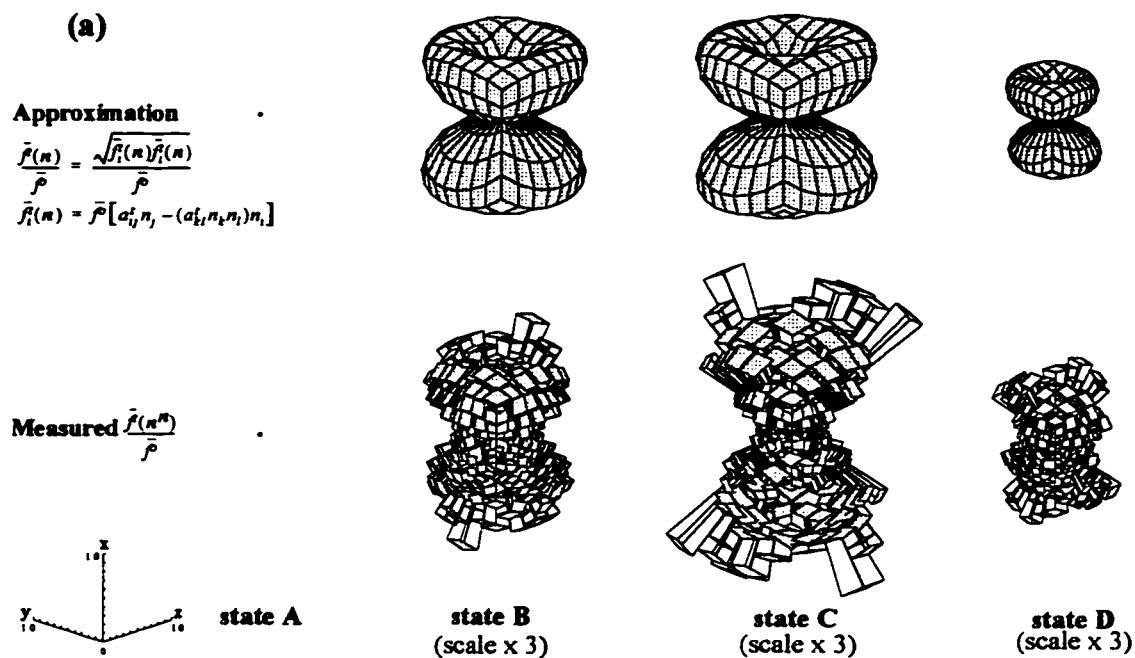


Figure 5-18 Evolution of anisotropy in average tangential contact forces during shear deformation (Test 4d)

5.4.8.4 Comparison of Anisotropies at their Peak States and the Influence of Confining Pressure

The magnitudes of anisotropies, a^r , a^n , and a^t for several confining pressures are plotted in a diagram of peak value versus applied axial strain, as shown in Figure 5•19. Both the maximum values and the corresponding axial strains can be compared on this diagram. The comparison can be made with reference to the maximum shear stress ratio, a_σ , which is plotted on the same diagram. This is because a_σ , a^r , a^n , and a^t are linked through a functional relationship termed “Stress-Force-Fabric” relationship.

For the case of disks in conditions of static equilibrium, where all anisotropy tensors are coaxial with the stress tensor, and magnitudes of anisotropy are small, Rothenburg (1980) has shown that the relationship takes the simple form:

$$a_\sigma = \frac{1}{2}(a^r + a^n + a^t) \quad (5\bullet 5)$$

The relationship in three dimensions is essentially the same as in two dimensions, except that a few corrections and terms must be added in the right hand side of the relationship in order to take into account the change in the dimensionality of space and in the shape of particles, as discussed in Chapter 6.

According to the relationship (5• 5), the macroscopic shear stress ratio is mobilized as a result of microscopic development in fabric and force anisotropies during shear deformation. The mobilized shear capacity is defined by the half sum of magnitudes of anisotropy, a^r , a^n , and a^t .

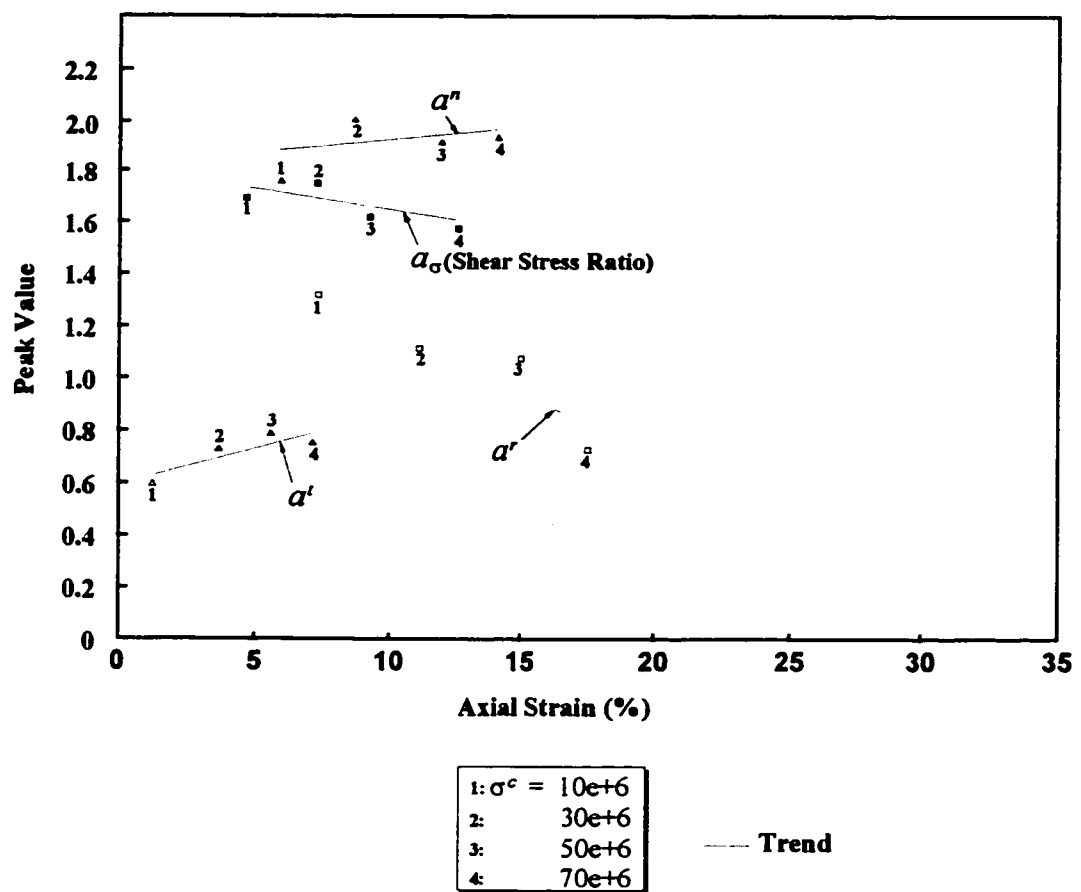


Figure 5-19 Comparison between anisotropies at their peak values and the influence of applied confining pressure

The magnitude of maximum a'' and its state of occurrence are the closest to a_σ . However, the maximum values of a'' are always higher than those of a_σ , and their states of occurrence always takes place after the peak of a_σ .

In terms of magnitudes of maximum anisotropy, a' is the second closest parameter to a_σ , followed by a'' in third position. This holds except for the large confining pressures (point 4) where the two parameters (a' and a'') are comparable.

Maximum a' values are attained well after the peak of a_σ ; those of a'' are attained well before the peak of a_σ .

Effect of Confining Pressure

From observation of trends of evolution of these parameters, it can be concluded that they are all dependent on the confining pressure. This dependence is the strongest for the fabric anisotropy a' , characterized by the steepest regression line.

5.4.8.5 Anisotropy in Average Branch Lengths

The evolution of this form of anisotropy is illustrated in Figure 5•20. The magnitude of anisotropy, a^z , increases linearly with axial deformation. It exhibits little sensitivity to the level of applied confining pressure (Figure 5•20b).

The development of a^z is a direct effect of particle shape and is much influenced by the ellipsoid orientations. At large strains, ellipsoidal particles have their major axis predominantly horizontal.

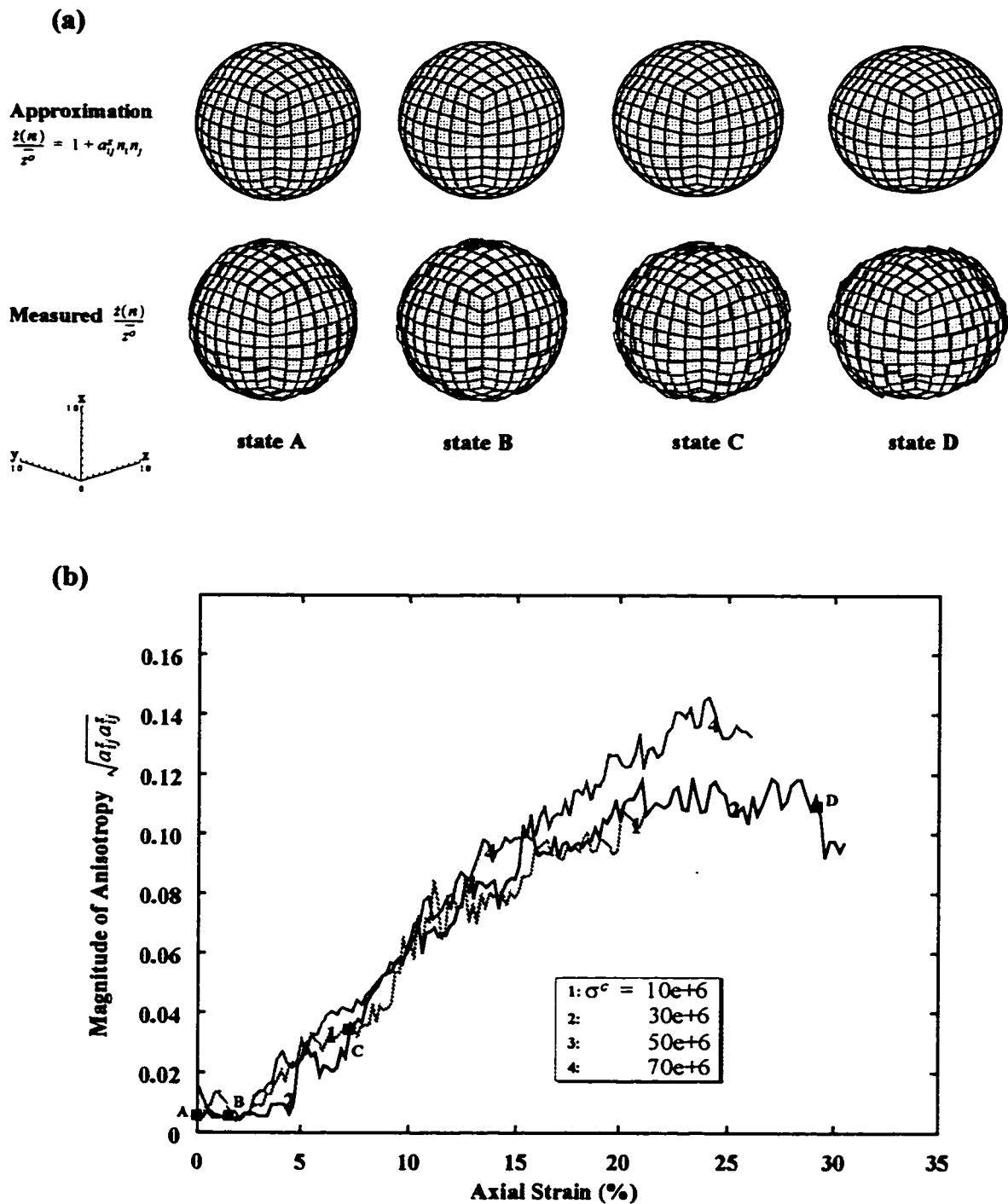


Figure 5-20 Evolution of anisotropy in average branch vector lengths during shear deformation (Test 4d)

Judging from the ellipsoidal shape of the distribution at state D, longer branch lengths characterize contacts in the horizontal direction and shorter branch lengths characterize contacts in the vertical direction.

This is consistent with the schematics in Figure 5•21b showing branch vector lengths of vertical and horizontal contacts between horizontally oriented particles. The branch vector for the vertical contact should always be shorter than the branch vector length for the horizontal contact. But, on average over all contacts in an assembly of ellipsoids, the branch vector length is essentially constant and its value does not depend on the applied confining pressure (Figure 5•21a).

Finally, it is observed that the average branch vector length \bar{z}^o is always higher than the geometric mean diameter $2\bar{r}$ defined as the diameter of a sphere having the volume of the mono-size ellipsoid particle. For mono-size assemblies of spheres there is always equality of these two parameters, which indicates another aspect of the particle shape effect.

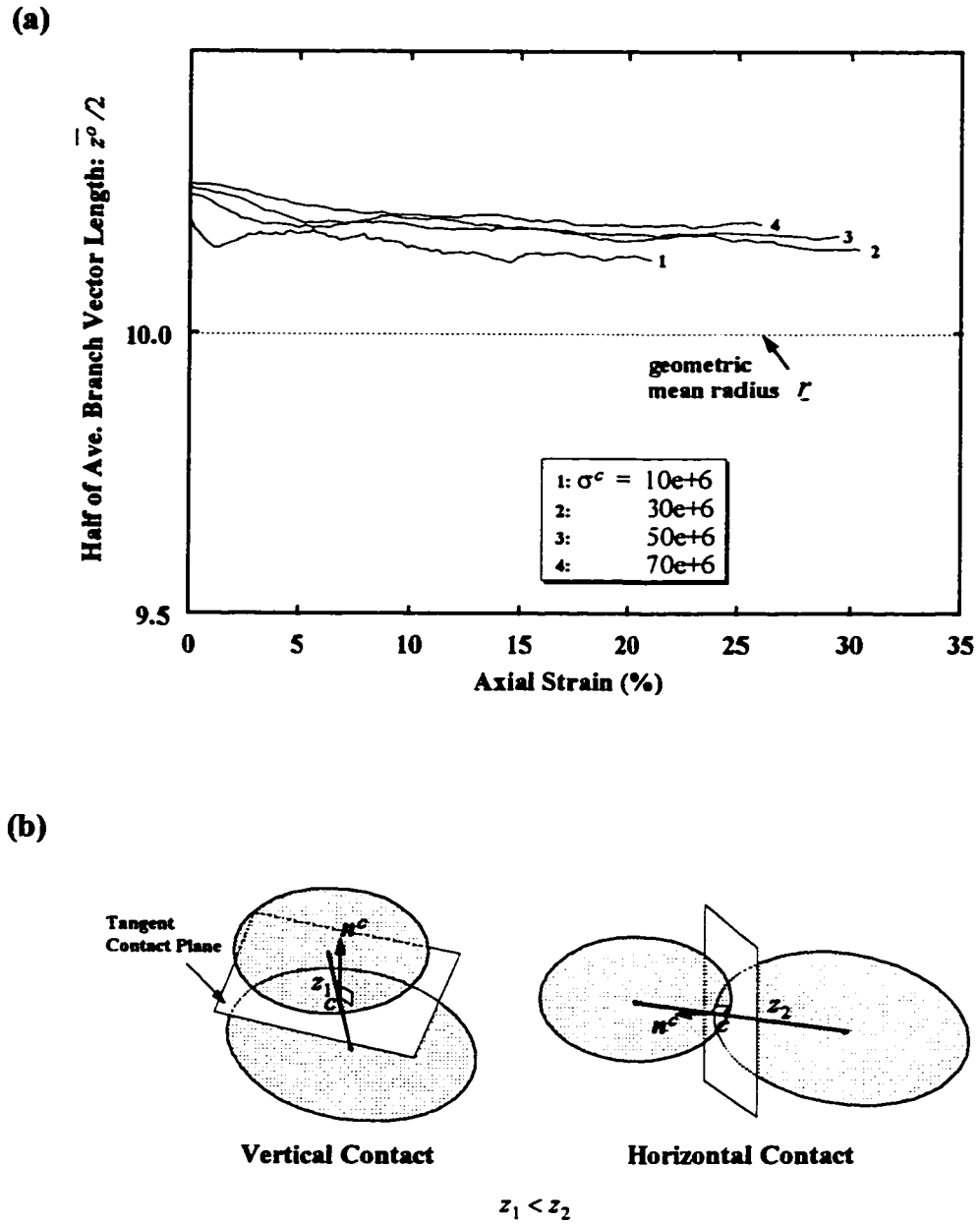


Figure 5-21 Evolution of the average branch vector length during shear deformation

5.5 Conclusions

From the results of the shape transformation procedure, it can be concluded that this method of assembly generation is an effective way of achieving initial samples of ellipsoids of high contact density before deviatoric testing. The shape of ellipsoids is certainly responsible for achieving coordination numbers of eleven and more when conditions of static equilibrium are maintained during the growth simulation process. Such values of coordination number cannot be numerically attained with randomly packed assemblies of spheres.

It has been observed that a change in the ellipsoids' aspect ratio, be it as small as $e = 0.05$, could trigger a mechanism of particle interlock and elevate the average coordination number from six or seven to values of ten and over. Further increase in the aspect ratio leads to values of the coordination number of twelve and slightly above under high confining pressure. There seems to be an optimal eccentricity for which the average coordination number is a maximum around $e = 0.16$. The packing density evidences a similar rise in value and reaches its maximum around the optimal eccentricity.

The anisotropies in all aspects of fabric and contact force components, initially very high because of the regularly packed structure of initial spheres, drop to relatively low values, but are not totally eliminated.

The shear deformation at constant mean pressure revealed characteristics of behaviour that are similar to real granular materials. The mobilized shear strength and dilation rates of simulated assemblies were seen to match typical values for dense sands.

The microscopic analysis revealed many aspects that were observed in physical tests

and numerical simulations in two and three dimensions. For example, Similarities include:

- i. Shapes of the spatial distributions of the different microscopic parameters.
- ii. Profiles of anisotropy development during shear deformation.

The effect of confining pressure is observed to affect both the microscopic and the macroscopic behaviour.

The effect of particle shape is present in all aspects of the behaviour of assemblies of ellipsoids. It not only influences initial parameters such as the coordination number or packing density, but it also contributes indirectly to all forms of anisotropy and also directly to the anisotropy in contact vector lengths and orientations.

CHAPTER VI: THE STRESS-FORCE-FABRIC RELATIONSHIP FOR ELLIPSOIDS

6.1 Introduction

The Stress-Force-Fabric relationship (S-F-F) is a term used for the explicitly formulated relationship between the components of the stress tensor and anisotropy tensors representing the global microscopic response of a system of particles subjected to a homogenous load pattern (for example, loading patterns used in conventional soil mechanics).

In this chapter, the S-F-F is formulated for ellipsoids and verified using results of numerical simulations. The relationship is tensorial in nature and is not easy to interpret in terms of such engineering parameters such as shear strength, dilatancy, etc. For this reason, a direct equation relating the shear stress ratio (measure of shear strength) to compo-

nents of anisotropy is preferable. This task can be very tedious, even under the simplest applied loading paths, as shown later. However, a great deal of information can be gained from deriving such a relationship, especially to better understand the shape effect on shear strength and other aspects of pressure sensitivity of assemblies of ellipsoids.

6.2 The Average Stress Tensor

The stress tensor has been previously expressed in terms of contact vectors as:

$$\sigma_{ij} = \frac{1}{V} \sum_{c \in V} f_i^c l_j^c \quad (6\bullet 1)$$

where the sum is taken over all contacts, c , in the assembly volume V .

Subsequent analytical developments utilize the particular formulation of the average stress tensor in terms of branch vectors.

By definition, the branch vector connects the centroids of two particles in contact. Referring to Figure 6•1, the branch vector $\mathbf{z}^c = \underline{AB}$ is related to the contact vector, $\mathbf{l}_1^c = \underline{AC}$, relative to particle A , and, $\mathbf{l}_2^c = \underline{BC}$, relative to particle B , as $\mathbf{z}^c = \mathbf{l}_2^c - \mathbf{l}_1^c$.

A physical contact contributes two individual contacts (one for each particle), thus:

$$\sigma_{ij} = \frac{1}{V} \sum_{c \in V} (f_{2i}^c l_{2j}^c + f_{1i}^c l_{1j}^c) \quad (6\bullet 2)$$

The term between brackets can be further transformed as follows:

$$f_{2i}^c l_{2j}^c + f_{1i}^c l_{1j}^c = f_i^c l_{2j}^c - f_i^c l_{1j}^c = f_i^c z_j^c = \frac{1}{2} (f_{1i}^c z_{1j}^c + f_{2i}^c z_{2j}^c) \quad (6\bullet 3)$$

Therefore:

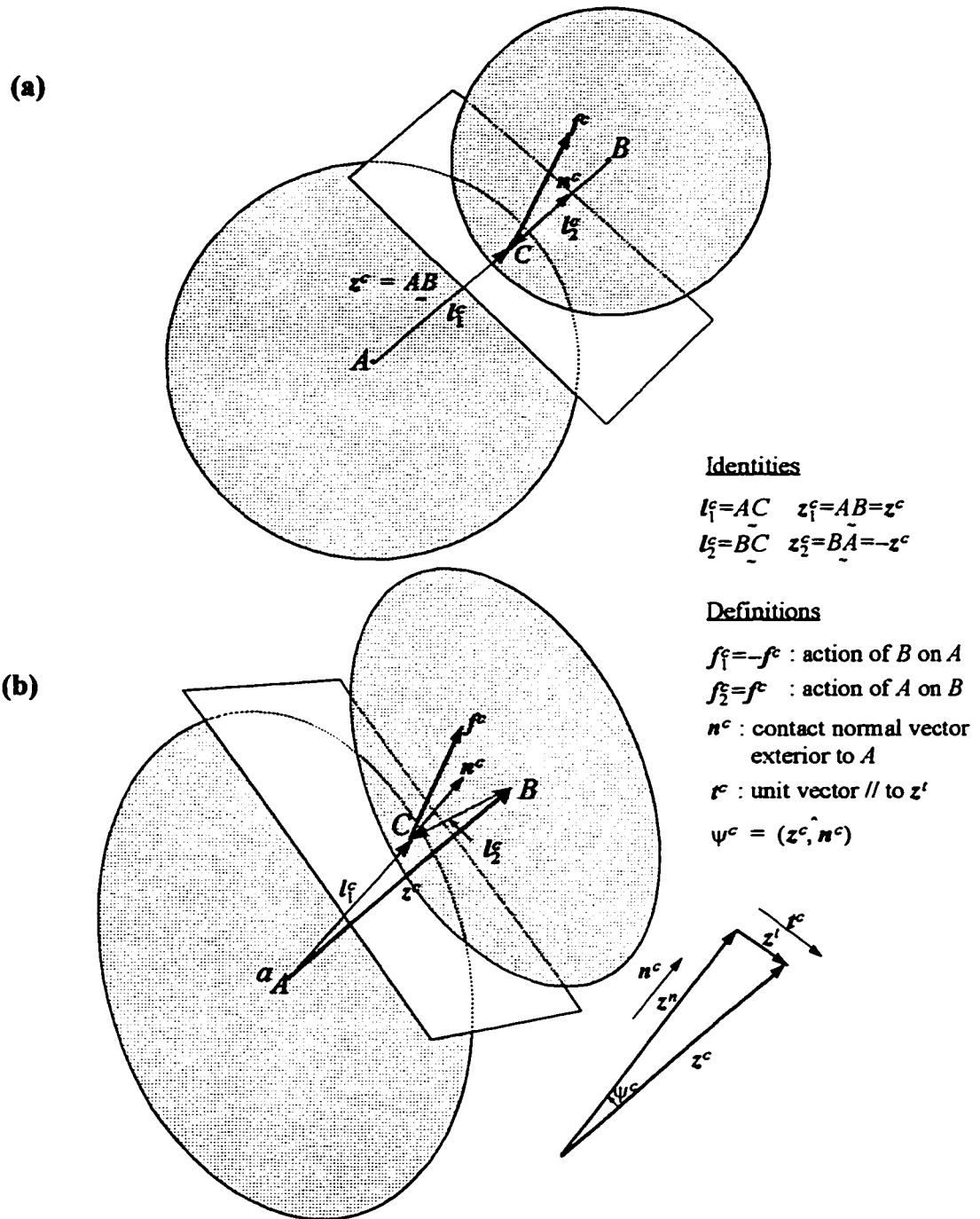


Figure 6-1 Contact vectors, branch vectors, and contact normal vectors
 (a) Spheres
 (b) Ellipsoids

$$\sigma_{ij} = \frac{1}{2V} \sum_{c \in V} (f_{2i}^c z_{2j}^c + f_{1i}^c z_{1j}^c) \quad (6.4)$$

Or:

$$\sigma_{ij} = \frac{1}{2V} \sum_{c \in V} f_i^c z_j^c \quad (6.5)$$

For infinite systems of particles, the average stress tensor assumes the following continuous form:

$$\sigma_{ij} = \frac{1}{2} m_v \int \bar{f}_i(\mathbf{n}) \bar{z}_j(\mathbf{n}) E(\mathbf{n}) d\mathbf{n} \quad (6.6)$$

The meaning of the variables in the right hand side are the same as those discussed in Chapter 2 for infinite systems. The only new variable introduced here is the average branch vector $\bar{z}_j(\mathbf{n})$.

In micromechanics research related to disks and spheres, treatment of the average branch vector is almost trivial due to its coincidence with the contact normal (Figure 6.1a):

$$\bar{z}_j(\mathbf{n}) = \bar{z}^o n_j \quad (6.7)$$

For non-spherical particles, treatment of the average branch vector is a major issue and this vector must essentially be treated similarly to the average contact force vector.

6.3 Distribution of Average Branch Vectors

The branch vector is generally not coincident with the contact normal direction (Figure 6.1b). Similarly to the contact force vector, the branch vector is decomposed into a normal component (associated with the size of particles in contact) and a tangential com-

ponent (describing the shape of particles at the vicinity of the contact) as:

$$z_j^c = z^n n_j^c + z_j^t \quad (6 \cdot 8)$$

where:

$$\begin{cases} z^n = z \xi n_k^c = z^c \cos \psi^c \\ z_j^t = z_j^c - z^n n_j^c = z^c \sin \psi^c t_j^c \end{cases} \quad (6 \cdot 9)$$

The unit vector $t^c = z^t/z^c$ is parallel to the tangent branch vector z^t ; z^c is the modulus of the vector z^c ; z^t is the modulus of the vector z^t ; and ψ^c is the angle between z^c and n^c .

The average branch vector calculated over a group of contacts of similar orientation is given by:

$$\bar{z}_j(n) = \bar{z}^n(n) n_j + \bar{z}_j^t(n) \quad (6 \cdot 10)$$

In finite assemblies of particles, the averages are discrete sums over contacts falling in the class of orientation represented by the unit vector n :

$$\begin{cases} \bar{z}^n(n) = \overline{z \xi n_k^c} = \left[\sum_{c \in (n)} z \xi n_k^c \right] / \Delta M_{(n)} \\ \bar{z}_j^t(n) = \overline{z_j^c - z^n n_j^c} = \left[\sum_{c \in (n)} (z_j^c - z^n n_j^c) \right] / \Delta M_{(n)} \end{cases} \quad (6 \cdot 11)$$

where $\Delta M_{(n)}$ is the number of contacts in the class of orientation n .

For infinite systems, the discrete average for orientation classes should be replaced by continuous functions of the orientation vector. Appropriate approximations of these functions can be established using spherical harmonics or Fourier series.

6.3.1 Distribution of Average Normal Branch Vectors

Similar to the average normal contact force, the average normal branch vector is an even function of orientation, *i.e.*, $\bar{z}^n(\mathbf{n}) = \bar{z}^n(-\mathbf{n})$, and as such it can be represented by a truncated Fourier series of even order terms. Results of numerical simulations show that the measured distributions are accurately approximated by second-order Fourier series:

$$\bar{z}^n(\mathbf{n}) = \bar{z}^o \{ 1 + a_{ij}^n n_i n_j \} \quad (6\cdot 12)$$

As an illustration, a measured distribution of normal branch vectors and its model approximation are shown in Figure 6•2a. The model seems to fit the numerical data very well. No additional higher terms are required in this case.

6.3.2 Distribution of Average Tangential Branch Vectors

The average tangential branch vector is geometrically similar to the average tangential contact force vector:

- i. Its average over groups of orientation is zero, *i.e.*, $\int_{\mathbf{n}} \bar{z}_i^t(\mathbf{n}) d\mathbf{n} = 0$,
- ii. the distribution function is odd, *i.e.*, $\bar{z}_i^t(-\mathbf{n}) = -\bar{z}_i^t(\mathbf{n})$, and,
- iii. it is orthogonal to the orientation group unit vector, *i.e.*, $\bar{z}_i^t n_i = 0$

These properties suggest that a similar model used to approximate the average tangential contact force distribution applies to the distribution of average tangential branch vectors. *i.e.*, the second-order model:

$$\bar{z}_i^t(\mathbf{n}) = \bar{z}^o [a_{ij}^t n_j - (a_{ki}^t n_k n_l) n_i] \quad (6\cdot 13)$$

Or, the fourth-order model:

$$\bar{z}_i^t(\mathbf{n}) = \bar{z}^o [a_{ij}^t n_j - (a_{ki}^t n_k n_l) n_i + b_{ijkl}^t n_j n_k n_l - (b_{klmn}^t n_k n_l n_m n_n) n_i] \quad (6\cdot 14)$$

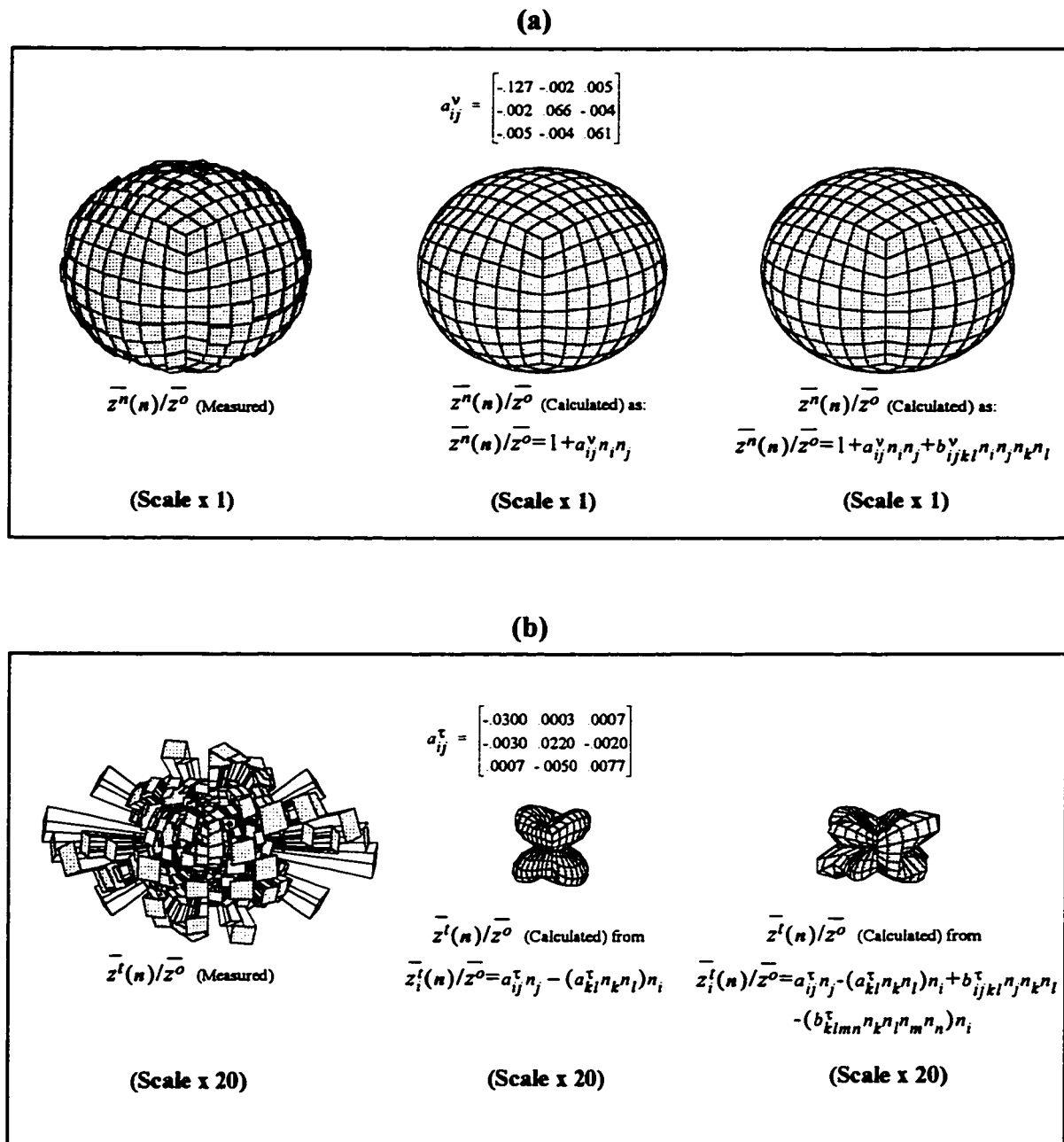


Figure 6-2 Measured and approximated distributions of average normal and tangential branch vectors

The plots in Figure 6•2b show that the above models provide poor quality approximations of data. Two assumptions are possible:

(1) The above models are really not suited to represent average branch vectors, perhaps because the branch vectors and contact forces are physically different parameters, although they share some geometrical similarities of a type outlined earlier, and also because the above models are strictly applicable to the type of tangential forces that are found in bonded elastic systems of spheres.

(2) The other possibility, which is most likely, is that the approximations are not computed properly, given the very small anisotropy that develops in average tangential branch vectors. In the example illustrated in Figure 6•2b, the tangential distributions are magnified by a factor of 20 to be comparable in size to the normal distributions in Figure 6•2a. The approximations are based on the calculated coefficient of anisotropy α_{ij}^t . Given the conditions of the performed simulation tests with ellipsoids, the tensor should remain coaxial with the principal directions of stress, which means that the directions x, y, and z must be principal directions for this tensor. As a result, the components α_{12}^t , α_{23}^t , and α_{31}^t should only represent fluctuations around the mean value zero. In the case of the average tangential forces this is what is actually observed, and the approximations are fairly accurate, but for average tangential branch vectors, the fluctuations are often of the same magnitude as the principal values of the tensor, which results in distorted and inaccurate approximations. Nonetheless, the tensor α_{ij}^t contains valuable information as to the level of anisotropy induced by the directional variation of tangential branch vectors and provides meaningful correction to the stresses calculated from the S-F-F relationship. For all

these reasons, the second-order model for tangential branch vectors is maintained and used directly to develop the S-F-F fabric relationship for ellipsoids.

6.4 The S-F-F Relationship for Infinite Systems of Ellipsoids

The objective here is to develop the S-F-F relationship in (6• 6) in terms of the anisotropy tensors used to express the distributions of the microscopic parameters in the relationship.

A direct way of achieving this is by substituting the model equations of the distributions in the right hand side of the relationship and integration of the obtained full expression. In the process of integration, the quantities which originally represented specific physical parameters will become mixed with each other in product terms and cannot be easily regrouped after integration. This is in addition to the difficulties of integration, which are substantial in this case. An alternative solution is to restrict the decomposition of the full expression to terms which will preserve a clear physical interpretation once the integration is performed. This is achieved by writing each distribution function as a sum of a term associated with a state of perfect isotropy (a spherical term) supplemented by another term representing the deviation from this isotropic state (a deviatoric term), *i.e.*,

$$\begin{cases} E(\mathbf{n}) = \frac{1}{4\pi} + E^*(\mathbf{n}) \\ \bar{z}_j(\mathbf{n}) = \bar{z}^0 n_j + \bar{z}_j^*(\mathbf{n}), \quad j=1..3 \\ \bar{f}_i(\mathbf{n}) = \bar{f}^0 n_i + \bar{f}_i^*(\mathbf{n}), \quad i=1..3 \end{cases} \quad (6\bullet 16)$$

Second-order Fourier series approximations of the deviatoric terms will be used as

follows:

$$\begin{cases} E^*(n) = a_{ij}^r n_i n_j / 4\pi \\ \bar{z}_j^*(n) = \bar{z}^o(a_{jp}^r n_p - (a_{pq}^v - a_{pq}^s) n_p n_q n_j), \quad j=1..3 \\ \bar{f}_i^*(n) = \bar{f}^o(a_{ik}^r n_k - (a_{kl}^n - a_{kl}^t) n_k n_l n_i), \quad i=1..3 \end{cases} \quad (6 \bullet 16)$$

The S-F-F relationship in (6• 6) can now be re-written as:

$$\sigma_{ij} = \frac{1}{2} m_v \int_n [\bar{f}^o n_i + \bar{f}_i^*(n)] [\bar{z}^o n_j + \bar{z}_j^*(n)] \left[\frac{1}{4\pi} + E^*(n) \right] dn \quad (6 \bullet 17)$$

and decomposed as:

$$\sigma_{ij} = \sigma_{ij}^o + \sigma_{ij}^r + \sigma_{ij}^s + \sigma_{ij}^f + \sigma_{ij}^{rz} + \sigma_{ij}^{rf} + \sigma_{ij}^{zf} + \sigma_{ij}^{rzf} \quad (6 \bullet 18)$$

where:

$$\begin{aligned} \sigma_{ij}^o &= \frac{1}{2} m_v \int_n [\bar{f}^o n_i] [\bar{z}^o n_j] \left[\frac{1}{4\pi} \right] dn \\ \sigma_{ij}^r &= \frac{1}{2} m_v \int_n [\bar{f}^o n_i] [\bar{z}^o n_j] [E^*(n)] dn \\ \sigma_{ij}^s &= \frac{1}{2} m_v \int_n [\bar{f}^o n_i] [\bar{z}_j^*(n)] \left[\frac{1}{4\pi} \right] dn \\ \sigma_{ij}^f &= \frac{1}{2} m_v \int_n [\bar{f}_i^*(n)] [\bar{z}^o n_j] \left[\frac{1}{4\pi} \right] dn \\ \sigma_{ij}^{rz} &= \frac{1}{2} m_v \int_n [\bar{f}^o n_i] [\bar{z}_j^*(n)] [E^*(n)] dn \\ \sigma_{ij}^{rf} &= \frac{1}{2} m_v \int_n [\bar{f}_i^*(n)] [\bar{z}^o n_j] [E^*(n)] dn \\ \sigma_{ij}^{zf} &= \frac{1}{2} m_v \int_n [\bar{f}_i^*(n)] [\bar{z}_j^*(n)] \left[\frac{1}{4\pi} \right] dn \\ \sigma_{ij}^{rzf} &= \frac{1}{2} m_v \int_n [\bar{f}_i^*(n)] [\bar{z}_j^*(n)] [E^*(n)] dn \end{aligned} \quad (6 \bullet 19)$$

The tensor σ_{ij}^o is spherical and corresponds to a fully isotropic state when all anisotropy tensors are equal to zero.

The tensors σ_{ij}^r , σ_{ij}^s , and σ_{ij}^f are deviatoric and represent contributions of the indi-

vidual anisotropies taken separately. Each contribution is calculated as if the corresponding anisotropy is the only one present in the system, the two other parameters being perfectly isotropic.

Tensors σ_{ij}^{zf} , σ_{ij}^{zf} , and σ_{ij}^{zf} are defined by pair products of anisotropy-related quantities.

Finally, the tensor σ_{ij}^{zf} is defined by a product of all anisotropy-related quantities.

Each component of the stress tensor partition corresponds to an ideal situation which is rarely encountered in simulations or in reality, but by virtue of this relationship, the complex simulated or real situation can always be analyzed by reference to this simplistic situation. For this reason, the S-F-F relationship is formulated through the expression of the stress tensor partition components in terms of second-order anisotropy tensors.

The idea of calculating the stress tensor as an additive partition of components with a particular relation to the different types of anisotropy present in a granular mass is very popular in the micromechanical research. Many similar stress partitions can be found in the literature (*e.g.*, Mehrabadi *et. al.*, 1982; Cundall and Strack, 1983; Thornton and Barnes, 1986; Rothenburg and Dusseault, 1987; amongst others). The method of partition followed here is identical to that of Rothenburg and Dusseault (1987) developed for the case of assemblies of spheres. The above partition can be viewed as a generalization to include the ellipsoidal shape of particles.

The results of integration are greatly simplified by adopting the following definitions:

$$\begin{aligned}
 \sigma^o &= \frac{m \bar{f}^o(\bar{z}^o/2)}{3} \\
 a_{ij}^{\Delta z} &= a_{ij}^v - a_{ij}^r \\
 a_{ij}^{\Delta f} &= a_{ij}^n - a_{ij}^t \\
 \beta_{ij}^{(2)} &= \frac{3}{4\pi} \int_{\mathbf{n}} n_i n_j d\mathbf{n} \\
 \beta_{ijkl}^{(4)} &= \frac{15}{4\pi} \int_{\mathbf{n}} n_i n_j n_k n_l d\mathbf{n} \\
 \beta_{ijklpq}^{(6)} &= \frac{105}{4\pi} \int_{\mathbf{n}} n_i n_j n_k n_l n_p n_q d\mathbf{n} \\
 \beta_{ijklpqrs}^{(8)} &= \frac{945}{4\pi} \int_{\mathbf{n}} n_i n_j n_k n_l n_p n_q n_r n_s d\mathbf{n}
 \end{aligned} \tag{6• 20}$$

The stress σ^o is interpreted as the mean stress for a perfectly isotropic system. This interpretation is directly implied by the result of integration of the first stress partition component σ_{ij}^o .

The second-order tensors $a_{ij}^{\Delta z}$ and $a_{ij}^{\Delta f}$ represent distances between normal and tangential anisotropy tensors associated with a common microscopic parameter (in this case, the average branch vector and the average contact force, respectively).

The β tensors are integrals over the unit sphere of elementary products of the unit vector components n_i . They vanish if the number of products is odd and assume positive integer values if the number of products is even.

Substitution of expressions of $E^*(\mathbf{n})$, $\bar{z}_i^*(\mathbf{n})$ and $\bar{f}_i^*(\mathbf{n})$ in (6• 16) into the system of stress components in (6• 19) and integration (using definitions in (6• 20)) yields:

$$\begin{aligned}
 \sigma_{ij}^o &= \sigma^o \beta_{ij}^{(2)} \\
 \sigma_{ij}^r &= \frac{\sigma^o}{5} \beta_{ijkl}^{(4)} a_{kl}^r \\
 \sigma_{ij}^z &= \frac{\sigma^o}{5} \{ \beta_{ik}^{(2)} a_{jk}^z + \beta_{ijkl}^{(4)} a_{kl}^{\Delta z} \} \\
 \sigma_{ij}^f &= \frac{\sigma^o}{5} \{ \beta_{ik}^{(2)} a_{jk}^f + \beta_{ijkl}^{(4)} a_{kl}^{\Delta f} \} \\
 \sigma_{ij}^{rz} &= \frac{\sigma^o}{35} \{ 7 \beta_{ikpq}^{(4)} a_{pq}^r a_{jk}^z + \beta_{ijklpq}^{(6)} a_{pq}^r a_{kl}^{\Delta z} \} \\
 \sigma_{ij}^{rf} &= \frac{\sigma^o}{5} \{ 7 \beta_{jkpq}^{(4)} a_{pq}^r a_{ik}^f + \beta_{ijklpq}^{(6)} a_{pq}^r a_{kl}^{\Delta f} \} \\
 \sigma_{ij}^{zf} &= \frac{\sigma^o}{35} \{ 35 \beta_{kp}^{(2)} a_{jp}^z a_{ik}^f + 7 \beta_{jkpq}^{(4)} a_{pq}^{\Delta z} a_{ik}^f + 7 \beta_{iklp}^{(4)} a_{jp}^z a_{kl}^{\Delta f} + \beta_{ijklpq}^{(6)} a_{pq}^{\Delta z} a_{kl}^{\Delta f} \} \\
 \sigma_{ij}^{zsf} &= \frac{\sigma^o}{105} \{ 105 \beta_{kprs}^{(4)} a_{rs}^r a_{jp}^z a_{ik}^f + 3 \beta_{jkpqrs}^{(6)} a_{rs}^r a_{pq}^{\Delta z} a_{ik}^f + 3 \beta_{iklpqs}^{(6)} a_{rs}^r a_{jp}^z a_{kl}^{\Delta f} \\
 &\quad + \beta_{ijklpqrs}^{(8)} a_{rs}^r a_{pq}^{\Delta z} a_{kl}^{\Delta f} \}
 \end{aligned} \tag{6• 21}$$

The determination of the β tensors is straightforward and involves products of the Kronecker delta tensor δ_{ij} . It is explained in Appendix B.

Referring to the results of Appendix B, the stress components can be calculated solely in terms of the anisotropy tensors and the Kronecker delta tensor as:

$$\begin{aligned}
 \sigma_{ij}^o &= \sigma^o \delta_{ij} \\
 \sigma_{ij}^r &= \frac{2\sigma^o}{5} a_{ij}^r \\
 \sigma_{ij}^z &= \frac{2\sigma^o}{5} \{ a_{ij}^z + \frac{3}{2} a_{ij}^{\Delta z} \} \\
 \sigma_{ij}^f &= \frac{2\sigma^o}{5} \{ a_{ij}^f + \frac{3}{2} a_{ij}^{\Delta f} \} \\
 \sigma_{ij}^{rz} &= \frac{2\sigma^o}{35} \{ 7 a_{ik}^r a_{jk}^z + 2 a_{ik}^r a_{jk}^{\Delta z} + 2 a_{ik}^{\Delta z} a_{jk}^r + a_{kl}^r a_{kl}^{\Delta z} \delta_{ij} \} \\
 \sigma_{ij}^{rf} &= \frac{2\sigma^o}{35} \{ 7 a_{jk}^r a_{ik}^f + 2 a_{jk}^r a_{ik}^{\Delta f} + 2 a_{jk}^{\Delta f} a_{ik}^r + a_{kl}^r a_{kl}^{\Delta f} \delta_{ij} \} \\
 \sigma_{ij}^{zsf} &= \frac{2\sigma^o}{35} \{ \frac{35}{2} a_{jk}^z a_{ik}^f + 7 a_{jk}^{\Delta z} a_{ik}^f + 7 a_{jk}^z a_{ik}^{\Delta f} \\
 &\quad + 2 a_{ik}^{\Delta z} a_{jk}^{\Delta f} + 2 a_{ik}^{\Delta f} a_{jk}^{\Delta z} + a_{kl}^{\Delta z} a_{kl}^{\Delta f} \delta_{ij} \}
 \end{aligned} \tag{6• 22}$$

The component σ_{ij}^{zsf} of the stress tensor involves third-order products of small quanti-

ties. It is usually negligibly small and is omitted from the above system of stress contributions.

6.4.1 Verification of the S-F-F Relationship

The validity of the S-F-F relationship can be verified using the results of numerical simulations with assemblies of ellipsoids. A direct verification involves the comparison of measured and calculated principal components of the stress tensor (from S-F-F). An indirect verification is by comparison of the measured and predicted shear stress ratios.

The shear capacity is usually measured by the peak of the shear stress ratio. This macroscopic parameter is defined by the ratio of the shear stress to the normal stress, *i.e.*,

$$a_{\sigma} = \frac{\sigma_t}{\sigma_n} = \frac{\sqrt{\lambda \sigma'_{ij} \sigma'_{ij}}}{\sigma_{kk}/3} \quad (6 \cdot 23)$$

where λ is some constant which depends on the definition of the shear stress. Here $\lambda = 3/2$ is chosen to match the commonly used definition of the shear stress as $\sigma_t = \sigma_1 - \sigma_3$ (in the case of axisymmetric triaxial tests, $\sigma_2 = \sigma_3$).

Both verifications are shown in Figure 6•3 to Figure 6•6.

A close agreement is observed between the measured and calculated principal stresses in general. At large strains, however, the agreement seems to slightly deteriorate, most remarkably for the minor and intermediate stresses. This is probably due to the increasingly important part contributed by the fourth-order anisotropy tensors in average tangential contact force and branch vector distributions at large strains.

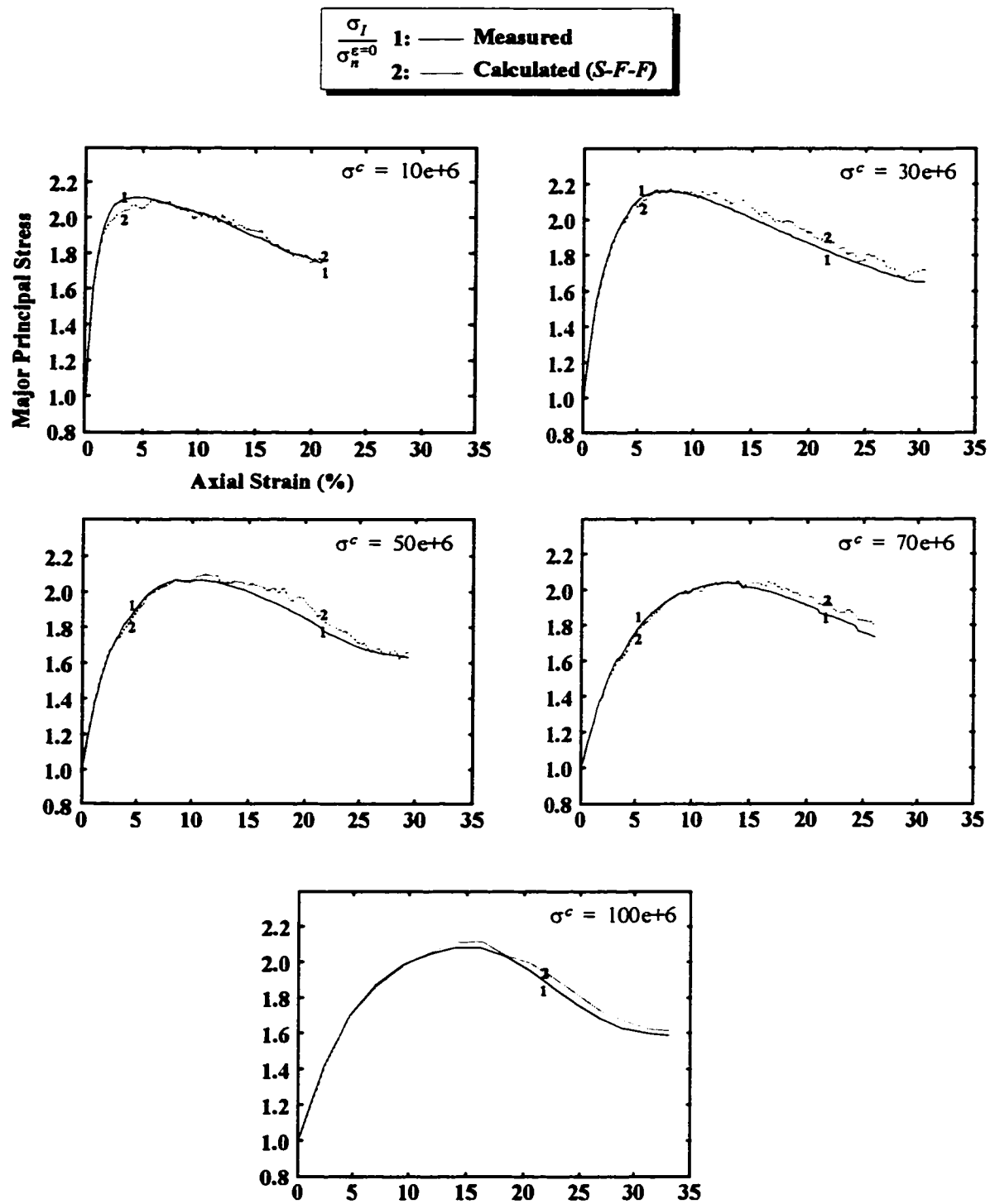


Figure 6-3 Verification of the S-F-F relationship (major principal stress)

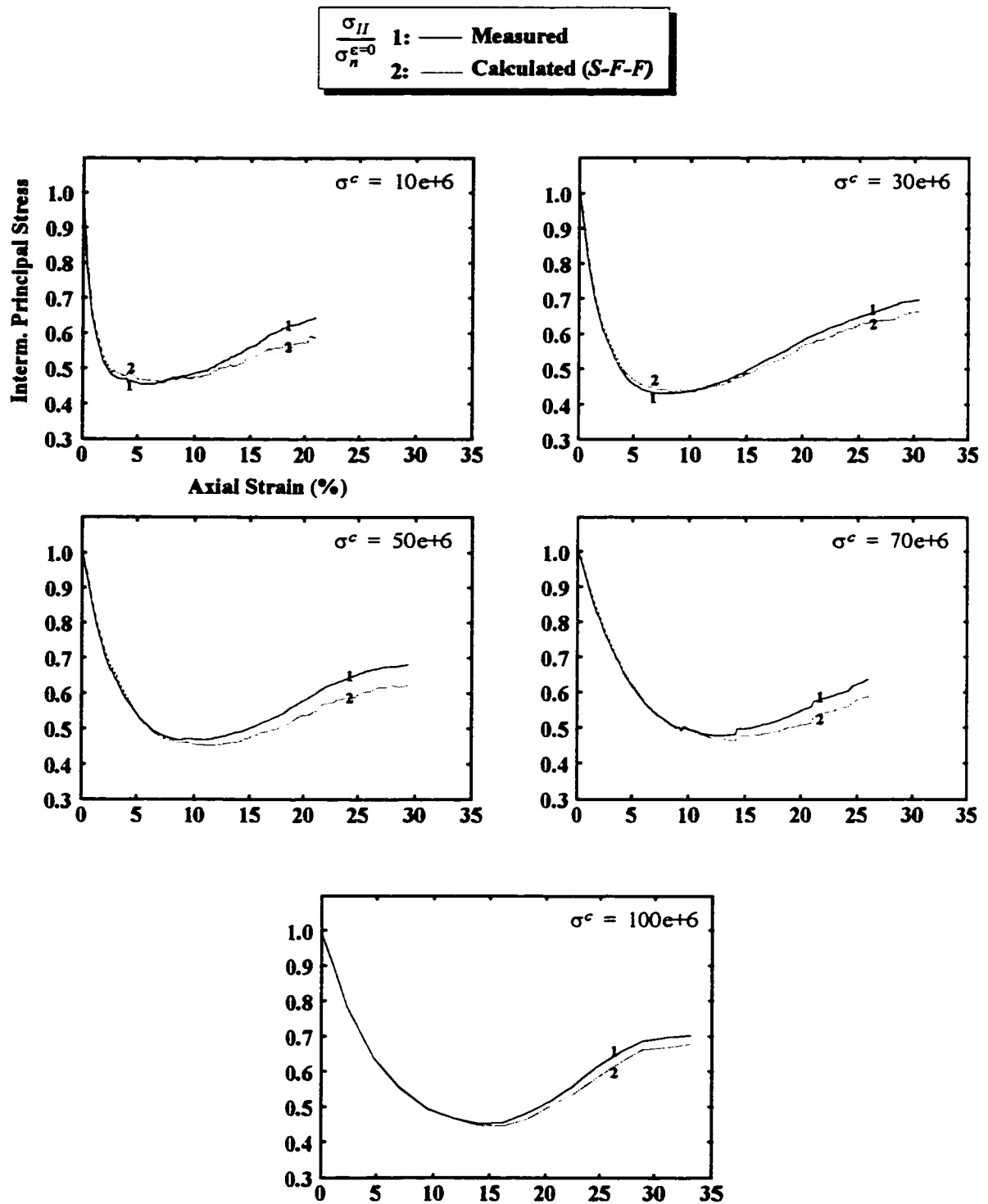


Figure 6-4 Verification of the S-F-F relationship (intermediate principal stress)

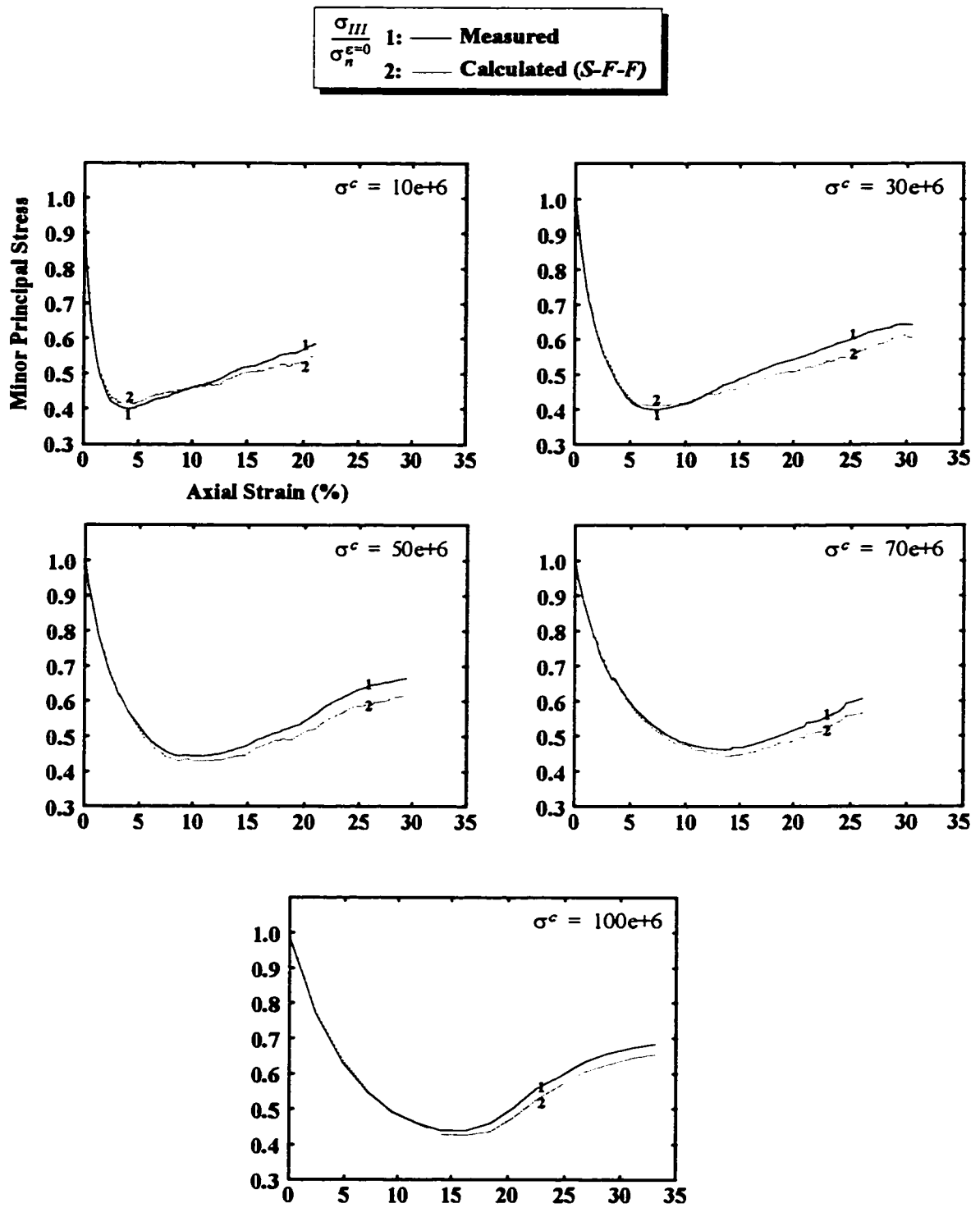


Figure 6-5 Verification of the S-F-F relationship (minor principal stress)

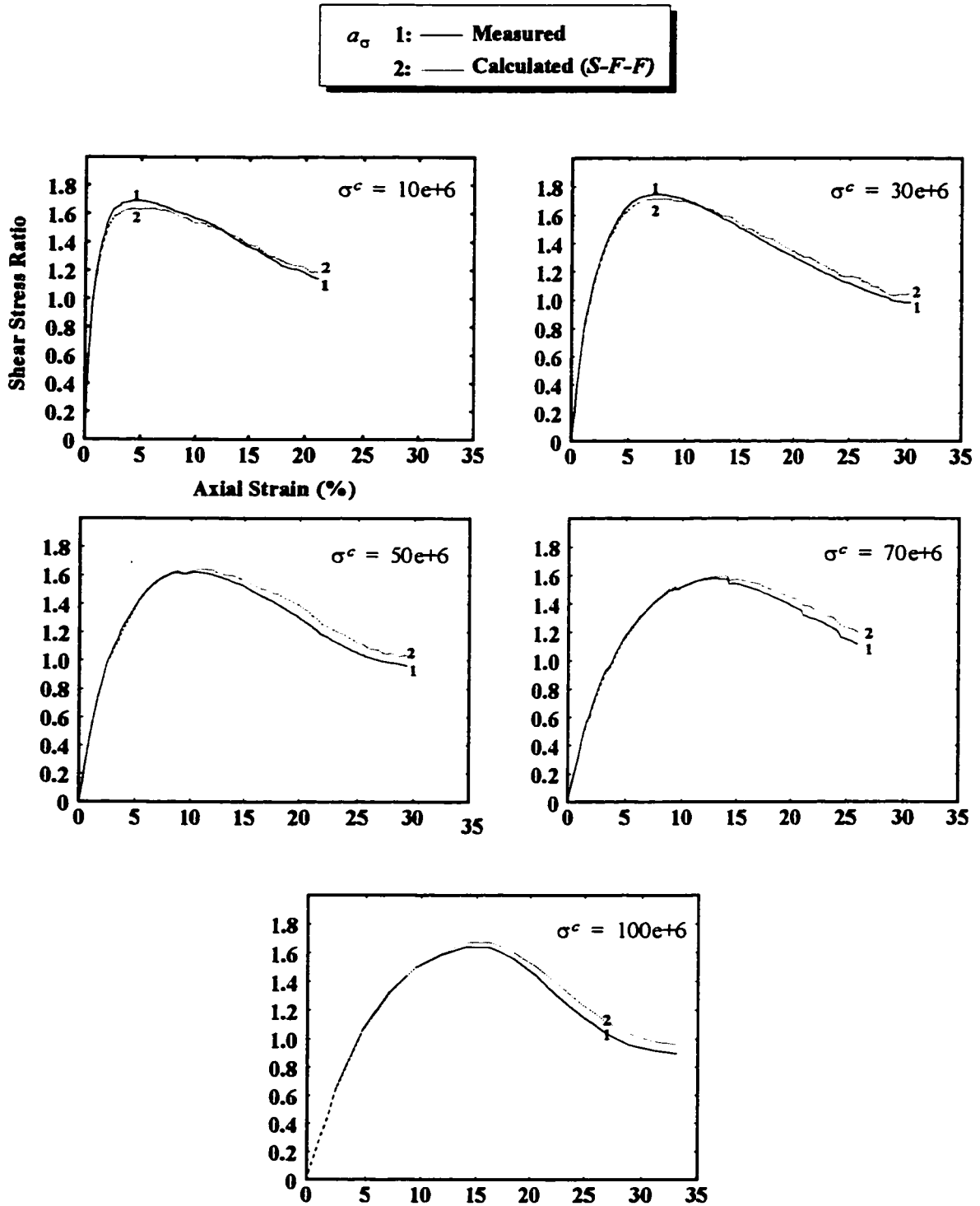


Figure 6-6 Verification of the S-F-F relationship (shear stress ratio)

These have not been included in the derivation of the S-F-F relationship. An equally good agreement is observed between the measured and calculated shear stress ratios.

The results of simulation tests with ellipsoids can only validate the derived tensorial S-F-F relationship in the particular case of the axisymmetric triaxial test. However, a fairly close S-F-F relationship was derived for spheres and has been validated in a more general system of applied stresses, that is, the true triaxial test (Chantawarangul, 1993).

It should be mentioned also that the presence of different levels of initial anisotropy within the assemblies of ellipsoids before deviatoric loading shows that the validity of the derived S-F-F relationship is not restricted to a particular state of initial anisotropy.

6.4.2 Analysis of Microscopic Contributions to the Average Stress Tensor

Now that the S-F-F relationship is validated, it is possible to proceed with analyzing the contributions to the stress tensor based on the decomposition of (6• 22).

Similarly to the S-F-F relationship verification, the analysis of the microscopic contributions can be performed by reference to the individual components of the stress tensor or by reference to the shear stress ratio. The first option is immediately available because of the tensorial form of the S-F-F relationship. The second option, however, requires that a direct relationship between the shear stress ratio and microscopic anisotropies be available. The derivation of such a relationship necessitates that some assumptions be made and therefore will be delayed for later.

The evolution of the normalized average stress components, $\sigma_{xx}/\sigma_n^{\epsilon=0}$, $\sigma_{yy}/\sigma_n^{\epsilon=0}$, and $\sigma_{zz}/\sigma_n^{\epsilon=0}$, and the normalized mean stress, $\sigma_n/\sigma_n^{\epsilon=0}$, with varying axial strain are shown in

Figure 6•7 through Figure 6•10, respectively, for a single confining pressure ($\sigma^c = 10e+6$). The normalized seven microscopic contributions making up the macroscopic stress tensor, *i.e.*, $\sigma_{ij} \equiv \sigma_{ij}^p + \sigma_{ij}^r + \sigma_{ij}^z + \sigma_{ij}^f + \sigma_{ij}^{rz} + \sigma_{ij}^{rf} + \sigma_{ij}^{zf}$, are superposed on the same plots. From these plots, the following observations can be made:

- i. Figure 6•7 to Figure 6•9 show that the contributions made by individual and combined microscopic anisotropies to the average stress tensor are quite different. The anisotropy in force magnitudes and the anisotropy in contact normal orientations (curves 4 and 2, respectively) prevail over other forms of anisotropy in shaping the stress behaviour during shear deformation of assemblies of ellipsoids. The contribution made by the anisotropy in branch vectors (curves 3) is small but increases in absolute value with deformations; for the major part of the test it contributes negatively to the stress tensor. The combined effects of individual anisotropies are consistent with individual contributions. Indeed, the stress contribution σ_{ij}^{rf} (curves 6) associated with the two largest individual contributors to the stress tensor (σ_{ij}^r and σ_{ij}^f) dominates the stress contributions σ_{ij}^{rz} and σ_{ij}^{zf} associated with smaller individual contributors (curves 5 and 6, respectively).
- ii. From the comparison of Figure 6•8 and Figure 6•9, it is observed that all components of the decomposition are axisymmetric tensors. They are also co-axial with the average stress tensor.

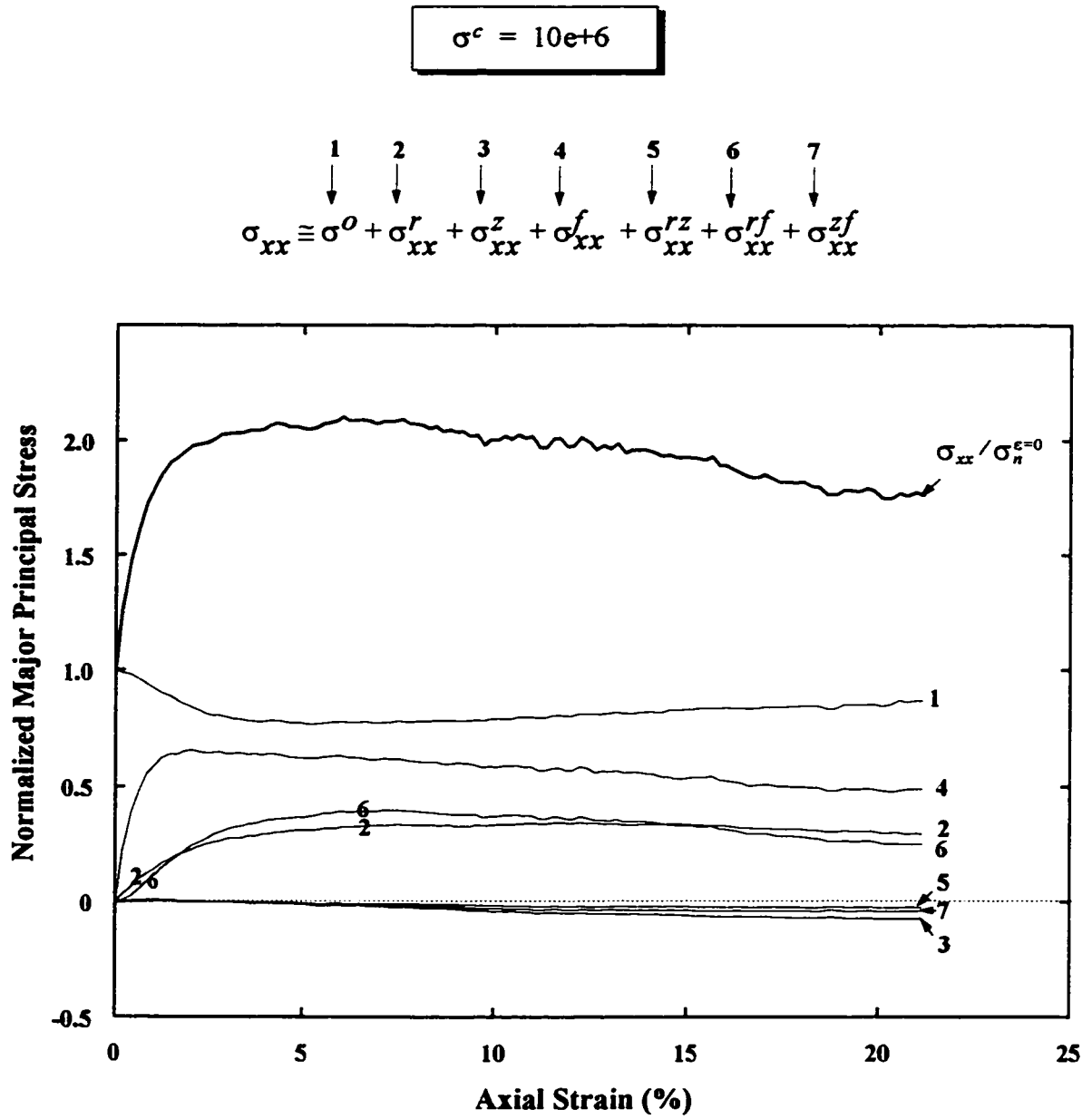


Figure 6-7 Major principal stress decomposition

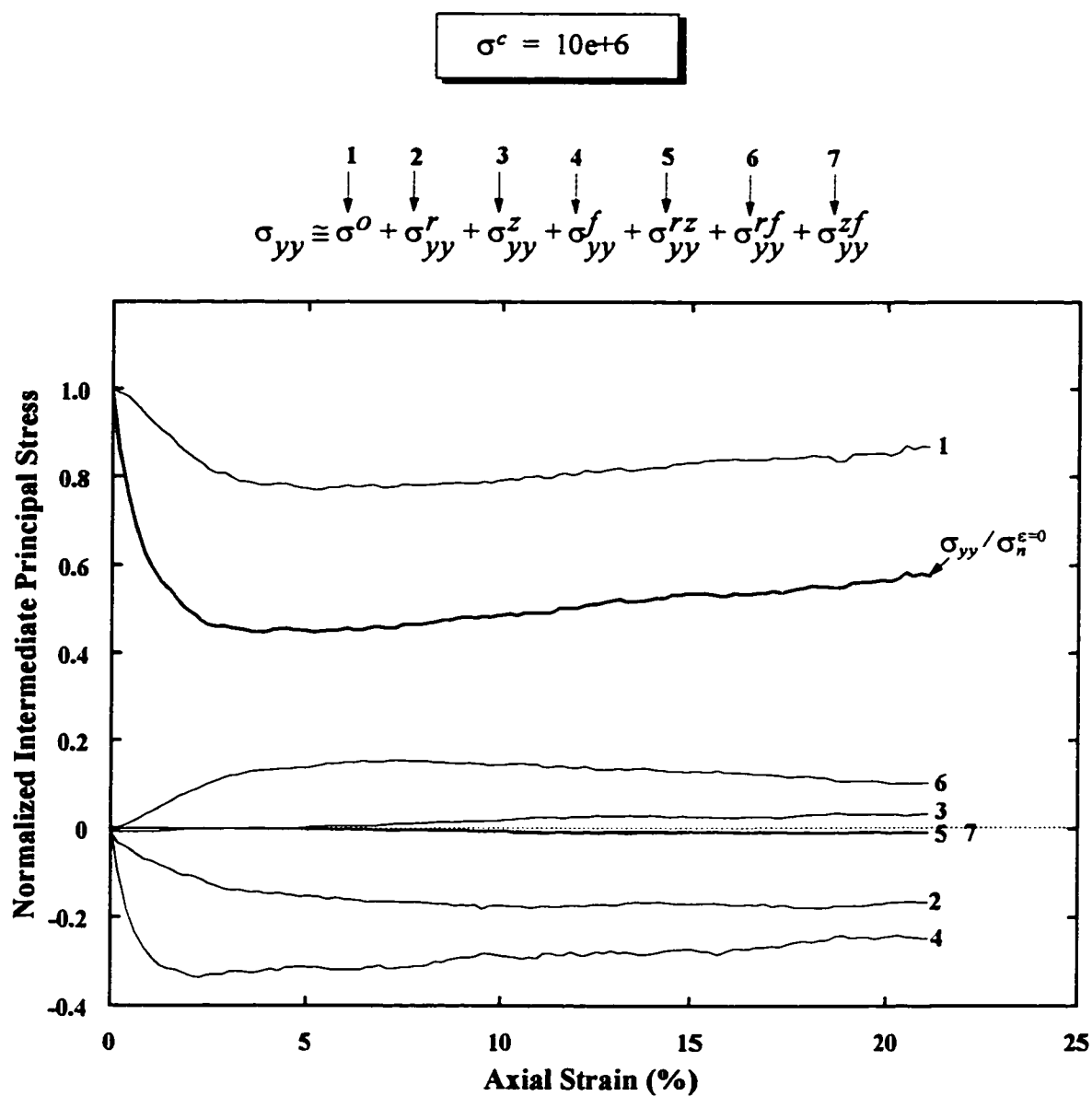


Figure 6-8 Intermediate principal stress decomposition

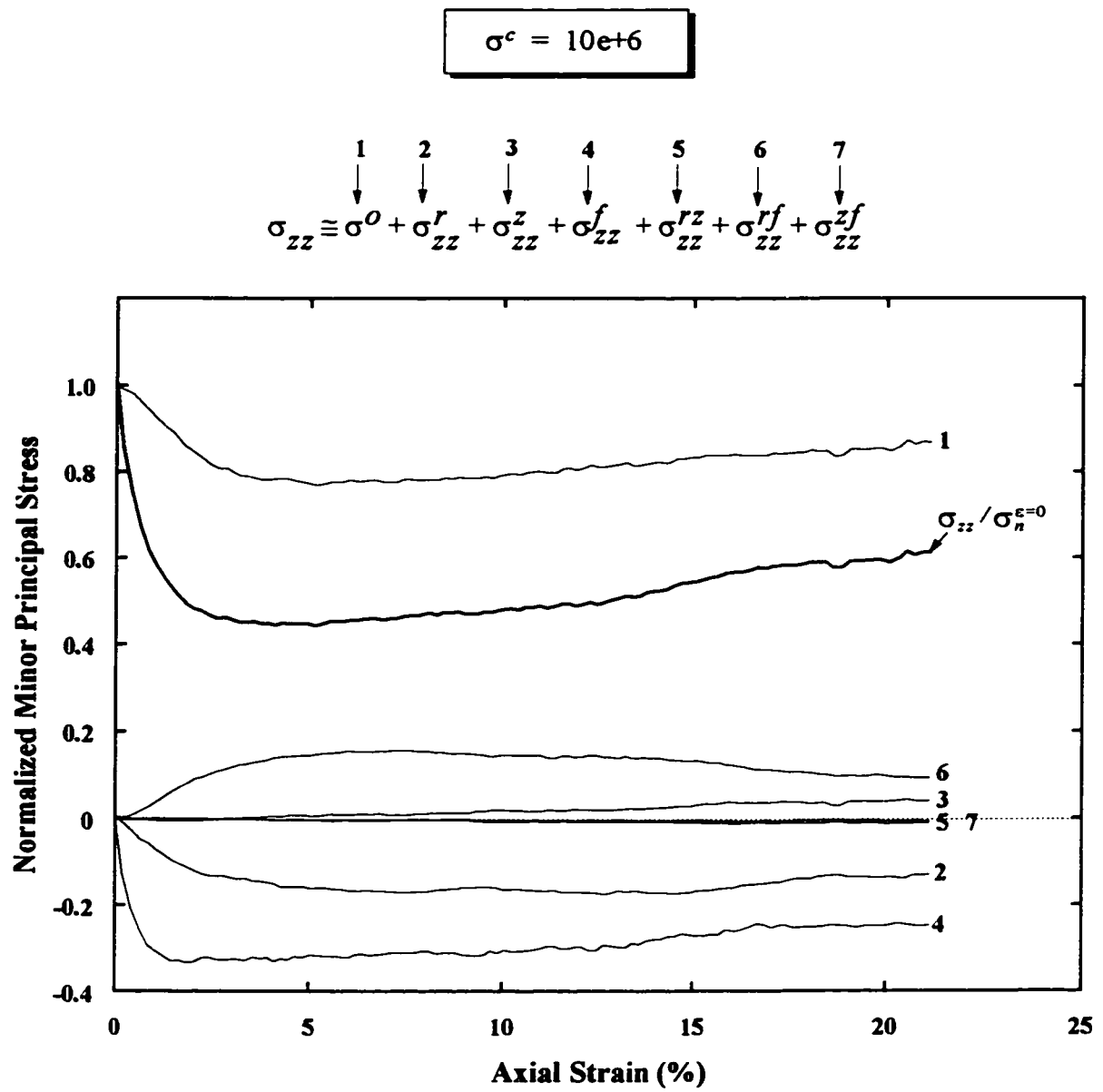


Figure 6-9 Minor principal stress decomposition

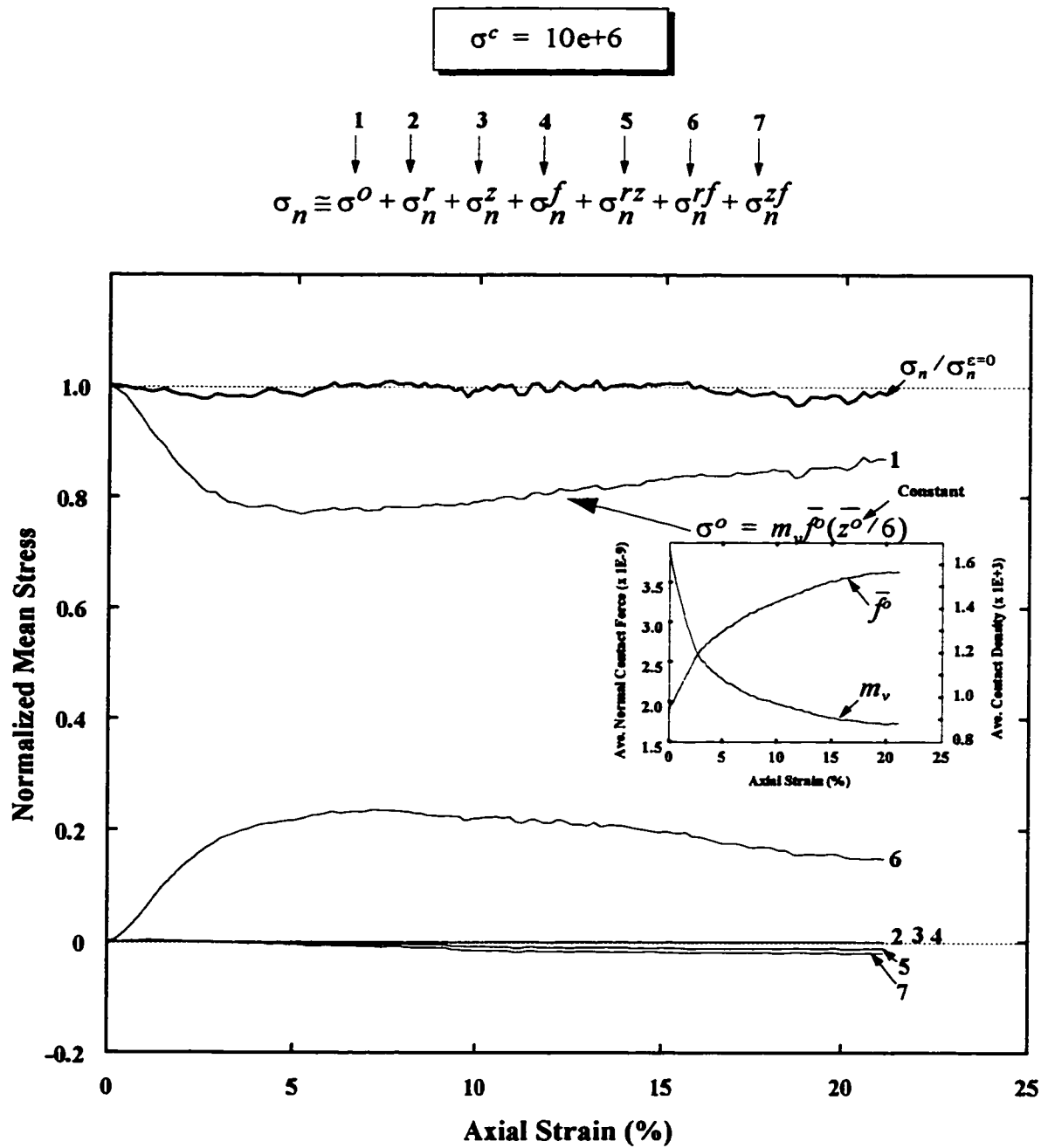


Figure 6-10 Mean stress decomposition

- iii. From the evolution of the normalized mean stress in Figure 6•10, it is observed as expected that the microscopic tensors σ_{ij}^r , σ_{ij}^z , and σ_{ij}^f (representing individual anisotropies) are deviatoric (curves 2, 3, and 4, respectively). On the other hand, the tensors σ_{ij}^s , σ_{ij}^f , and σ_{ij}^f are not deviatoric (curves 5, 6, and 7, respectively). In fact, the tensor σ_{ij}^f (curves 6), which has the second largest mean stress, is responsible for keeping the overall mean stress constant by opposing the decline of the spherical tensor σ_{ij}^s . This is clearly observable from the trends of curves 1 and 6 (Figure 6•10).
- iv. It is seen that the spherical tensor $\sigma^o = m_v \bar{f}^o \bar{z}^o / 6$ decreases to a minimum value then increases at very low rate, while the mean pressure associated with σ_{ij}^f simply behaves in the opposite sense. The decline in the spherical tensor results from the continuous rise in average normal contact force magnitude \bar{f}^o and decline in the average contact density m_v , while the average branch length \bar{z}^o is staying almost constant.

6.4.3 Specific Effects Related to Particle Shape

The development of anisotropy in branch vector lengths is the direct manifestation of the effect of particle shape. Particle shape is also indirectly responsible of anisotropy development in contact normal orientations and average contact forces.

This form of anisotropy was seen to grow with shear deformation (curves 3 in the above plots).

Another plot that helps visualize the direct effect of particle shape on the macro-re-

sponse is generated by comparing the average stress tensor (calculated using the stress-force-fabric relationship) in the genuine case to the case where the branch vector length anisotropy tensor is eliminated from the S-F-F relationship.

The results are shown in Figure 6•11 where the principal components of stress and the sine of the angle of internal friction (according to a Mohr-Coulomb failure criterion) are plotted with varying applied axial strain (for a single confining stress).

As can be seen, the effect of shape is more significant at large strains. The assembly's geometry is more open to changes at large strains and particles can move with greater freedom in lateral directions. Inter-particle rotations are also more developed and this creates larger deviation angles between branch vectors and contact normals for contacts in the lateral direction, by comparison with those in the direction of maximum load. Since a larger deviation angle means a shorter branch length, the bias in angles of deviations is manifested in a bias in average branch lengths, and this explains the observed development of this form of anisotropy.

6.5 Microscopic Anisotropy and its Relation to Shear Strength

From an engineering point of view, the analysis of microscopic contributions to the shear capacity is more valuable than individual stresses. For this reason much emphasis has been put on deriving a relationship between material strength and microscopic anisotropies by researchers in the area of micromechanics of soil (*e.g.*, Oda, 1972; Rothenburg and Dusseault, 1987; Rothenburg and Bathurst, 1989; amongst others).

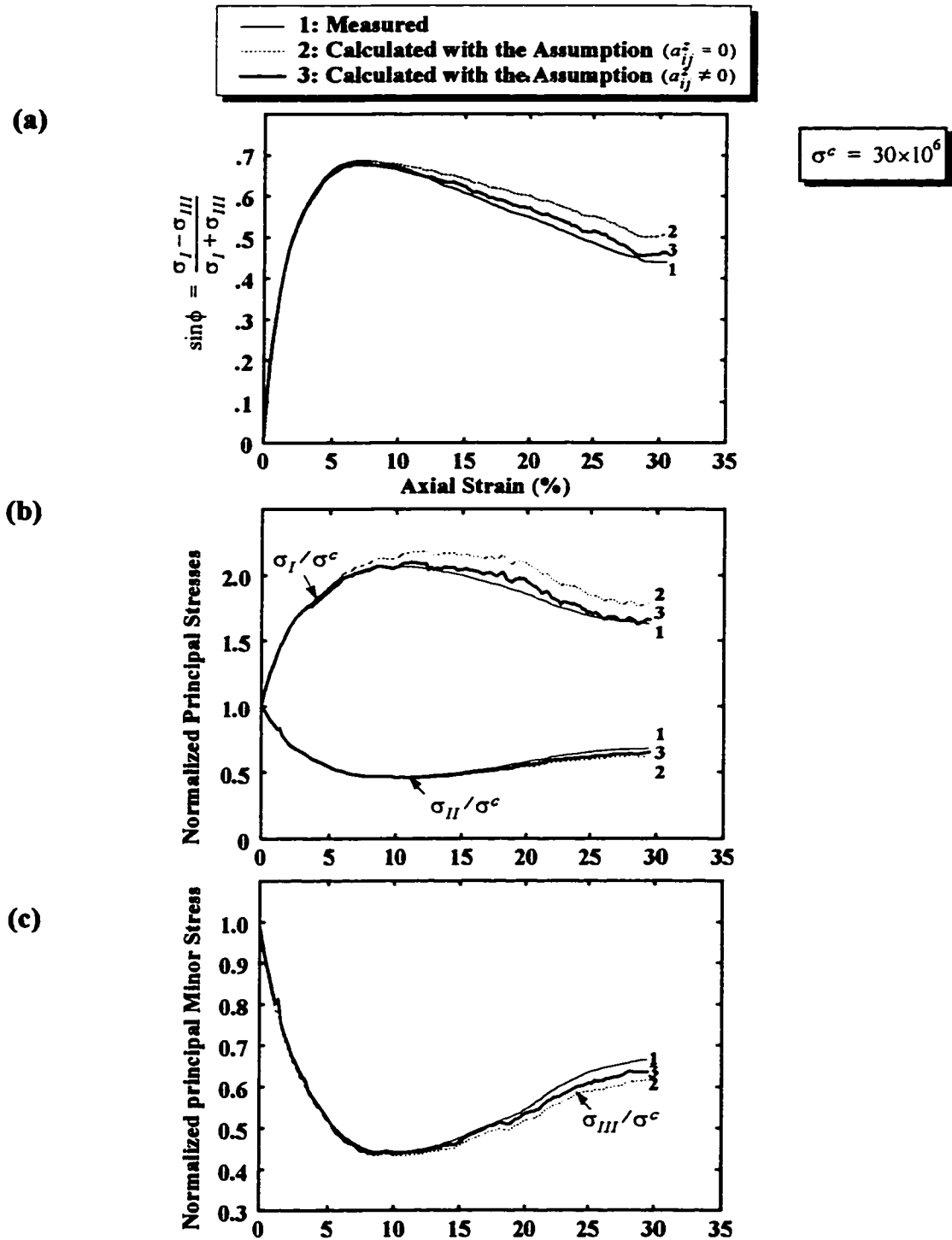


Figure 6-11 Direct effect of particle shape on the S-F-F relationship

The complexity of such a relationship increases with the complexity of the applied stress path and more importantly with the dimensionality of the problem.

The derivation proposed here makes use of a very simple stress path, the axisymmetric triaxial stress regime. The absence of stress rotations simplifies the intricacies of having to work with changing principal stress spaces and enables an exact analytical derivation of the shear stress ratio-anisotropy relationship for ellipsoids.

6.5.1 Shear Stress Ratio Equation

The “Shear Stress Ratio-Anisotropy” relationship is obtained by substituting into the definition of the shear stress ratio the expressions of the shear and normal stresses derived from the S-F-F relationship.

The calculation of the shear stress $\sqrt{\lambda \sigma'_{ij} \sigma'_{ij}}$ is particularly challenging: (1) It involves the calculation of the stress tensor deviator σ'_{ij} ; (2) It involves the product of each deviator stress component by itself. A stress component consists of the sum of 13 separate terms as can be seen from (6• 22). A full decomposition of the product $\sigma'_{ij} \sigma'_{ij}$ will result in 169 terms of which the square root must be taken. As such, the relationship obtained will be complex in its formulation and of little interest.

Useful information regarding the part of contribution of the different individual anisotropies to the material shear strength requires a simplification of the equation, using appropriate assumptions which can be verified numerically.

6.5.1.1 Normal Stress

The calculation of the normal stress from (6• 22) is straightforward and the result is:

$$\sigma_n = \sigma^o \left\{ 1 + \frac{2}{15} (a_{ij}^r a_{ij}^v + a_{ij}^r a_{ij}^n + a_{ij}^v a_{ij}^n + 1.5 a_{ij}^s a_{ij}^t) \right\} \quad (6 \bullet 24)$$

6.5.1.2 Shear Stress

The stress tensor deviator components must be calculated prior to calculating the shear stress. They are expressed in a simple form as:

$$\begin{aligned} \sigma'_{ij} = & \frac{2\sigma^o}{5} [a_{ij}^r + a_{ij}^v + \frac{3}{2}a_{ij}^s + a_{ij}^n + \frac{3}{2}a_{ij}^t] \\ & + \frac{2\sigma^o}{35} [7a_{ij}^{\{r\tau\}} + 4a_{ij}^{\{r\Delta z\}}] \\ & + \frac{2\sigma^o}{35} [7a_{ij}^{\{tr\}} + 4a_{ij}^{\{r(\Delta n)\}}] \\ & + \frac{2\sigma^o}{35} [\frac{35}{2}a_{ij}^{\{t\tau\}} + 7a_{ij}^{\{t(\Delta z)\}} + 7a_{ij}^{\{(\Delta n)\tau\}} + 4a_{ij}^{\{(\Delta z)(\Delta n)\}}] \end{aligned} \quad (6 \bullet 25)$$

where the following notations were used:

- $a_{ij}^{\{x\}}$ denote the symmetric part of a tensor, i.e., $a_{ij}^{\{x\}} = \frac{1}{2}(a_{ij}^x + a_{ji}^x)$.
- $a_{ij}^{\{x\}}$ is the deviatoric part of a tensor: $a_{ij}^{\{x\}} = a_{ij}^x - \frac{a_{kk}^x}{3}\delta_{ij}$.
- a_{ij}^{xy} is a tensor product as: $a_{ij}^{xy} = a_{ik}^x a_{kj}^y$.

Under the assumption of coaxiality of the tensorial parameters in the right hand side of (6• 25), the following observations are essential to simplify the shear stress expression.

“Cauchy-Shwartz” Type of Identity Between Proportional Second-Order Tensors

If two tensors a_{ij}^x and a_{ij}^y are proportional then,

$$|a_{ij}^x a_{ij}^y| = \sqrt{a_{ij}^x a_{ij}^x} \sqrt{a_{ij}^y a_{ij}^y} \quad (6 \bullet 26)$$

Or:

$$a_{ij}^x a_{ij}^y = s_x^y \sqrt{a_{ij}^x a_{ij}^x} \sqrt{a_{ij}^y a_{ij}^y} \quad (6 \bullet 27)$$

where s_x^y denotes the sign taken by the left hand sign of the equation, *i.e.*,

$$s_x^y = \text{sgn}(a_{ij}^x a_{ij}^y) \quad (6\bullet 28)$$

The provision for a parameter to fix the sign is necessary because of the nature of the tensors encountered in simulations. The proportionality can be direct or inverse depending on the sense of co-axiality of two tensors relative to each other.

Square of the Sum of Proportional Tensors

Equation (6• 27) implies the following result which is relevant to the shear stress calculation: the square of the sum of two proportional tensors (a scalar quantity) is equal to the square of the sum of their respective moduli affected by appropriate signs. *i.e.*,

$$(a_{ij}^x + a_{ij}^y)(a_{ij}^x + a_{ij}^y) = (\sqrt{a_{ij}^x a_{ij}^x} + s_x^y \sqrt{a_{ij}^y a_{ij}^y})^2 \quad (6\bullet 29)$$

Therefore:

$$\sqrt{(a_{ij}^x + a_{ij}^y)(a_{ij}^x + a_{ij}^y)} = |\sqrt{a_{ij}^x a_{ij}^x} + s_x^y \sqrt{a_{ij}^y a_{ij}^y}| \quad (6\bullet 30)$$

The relationship (6• 30) can be extended to the sum of three proportional tensors as:

$$\sqrt{(a_{ij}^x + a_{ij}^y + a_{ij}^z)^2} = |\sqrt{a_{ij}^x a_{ij}^x} + s_x^y \sqrt{a_{ij}^y a_{ij}^y} + s_x^z \sqrt{a_{ij}^z a_{ij}^z}| \quad (6\bullet 31)$$

And, to the sum of any number N of proportional tensors $(a_{ij}^x, a_{ij}^y, \dots, a_{ij}^N)$ as:

$$\sqrt{(a_{ij}^x + a_{ij}^y + \dots + a_{ij}^N)^2} = |\sqrt{a_{ij}^x a_{ij}^x} + s_{x_1}^{x_2} \sqrt{a_{ij}^{x_2} a_{ij}^{x_2}} + \dots + s_{x_1}^{x_N} \sqrt{a_{ij}^{x_N} a_{ij}^{x_N}}| \quad (6\bullet 32)$$

By denoting the modulus of an arbitrary second-order tensor a_{ij}^x by $\alpha^x = \sqrt{a_{ij}^x a_{ij}^x}$, equation (6• 32) can be re-written as:

$$\sqrt{(a_{ij}^x + a_{ij}^y + \dots + a_{ij}^N)^2} = |\alpha^{x_1} + s_{x_1}^{x_2} \alpha^{x_2} + \dots + s_{x_1}^{x_N} \alpha^{x_N}| \quad (6\bullet 33)$$

If the 13 tensors involved in the expression of the deviatoric stress tensor in (6• 25)

are proportional, then the relationship (6• 33) can be applied to calculate the shear stress as:

$$\begin{aligned}\sigma_i = \sqrt{\lambda \sigma'_{ij} \sigma'_{ij}} = \sqrt{\lambda} \sigma^o \{ & \frac{2}{5} (a^r + s_r^v a^v + 1.5 s_r^z a^z + s_r^n a^n + 1.5 s_r^t a^t) \\ & + \frac{2}{35} (7 s_r^{(\tau)} a^{(\tau)} + 4 s_r^{[r(\Delta z)]} a^{[r(\Delta z)]}) \\ & + \frac{2}{35} (7 s_r^{(tr)} a^{(tr)} + 4 s_r^{[r(\Delta f)]} a^{[r(\Delta f)]}) \\ & + \frac{2}{35} (17.5 s_r^{(\tau)} a^{(\tau)} + 7 s_r^{[r(\Delta z)]} a^{[r(\Delta z)]}) \\ & + \frac{2}{35} (7 s_r^{[(\Delta f)\tau]} a^{[(\Delta f)\tau]} + 4 s_r^{[(\Delta z)(\Delta f)]} a^{[(\Delta z)(\Delta f)]}) \} \end{aligned} \quad (6• 34)$$

Again, the symbols (' , []) in the above equation are used to indicate a deviatoric and a symmetric part of a tensor, respectively.

For instance, $a^{[r(\Delta z)]}$ stands for the modulus of the deviatoric part of the symmetric part of a tensor obtained as the product of a_{ij}^r and $a_{ij}^{\Delta z}$. Therefore, $a^{[r(\Delta z)]}$ is a concise notation bearing the necessary information to retrieve the variable it corresponds to. For example, $a^{[r(\Delta z)]}$ can be retrieved as:

$$a^{[r(\Delta z)]} = \sqrt{a_{ij}^{[r(\Delta z)]} a_{ij}^{[r(\Delta z)]}} \quad (6• 35)$$

where:

$$a_{ij}^{[r(\Delta z)]} = \frac{1}{2} (a_{ik}^r a_{kj}^{\Delta z} + a_{ik}^{\Delta z} a_{kj}^r) - \frac{a_{kl}^r a_{kl}^{\Delta z}}{3} \delta_{ij} \quad (6• 36)$$

The sign affixed to $a^{[r(\Delta z)]}$, i.e., $s_r^{[r(\Delta z)]}$, is also written in a way that indicates its meaning. According to the general definition in (6• 28):

$$s_r^{[r(\Delta z)]} = \text{sgn}(a_{ij}^r a_{ij}^{[r(\Delta z)]}) \quad (6• 37)$$

Note that all the signs are calculated with reference to the fabric anisotropy tensor a_{ij}^r (first term in the S-F-F relationship). However, any other basic anisotropy tensor could as

well be the reference tensor, and the signs would change accordingly.

Proof of the Proportionality of Tensorial Quantities in the Shear Stress Equation

So far, it has been established that if the assumption of proportionality of the tensors forming the right hand side of the stress tensor deviator equation in (6• 25) is valid, then the “Shear Stress-Anisotropy” equation in (6• 34) applies and could be used to formulate the shear stress ratio in terms of anisotropies. The legitimacy of such an assumption is certainly restricted to particular conditions of anisotropy development. In the next and following sections a proof is given that the assumption is legitimate if the five basic anisotropy tensors a_{ij}^r , a_{ij}^n , a_{ij}^t , a_{ij}^v , and a_{ij}^s , are all axisymmetric and co-axial. These conditions are fulfilled under special stress loading paths, such as the constant mean pressure axisymmetric triaxial tests performed with assemblies of ellipsoids. The results of numerical simulations will be used to verify numerically the validity of axisymmetry and co-axiality.

Before proceeding with the verification of the assumption of axisymmetry and coaxiality, a basic issue is to prove that coaxiality and axisymmetry lead to proportionality of all the 13 tensor components in the right hand side of (6• 25). If each pair of tensors is to be checked, the number of checks will be relatively large ($13 \cdot (13-1)/2$). Instead, the proportionality will be established with reference to a constant deviatoric axisymmetric tensor.

The 13 terms in the right hand side of equation (6• 25) consist of deviatoric tensors of two types:

1. Basic anisotropy tensors, a_{ij}^r , a_{ij}^n , a_{ij}^t , a_{ij}^v and a_{ij}^z (assumed to be axisymmetric and coaxial)
2. Products of the form $a_{ij}^{(xy)}$ or $a_{ij}^{(xy)I}$, where the tensors a_{ij}^x and a_{ij}^y are either basic anisotropy tensors or any of the additional tensors $a_{ij}^{\Delta x}$ or $a_{ij}^{\Delta f}$ obtained by difference of basic tensors.

Basic Anisotropy Tensors

Any second-order basic anisotropy tensor can be written in its principal directions as:

$$[a_{ij}^x] = \begin{bmatrix} a_I^x & 0 & 0 \\ 0 & a_{II}^x & 0 \\ 0 & 0 & a_{III}^x \end{bmatrix} \quad (6 \bullet 38)$$

The tensor is axisymmetric, therefore $a_{II}^x = a_{III}^x$ (assuming the axial symmetry around the first direction which is the direction of loading). It is also deviatoric, therefore:

$$a_{ij}^x = a_I^x \eta_{ij} \quad (6 \bullet 39)$$

where:

$$[\eta_{ij}] = \begin{bmatrix} 1 & 0 & 0 \\ 0 & -1/2 & 0 \\ 0 & 0 & -1/2 \end{bmatrix} \quad (6 \bullet 40)$$

According to (6• 39), all the basic anisotropy tensors are proportional to the reference constant axisymmetric and deviatoric tensor η_{ij} . As a consequence, the two tensors $a_{ij}^{\Delta x}$ and $a_{ij}^{\Delta f}$ are also proportional to η_{ij} .

Products of Basic Anisotropy Tensors

To examine the case of tensor products of type $a_{ij}^{(xy)}$, the tensors a_{ij}^x and a_{ij}^y are re-

ferred to their common principal axes. Therefore, according to (6• 39):

$$\alpha_{ij}^{xy} = \alpha_{ik}^x \alpha_{kj}^y = \alpha_i^x \alpha_j^y \eta_{ik} \eta_{kj} \quad (6• 41)$$

Thus:

$$\alpha_{ij}^{(xy)} = \alpha_i^x \alpha_j^y (\eta_{ik} \eta_{kj})' \quad (6• 42)$$

The calculation of the deviatoric part of the square tensor (matrix) $(\eta_{ik} \eta_{kj})'$ from the definition of η_{ij} in (6• 40) shows that:

$$(\eta_{ik} \eta_{kj})' = \eta_{ij} / 2 \quad (6• 43)$$

Therefore:

$$\alpha_{ij}^{(xy)} = \alpha_i^x \alpha_j^y (\eta_{ij} / 2) \quad (6• 44)$$

Any tensor of the form $\alpha_{ij}^{(xy)}$ is proportional to η_{ij} .

Similarly, the proportionality of tensors of the form $\alpha_{ij}^{(xy)}$ and η_{ij} can be established.

Verification of Axisymmetry and Coaxiality For Basic Tensors

The plots in Figure 6•12 display the principal components of the five basic anisotropy tensors for a single confining pressure (similar plots are obtained for other confining pressures). The axisymmetry is implied in these plots where the intermediate and minor principal coefficients evolve almost identically.

The axisymmetry of these tensors was also implied before by plots of the components of the stress tensor decomposition in Figure 6•7 through Figure 6•10.

The Shear Stress Ratio Equation

In order to obtain a consistent “Shear Stress Ratio-Anisotropy” equation with the assumption of proportionality of basic anisotropy tensors, the expression of the normal stress equation in (6• 24) should be re-written using this assumption. The result is:

$$D_{\sigma} = \sigma_n / \sigma^o = 1 + \frac{2}{15}(s_r^v a^r a^v + s_r^n a^r a^n + s_v^n a^v a^n + 1.5 s_t^t a^t a^t) \quad (6• 46)$$

where signs are determined according to the general equation (6• 27).

Finally, the ratio of the shear stress in (6• 34) to the normal stress in (6• 45) provides the definitive form of the “Shear Stress Ratio-Anisotropy” equation as:

$$\begin{aligned} a_{\sigma} = \sqrt{\lambda} \{ & \frac{2}{5}(a^r + s_r^v a^v + 1.5 s_r^t a^t + s_r^n a^n + 1.5 s_t^t a^t) \\ & + \frac{2}{35} (7 s_r^{(r\tau)} a^{(r\tau)} + 4 s_r^{(r(\Delta z))} a^{(r(\Delta z))}) \\ & + \frac{2}{35} (7 s_r^{(tr)} a^{(tr)} + 4 s_r^{(r(\Delta n))} a^{(r(\Delta n))}) \\ & + \frac{2}{35} (17.5 s_r^{(r\tau)} a^{(r\tau)} + 7 s_r^{(r(\Delta z))} a^{(r(\Delta z))}) \\ & + \frac{2}{35} (7 s_r^{((\Delta n)\tau)} a^{((\Delta n)\tau)} + 4 s_r^{((\Delta z)(\Delta n))} a^{((\Delta z)(\Delta n))}) \} / \\ & \{ 1 + \frac{2}{15}(s_r^v a^r a^v + s_r^n a^r a^n + s_v^n a^v a^n + 1.5 s_t^t a^t a^t) \} \end{aligned} \quad (6• 46)$$

The validity of the above equation can be verified by comparing the values of the shear stress ratio calculated from its basic definition via the component form of the S-F-F relationship to the values computed from the above relationship. The two methods of calculation are summarized in the plots of Figure 6•13, which show that two methods are identical.

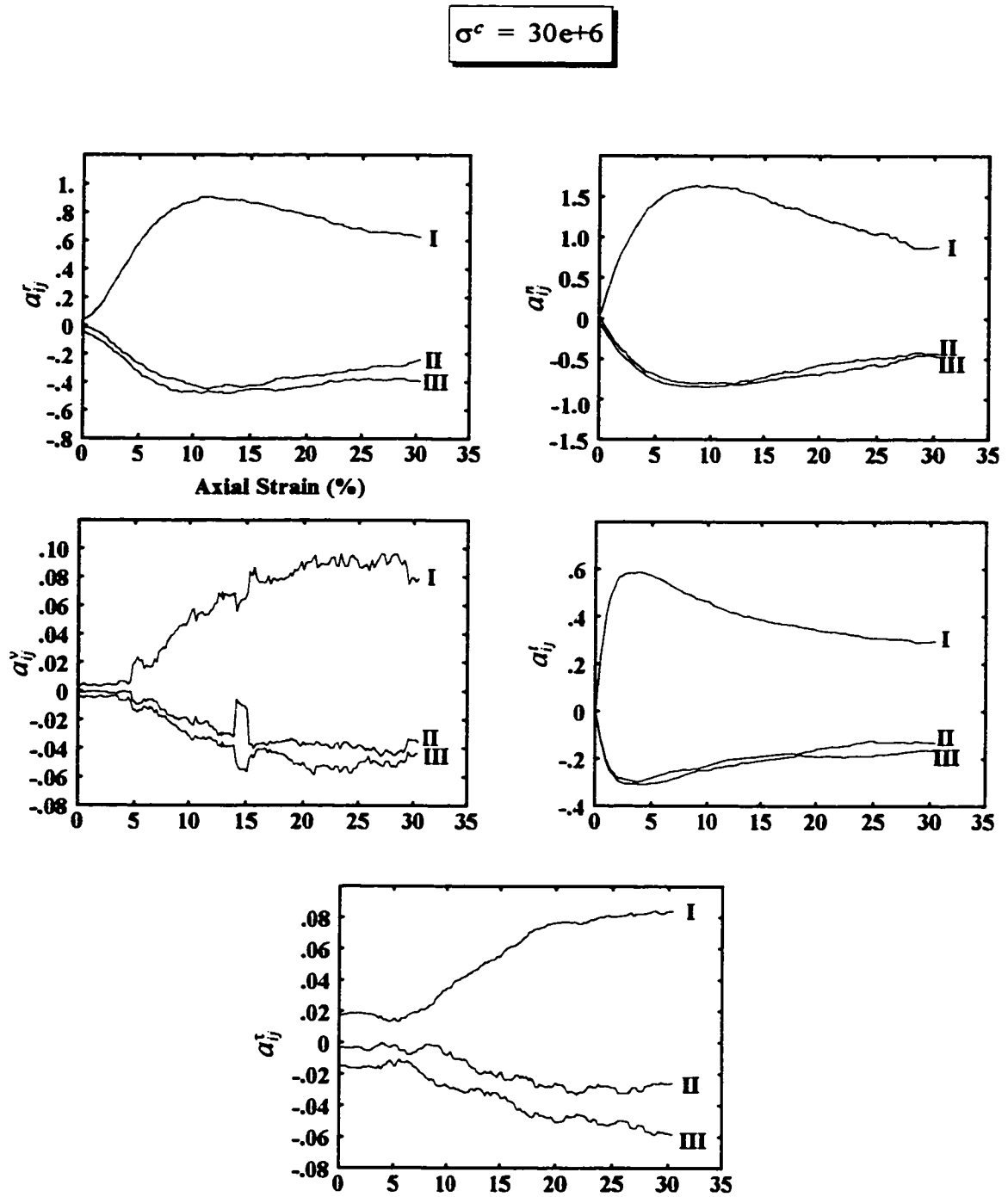


Figure 6-12 Verification of coaxiality and axisymmetry of anisotropy tensors

6.5.2 Anisotropy Contributions to the Material Shear Strength

In the plots of the average stress tensor decomposition, contributions of anisotropy to the stress behaviour has been assessed qualitatively. The concern in this section is to provide a qualitative and a quantitative assessment of anisotropy contributions to the material shear strength of assemblies of ellipsoids.

For more clarity and consistency with the notations used for the decomposition of the average stress tensor, the shear stress equation in (6• 46) is re-written as:

$$a_{\sigma} = a_{\sigma}^o + a_{\sigma}^r + (a_{\sigma}^v + a_{\sigma}^t) + (a_{\sigma}^n + a_{\sigma}^t) + a_{\sigma}^{rz} + a_{\sigma}^{rf} + a_{\sigma}^{zf} \quad (6• 47)$$

where:

$$\begin{aligned} a_{\sigma}^o &= 0 \\ a_{\sigma}^r &= \sqrt{\lambda} (\frac{2}{3} a^r) / D_{\sigma} \\ \begin{cases} a_{\sigma}^v &= \sqrt{\lambda} (\frac{2}{3} s^v a^v) / D_{\sigma} \\ a_{\sigma}^t &= \sqrt{\lambda} [\frac{2}{3} (1.5 s^t a^t)] / D_{\sigma} \end{cases} \\ \begin{cases} a_{\sigma}^n &= \sqrt{\lambda} (\frac{2}{3} s^n a^n) / D_{\sigma} \\ a_{\sigma}^t &= \sqrt{\lambda} [\frac{2}{3} (1.5 s^t a^t)] / D_{\sigma} \end{cases} \\ a_{\sigma}^{rz} &= \sqrt{\lambda} [\frac{2}{35} (7 s_r^{(rz)} a^{(rz)} + 4 s_r^{[(\Delta z)]} a^{[(\Delta z)]})] / D_{\sigma} \\ a_{\sigma}^{rf} &= \sqrt{\lambda} [\frac{2}{35} (7 s_r^{(rf)} a^{(rf)} + 4 s_r^{[(\Delta f)]} a^{[(\Delta f)]})] / D_{\sigma} \\ a_{\sigma}^{zf} &= \sqrt{\lambda} \{ \frac{2}{35} [17.5 s_r^{(zf)} a^{(zf)} + 7 s_r^{[(\Delta z)]} a^{[(\Delta z)]} \\ &\quad + 7 s_r^{[(\Delta f)]} a^{[(\Delta f)]} + 4 s_r^{[(\Delta z)(\Delta f)]} a^{[(\Delta z)(\Delta f)]}] \} / D_{\sigma} \end{aligned} \quad (6• 48)$$

and where $D_{\sigma} = \sigma_n / \sigma^o$ is the normalized normal stress given by (6• 45).

The plots in Figure 6•14 and Figure 6•15 depict the above decomposition for all stages of deformation of the initial sample of 1000 ellipsoids tested at the constant confining pressure $\sigma^c = 10e+6$.

a_{σ} 1: Calculated from the "S-F-F" Relationship (Components Form)
2: Calculated from the "Shear Stress Ratio" Equation

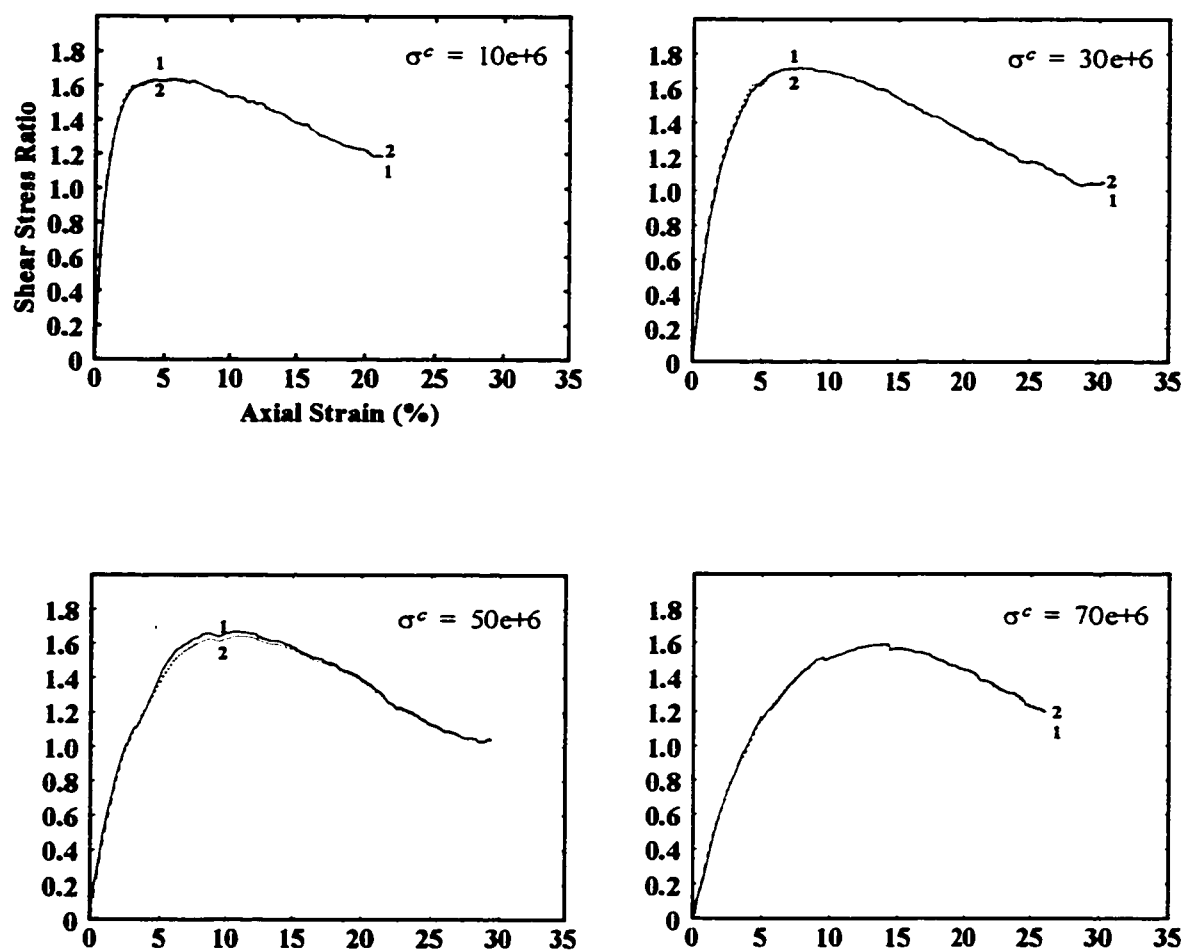


Figure 6-13 Verification of the shear stress ratio equation

A general observation about the trends of the different anisotropy contributions in Figure 6•14 is that they are in agreement with those observed earlier with the components of the average stress decomposition.

A qualitative resemblance exists between α'_g (curve 2), α''_g (curve 4a), α'_g (curve 4b), α''_f (curve 6), and the overall shear stress ratio. They are all characterized by an initial increase (at different slopes) to a maximum value, followed by a decrease to a stable value near steady-state. This decrease is initiated at different axial strains and with different rates for different anisotropies.

Among all shear stress ratio components, α''_g (curve 4a) displays the closest trend to the overall stress ratio, which indicates the dominance of this form of anisotropy over other forms of anisotropy.

The plots of percent contributions to the shear strength in Figure 6•15 show that beginning at an early stage of the test, α''_g dominates the other forms of anisotropy by providing the largest contribution to the sample's shear resistance (curve 4a). After a sudden drop at the very beginning, α''_g quickly increases within the first few percent of axial deformation to a level which will be only slightly increased by the end of the test (from 41% up to 45% of shearing resistance). On the other hand, α'_g (curve 4b) attains its peak contribution soon after deformation is applied and then decreases until strain softening begins, where it stabilizes to a value of about 18% of the total material shearing resistance.

The role of fabric anisotropy is dominated by the anisotropy in contact normal orientations (curve 2). α'_g abruptly decreases at the beginning and then immediately begins increasing, but at a slower rate than α''_g .

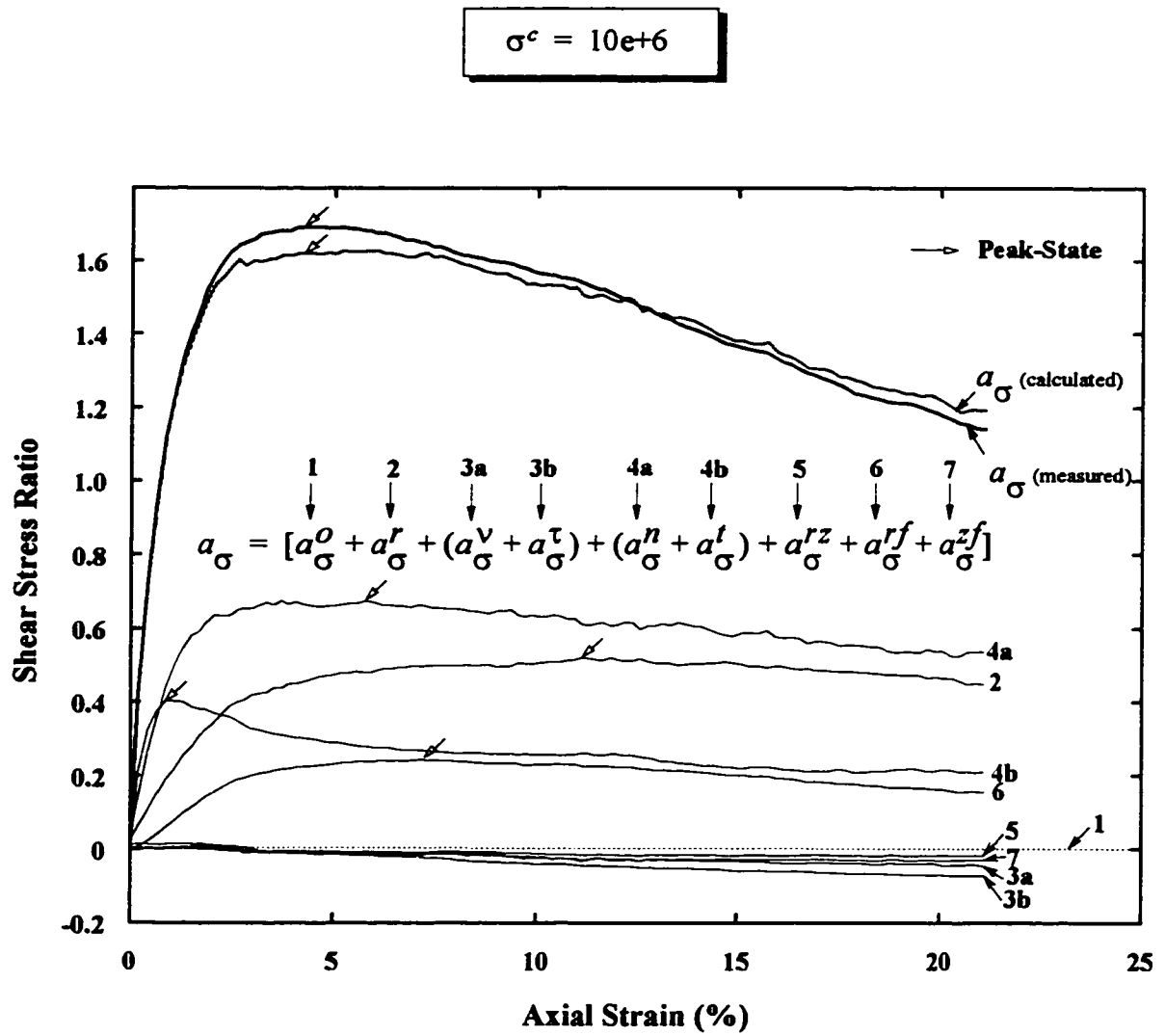


Figure 6-14 Shear stress ratio decomposition

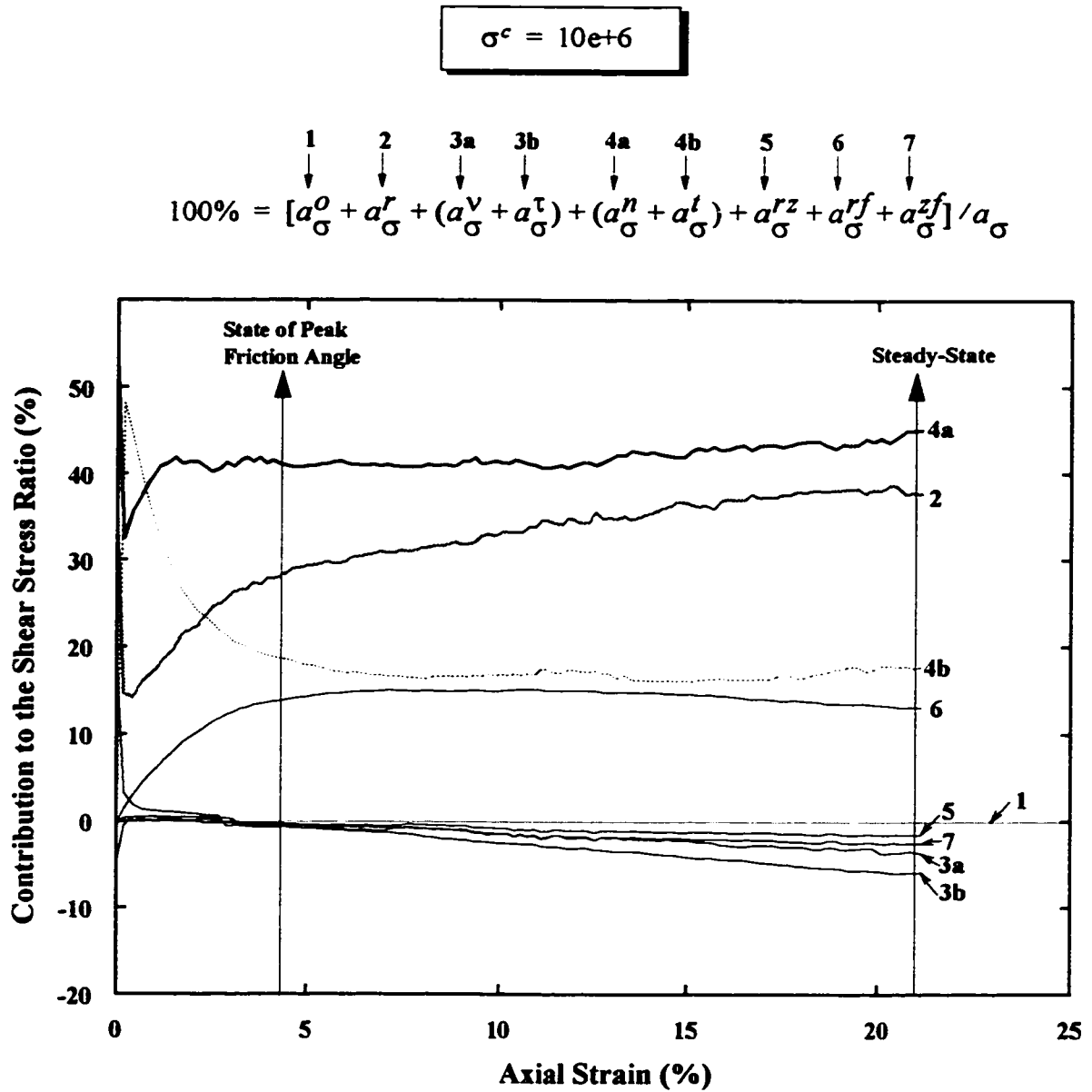


Figure 6-15 Percent contributions of microscopic anisotropies to the mobilized shear strength

The range of values of the contribution, α'_σ , varies from 15% at the beginning of deformation to 38% near steady-state.

6.5.2.1 Another Illustration of the Direct Effect of Particle Shape

A useful illustration of the direct effect of particle shape is by the plot of the evolution during shear deformation of $\alpha_\sigma^v + \alpha_\sigma^t + \alpha_\sigma^r/2 + \alpha_\sigma^f/2$. This quantity represents the total contribution of particle shape-related components of anisotropy in average branch vectors, α_σ^v and α_σ^t , and their shares in the joint effects with other anisotropies, $\alpha_\sigma^r/2$ and $\alpha_\sigma^f/2$, to the mobilized material shear strength (Figure 6•16).

It is seen that the shape effect contributes positively (before the peak-state) then negatively to the mobilized shear strength. This contribution varies linearly with axial strain. At a very large strain, it can total up to -12% of the total shear strength. At the peak-state, however, its contribution is negligibly small. The change in the sense of contribution that takes place some time before the peak of internal friction marks the end of the initial anisotropy's effect on the behaviour of the assembly of particles (Figure 6•16).

6.5.3 Sense of Anisotropy Contributions to the Material Shear Strength

In order to trace the evolution of the sense of contributions of each term during deformation, signs of first order basic contributions were plotted with varying applied axial strain for four confining stresses (Figure 6•17).

6.5.3.1 Individual Contributions of α_{ij}^n and α_{ij}^t

The signs of the α_{ij}^n and α_{ij}^t contributions are plotted in Figure 6•17a, b, respectively.

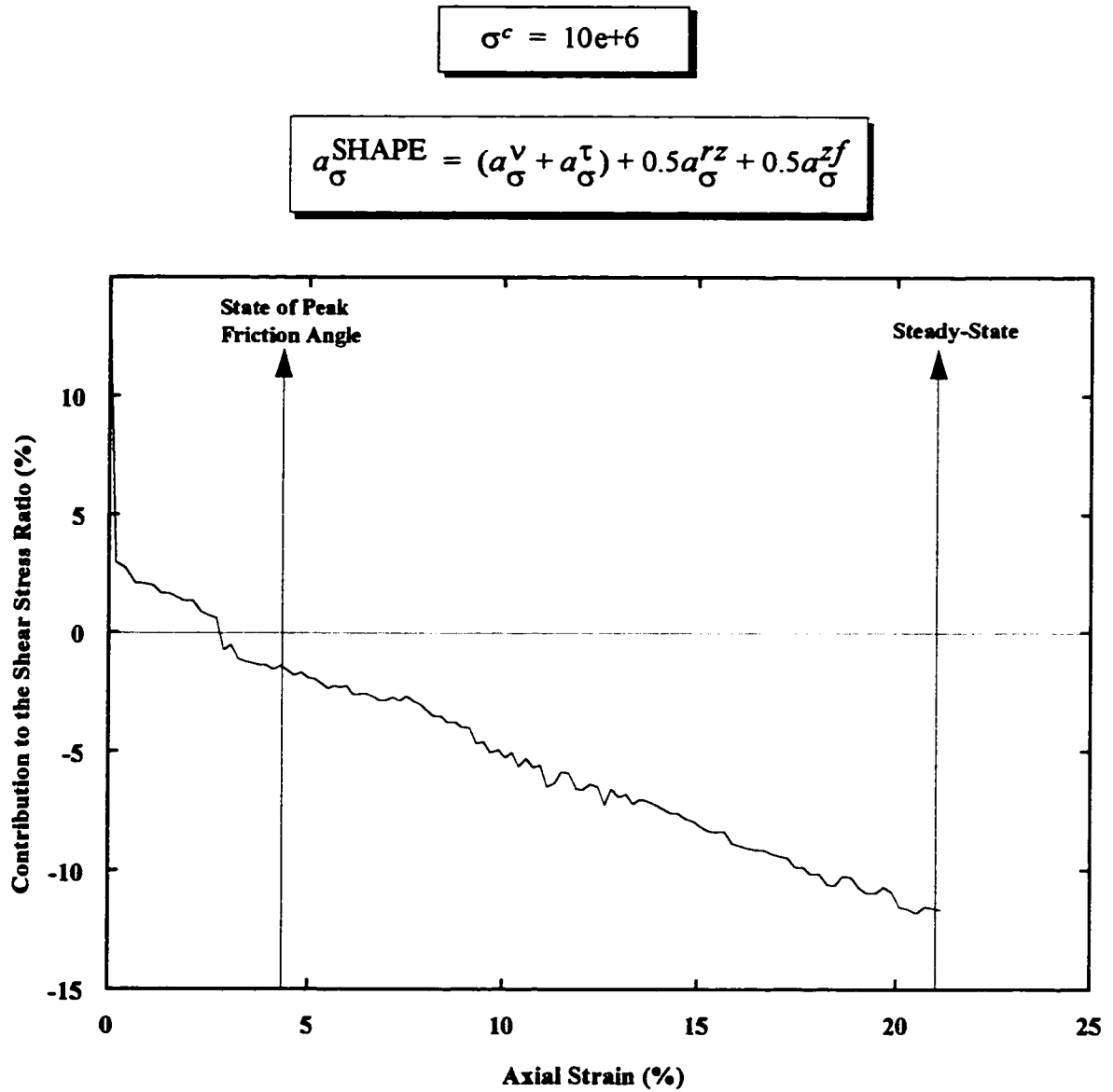


Figure 6-16 Percent contribution of particle shape-related anisotropies to the mobilized shear strength

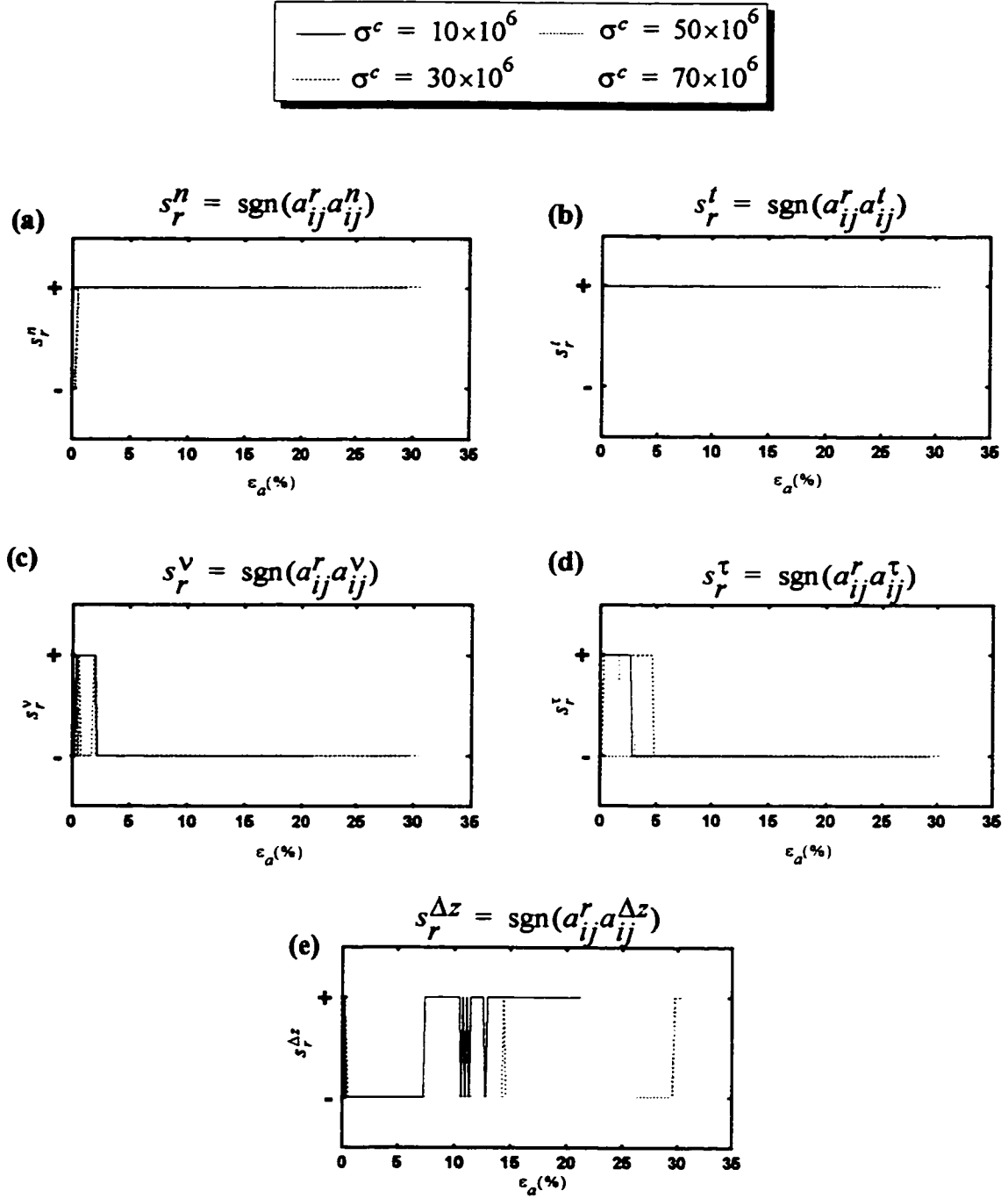


Figure 6-17 Sense of coaxiality of basic anisotropy tensors

As can be seen, their contribution to the material shear strength is always positive, *i.e.*, $s_r^a = +$ and $s_r^t = +$.

6.5.3.2 Individual Contributions of a_{ij}^v and a_{ij}^t

The signs of a_{ij}^v and a_{ij}^t contributions are plotted in Figure 6•17c, d, respectively. They have negative contributions to the shear strength (for the larger part of the test). The continuous positive sign during the first percents of axial strain is attributed to the presence in the system of an initial anisotropy. At large axial strains, constant signs prevail as: $s_r^v = -$ and $s_r^t = -$.

6.5.3.3 Sense of Coaxiality of the Differential Anisotropy Tensor $a_{ij}^{\Delta z}$

The differential average branch vector anisotropy tensor $a_{ij}^{\Delta z}$ has a changing coaxiality depending on the applied confining pressure (Figure 6•17e).

For the lowest pressure $\sigma^c = 10\text{e}+6$, the sign $s_r^{\Delta z}$ changes from positive to negative at an axial strain of about 7.5%. The sign stays predominantly negative until the end. For higher confining pressures, the sign $s_r^{\Delta z}$ is always predominantly negative, $s_r^{\Delta z} = -$.

This result means that for larger confining stresses the normal average branch vector a_{ij}^v always dominates the tangential component a_{ij}^t , whereas for the lowest confining stress the dominance is shared. The plot of magnitudes of a_{ij}^v and a_{ij}^t in Figure 6•18a shows this effect.

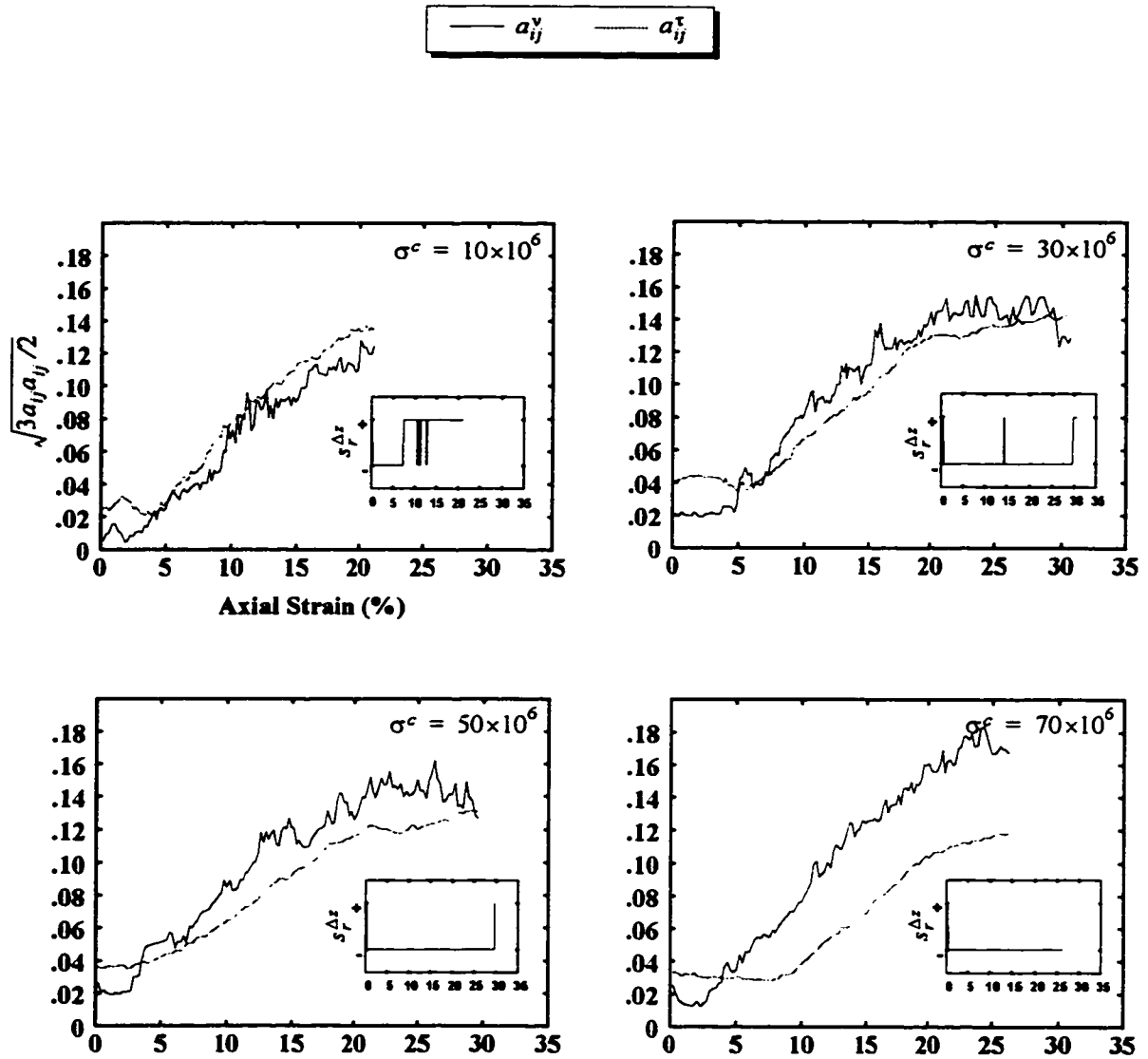


Figure 6-18 Effect of the confining pressure on the difference between anisotropies in normal and tangential average branch vectors

6.5.3.4 Joint Contribution of α_{ij}^r and α_{ij}^z

The joint contribution of α_{ij}^r and the pair $(\alpha_{ij}^v, \alpha_{ij}^s)$ to the material shear strength is embodied in terms having the signs: $s_r^{(\tau\gamma)}$, and $s_r^{[(\Delta z)\gamma]}$. These signs are dependent on individual anisotropies and can be predicted from the basic signs in Figure 6•17 by a simple product of basic signs.

At large strains, $s_r^{(\tau\gamma)} = -$ and $s_r^{[(\Delta z)\gamma]} = -$.

6.5.3.5 Joint Contribution of α_{ij}^r and α_{ij}^f

The terms representing the joint contribution of α_{ij}^r and $(\alpha_{ij}^n, \alpha_{ij}^t)$ to the material shear strength have the signs: $s_r^{(\tau\gamma)}$, and $s_r^{[(\Delta n)\gamma]}$.

At large strains: $s_r^{(\tau\gamma)} = +$ and $s_r^{[(\Delta n)\gamma]} = +$.

Note that the sign $s_r^{\Delta f}$ representing the sense of coaxiality of the difference between α_{ij}^n and α_{ij}^t , is always positive, because α_{ij}^n largely dominates α_{ij}^t .

6.5.3.6 Joint Contribution of α_{ij}^z and α_{ij}^f

Finally, the second-order contribution due to the pairs $(\alpha_{ij}^v, \alpha_{ij}^s)$ and $(\alpha_{ij}^n, \alpha_{ij}^t)$ consists of four terms signed by: $s_r^{(\tau\gamma)}$, $s_r^{[(\Delta z)\gamma]}$, $s_r^{[(\Delta n)\gamma]}$, and $s_r^{[(\Delta z)(\Delta n)\gamma]}$.

At large strains: $s_r^{(\tau\gamma)} = -$, $s_r^{[(\Delta z)\gamma]} = -$, $s_r^{[(\Delta n)\gamma]} = -$, and $s_r^{[(\Delta z)(\Delta n)\gamma]} = -$.

6.5.3.7 Shear Stress Ratio Equation at Large Strains

At large strains, the shear stress ratio equation becomes:

$$\begin{aligned}
 a_{\sigma} = & \sqrt{\lambda} \{ \frac{2}{3} (a^r - a^v - 1.5a^{\tau} + a^n + 1.5a^t) \\
 & - \frac{2}{35} (7a^{(r\tau)} + 4a^{[r(\Delta z)]}) \\
 & + \frac{2}{35} (7a^{(tr)} + 4a^{[r(\Delta f)]}) \\
 & - \frac{2}{35} (17.5a^{(r\tau)} + 7a^{((\Delta z)\tau)} + 7a^{((\Delta f)\tau)} + 4a^{[(\Delta z)(\Delta f)]}) \} / \\
 & \{ 1 + \frac{2}{15} (-a^r a^v + a^r a^n - a^v a^n - 1.5a^{\tau} a^t) \}
 \end{aligned} \tag{6-49}$$

At large strains, the contact normal orientation anisotropy, a_{ij}^r , the average normal and tangential contact forces anisotropies, a_{ij}^n and a_{ij}^t , respectively, and their products contribute positively to the material shear strength. The average normal and tangential branch vector anisotropies, a_{ij}^v and a_{ij}^{τ} respectively, and their products with the above anisotropies, have negative contributions at large strains. These results agree with plots in Figure 6•14 and Figure 6•15.

In fact, the relationship in (6• 49) is valid from before the state of peak friction angle. It is believed that if the sample was initially isotropic, the relationship would hold for the full range of applied shear deformations.

6.6 Conclusions

In this chapter, the Stress-Force-Fabric relationship was developed for ellipsoids by including the direct visible effect of shape characterized by components of anisotropy in average normal and tangential branch vector.

The particle shape factor was modeled by normal and tangential components of average branch vector anisotropy. It has been seen that it represents a minor but decisive contribution to the material shear strength. It helps to close the gap between theoretical and

measured stress-strain curves, especially at large strains.

The average stress tensor was decomposed as a sum of contributions due to the individual microscopic anisotropies and their combined effects as:

$$\sigma_{ij} \equiv \sigma_{ij}^o + \sigma_{ij}^r + \sigma_{ij}^z + \sigma_{ij}^f + \sigma_{ij}^{rz} + \sigma_{ij}^{rf} + \sigma_{ij}^{zf} \quad (6 \cdot 50)$$

\downarrow
Total

\downarrow
Full
Isotropy

\downarrow
 a_{ij}^r
only

\downarrow
 a_{ij}^z
only

\downarrow
 a_{ij}^f
only

\downarrow
 $a_{ij}^r \& a_{ij}^z$

\downarrow
 $a_{ij}^r \& a_{ij}^f$

\downarrow
 $a_{ij}^z \& a_{ij}^f$

where the tensor a_{ij}^z stands for the pair of components (a_{ij}^y, a_{ij}^x) , and a_{ij}^f stands for the pair of components (a_{ij}^n, a_{ij}^t) .

The relationship was validated numerically on simulated assemblies of ellipsoids in the pure deviatoric triaxial test (absence of stress rotations).

The following observations on the evolution of the decomposition during shear deformation were made:

1. All tensor contributions are symmetric and co-axial with the original average stress tensor.
2. The spherical tensor $\sigma_{ij}^o = m_v \bar{p}(\bar{z}^o/6)\delta_{ij}$ is not constant but experiences a decrease to a minimum value, then gradually increases and stabilizes at large strains. This behaviour was seen to be the product of an ever increasing average normal contact force \bar{p} and an ever decreasing average contact density m_v .
3. Tensors σ_{ij}^r , σ_{ij}^f , and σ_{ij}^{rf} , behave similarly to the total stress. Tensors σ_{ij}^r , σ_{ij}^f , are deviatoric, but not σ_{ij}^{rf} . The latter has a mean value which behaves in the opposite sense to the spherical tensor in order to keep the mean total stress constant as prescribed by the test. These three tensors total more than 90% of the average stress tensor.

4. Tensors σ_{ij}^z , σ_{ij}^{rz} , σ_{ij}^{zf} vary linearly with deformation. Tensors σ_{ij}^{rz} , σ_{ij}^{zf} are not deviatoric; however, they are small and can be neglected. The tensor σ_{ij}^z is deviatoric and its negative contribution to the total stress increases with shear deformation.

A direct expression of the mobilized shear strength as a sum of individual and combined anisotropy contributions was formulated by assuming co-axiality and axisymmetry as:

$$a_\sigma = a_\sigma^r + \underbrace{(a_\sigma^v + a_\sigma^z)}_{a_\sigma^z} + \underbrace{(a_\sigma^n + a_\sigma^t)}_{a_\sigma^f} + a_\sigma^{rz} + a_\sigma^{rf} + a_\sigma^{zf} \quad (6 \cdot 51)$$

The relationship was verified by results of simulation. It yielded concepts already known from earlier research concerning details of anisotropy development and interactions between fabric and average contact force anisotropies, and also concerning levels of microscopic contributions to the mobilized shear strength during shear deformation. A summary of findings is as follows:

1. All terms in the above decomposition can be grouped into two classes of behaviour:
 - a. Behaviors resembling the total shear stress ratio's behaviour with an increase to a maximum value followed by a gradual decrease towards a steady level. Positive contributions a_σ^r , a_σ^n , a_σ^t , and a_σ^{rf} belong to this class.

- b. Linear decreasing variations with the applied axial strain. Post-peak negative contributions α_σ^v , α_σ^s , α_σ^z , and α_σ^f belong to this class.
2. The rates of mobilization of the first class of anisotropies to their maximum intensities are very much different. The contribution α_σ^t is the fastest to mobilize (within the first few percent of axial deformation) followed by α_σ^n , then α_σ^r . The mobilization of maximum α_σ^n takes place before the peak of the shear stress ratio α_σ . The two mobilizations are very close, however, but not simultaneous because of influences due to α_σ^t and α_σ^r .
3. The average contact force anisotropy contribution $\alpha_\sigma^f = (\alpha_\sigma^n + \alpha_\sigma^t)$ comprises the largest proportion of the mobilized shear stress ratio. At the peak of internal friction, α_σ^n accounts for about 41% and α_σ^t for about 18% of α_σ . At large strains, they account for 45% and 18%, respectively (Table 6•1).
4. The contact normal orientation anisotropy contribution α_σ^r increases very gradually to its peak value from 28% (at peak-state) to 38% (at steady-state). The combined contribution α_σ^f has the same level (13%) at peak-state and steady-state (Table 6•1).
5. Among the first class of contributions, α_σ^r is the parameter that features the largest variation (10%) between the peak-state and steady-state. An additional 4% comes from the increase in α_σ^n . This is in excess of the 100% total contribution and must be eliminated. The second class of parameters, *i.e.*, α_σ^v , α_σ^s ,

CHAPTER VI: THE STRESS-FORCE-FABRIC RELATIONSHIP FOR ELLIPSOIDS

a_{σ}^r , and a_{σ}^f provides the necessary balance by contributing negatively to the mobilized shear strength.

Term State	a_{σ}^r	$a_{\sigma}^f = (a_{\sigma}^n + a_{\sigma}^t)$		a_{σ}^f	$a_{\sigma}^z = (a_{\sigma}^v + a_{\sigma}^s)$		a_{σ}^r	a_{σ}^f
		a_{σ}^n	a_{σ}^t		a_{σ}^v	a_{σ}^s		
Peak-State	28%	59%		13%	0%		0%	0%
		41%	18%		0%	0%		
Steady-State	38%	63%		13%	-9.75%		-1.75%	-2.5%
		45%	18%		-6%	-3.75%		

Table 6•1 Percent contributions of microscopic anisotropies to the mobilized material shear strength

CHAPTER VII: STATISTICAL AND GEOMETRICAL ANALYSIS OF CONTACTS

7.1 Introduction

In this chapter, a statistical analysis of contacts is carried out using the data collected from the simulation results with assemblies of ellipsoids. The description of contact normals and contact vectors by statistical distributions was the subject of thorough discussion in connection with the analysis of the Stress-Force-Fabric relationship in the previous chapters. Herein, other aspects of the contacts which did not receive much attention before are looked upon. The principal parameters employed for performing statistics on contacts are: the pair of contact vectors associated with a physical contact, the contact normal orientation and the particle orientation.

The objectives of this chapter are twofold:

1. To study the effect of shape on the distribution of contacts around a particle surface.
2. To estimate the effect of shape on the anisotropy in contact normal orientations.

7.2 Distribution of Local Contact Vector Orientations

The contact normal vector is not sufficient to describe the fabric of irregular-shaped particles. Appropriate information about the size and shape of particles in the vicinity of contact with other particles must be included in the description of fabric and this is provided by the contact vector. Through the study of this parameter the direct effect of particle shape and size can be analyzed. For mono-size assemblies of ellipsoids, the effect of size is not present and the particle shape alone can be studied. One simple aspect of possible investigation is whether or not an elongated particle has a preferred area on its surface to form contacts with other particles (regardless of its position and orientation in the sample volume space)? More specifically, what is the probability of occurrence of a contact at a given point on the surface of an ellipsoid, if all biases due to position and orientation of the particle are eliminated?

The distribution of densities of probability of contact occurrence can be approximated from the measured histogram distribution of the contact vector orientation (*i.e.*, in *local ellipsoid principal axes*). Examples of measured histograms of the local contact vector distribution are plotted in Figure 7•1a. Four states of deformation are represented, as well as a second-order Fourier approximation of the first histogram distribution:

$$\begin{cases} S_l(\mathbf{n}') = \frac{1}{4\pi}(1 + a_{ij}^{c\nu L} n_i' n_j') \\ a_{ij}^{c\nu L} = a_{ji}^{c\nu L}, \quad a_{kk}^{c\nu L} = 0 \end{cases} \quad (7 \cdot 1)$$

The tensor $a_{ij}^{c\nu L}$ is a measure of the anisotropy in contact distribution around the surface of a particle. The plot of the magnitude of $a_{ij}^{c\nu L}$ (for four confining pressures) during the entire range of applied strain (Figure 7•1b) shows that the change in the initial anisotropy with varying applied strain is very small. The local contact vector orientation is statistically independent from particle orientation and coordination number (which undergo considerable change during the course of the test). The variation with the confining pressure is also insignificant considering the wide range of tested confining pressures. These results suggest that the probability of distribution of contacts around a particle is only dependent on the shape of the particle. One type of dependence, obtained during the particle growth simulations, is illustrated in Figure 7•1c. The anisotropy in the contact distribution around a particle seems to increase with the elongation aspect ratio in a rather linear fashion. For sub-spherical shapes, however, a profile in “U” is observed, where the anisotropy is almost equal to zero for a particular value of the aspect ratio ($a/b = 1.07$). The question is whether or not the existence of such a particular value of the aspect ratio is a constant property or is simply an effect of the simulation test conditions? Most likely, the observed phenomenon is related to the highly anisotropic fabric of the initial sample of spheres before the growth process started.

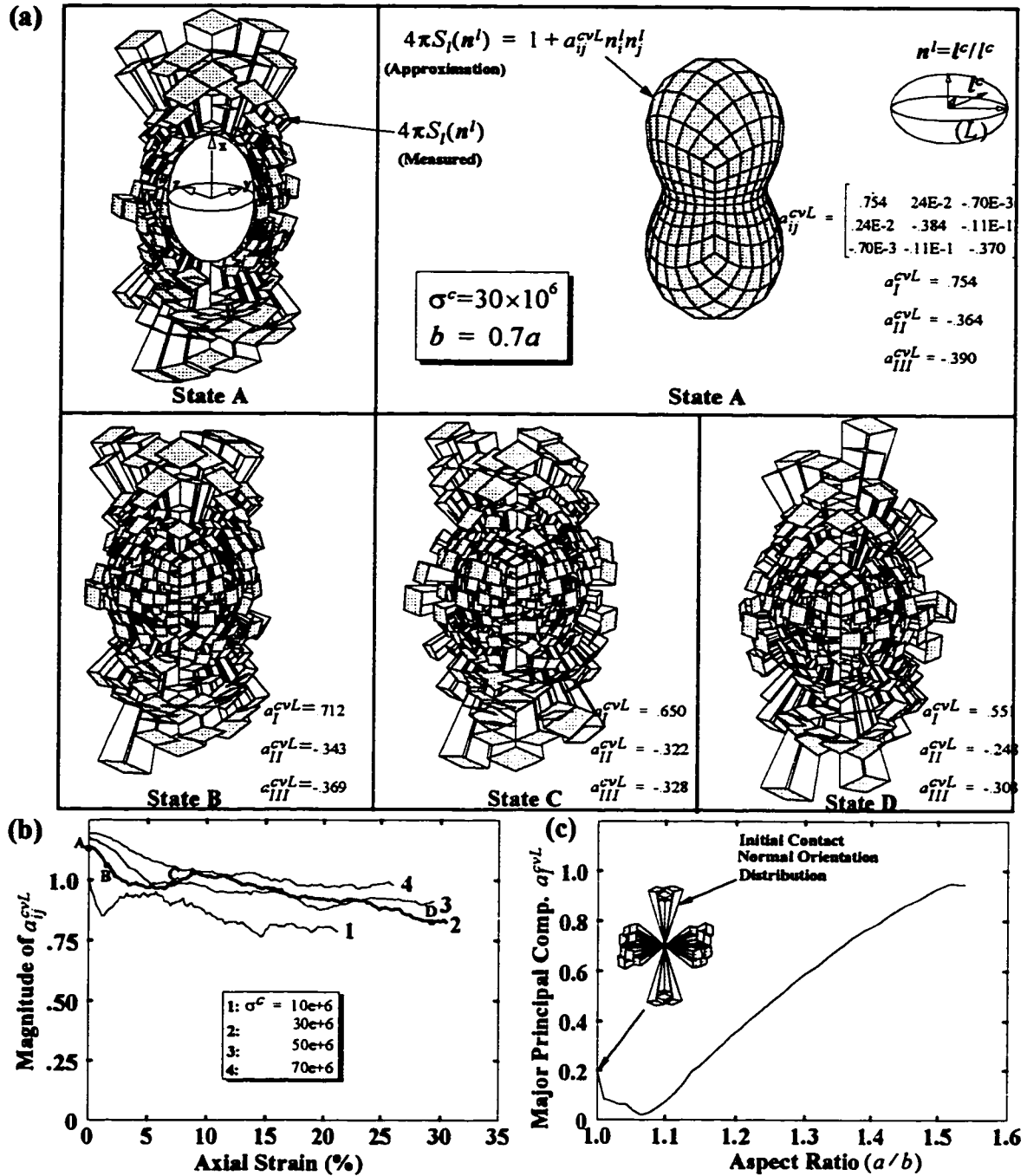


Figure 7•1 Anisotropy in local contact vector orientations
 (a) Measured and approximated distributions (4 states)
 (b) Variation with applied strain, and confining pressure
 (c) Variation with particle shape

The initial sample before compaction was packed in cubic-centered structure with only three possible directions of contacts (one vertical and two horizontals). After compaction, the contact normal orientation distribution was highly anisotropic, as can be seen from the histogram plot in Figure 7•1c. The absence of randomness in contact distribution (even if is biased) explains that the initial distribution of contact occurrence around spheres be anisotropic. The “U” shape corresponds to the destruction of the initially highly organized structure of spheres that immediately followed the incremental change of particle shape. The randomness of fabric being retrieved, the major principal value a_1^{vL} had to drop to zero to reflect only the shape of particles.

7.2.1 Density and Distribution Functions of Local Contact Probability

The transition from densities to cumulative probabilities over finite regions requires integrating the density of probability function over the region of interest. Let it be an arbitrary region characterized, in spherical coordinates, by the pair of polar angles (α'_1, α'_2) and the pair of azimuth angles (β'_1, β'_2) , then:

$$\text{Prob}(\alpha'_1 \leq \alpha' \leq \alpha'_2, \beta'_1 \leq \beta' \leq \beta'_2) = \int_{\alpha'_1}^{\alpha'_2} \int_{\beta'_1}^{\beta'_2} S_I(\alpha, \beta) \underbrace{\sin \beta d\alpha d\beta}_{\text{Element of Area on the Unit Sphere}} \quad (7\bullet 2)$$

The same probability can be decomposed as:

$$\begin{aligned} \text{Prob}(\alpha'_1 \leq \alpha' \leq \alpha'_2, \beta'_1 \leq \beta' \leq \beta'_2) &= F_I(\alpha'_2, \beta'_2) - F_I(\alpha'_1, \beta'_2) \\ &\quad - F_I(\alpha'_2, \beta'_1) + F_I(\alpha'_1, \beta'_1) \end{aligned} \quad (7\bullet 3)$$

where:

$$F_I(\alpha', \beta') = \int_0^{\alpha'} \int_0^{\beta'} S_I(\alpha, \beta) \sin \beta d\alpha d\beta \quad (7\bullet 4)$$

Therefore, all probabilities can be expressed in terms of the single *distribution of probability* function $F_I(\alpha', \beta')$. This function represents, in this case, the probability of finding a contact in an arbitrary region delimited by two unit vectors $\mathbf{n}'_1(0, 0)$ (x-axis) and $\mathbf{n}'_2(\alpha', \beta')$.

The properties of the distribution function are:

- i. It varies between 0 and 1.
- ii. If integrated over the whole space it should yield the certainty probability, *i.e.*,

$$F_I(2\pi, \pi) = 1 \quad (7 \cdot 5)$$

- iii. The function is ever increasing. This is because positive probabilities are cumulated.

Before calculating the distribution function, $F_I(\alpha, \beta)$, the density of probability function $S_I(\alpha, \beta)$ must be calculated first. In the system of principal directions of the tensor a_{ij}^{cyl} , the equation (7• 1) can be re-written as:

$$S_I(\alpha, \beta) = \frac{1}{4\pi} \{ 1 + a_I^{cyl} \cos^2 \beta + (a_{II}^{cyl} \cos^2 \alpha + a_{III}^{cyl} \sin^2 \alpha) \sin^2 \beta \} \quad (7 \cdot 6)$$

where the components of the unit vector $\mathbf{n} = (\cos \beta, \cos \alpha \sin \beta, \sin \alpha \sin \beta)$ in terms of (α, β) were substituted in (7• 1).

For the performed tests with assemblies of prolate spheroids, the deviatoric anisotropy tensor a_{ij}^{cyl} is axisymmetric, thus:

$$a_{III}^{cyl} = a_{II}^{cyl} = -\frac{1}{2}a_I^{cyl} \quad (7 \cdot 7)$$

Substituting of the above identities into (7• 6) yields:

$$S_I(\beta) = \frac{1}{4\pi} [1 + a_f^{vL} \cos^2 \beta - (\frac{1}{2} a_f^{vL}) \sin^2 \beta] \quad (7 \cdot 8)$$

The obtained density of probability function is independent from the polar angle α (*i.e.*, axisymmetric). Its variation with the azimuth angle β is shown in Figure 7•2a (for a wide range of values of parameter a_f^{vL}). Results of simulations, however, give values of a_f^{vL} within the interval [0.5, 0.8], as shown by the plot in Figure 7•2a.

Uncoupling variables α and β in equation (7• 4) results in:

$$F_I(\alpha', \beta') = \int_0^{\alpha'} d\alpha \int_0^{\beta'} S_I(\beta) \sin \beta d\beta \quad (7 \cdot 9)$$

Or:

$$F_I(\alpha', \beta') = \frac{\alpha'}{2\pi} \cdot G_I(\beta') \quad (7 \cdot 10)$$

where:

$$G_I(\beta') = \int_0^{\beta'} 2\pi S_I(\beta) \sin \beta d\beta \quad (7 \cdot 11)$$

The distribution function $F_I(\alpha', \beta')$ is linear with respect to the polar angle α' , implying that for a fixed azimuth angle β' the probability of observing a contact in a given polar position is uniform.

By assigning to α' the value of its full range of variation 2π in equation (7• 10), the function $G_I(\beta')$ can be equated to:

$$G_I(\beta') = F_I(2\pi, \beta') \quad (7 \cdot 12)$$

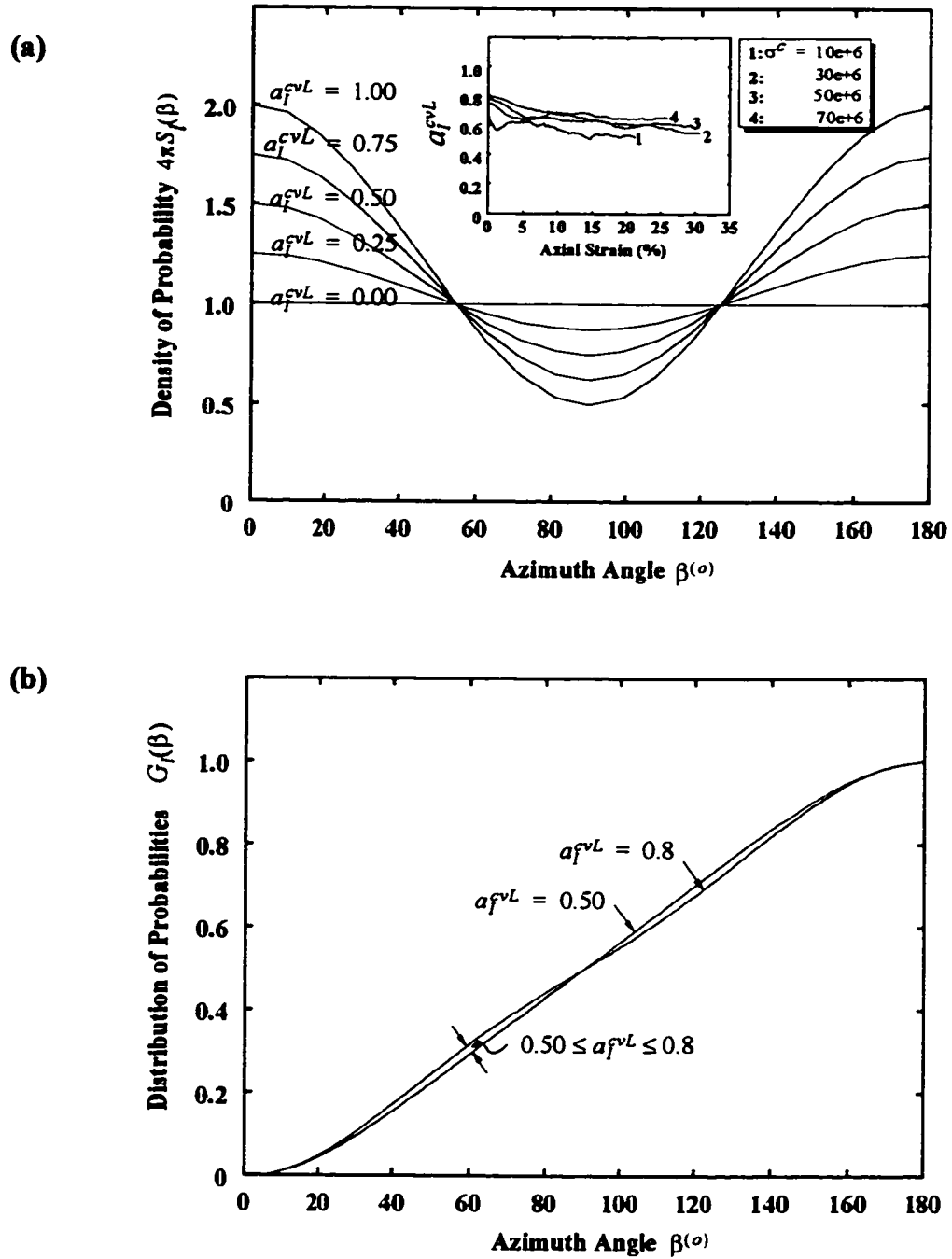


Figure 7•2 Contact probability calculations
 (a) Density of probability function
 (b) Cumulative probabilities

As such, the function $G_l(\beta)$ represents the probability of observing a contact in a position described by an azimuth angle between 0 and β , and a polar angle α anywhere between 0 and 2π .

From its definition in (7• 11), the function $G_l(\beta)$ can also be interpreted as the probability distribution of the random variable β associated with the density of probability function $2\pi S_l(\beta) \sin \beta$. Integration of the right hand side of (7• 11) yields:

$$G_l(\beta) = \frac{1}{2} [1 - (1 - \frac{1}{2} a_f^{vL}) \cos \beta - (\frac{1}{2} a_f^{vL}) \cos^3 \beta] \quad (7• 13)$$

Curves of variation of the function $G_l(\beta)$ are displayed in Figure 7•2b, for the range of values of a_f^{vL} experienced during simulations of assemblies of ellipsoids at various confining pressures (Figure 7•2a).

7.2.2 Probability Distribution of Contact Vector Lengths

A third interpretation of the function $G_l(\beta)$ can be obtained in relation to the determination of the contact vector length probability distribution for assemblies of prolate spheroids.

A contact with a position (α, β) on the surface of an ellipsoid of semi-axes $(a \geq b \geq c)$ has a vector length:

$$l(\alpha, \beta) = 1 / \sqrt{\frac{\cos^2 \beta}{a^2} + \sin^2 \beta \left[\frac{\cos^2 \alpha}{b^2} + \frac{\sin^2 \alpha}{c^2} \right]} \quad (7• 14)$$

For prolate spheroids: $b = c$; therefore the above expression simplifies to:

$$l(\beta) = 1 / \sqrt{\frac{\cos^2 \beta}{a^2} + \frac{\sin^2 \beta}{b^2}} \quad (7• 15)$$

The above function is not one-to-one. Each admissible length, l , is associated with two azimuth angles: $0 \leq \beta \leq \pi/2$ and $\pi - \beta$ (calculated by inverting (7• 15)).

The probability that a contact be characterized by a vector length between two limits $l_1(\beta_1) \leq l_2(\beta_2)$, where $\pi/2 \geq \beta_1 \geq \beta_2 \geq 0$, is calculated as:

$$\text{Prob}(l_1 \leq l \leq l_2) = [G_l(\beta_1) - G_l(\beta_2)] + [G_l(\pi - \beta_2) - G_l(\pi - \beta_1)] \quad (7• 16)$$

It can be verified that:

$$G_l(\pi - \beta) = 1 - G_l(\beta) \quad (7• 17)$$

Therefore:

$$\text{Prob}(l_1 \leq l \leq l_2) = 2[G_l(\beta_1) - G_l(\beta_2)] \quad (7• 18)$$

7.2.3 Application to Predicting Proportions of Contact Vector Lengths

In order to prove the veracity of relationship (7• 18), a selected grouping of contacts was based on contact vector lengths. The full range of contact vector lengths $[b, a]$ is divided into three intervals. A given contact necessarily falls in one of six groups corresponding to a combination of two of the three intervals of lengths.

Statistics of contacts falling in each group were extracted from results of numerical simulations. The same statistics can be estimated based on the relationship (7• 18), and compared to the measured values.

In the following sub-section, the method of estimation of statistics of contacts and comparison with simulated data are presented.

7.2.3.1 Grouping of Contacts

The contact groups are illustrated in Figure 7•3. Given the symmetries of the ellipsoid geometry, it is sufficient to define the contact position by reference to the portion of the surface covering ($\frac{1}{8}$) of the volume of the ellipsoid. Moreover, for prolate spheroids, all meridians have the same length and curvature. Therefore, the local contact position can be described by reference to a single meridian (a quarter of an ellipse).

The contact vector length can vary between the minor semi-axis, $b = c$, and the major semi-axis a . As mentioned before, the interval of variation $[b, a]$ is partitioned into three sub-intervals:

- i. Contact vectors within the range of short lengths $[b, b+(a-b)/3]$. This category of contact vectors will be referred to by the letter “s” (as short).
- ii. Contact vectors within the intermediate range $[b+(a-b)/3, b+2(a-b)/3]$ labelled by the letter “i” (as intermediate).
- iii. Contact vectors within the long range $[b+2(a-b)/3, a]$. The letter “l” (as long) is used for this group.

The groups of contacts are the six possible combinations: “s-s”, “s-i”, “s-l”, “i-i”, “i-l”, “l-l”. For instance, a contact of type “s-i” combines a short contact vector length from one particle and an intermediate contact vector length from the other particle.

Let $f_{(x)} = M_{(x)}/\tilde{M}$ be the fraction of contact vectors of type (x), and let $f_{(x-y)} = M_{(x-y)}/\tilde{M}$ be the fraction of contacts of type (x-y) where \tilde{M} is the total number of physical contacts in the assembly of particles.

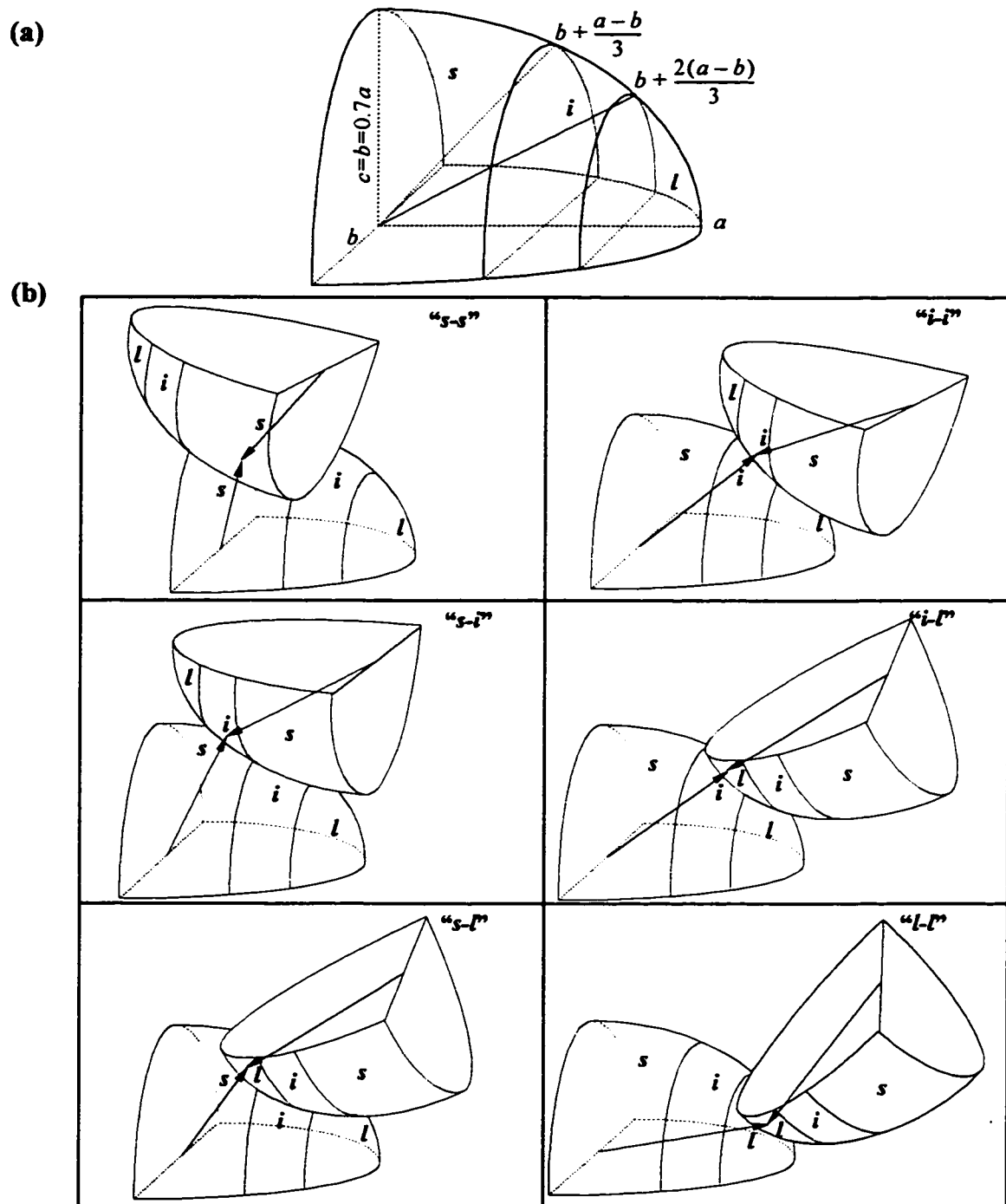


Figure 7•3 Contact groups of given vector lengths
 (a) Definition
 (b) Illustration

Based on the relationship (7• 18), a distribution of probability function for contact vector lengths can be defined as:

$$H_l(l) = \text{Prob} (l \leq l^c \leq a) = 2[G_l(\beta^l) - G_l(0)] = 2G_l(\beta^l) \quad (7• 19)$$

The plot of the distribution function is shown in Figure 7•4a.

The relationship between the vector length and azimuth angle is illustrated by the plot of Figure 7•4b.

By reference to Figure 7•4a, the fraction of contact vector types are estimated as:

$$\begin{cases} f_{(s)} = H_l(b) - H_l(b + (a - b)/3) \\ f_{(i)} = H_l(b + (a - b)/3) - H_l(b + 2(a - b)/3) \\ f_{(l)} = H_l(b + 2(a - b)/3) - H_l(a) \end{cases} \quad (7• 20)$$

The fraction of small, intermediate and long contact vectors are calculated to be, 54%, 27%, and 19%, respectively. It can be verified that these fractions are similar to the proportions of the surface areas of the prolate spheroid shape covered by the small, intermediate and long contact vectors, respectively.

The fraction of contact types are calculated from the former estimates as:

$$\begin{cases} f_{(x-x)} = f_{(x)}^2 \\ f_{(x-y)} = 2f_{(x)}f_{(y)} \quad (x \neq y) \end{cases} \quad (7• 21)$$

The above relationships are derived from probability calculations. The presence of the coefficient 2 in rectangular fractions ((s-i), (s-l), (i-l)) is explained by the possibility that the two particles can be interchanged.

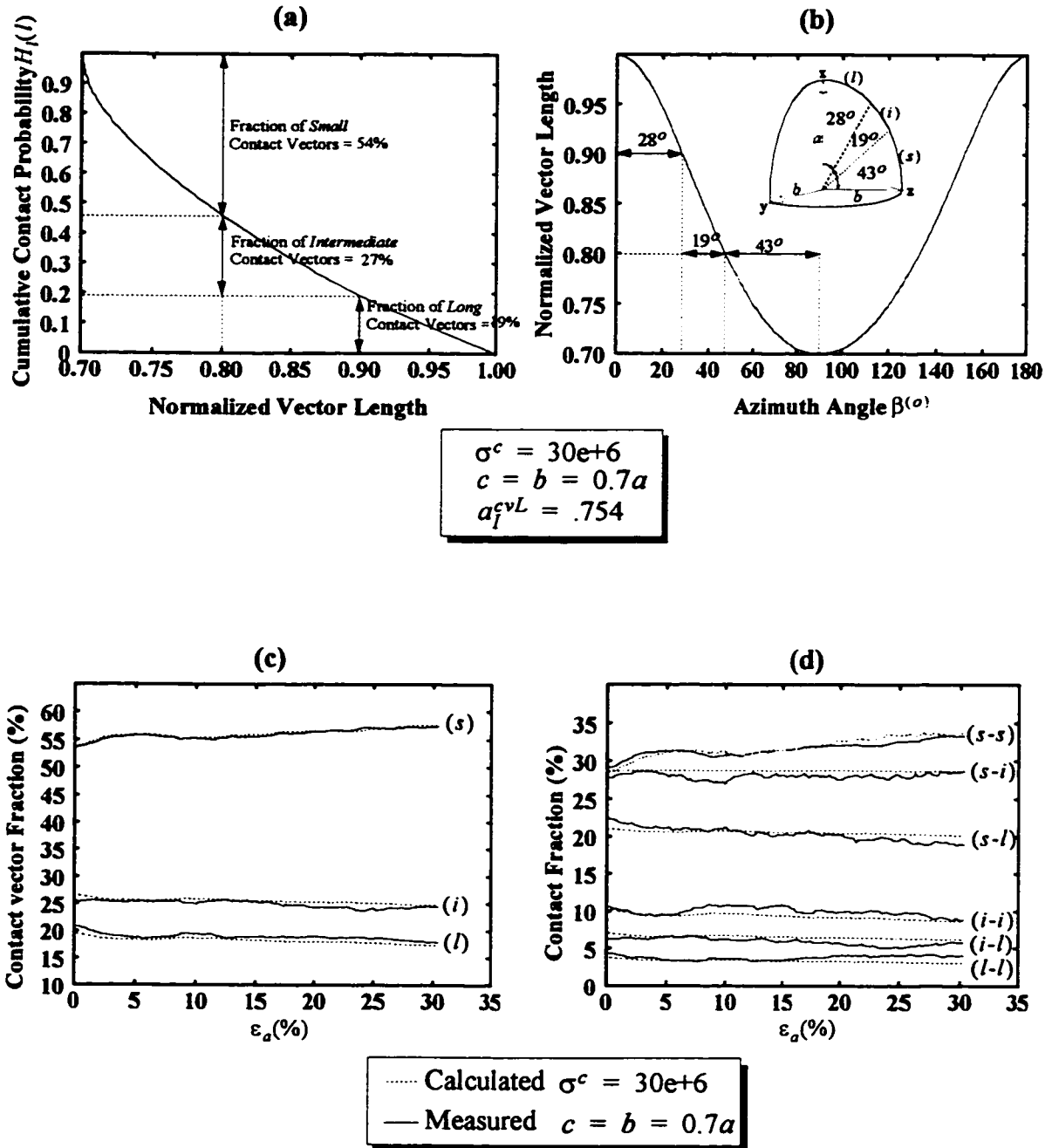


Figure 7-4 Measured and estimated fractions of contact vectors and contact types for well-defined groups of contacts

Figure 7•4c illustrates the comparison between measured and calculated contact vector fractions. Figure 7•4d illustrates the comparison between measured and calculated contact type fractions. The comparison is illustrated for a single confining pressure; however, a similar close agreement between the theoretical and measured fractions holds for other confining pressures.

7.2.4 Relationship Between Local Contact Probabilities and Particle Surface Areas

The concern in this section is to examine the veracity of the assumption of a possible relationship of proportionality between the probability of contact occurrence over a region on the surface of an ellipsoid and the area of that region. The verification is carried out for particular regions shown in Figure 7•5a, *i.e.*, those characterized in spherical coordinates by $(0 \leq \alpha \leq 2\pi, 0 \leq \beta \leq \beta')$.

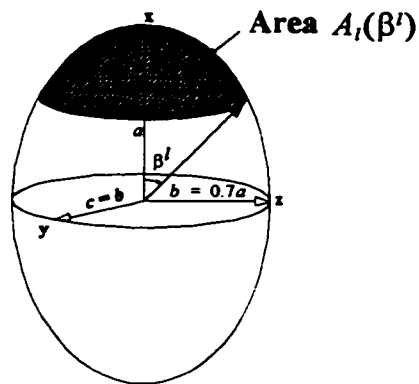
If the assumption is valid, then the area of the region of a prolate spheroid delimited by the azimuth angles 0 and β , denoted by $A_I(\beta)$, should be, for some value of the parameter α_f^{VL} , proportional to the distribution function $G_I(\beta)$.

In order to obtain a normalized area distribution, the coefficient of proportionality must be $1/A_I(\pi)$, where $A_I(\pi)$ is the total prolate spheroid surface area.

Therefore, the proposed relationship can be written as:

$$G_I(\beta) \equiv A_I(\beta) / A_I(\pi) \quad (7 \cdot 22)$$

(a)



(b)

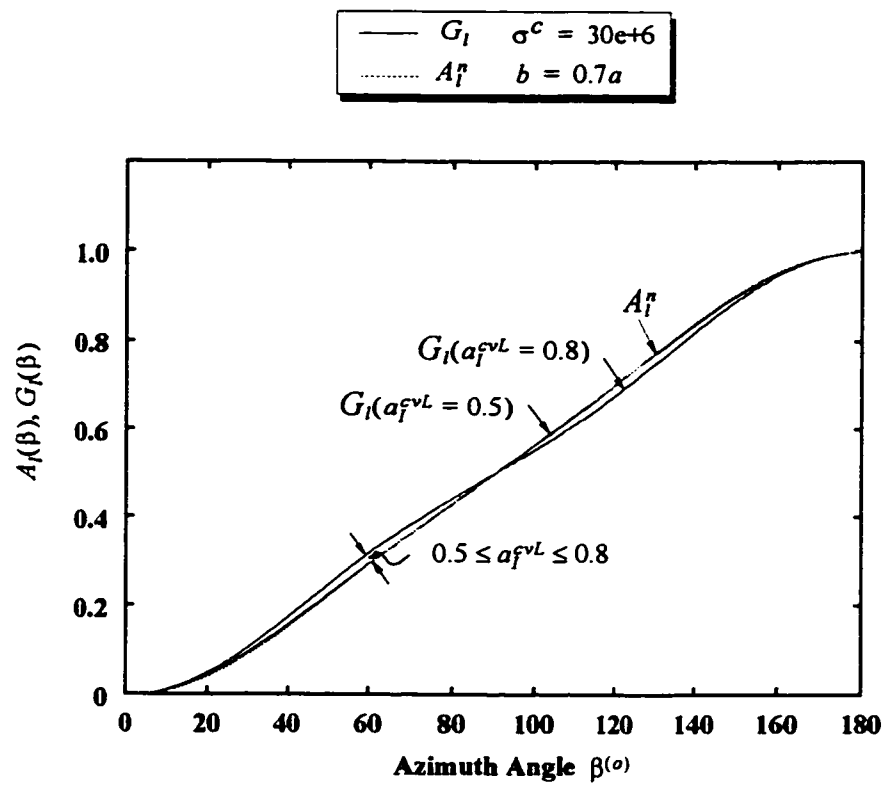


Figure 7-5 Illustration of a comparison between calculated distributions of local contact probabilities and ellipsoid surface areas

7.2.4.1 Calculation of the Distribution of Normalized Particle Surface Areas

The areas $A_l(\beta)$ can be calculated analytically as:

$$A_l(\beta) = \frac{\pi ab}{\tilde{e}} \{ \sin^{-1}(\xi) + \xi \sqrt{1 - \xi^2} \} \quad (7 \cdot 23)$$

where:

$$\xi = \frac{\sqrt{l^2(\beta) - b^2}}{a} \quad (7 \cdot 24)$$

and where $l(\beta)$ is the contact vector length given by (7• 15), and $\tilde{e} = \sqrt{a^2 - b^2}/a$ is a measure of particle eccentricity.

The result of comparison is shown in Figure 7•5b (for the particular aspect ratio $a = 0.7b$). Figure 7•5b displays the curves of variation of the normalized surface area $A_l^*(\beta) = A_l(\beta)/A_l(\pi)$, and the function $G_l(\beta)$ (for values of the parameter a_f^{cvL} at the two ends of the range of values [0.5, 0.8]). As can be seen, the assumption expressed in the relationship (7• 22) is fairly accurate for the range of values of a_f^{cvL} experienced in simulations. The relationship (7• 22) can be used to estimate the distribution of local contact vector lengths when the measured distribution is not available. The error on the estimated parameter a_f^{cvL} is expected to vary between 0 and 0.3 (*i.e.*, the difference between the maximum and minimum values 0.8 and 0.5, respectively).

7.3 Distribution of Particle Orientations

The test results reveal that the initial random particle orientation is affected by the applied load. An increased number of particles become oriented with their major axis per-

pendicular to the direction of loading. Several plots indicate this tendency: (1) from the visual comparison of ellipsoids' major axes orientations between the initial state of the assembly and the beginning of the steady state as illustrated in Figure 7•6; (2) from the histogram distribution of ellipsoids' long axes at these two states (Figure 7•7a). The initial fairly isotropic distribution (circular shape) evolves to a shape in the form of a “donut” at a large strain. The “donut” is sitting on the plane perpendicular to the direction of loading (vertical), which indicates that the dominant ellipsoid orientation inside the assembly is sub-horizontal.

From a physical point of view, those ellipsoids initially having vertical or sub-vertical long-axis orientation will develop larger moments near their long axis (larger arm), and smaller moments at the other contact locations (smaller arm). The moment imbalance and the search for stability causes the ellipsoids to rotate their long axis to a position normal to the maximum load direction.

7.3.1 Evolution of Anisotropy in Particle Orientations During Shear Deformation

The distribution of long-axes' orientations can be approximated by a truncated Fourier series function as:

$$\begin{cases} S_E(\mathbf{n}^E) = \frac{1}{4\pi} (1 + a_{ij}^E n_i^E n_j^E) \\ a_{ij}^E = a_{ji}^E, \quad a_{kk}^E = 0 \end{cases} \quad (7 \bullet 25)$$

The tensor a_{ij}^E represents the deformation-induced anisotropy in ellipsoid orientations. Its magnitude a^E increases with increasing axial strain (Figure 7•7b).

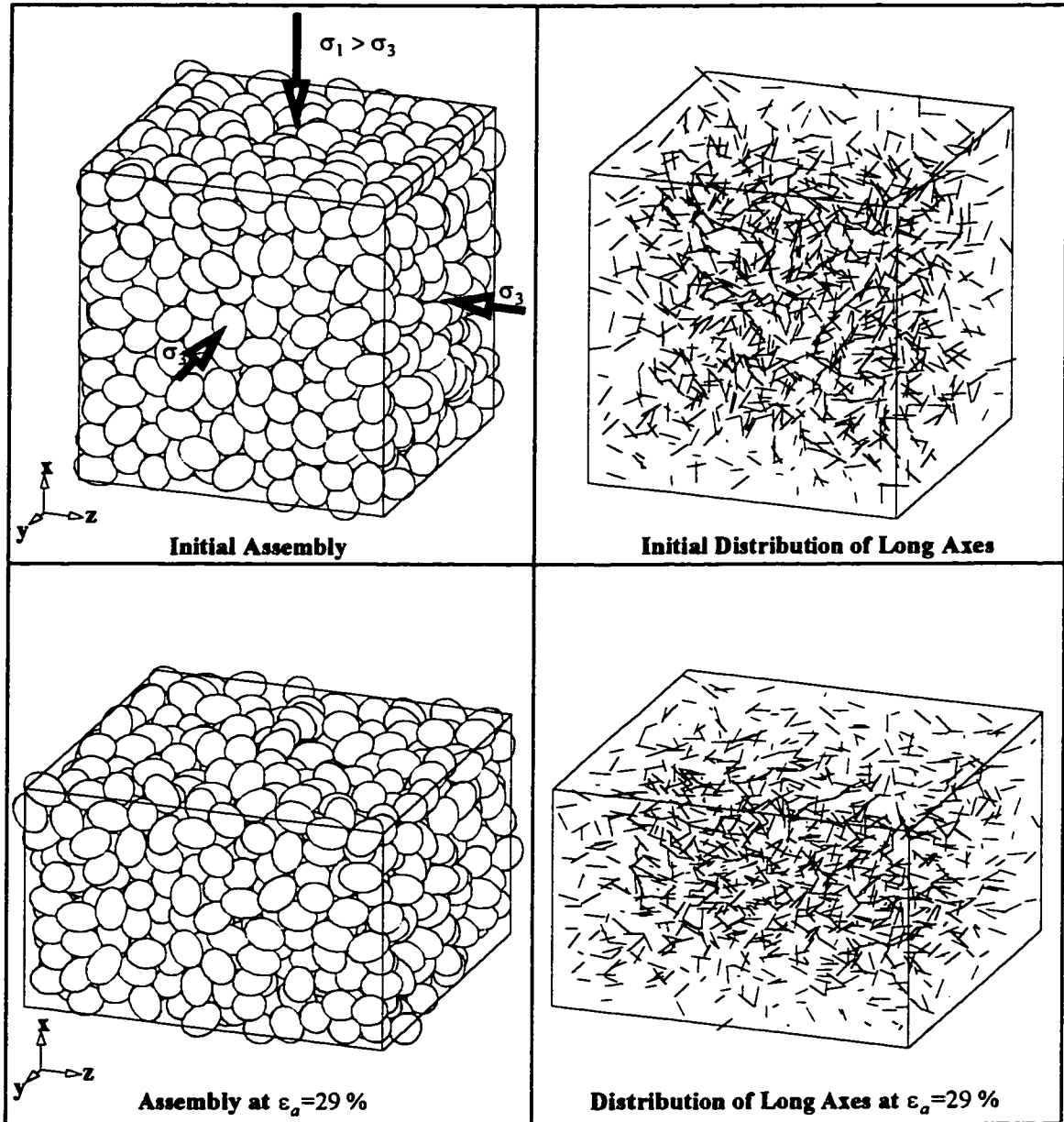


Figure 7-6 Geometry of a strained assembly (initially and at a large strain)

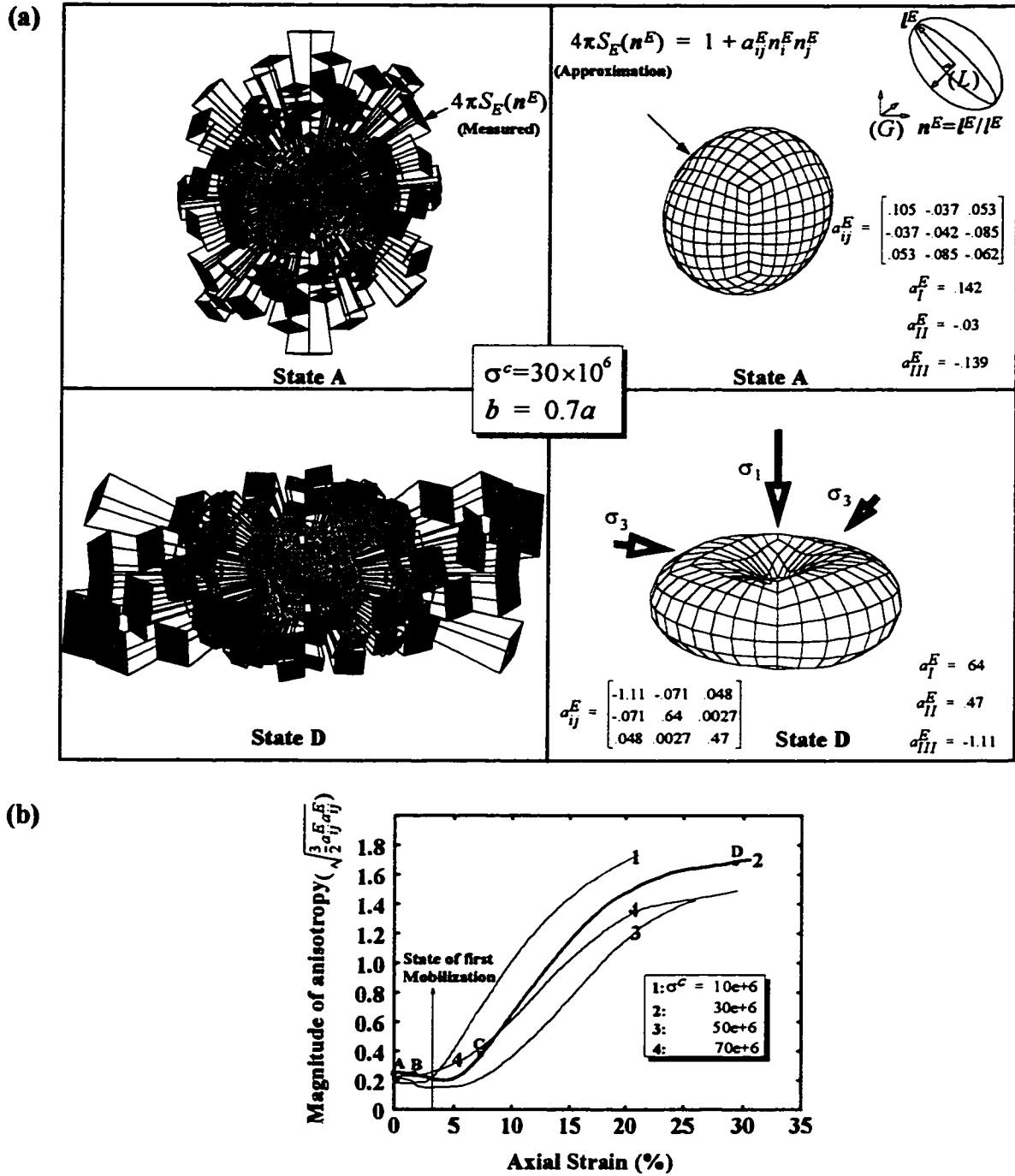


Figure 7•7 Illustration of induced anisotropy in ellipsoids' orientations
 (a) Histogram distributions (initially and at a large strain)
 (b) Magnitude of anisotropy vs. applied axial strain

It is observed that the initial anisotropy is essentially not altered but reinforced by shear deformation. It is interesting to note that this form of anisotropy is not mobilized until after the sample undergoes more than 3% applied axial strain (irrespective of the value of the applied confining stress). This corresponds to the state of the assembly where rotations start developing. Subsequently, the magnitude of anisotropy α^E is characterized by a hyperbolic type of increase, and convergence to a steady state of anisotropy at large strains.

7.4 Relationship Between Anisotropies in Contact Normal Orientation and Particle Orientation

It is difficult to uncouple and study separately the mechanisms of development in contact normal orientations and particle orientations, because these two mechanisms are associated with the same physical process, which is the creation and destruction of contacts. The interaction between the two mechanisms was illustrated previously when studying the effect of rotation on contact creation/destruction involving ellipsoidal particles.

This section is dedicated to a more-detailed treatment of a relationship between the two forms of anisotropy.

7.4.1 Relationship in Two Dimensions

A functional relationship exists between the contact normal orientation in the global coordinates θ_G^N , the local contact vector orientation β' , and the particle orientation, θ^E . The relationship is simple for disks in two dimensions and can be written as:

$$\theta_G^N = \beta' + \theta^E \quad (7 \cdot 26)$$

It is geometrically associated with the situation depicted in Figure 7•8a.

For ellipses in 2D, the effect of shape must be included in the relationship which takes the new form:

$$\theta_G^n = \Delta\theta' + \beta' + \theta^E \quad (7\bullet 27)$$

where $\Delta\theta'$ is called the deviation angle and measures the deviation of the contact normal from the local contact vector orientation as shown in Figure 7•8b. With the convention that the counterclockwise angles be counted positively, the deviation angle can be calculated in terms the particle semi-axes and the local contact vector orientation as follows:

$$\Delta\theta'(\beta') = \begin{cases} \Delta\theta'_+ & \text{if } 0 \leq \beta' \leq \frac{\pi}{2} \text{ or } \pi \leq \beta' \leq \frac{3\pi}{2} \\ -\Delta\theta'_+ & \text{if not} \end{cases} \quad (7\bullet 28)$$

where:

$$\Delta\theta'_+ = \cos^{-1} \left(\frac{\frac{\cos^2 \beta'}{a^2} + \frac{\sin^2 \beta'}{b^2}}{\sqrt{\frac{\cos^2 \beta'}{a^4} + \frac{\sin^2 \beta'}{b^4}}} \right) \quad (7\bullet 29)$$

It can be seen that if $a = b$, then the relationship (7• 29) yields $\Delta\theta' = 0$ (case of circular particles).

The plot of the deviation angle $\Delta\theta'$ with varying azimuth angle β' is shown in Figure 7•9.

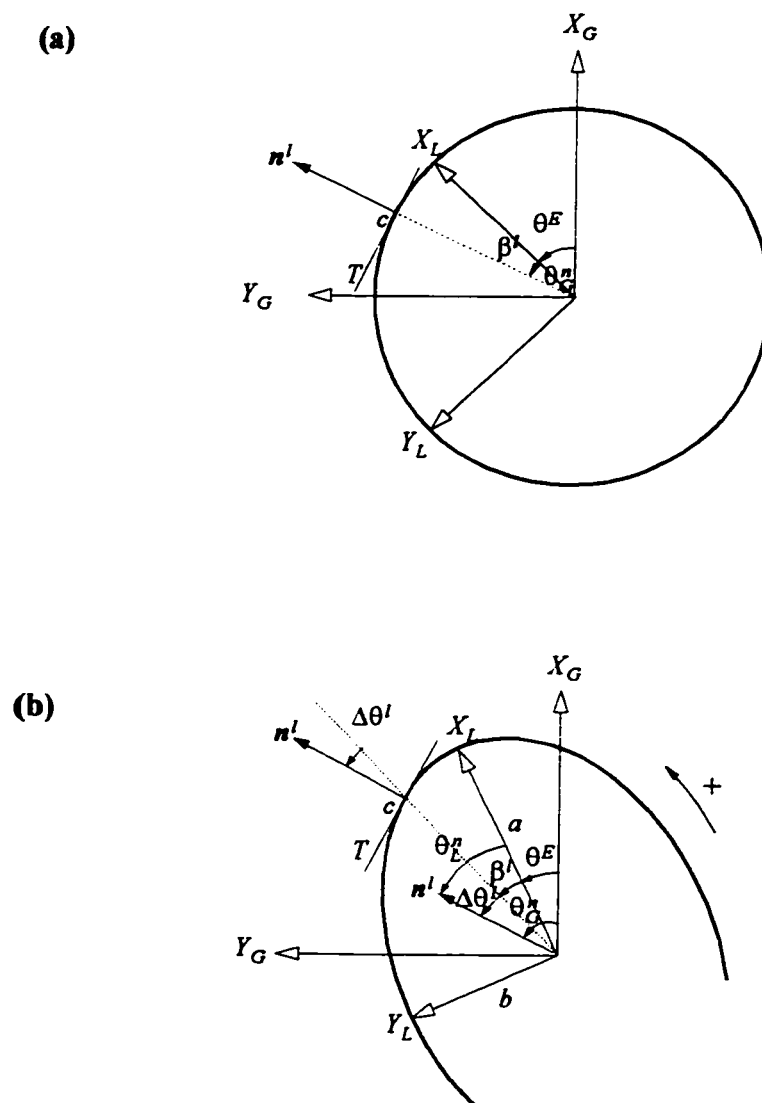


Figure 7-8 Relationship between orientations of the contact normal vector, the local contact vector, and the particle long-axis
(a) Disk
(b) Ellipse

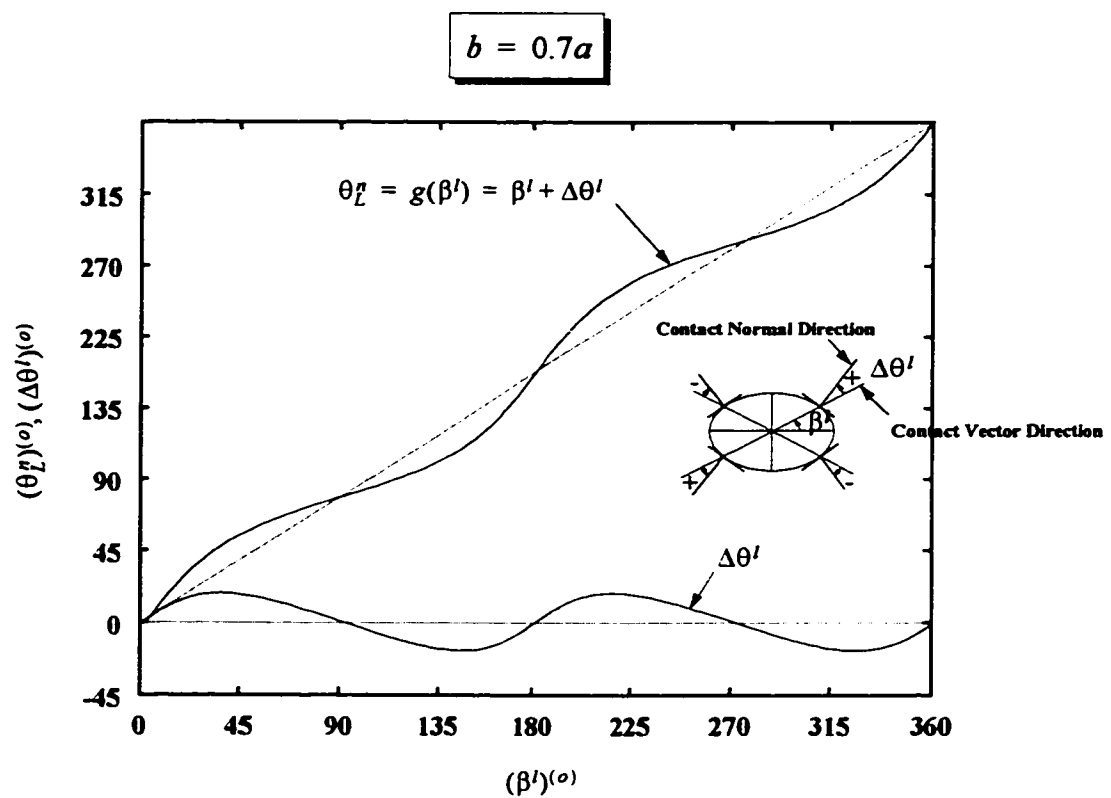


Figure 7-9 Variations of the deviation angle (between contact normal and contact vector) with varying contact position

The relationship in (7• 27) defines a continuous random variable θ_G^n as a sum of a continuous random variable, θ^E , and, a function of a continuous random variable, $g(\beta')$, *i.e.*:

$$\theta_G^n = g(\beta') + \theta^E \quad (7• 30)$$

where the subscript “G” is used for the global set of coordinates.

The function $g(\beta')$ is defined by:

$$g(\beta') = \beta' + \Delta\theta'(\beta') \quad (7• 31)$$

It represents the orientation of the contact normal vector in the ellipse local set of principal axes. This angle is denoted by θ_L^n in Figure 7•9; therefore:

$$\theta_L^n = g(\beta') \quad (7• 32)$$

where the subscript “L” is used for the local set of ellipse coordinates.

It is possible to derive the density of probability of a random variable defined in terms of other known random variables if certain conditions are fulfilled. In the case of the relationship (7• 30), the only necessary condition is that the function $g(\beta')$ be monotonic (*i.e.*, increasing or decreasing) and differentiable over the interval of variation of the random variable β' , $[0, 2\pi]$. If not, the interval must be divided into sub-intervals where the function is locally monotonic and differentiable. The plot of the function $\theta_L^n = g(\beta')$ is shown in Figure 7•8c. The function is increasing and differentiable, which means that the function is one-to-one, and that the inverse function $\beta' = g^{-1}(\theta_L^n)$ exists and is increasing and differentiable. It can be shown that under these conditions, the resulting density of probability of the local contact normal orientation $\theta_L^n = g(\beta')$ is given by:

$$S_{\theta_L^*}(\theta) = \frac{d}{d\theta}[g^{-1}(\theta)] \cdot S_i(g^{-1}(\theta)) \quad (7 \cdot 33)$$

where S_i is the density of probability of the random variable β' .

The derivation of relationship (7• 33) follows a simple logic of probability calculations. A brief outline of this logic is as follows:

Let $F_{\theta_L^*}(\theta)$ be the probability distribution function of the random variable $\theta_L^* = g(\beta')$, then by definition:

$$\begin{aligned} F_{\theta_L^*}(\theta) &= \text{Prob}\{\theta_L^* \leq \theta\} = \text{Prob}\{g(\beta') \leq \theta\} \\ &= \text{Prob}\{\beta' \leq g^{-1}(\theta)\} \\ &= F_{\beta'}(g^{-1}(\theta)) \end{aligned} \quad (7 \cdot 34)$$

The second identity in the above chain of identities is possible because the function $g^{-1}(\beta')$ is increasing. The relationship (7• 33) is the direct result of differentiating the last identity in (7• 34).

Now that the density of probability of the random variable function $g(\beta^c)$ is determined, the density of probability of the sum, $\theta_G^* = g(\beta^c) + \theta^E$, can be calculated by following a similar logic to that used for deriving the density of probability of $g(\beta^c)$. The result is as follows:

$$S_{\theta_G^*}(\theta) = \int_0^{2\pi} S_{\theta_L^*, E}(u, \theta - u) du \quad (7 \cdot 35)$$

where $S_{\theta_L^*, E}$ is the joint density of probability of the pair of random variables (θ_L^*, θ^E) . Unfortunately, it was not possible to calculate an accurate approximation of the joint probability based on measured data, because this would require that the crossed classes of orientations of the pair (θ_L^*, θ^E) contain a minimum number of observations to adequately

represent the class. It has been seen previously that the 1000 particle assemblies in three dimensions can barely support histogram calculations of single random variables since the number of observations per class is just large enough to calculate meaningful averages of these variables (on average between 15 to 30 observations per class for contact variables such as θ_L^r and only 5 observations per class for particle variables such as θ^E). Crossed classes would contain even fewer observations than single classes. In two dimensions, there are no reports of the joint distribution data available that could be used to develop the relationship in (7• 35). Nonetheless, at this stage of the relationship, the proof of a functional equation relating tensors of anisotropies in contact normal orientations, particle orientations and local contact orientations has been established.

One way to pursue further the development of the relationship is to assume that the distribution of contact vector orientations is statistically independent from the distribution of particle orientations. This means that the joint density of probability will degenerate to the product of the marginal densities and the relationship (7• 35) to:

$$S_{\theta_G^n}(\theta) = \int_0^{2\pi} S_{\theta_L^n}(u) S_E(\theta - u) du \quad (7• 36)$$

where S_E is the probability density function of θ^E .

Substituting of (7• 33) in the above equation results in:

$$S_{\theta_G^n}(\theta) = \int_0^{2\pi} \frac{d}{du} [g^{-1}(u)] \cdot S_l(g^{-1}(u)) S_E(\theta - u) du \quad (7• 37)$$

By operating the variable change, $v = g^{-1}(u)$, the above equation can be re-written as:

$$S_{\theta^E}(\theta) = \int_0^{2\pi} S_I(v) S_E(\theta - g(v)) dv \quad (7 \cdot 38)$$

Provided that the probability density functions $S_I(\beta)$ and $S_E(\theta^E)$ be known in two dimensions, the relationship between tensors of anisotropy can now be derived from integrating the right hand side of the above equation.

The near constancy of the local contact vector distribution shape observed during simulations, concern a virtual particle representing some “average” particle behaviour with respect to the local contact vector distribution. However, the environment surrounding specific particles is different from one location to another and this is easy to understand. For instance, if the distribution of contacts is initially uniformly distributed in the sample space (isotropic distribution), heterogeneity will soon affect this distribution owing to the disintegration of contacts in the lateral directions. By assuming the above statistical independence while extending the average behaviour to all particles, it is implicitly assumed that the process of contact formation and destruction (which is the main mechanism of anisotropy development) is at a stage where homogeneity of contact distribution is still a reasonable assumption. This assumption holds in the smaller range of axial deformation.

In order to be able to work with the assumption of independence over the full range of applied deformation, it is necessary to distinguish between two types of contributions to the anisotropy that develops in contact normal orientations: (1) due to ellipsoids’ rotations; and (2) due to other factors. Therefore, the total distribution of contact normal orientation distribution must be split into two terms as follows:

$$S_{\theta_G^r}(\theta) = \frac{1}{2\pi} [1 + a'_{\text{Rot}} \cos 2(\theta - \theta_o)] + \frac{1}{2\pi} [(a' - a'_{\text{Rot}}) \cos 2(\theta - \theta_o)] \quad (7 \cdot 39)$$

According to the assumption of statistical independence, only the term of “rotations” is considered.

Published results of numerical simulations with ellipses in two dimensions (*e.g.*, Bathurst & Rothenburg, 1992; Rothenburg and Bathurst, 1992) show that a “peanut” shape was observed for the distribution of particle orientation, S_E , during these simulations. There are no data available for the distribution of the local contact vector orientation, but there are strong indications that the shape of S_l will also be a “peanut” (at least by analogy with the 3D case, for example); therefore, the following assumption should be plausible:

$$\begin{cases} S_E(\theta^E) = \frac{1}{2\pi} [1 + a^E \cos 2(\theta^E - \theta_o^E)] \\ S_l(\beta') = \frac{1}{2\pi} [1 + a^{cVL} \cos 2(\beta' - \beta_o)] \end{cases} \quad (7 \cdot 40)$$

where θ_o^E and β_o are major directions of anisotropy in particle orientations and local contact vector orientations, respectively.

Substituting the above equations into (7• 38), and integrating results in:

$$S_{\theta_G^r}(\theta) = \frac{1}{2\pi} \{ 1 + a^E((c_1 + a^{cVL}c_2)\cos 2\theta) + a^E(s_1 + a^{cVL}s_2)\sin 2\theta \} \quad (7 \cdot 41)$$

where:

$$\begin{cases} c_1 = \frac{1}{2\pi} \int_0^{2\pi} \cos[2(g(v) + \theta_o^E)] dv \\ c_2 = \frac{1}{2\pi} \int_0^{2\pi} \cos 2(v - \beta_o) \cos[2(g(v) + \theta_o^E)] dv \\ s_1 = \frac{1}{2\pi} \int_0^{2\pi} \sin[2(g(v) + \theta_o^E)] dv \\ s_2 = \frac{1}{2\pi} \int_0^{2\pi} \cos 2(v - \beta_o) \sin[2(g(v) + \theta_o^E)] dv \end{cases} \quad (7 \cdot 42)$$

The relationship in (7• 41) should be compared with the usual peanut shape of the contact normal orientation distribution:

$$S_{\theta_o^E}(\theta) = \frac{1}{2\pi} [1 + a^r \cos 2(\theta - \theta_o)] \quad (7 \cdot 43)$$

where a^r and θ_o are the coefficient and major direction of anisotropy, respectively.

The comparison of relationships (7• 41) and (7• 43) suggests that the anisotropy coefficient a^r and the direction of anisotropy θ_o are given as:

$$\begin{cases} a_{R\alpha}^r = a^E \sqrt{(c_1 + a^{cvL} c_2)^2 + (s_1 + a^{cvL} s_2)^2} \\ \cos 2\theta_o = (c_1 + a^{cvL} c_2) / \sqrt{(c_1 + a^{cvL} c_2)^2 + (s_1 + a^{cvL} s_2)^2} \\ \sin 2\theta_o = (s_1 + a^{cvL} s_2) / \sqrt{(c_1 + a^{cvL} c_2)^2 + (s_1 + a^{cvL} s_2)^2} \end{cases} \quad (7 \cdot 44)$$

7.4.1.1 Assemblies of Ellipses in the Biaxial Test

Assemblies of ellipses in the biaxial test are usually characterized by typical directions of anisotropy, as has been observed many times by numerical simulations (*e.g.*, Rothenburg and Bathurst, 1992). The following values are observed for the contact normal orientation and particle orientation distributions:

$$\begin{cases} \theta_o = 0 & \text{(Vertical)} \\ \theta_o^E = \frac{\pi}{2} & \text{(Horizontal)} \end{cases} \quad (7 \cdot 45)$$

For the direction of anisotropy of the local contact vector orientation distribution, the analogy with the three-dimensional case suggests that $\beta_o = 0$. With these particular values of anisotropy directions the coefficients $c_{i,(i=1,2)}$ and $s_{i,(i=1,2)}$ become equal to:

$$\begin{cases} c_1 = -\frac{1}{2\pi} \int_0^{2\pi} \cos[2g(v)] dv \\ c_2 = -\frac{1}{2\pi} \int_0^{2\pi} \cos 2v \cos[2g(v)] dv \\ s_1 = -\frac{1}{2\pi} \int_0^{2\pi} \sin[2g(v)] dv \\ s_2 = -\frac{1}{2\pi} \int_0^{2\pi} \cos 2v \sin[2g(v)] dv \end{cases} \quad (7 \cdot 46)$$

The integrals defining the coefficients $c_{i,(i=1,2)}$ and $s_{i,(i=1,2)}$ were numerically integrated for varying ellipse aspect ratio. The results are plotted in Figure 7•10a. As can be seen, the $s_{i,(i=1,2)}$ coefficients are always equal to zero and $c_{i,(i=1,2)}$ are always different from zero. The coefficient c_1 , which is always positive, increases with increasing aspect ratio, and the coefficient c_2 , which is always negative, decreases in absolute value with increasing aspect ratio.

For a given aspect ratio, an arbitrary coefficient corresponds to the area of the domain delimited by the integral function curve defining the coefficient and the coordinate axes (Figure 7•10b).

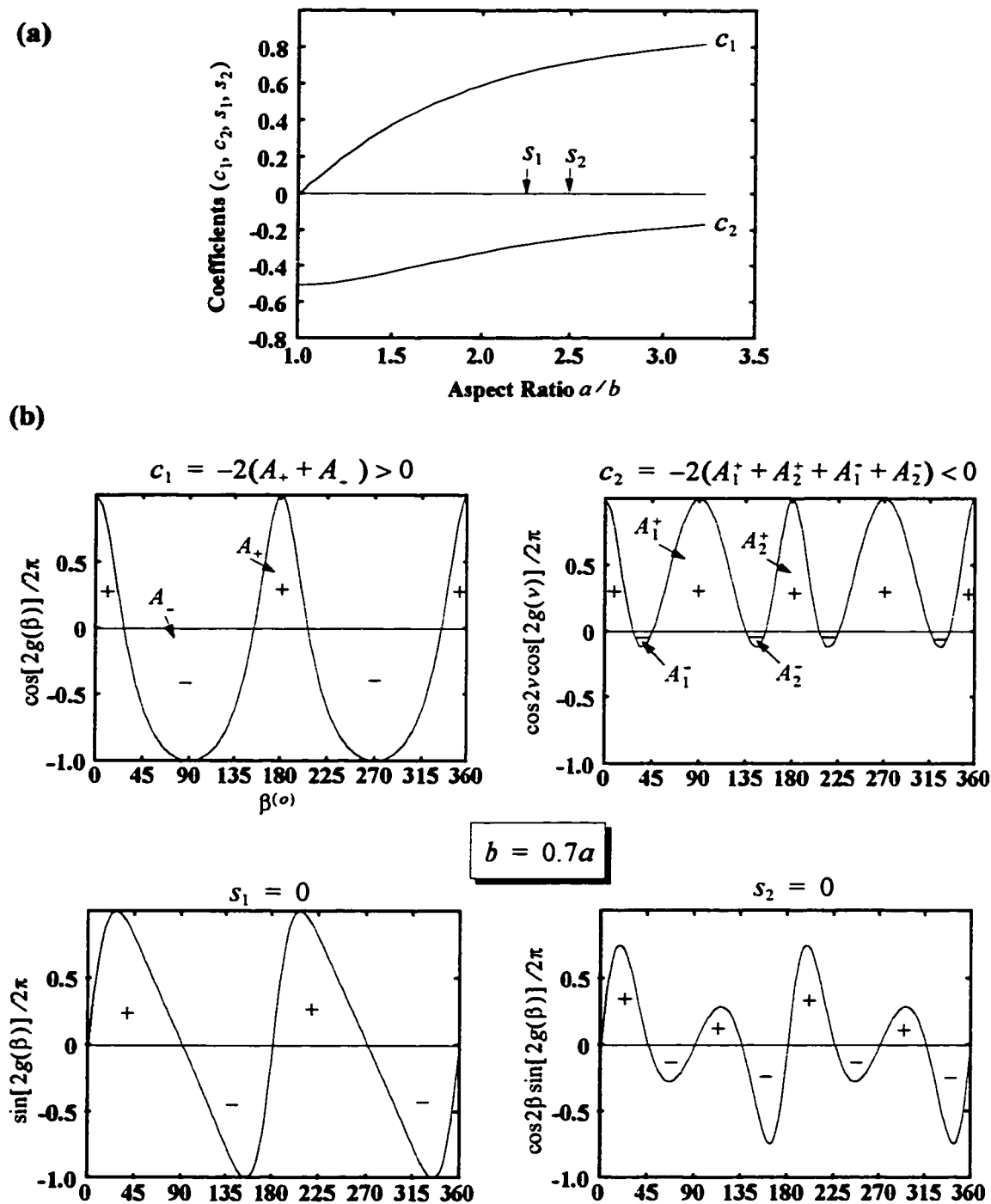


Figure 7•10 Illustration of coefficients, c_1 , c_2 , s_1 , and s_2 , and their variation with particle shape

As a result of having $s_1 = s_2 = 0$, the general relationship in (7• 44) can be simplified as follows:

$$\begin{cases} a_{R\alpha}^r = a^E |c_1 + a^{cvL} c_2| \\ \cos 2\theta_o = (c_1 + a^{cvL} c_2) / |c_1 + a^{cvL} c_2| \\ \sin 2\theta_o = 0 \end{cases} \quad (7• 47)$$

According to the above result, the contribution of rotations to the fabric anisotropy $a_{R\alpha}^r$ is proportional to the degree of anisotropy in particle orientations a^E . The coefficient of proportionality is linearly dependent on parameter a^{cvL} .

As already mentioned, no data are available in two dimensions for this parameter, but it is possible to estimate it from the assumption (proven to be fairly accurate in 3D) that the density of probability of finding a contact at a certain location on the circumference of an ellipse is proportional to the elemental length around that location (Figure 7• 11a). The assumption can be written as follows:

$$S_I(\beta') d\beta \equiv \frac{ds}{C_E} \quad (7• 48)$$

where C_E is the ellipse circumference.

The elemental length ds can be calculated in terms of β' as illustrated in Figure 7• 11a. The result is:

$$ds = l d\beta \cos \Delta\theta' \quad (7• 49)$$

Therefore:

$$S_I(\beta') \equiv \frac{l \cos \Delta\theta'}{C_E} \quad (7• 50)$$

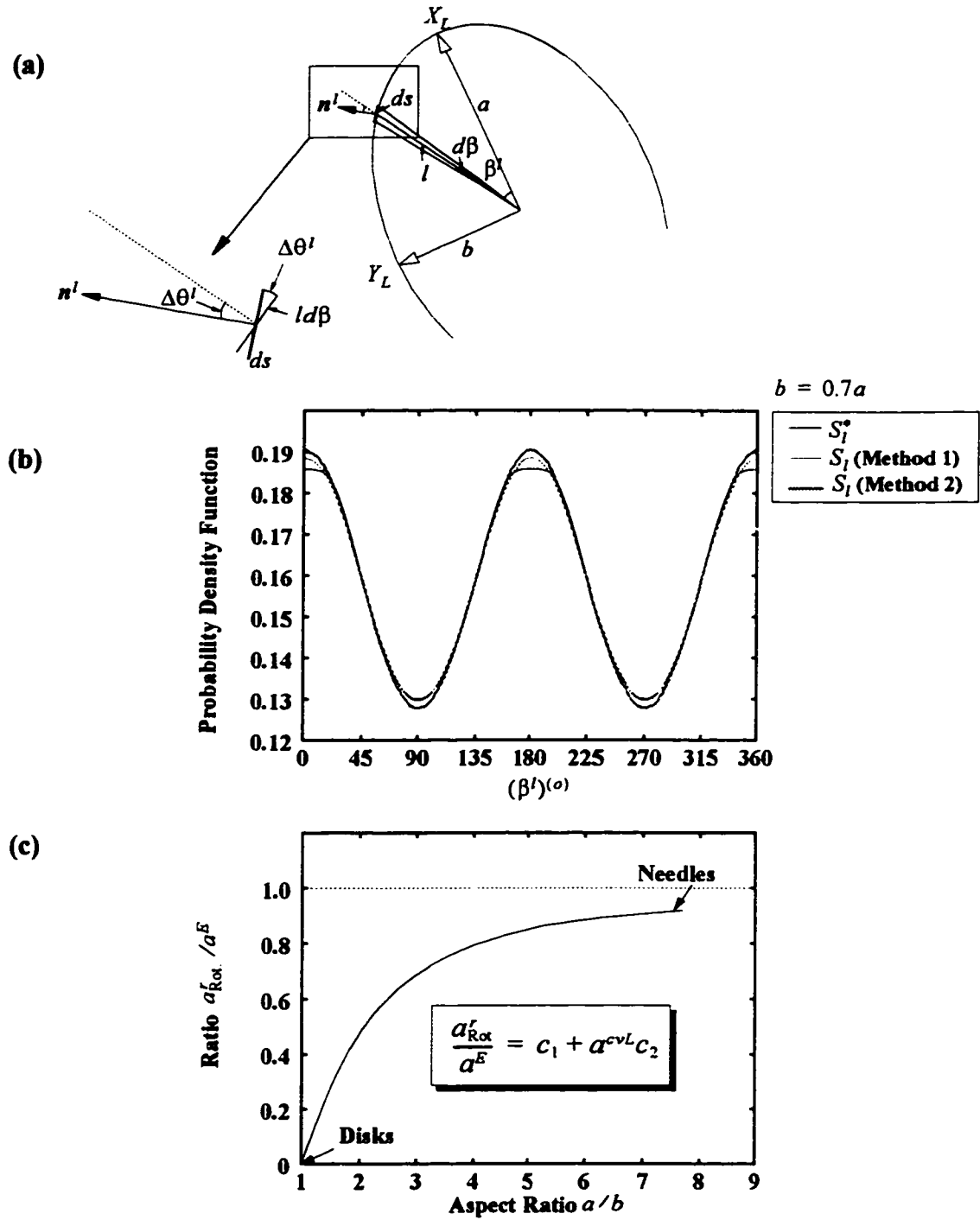


Figure 7•11 Contribution of rotations to the anisotropy in contact normal orientations

Substituting of l from (7• 15), and $\Delta\theta'$ from (7• 29), into the above equation results in the density of probability of local contact vectors being approximated by:

$$S_l(\beta') \cong \frac{1}{C_\varepsilon} \sqrt{\frac{\frac{\cos^2 \beta'}{a^4} + \frac{\sin^2 \beta'}{b^4}}{\left(\frac{\cos^2 \beta'}{a^2} + \frac{\sin^2 \beta'}{b^2}\right)^3}} \quad (7• 51)$$

The coefficient of anisotropy α^{cvL} should be such that the actual distribution $S_l(\beta') = \{1 + \alpha^{cvL} \cos 2\beta'\} / 2\pi$ be as close as possible to the above approximation. Two methods are available to estimate α^{cvL} :

1. Calculate α^{cvL} as:

$$\alpha^{cvL} \cong 2 \int_0^{2\pi} S_l^*(\beta) \cos 2\beta d\beta \quad (7• 52)$$

2. Calculate α^{cvL} by the Least Squares method. The minimization of the squares' sum, $\Sigma(S_l(\beta_i) - S_l^*(\beta_i))^2$, yields:

$$\alpha^{cvL} \cong - \sum_{i=1}^N \cos 2\beta_i (1 - 2\pi S_l^*(\beta_i)) / \sum_{i=1}^N \cos^2 2\beta_i \quad (7• 53)$$

where S_l^* denotes the approximation of the actual S_l density function; S_l^* is given by the right hand side of equation (7• 51); $(\beta_i)_{i=1,N}$ is an arbitrary subdivision of the interval $[0, 2\pi]$.

The approximation S_l^* and predicted density functions, based on the above methods, are plotted in Figure 7•11b.

The values calculated by the Least Squares method were substituted into relationship (7• 47) to calculate the ratio $\alpha_{\text{Rot}}^L / \alpha^E$ for varying ellipse aspect ratios. The results are presented in the plot of Figure 7•11c.

As can be seen, the contribution of rotations to fabric anisotropy increases with particle eccentricity. This is consistent with the fact that the moment of inertia around the centre mass of an ellipse increases with eccentricity and therefore two ellipses A and B with the same masses but different eccentricities, say, $(a/b)_A > (a/b)_B$ will rotate by angles $\Delta\theta_A > \Delta\theta_B$ under the same applied moment, which shows that rotation increases with particle eccentricity and so does the fabric anisotropy related to rotations. Figure 7•11c shows also that the quantity $c_1 + \alpha^{cvL}c_2$ is always positive. This implies that the relationship (7•47) can be simplified as follows:

$$\begin{cases} a_{\text{rot}}^r = \alpha^E(c_1 + \alpha^{cvL}c_2) \\ \theta_o = 0 \end{cases} \quad (7•54)$$

which shows that the direction of anisotropy in contact normal orientations (vertical direction) is accurately predicted.

The relationship illustrated in Figure 7•11c is based on the assumption that the local environment of each particle remains homogeneous during the deformation process. It is quite conceivable that at large strains, when α^E reaches its limit, the assumption will break down and particle rotations will no longer be able to compensate for the tendency to contact disintegration.

7.4.2 Relationship in Three Dimensions

For ellipsoids in 3D, the relationship between the contact normal orientation (in global coordinates), the ellipsoid orientation, and the local contact vector orientation is more complex than in 2D. An ellipsoid in 3D is characterized by two additional degree of free

motion and the definition of a particle orientation involves at least three angles (for example, Euler's angles illustrated in Figure 7•12). Euler's angles are defined by three rotation angles such that after the third rotation the global set of axes and the local set of ellipsoid axes are the same.

If the three Euler's angles are denoted by Θ^E , Φ^E , and Ψ^E , and the corresponding rotations are represented by matrices R_{Θ^E} , R_{Φ^E} , and R_{Ψ^E} , respectively, then the components of the unit contact normal vector in local coordinates, $[\mathbf{n}]^L$, and those in global coordinates, $[\mathbf{n}]^G$, would be related as follows:

$$[\mathbf{n}]^G = R_{(-\Phi^E)} \cdot R_{(-\Theta^E)} \cdot R_{(-\Psi^E)} \cdot [\mathbf{n}]^L \quad (7•55)$$

The components of the unit contact normal vector in local coordinates $[\mathbf{n}]^L$ can be expressed only in terms of the pair of angles defining the local contact vector orientation (α', β') and the ellipsoid semi-axes $(a \geq b \geq c)$ as:

$$[\mathbf{n}]^L = \begin{bmatrix} \cos \beta' / a^2 \\ \cos \alpha' \sin \beta' / b^2 \\ \sin \alpha' \sin \beta' / c^2 \end{bmatrix} / \sqrt{\frac{\cos^2 \beta'}{a^4} + \left(\frac{\cos^2 \alpha'}{b^4} + \frac{\sin^2 \alpha'}{c^4} \right) \sin^2 \beta'} \quad (7•56)$$

Substitution of the right hand side of equation (7•56) and expressions of matrices R_{Θ^E} , R_{Φ^E} , and R_{Ψ^E} , given in Figure 7•12, into the relationship (7•55) results in an expression of the unit contact normal vector components in global coordinates $[\mathbf{n}]^G$ in terms of the five random variables: Θ^E , Φ^E , Ψ^E , α' , and β' .

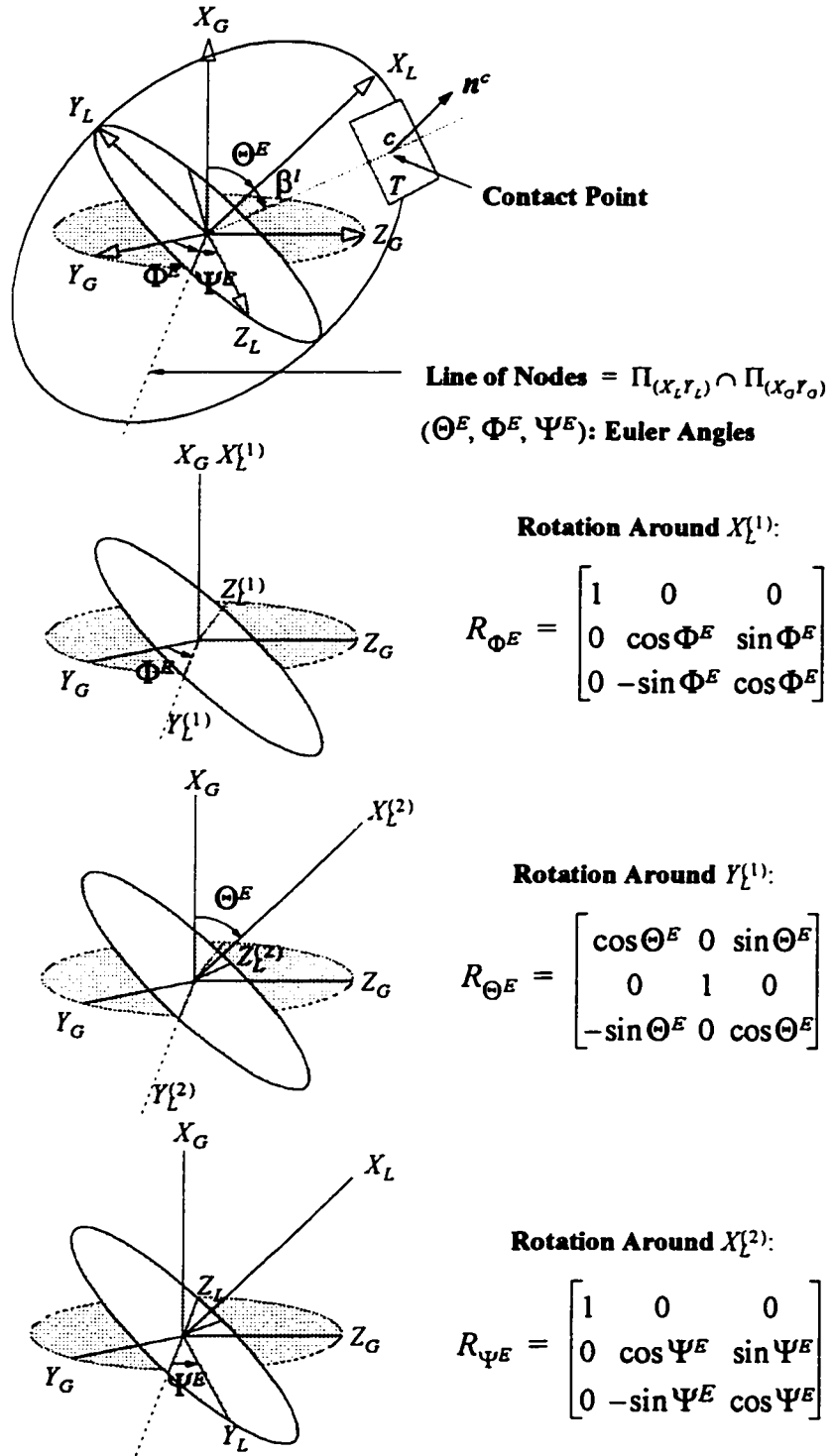


Figure 7-12 Definition of an ellipsoid's orientation in terms of Euler's angles

In view of the complexity of the above equations, an analytical relationship between the probability density functions of the random vector $[n]^G$ and variables characterizing the ellipsoid orientation (Θ^E , Φ^E , and Ψ^E) and the local contact location (α' , β') seems to be difficult to derive.

Even in the case of prolate spheroids, where the number of independent parameters is reduced, the task of relating probabilities analytically can be very tedious and is not pursued further.

7.5 Conclusions

In this chapter, the effect of shape was analyzed in connection with parameters describing the load-induced fabric anisotropy during shear deformation of simulated assemblies of ellipsoids. The findings are summarized below.

- i. The average distribution of contact location on the surface of an ellipsoid is affected by the shape of the particle and seems to be uniquely dependent on this parameter. These distributions were used to predict the proportions of contacts characterized by vector lengths in the short, intermediate and long ranges and compared to measured proportions. The prediction matched the observation and more than 50% of contacts were found to be located in the short range of vector lengths. It seems that the stability of an elongated particle is conditioned by the creation of contacts near its flat surface areas.

- ii. The anisotropy in particle orientations was also observed to be biased by the shape of particles, especially at large strains where the orientation of ellipsoid long axes is predominantly horizontal.
- iii. A model to estimate the influence of shape on the contact normal orientation anisotropy was developed for plane ellipses. The model predicts that the fraction of contribution to the contact normal orientation anisotropy, α_{Rot}^r , is proportional to the degree of anisotropy in particle orientations α^E . The coefficient of proportionality $\alpha_{\text{Rot}}^r / \alpha^E$ is linearly dependent on the degree of anisotropy in local contact vector orientation α^{vL} . For a given state of the assembly of particles, the contribution $\alpha_{\text{Rot}}^r / \alpha^E$ increases with increasing ellipse eccentricity: from zero (for disks) to one (for needles). The model in three dimensions is analytically complex because of the presence of many random variables in highly non-linear expressions.

CHAPTER VIII: CONCLUSIONS AND RECOMMENDATIONS

8.1 General

The purpose of this study was to develop a three-dimensional discrete element model to simulate the mechanical behaviour of dry systems of granules of non-spherical shapes. This work was motivated by the observation that spheres have a tendency to roll and to lock up at low coordination numbers, unlike real dense sands, and could not replicate some of the aspects of the behaviour of actual systems of non-spherical particles, especially those related to particle shape effects. These effects are not negligible, as proved by this 3D study and by previous studies in two and three dimensions (Konishi *et al.*, 1982, 1983; Oda *et al.*, 1983; Rothenburg and Bathurst, 1992, 1993; Mirghasemi, 1994; amongst others). The ellipsoidal shape of particles was the best candidate for constructing the new

CHAPTER VIII: CONCLUSIONS AND RECOMMENDATIONS

model as it has many features advantageous to developing such a model: uniformity, continuous outward normals, elongated and flat shape, and a simple mathematical representation in space. The major challenge was the implementation of a reliable inter-ellipsoid contact detection scheme that would not fail in detecting any contact, irrespective of particles' relative positions, dimensions and orientations, but would involve a reasonable computational effort.

The modeling of granular materials by the method of discrete elements methods has uncountable qualities of flexibility, generality, easy access to any microscopic data of any kind, and so on. However, it suffers from the fact that it involves an intense effort of computer calculation. The state of an assembly in the course of deformation needs to be updated at every time-step. The time-step is not fully controlled by the user of the model, but by considerations of stability of the explicit finite difference scheme used to update positions of particles after undergoing incremental motions. The time-step can be very small and conducting tests with a relatively large-sized sample up to the beginning of steady-state of deformation can require millions of cycles (this was the case with ellipsoids).

The computational cost at every cycle is dependent on the robustness of the contact detection scheme, the size of the sample, and the density of contacts within the assembly of particles. The simulations reported here were intended to replicate the mechanical behaviour of dense sands. A reasonable size of the assembly of particles that allows a meaningful representation of average microscopic parameters, based on statistics of contacts and particles, should be of the order of several hundreds. One thousand particles was selected as the size of the main assembly to be used for the analysis of results. Initial assem-

CHAPTER VIII: CONCLUSIONS AND RECOMMENDATIONS

bly coordination numbers were set to their maximum (on average twelve contacts per particle) by a special method of sample preparation. At the densest state of the assembly of particles, the program must compute at each cycle 6000 physical contacts, and near steady-state, 3000 contacts. A lower limit of contacts calculated for a typical test is, $7e+6 \times 3000 = 21e+9$ contacts; the upper limit is double this number. It was therefore of primary importance to construct a detection scheme of high efficiency, once the method of solving the ellipsoid-to-ellipsoid intersection problem was selected.

This task and the treatment of the mechanics of ellipsoidal rigid bodies were successfully implemented in an existing discrete element program (TRUBAL) originally designed to work with spherical particles. All results of simulation reported in this study were obtained with the modified program TRUBAL for ellipsoids.

The other objective was to utilize the numerical model to shed some light on the peculiar aspects of the behaviour of assemblies of ellipsoids, and, in particular, those related to the pressure sensitivity of granular systems and influence of particle shape. A simple shape was selected where only the elongation aspect ratio was different than one (prolate spheroids), allowing in the meantime for creation of analogues of two-dimensional ellipses for comparison of results between the two cases. The effect of gradation on the mechanical behaviour was also eliminated from interfering with the shape effect by testing mono-size assemblies of prolate spheroids.

Both effects have been examined from the macroscopic and microscopic point of view throughout this thesis.

The conclusions that can be drawn from this study are summarized below. Recom-

mendations for future research are suggested at the end of the Chapter.

8.2 Microscopic Description of Granular Material Behaviour

The approach proposed by Rothenburg (1980) to represent spatial variations of microscopic variables using approximations by truncated Fourier series proved well adapted to the case of ellipsoids. However, departures from the second-order approximations were observed, especially for the average tangential contact force distribution. The correction by an additional fourth-order anisotropy tensor-related term was sufficient to adjust the second-order Fourier approximation to simulated data. The differences between observed and approximated second-order Fourier distributions of average normal and tangential contact forces were represented by:

$$\begin{cases} \Delta E(\mathbf{n}) = \frac{1}{4\pi} (b_{ijkl}^r n_i n_j n_k n_l) \\ \Delta \bar{f}(\mathbf{n}) = \bar{f} (b_{ijkl}^n n_i n_j n_k n_l) \\ \Delta \bar{f}_i^t(\mathbf{n}) = \bar{f} (b_{ijkl}^t n_j n_k n_l - b_{iklm}^t n_j n_k n_l n_m n_i) \quad i=1, 3 \\ b_{ijkl}^r = b_{\pi(ijkl)}^r \\ b_{ijkl}^n = b_{\pi(ijkl)}^n \\ b_{ijkl}^t = b_{\pi(ijkl)}^t \end{cases} \quad (8 \cdot 1)$$

where b_{ijkl}^r , b_{ijkl}^n , and b_{ijkl}^t , describe fully symmetric fourth-order anisotropy tensors; π denotes an arbitrary permutation of indices $(ijkl)$; \bar{f} is the normal contact force magnitude average, taken over groups of contact normal orientation (not over individual contacts); and \mathbf{n} is the unit contact normal vector.

Methods of estimation of these tensors from simulated data were proposed based on derived tensorial relationships between the fourth-order anisotropy tensors b_{ijkl}^r , b_{ijkl}^n , and

b'_{ijkl} , and well-defined second and fourth-order tensors that can be estimated from a finite number of contacts. They are termed fabric tensors (ΔR_{ij} , ΔR_{ijkl}), average normal contact force tensors (ΔF_{ij}^n , ΔF_{ijkl}^n), and average tangential contact force tensors (ΔF_{ij}^t , ΔF_{ijkl}^t), respectively. They are defined for finite systems of particles as discrete sums:

$$\begin{aligned}
 &\text{Fabric Tensors} \quad \left\{ \begin{aligned} \Delta R_{ij} &= \frac{1}{M} \sum_{c \in V} n_i^c n_j^c \\ \Delta R_{ijkl} &= \frac{1}{M} \sum_{c \in V} n_i^c n_j^c n_k^c n_l^c \end{aligned} \right. \\
 &\text{Average Normal} \\
 &\text{Contact Force Tensors} \quad \left\{ \begin{aligned} \Delta F_{ij}^n &= \frac{1}{4\pi} \sum_g \Delta \bar{f}^n(n^g) n_i^g n_j^g |\Delta n^g| \\ \Delta F_{ijkl}^n &= \frac{1}{4\pi} \sum_g \Delta \bar{f}^n(n^g) n_i^g n_j^g n_k^g n_l^g |\Delta n^g| \end{aligned} \right. \quad (8 \cdot 2) \\
 &\text{Average Tangential} \\
 &\text{Contact Force Tensors} \quad \left\{ \begin{aligned} \Delta F_{ij}^t &= \frac{1}{4\pi} \sum_g \Delta \bar{f}^t(n^g) n_j^g |\Delta n^g| \\ \Delta F_{ijkl}^t &= \frac{1}{4\pi} \sum_g \Delta \bar{f}^t(n^g) n_j^g n_k^g n_l^g |\Delta n^g| \end{aligned} \right.
 \end{aligned}$$

Here, M is the total number of contacts; V is the assembly volume; n^g is the unit contact normal vector of the group of orientations (g); and $|\Delta n^g|$ is the size of this group.

The fourth-order tensor b'_{ijkl} , in particular, reflects the departure in the tangential contact force behaviour from the assumed second-order model, which was previously found to be accurate for bonded systems of spheres. Such departures exist even for the latter systems but they are not as dramatic as revealed in the case of systems made of cohesionless non-circular shaped particles where large-scale local deformations can take place.

The 3D-plots of the average tangential contact force distribution were transferred to the plane in order to better visualize the effect of the fourth-order term in the approximation of these distributions. It was observed that both the size of the distribution and the di-

rection of maximum average tangential contact force were adjusted by the fourth term to match actual data.

A new method of decomposition of the space in classes of orientation was proposed and used for 3D-histogram plots of different microscopic variables. The method generates nearly equal size classes instead of the very much scattered class sizes obtained by the classical space partitioning with a single set of spherical coordinates. The biases induced by differences in class sizes when calculating averages over groups of contacts are eliminated by this method.

The link that exists between the macroscopic behaviour and microscopic behaviour was also discussed from the particular perspective of expressing the average stress tensor (for discrete systems) in terms of microscopic parameters representing different anisotropies (whether pre-existing and/or developed as a response to the applied load). These anisotropies concern primarily biases in the spatial distributions of contact normal orientations, contact vector length and orientations, and components of contact forces. The equation of the stress tensor as a discrete sum of microscopic quantities for finite systems expresses this link directly, comprehensively, and without approximation. The equation simply translates the condition of equilibrium inside the system of particles. For large systems, the spectrum of possible orientations of the unit contact normal vector tends to cover the three-dimensional space. As a result, the discrete sum can be extended to a continuous integral over the unit sphere (three-dimensional space), and the discontinuous distributions to continuous functions. The relative simplicity of the continuous integral opens prospects of further development of the relationship, once the continuous distributions can

be given precise mathematical descriptions.

8.3 Inter-Ellipsoid Contact Detection Algorithm

A series of direct tests conducted with the developed three-dimensional inter-ellipsoid contact detection scheme was used to validate the scheme. In particular, a comparison with a two-dimensional scheme for plane ellipses, based on a sample comprising of 1000 ellipses and nearly 3000 contacts, showed that the differences in estimated overlap distances by the two schemes are only detectable at the third decimal.

Coordination numbers of twelve and more were computed for dense assemblies of smooth ellipsoids in static equilibrium. These coordination numbers resulted from a progressive shape transformation process where the assembly evolved under a constant mean pressure. The obtained assembly coordination numbers matched perfectly the predictions made based on theoretical grounds. This result can be regarded as another validation of the inter-ellipsoid contact detection scheme.

8.4 Results of Particle Growth

Results of the shape transformation procedure demonstrate that this is an effective way of generating samples of ellipsoids of high contact density. The shape of ellipsoids is certainly responsible for achieving coordination numbers of eleven and more, when conditions of static equilibrium can be enforced throughout the growth simulation process. Such values of coordination number cannot be numerically attained with randomly packed assemblies of spheres.

It was also revealed that a small increase in aspect ratio of prolate spheroids, even as small as 5%, is enough to generate a jump in the coordination number from six or seven to over ten contacts per particle on average. This trend was observed in two-dimensional assemblies of ellipses in similar conditions of growth.

There seems to be an optimal aspect ratio of about 1: 1.4 at which the average packing density and coordination number of the growing assembly of prolate spheroids are the largest. The same phenomenon was observed in two dimensions with an optimal aspect ratio which is close to the three-dimensional value. Similarities between the 2D and 3D cases concern also the variations of initial coordination number and packing density with eccentricity (Rothenburg and Bathurst, 1992).

8.5 Behaviour of Assemblies of Ellipsoids in the Deviatoric Compression Test at Constant Mean Pressure

A series of deviatoric compression tests at constant mean pressure has been performed with the numerical ellipsoidal model using assemblies of mono-size prolate spheroids of three sizes (27, 125, 1000). The larger assembly was tested at five different confining pressures to investigate the effect of confining pressure.

The results of the simulations are summarized below.

8.5.1 Macroscopic Behaviour

The constant mean pressure deviatoric compression of assemblies of mono-size prolate spheroids revealed characteristics of behaviour that are similar to real granular materials, both qualitatively and quantitatively. The mobilized shear strength of simulated

CHAPTER VIII: CONCLUSIONS AND RECOMMENDATIONS

assemblies are comparable to those of dense sands (internal friction angles between 39 and 43 degrees). Maximum dilation rates are also in the range of experimentally observed values for typical dense sands.

The influence of the confining pressure on the macroscopic behaviour of assemblies of ellipsoids is in accordance with what is already known from experimental and previous numerical simulations results. The most characteristic features of the pressure sensitivity of dense granular materials were observed such as:

1. Decrease in peak friction angle with increasing confining pressure.
2. Increase in the axial strain at peak friction angle with increasing confining pressure.
3. Decrease in peak dilation rate with increasing confining pressure.
4. Increase in the axial strain at peak dilation rate with increasing confining pressure.
5. It was observed that the peak internal friction angle and the peak of dilation rate do not take place at the same axial deformation. The former always precedes the latter.

In relation to the steady-state of deformation:

6. The ultimate internal friction angle, ϕ_{cv} , is independent of confining pressure and initial conditions.
7. The steady-state void ratio, e_{cv} , is a function of the confining pressure.

8.5.2 Microscopic Behaviour

The microscopic analysis of assemblies of ellipsoids revealed similar aspects to those observed in physical tests and numerical simulations in two and three dimensions. These aspects concern primarily the load transfer and mechanisms of anisotropy development in fabric and contact force magnitudes, the three-dimensional shapes of the distributions of the different microscopic parameters, and the curves of variation of magnitudes of anisotropy, during shear deformation.

The shape effect was observed to affect the initial curvatures of variations during shear deformation of the assembly coordination number and magnitude of contact normal orientation anisotropy. An initial flat curvature in both cases was observed, and was interpreted as a delay in contact disintegration due to the elongated shape of ellipsoids. This delay is contributed to by the component of rotation of elongated ellipsoids in contact. This component acts against the effort of separation of ellipsoids in contact. However, the delay was not observed for very low confining pressures. This observation suggests that the phenomenon cannot take place under a very low confining pressure. For spherical particles, however, this component of rotation is zero, and the decrease in the average coordination number follows immediately the application of deformation to the sample of particles.

The following observations were made in relation to the microscopic manifestation of the pressure sensitivity of assemblies of ellipsoids:

1. The average change of the assembly coordination number during shear deformation (proportional to the difference between initial and steady-state values

of assembly coordination number) is not sensitive to the applied confining pressure. However, the initial rate of change of the assembly coordination number is sensitive to the applied confining pressure. This sensitivity quickly diminishes as shear deformation develops and particles become able to move more freely within their immediate surroundings.

2. The standard deviation of the particle coordination number distribution undergoes minor changes both with respect to shear deformation as well as with respect to confining pressure.
3. The magnitude of the average normal contact force and its rate of change depend on confining pressure.
4. Degrees of anisotropy in contact normal orientation, average normal contact force, and average tangential contact force, develop with different initial rates depending on the applied confining pressure. The effect of confining pressure propagates until the steady-state of deformation is reached, where the curves corresponding to a parameter and different values of confining pressure tend towards a single constant limit.
5. More specifically, it has been observed that the initial rates of development of all above forms of anisotropy decrease with increasing confining pressure. The peak anisotropy values, however, decreased sharply for the anisotropy in contact normals, and very moderately increased for average normal and tangential contact force anisotropies, with increasing confining pressure.

8.6 Average Stress Tensor Decomposition

A general Stress-Force-Fabric relationship was developed for ellipsoids by including the direct effect of shape embodied in the spatial anisotropies in average normal and tangential branch vectors, a_{ij}^v and a_{ij}^t , respectively. The relationship can be written in a decomposed form where the components of the decomposition have clear physical interpretations in terms of microscopic anisotropies:

$$\sigma_{ij} \cong \underbrace{\sigma_{ij}^o}_{\text{Total}} + \underbrace{\sigma_{ij}^r}_{\text{Full Isotropy}} + \underbrace{\sigma_{ij}^z}_{a_{ij}^v \text{ only}} + \underbrace{\sigma_{ij}^f}_{a_{ij}^t \text{ only}} + \underbrace{\sigma_{ij}^{rz}}_{a_{ij}^v \& a_{ij}^t \text{ only}} + \underbrace{\sigma_{ij}^{rf}}_{a_{ij}^v \& a_{ij}^t} + \underbrace{\sigma_{ij}^{zf}}_{a_{ij}^v \& a_{ij}^t} \quad (8 \cdot 3)$$

where the tensor a_{ij}^z stands for the pair of components (a_{ij}^v, a_{ij}^t) , and a_{ij}^f stands for the pair of components (a_{ij}^n, a_{ij}^t) .

The tensors in the decomposition are expressed in terms of tensors of anisotropies as below:

$$\begin{aligned} \sigma_{ij}^o &= \sigma^o \delta_{ij} \\ \sigma_{ij}^r &= \frac{2\sigma^o}{5} a_{ij}^r \\ \sigma_{ij}^z &= \frac{2\sigma^o}{5} \left\{ a_{ij}^v + \frac{3}{2} a_{ij}^t \right\} \\ \sigma_{ij}^f &= \frac{2\sigma^o}{5} \left\{ a_{ij}^n + \frac{3}{2} a_{ij}^t \right\} \\ \sigma_{ij}^{rz} &= \frac{2\sigma^o}{35} \{ 7a_{ik}^r a_{jk}^t + 2a_{ik}^r a_{jk}^{\Delta z} + 2a_{ik}^{\Delta z} a_{jk}^r + a_{ki}^r a_{ki}^{\Delta z} \delta_{ij} \} \\ \sigma_{ij}^{rf} &= \frac{2\sigma^o}{35} \{ 7a_{jk}^r a_{ik}^f + 2a_{jk}^r a_{ik}^{\Delta f} + 2a_{jk}^{\Delta f} a_{ik}^r + a_{ki}^r a_{ki}^{\Delta f} \delta_{ij} \} \\ \sigma_{ij}^{zf} &= \frac{2\sigma^o}{35} \left\{ \frac{35}{2} a_{jk}^t a_{ik}^f + 7a_{jk}^{\Delta z} a_{ik}^f + 7a_{jk}^t a_{ik}^{\Delta f} \right. \\ &\quad \left. + 2a_{ik}^{\Delta z} a_{jk}^{\Delta f} + 2a_{ik}^{\Delta f} a_{jk}^{\Delta z} + a_{ki}^{\Delta z} a_{ki}^{\Delta f} \delta_{ij} \right\} \end{aligned} \quad (8 \cdot 4)$$

where:

$$\begin{cases} \sigma^o = m \sqrt{\bar{p} \bar{z}^o} / 6 \\ a_{ij}^{\Delta r} = a_{ij}^v - a_{ij}^r \\ a_{ij}^{\Delta f} = a_{ij}^n - a_{ij}^f \end{cases} \quad (8 \cdot 5)$$

and where m_v is the average contact density; \bar{p} and \bar{z}^o are the group averages of the normal contact force magnitude and contact branch vector length, respectively.

The relationship was validated using results of simulation tests with samples of ellipsoids in the axisymmetric triaxial compression tests at constant mean pressure.

A direct expression of the macroscopic mobilized shear strength as a sum of microscopic individual and joint anisotropy contributions, similar in form to the average stress decomposition, was derived from the tensorial Stress-Force-Fabric relationship. Assumptions of co-axiality and axisymmetry of the individual second-order anisotropy tensors were essential to the derivation.

The result expressed in terms of shear stress ratio, defined as the ratio of the shear stress, $\sigma' = \sqrt{3\sigma'_{ij}\sigma'_{ij}}/2$, to the normal stress, $\sigma^n = \sigma_{kk}/3$, i.e., $a_\sigma = \sigma'/\sigma^n$ can be written as:

$$a_\sigma = a_\sigma^r + \underbrace{(a_\sigma^v + a_\sigma^r)}_{a_\sigma^z} + \underbrace{(a_\sigma^n + a_\sigma^f)}_{a_\sigma^f} + a_\sigma^{rz} + a_\sigma^{rf} + a_\sigma^{zf} \quad (8 \cdot 6)$$

In the absence of initial anisotropy, the microscopic contributions in the right hand side of the above equation have constant signs (either positive or negative) throughout the course of deformation. However, in the presence of inherent anisotropy, the signs of these contributions become constant only after the effect of initial anisotropy is eliminated by deformation. It usually takes a small amount of applied axial strain before these signs sta-

bilize. For instance, at large strains, the shear strength decomposition terms and corresponding percents of contribution to the total shear strength are given as below:

$$\begin{aligned}
 a_{\sigma}^r &= \sqrt{3/2} \left(\frac{2}{3} a^r \right) / D_{\sigma} & (38\%) \\
 a_{\sigma}^z \begin{cases} a_{\sigma}^v &= -\sqrt{3/2} \left(\frac{2}{3} a^v \right) / D_{\sigma} & (-6\%) \\ a_{\sigma}^s &= -\sqrt{3/2} \left[\frac{2}{3} (1.5 a^s) \right] / D_{\sigma} & (-3.75\%) \end{cases} \\
 a_{\sigma}^f \begin{cases} a_{\sigma}^n &= \sqrt{3/2} \left(\frac{2}{3} a^n \right) / D_{\sigma} & (45\%) \\ a_{\sigma}^t &= \sqrt{3/2} \left[\frac{2}{3} (1.5 a^t) \right] / D_{\sigma} & (18\%) \end{cases} \quad (8 \cdot 7) \\
 a_{\sigma}^{rz} &= -\sqrt{3/2} \left\{ \frac{2}{35} (7 a^{(rz)} + 4 a^{[r(\Delta z)]}) \right\} / D_{\sigma} & (-1.75\%) \\
 a_{\sigma}^{rf} &= \sqrt{3/2} \left\{ \frac{2}{35} (7 a^{(rf)} + 4 a^{[r(\Delta f)]}) \right\} / D_{\sigma} & (13\%) \\
 a_{\sigma}^{zf} &= -\sqrt{3/2} \left\{ \frac{2}{35} [17.5 a^{(zf)} + 7 a^{[(\Delta z)]} \right. & (-2.5\%) \\
 & \quad \left. + 7 a^{[(\Delta f)]} + 4 a^{[(\Delta z)(\Delta f)]}] \right\} / D_{\sigma}
 \end{aligned}$$

where:

$$D_{\sigma} = 1 + \frac{2}{15} (-a^r a^v + a^r a^n + a^v a^n + 1.5 a^s a^t) \quad (8 \cdot 8)$$

Quantities of type a^x are magnitudes of basic anisotropy tensors as, $a^x = \sqrt{a_{ij}^x a_{ij}^x}$. The quantities appearing in the joint anisotropy contributions in (8• 7) and having expressions of the type, $a^{(xy)}$ or $a^{[xy]}$, denote magnitudes of anisotropy products of basic anisotropy tensors. The symbols, ' and [], in superscript, denote deviatoric and symmetric parts of a tensor, respectively. For instance, $a^{[r(\Delta z)]}$ stands for the modulus of the deviatoric part of the symmetric part of a tensor obtained as the product of a_{ij}^r and $a_{ij}^{\Delta z}$. The quantity, $a^{[r(\Delta z)]}$ can be retrieved as below:

$$a^{[r(\Delta z)]} = \sqrt{a_{ij}^{[r(\Delta z)]} a_{ij}^{[r(\Delta z)]}} \quad (8 \cdot 9)$$

where:

$$a_{ij}^{[r(\Delta z)]} = \underbrace{\frac{1}{2}(a_{ik}^r a_{kj}^{\Delta z} + a_{ik}^{\Delta z} a_{kj}^r)}_{\text{Symmetric part}} - \underbrace{\frac{a_{kl}^r a_{kl}^{\Delta z}}{3} \delta_{ij}}_{\text{Spherical part}} \quad (8 \cdot 10)$$

The relationship was validated numerically. Some concepts already known from earlier research (concerning details of anisotropy development and levels of microscopic contributions to shear strength) were proved true for the three-dimensional system of ellipsoids. However, there are new findings which concern the particle shape effect on the mobilized shear strength and the behaviour and level of contribution to the mobilized shear strength of the component of joint anisotropy a_g^f .

1. The shape factor modeled by the quantity, $a_g^v + a_g^s + a_g^{rz}/2 + a_g^{zf}/2$, was seen to represent a minor but decisive element of contribution to the material shear strength. It helps to close the gap between theoretical and measured stress-strain curves, especially at large strain. Its negative contribution grows linearly with increasing axial deformation, and can total up to 12% of the total mobilized shear strength at large strains.
2. The tensor σ_{ij}^f , representing the joint contribution of anisotropies in contact normal orientation and average contact forces, has the second largest mean stress after the spherical tensor σ_{ij}^g . It is responsible for keeping the overall mean stress constant by opposing the decline of the spherical tensor σ_{ij}^g . The positive contribution, a_g^f , accounts for 13% of the total mobilized shear strength.

8.7 Effect of Particle Shape on Fabric Anisotropy

The effect of shape was analyzed in connection with parameters describing the deformation-induced anisotropy in particle orientations during shear deformation, represented by a second-order anisotropy tensor a_{ij}^E , and also based on the measured distribution of contact occurrence around an “average ellipsoid”. This distribution assumes in three-dimensions a “peanut” shape that exhibits a form of anisotropy represented by a second-order tensor a_{ij}^{cvL} . The findings are summarized as follows:

1. The average distribution of contact locations on the surface of an average ellipsoid is affected only by the particle shape.
2. This distribution of contact location on the surface of an average ellipsoid was successfully used to predict the proportions of contacts characterized by vector lengths in the short (s), intermediate (i), and long (l) ranges. The definition of these ranges stemmed from a regular sub-division of the full range of possible lengths in three equal intervals. Proportions of pairs of particles sharing contacts of an ($s-s$), ($s-i$), ($s-l$), ($i-i$), ($i-l$), or ($l-l$) type of contact could also be predicted only based on the value of the tensor a_{ij}^{cvL} .
3. It has been observed that for an aspect ratio of particles of 1:1.43 more than 50% of contacts are located in the short range of vector lengths. It seems that the stability of an elongated particle is conditioned by the creation of contacts near its flat surface areas, even in the absence of gravity. Hence, an elongated particle uses its ability to rotate by adjusting its orientation as to keep a larger proportion of contacts near its flat areas. In the long term, this creates consider-

able anisotropy (increase in the magnitude of tensor a_{ij}^E), especially at large strains, where the orientation of ellipsoids' long axes becomes predominantly horizontal.

4. A probabilistic model to estimate the influence of shape on the contact normal orientation anisotropy, represented by the second anisotropy tensor a_{ij}^r , was developed for plane ellipses. The model, in three dimensions, is analytically complex because of the interference of many random variables in highly non-linear expressions. These expressions are analytically intractable, and perhaps a numerical model would be more appropriate to use for predicting the shape effect on the anisotropy of contact normal orientations.
5. The two-dimensional model predicts that the shape contribution to the contact normal orientation anisotropy, measured by some fraction a_{rot}^r of the total anisotropy a^r , is proportional to the degree of anisotropy in particle orientations a^E . The coefficient of proportionality a_{rot}^r / a^E is a linear expression of the degree of anisotropy in local contact vector orientation a^{cVL} .
6. For a given state of the assembly of particles, the contribution a_{rot}^r / a^E increases with particle eccentricity from zero (for disks) to one (for needles). This means that the rotation of disks has no ability to create new contacts or to break existing contacts, and therefore has a zero contribution to the fabric anisotropy a^r . The more a particle shape departs from a circular shape, the more its contribution to this form of anisotropy increases. However, this contribution is always limited by the ability of the assembly to develop anisotropy in particle orienta-

tion α^E . It is only a fraction of this form of anisotropy. The model predicts that if the aspect ratio of ellipses is very large (needles), then most of the developed anisotropy in particle orientation will be mobilized to contribute to the anisotropy in contact normal orientations α^r .

8.8 Recommendations for Future Research

In order to complete the understanding of the behaviour of granular assemblies of particles, a relationship between an average strain tensor, defined for particulate systems, and mechanisms of contact displacements, must be developed. This is the missing link in the chain of macroscopic-to-microscopic relationships established up to date to model the behaviour of granular materials.

8.8.1 The Average Strain Tensor

The first step towards this objective has been already undertaken by defining a strain tensor for granular assemblies that has the same properties as the continuum mechanics strain tensor. A procedure similar to the one used to define the stress tensor from continuum mechanics was employed to define such a strain tensor. The strain tensor for two-dimensional systems of arbitrarily shaped particles can be defined as an area average of individual contact contributions.

Kruyt and Rothenburg (1996) proposed to write the average strain tensor of plane systems as:

$$\varepsilon_{ij} = \frac{1}{A} \sum_c \Delta U_i^c \hat{h}_j^c \quad (8 \cdot 11)$$

where A is the area of the planar assembly (Figure 8•1a); ΔU_i^c is the relative displacement vector of the pair of particles defining the contact c ; and \hat{h}_j^c is the counter-clockwise rotated contact vector between polygonal units (Figure 8•1b).

Figure 8•1a shows a set of polygons covering the entire assembly. The set is obtained by connecting the centroids of particles in contact. As can be seen from the figure, no polygon can be divided into two or more sub-polygons. The polygon system, and the resulting average strain tensor definition, are both unique.

As seen in Figure 8•1b, the definition of vectors \hat{h}^c depends on the polygon shapes; therefore, the calculation of the strain tensor must be preceded by the identification of the set of polygons with the property of indivisibility mentioned above. This constitutes a drawback in the definition of the strain tensor, especially in the three-dimensional case where the procedure of identification of the set of “indivisible” polyhedra requires a special identification algorithm.

The extension of the strain tensor to three-dimensional systems is as follows:

$$\varepsilon_{ij} = \frac{1}{V} \sum_c \Delta U_i^c \hat{h}_j^c \quad (8 \bullet 12)$$

The relative contact displacement during an increment of time Δt is calculated as:

$$\Delta U_i = V_i \Delta t \quad (8 \bullet 13)$$

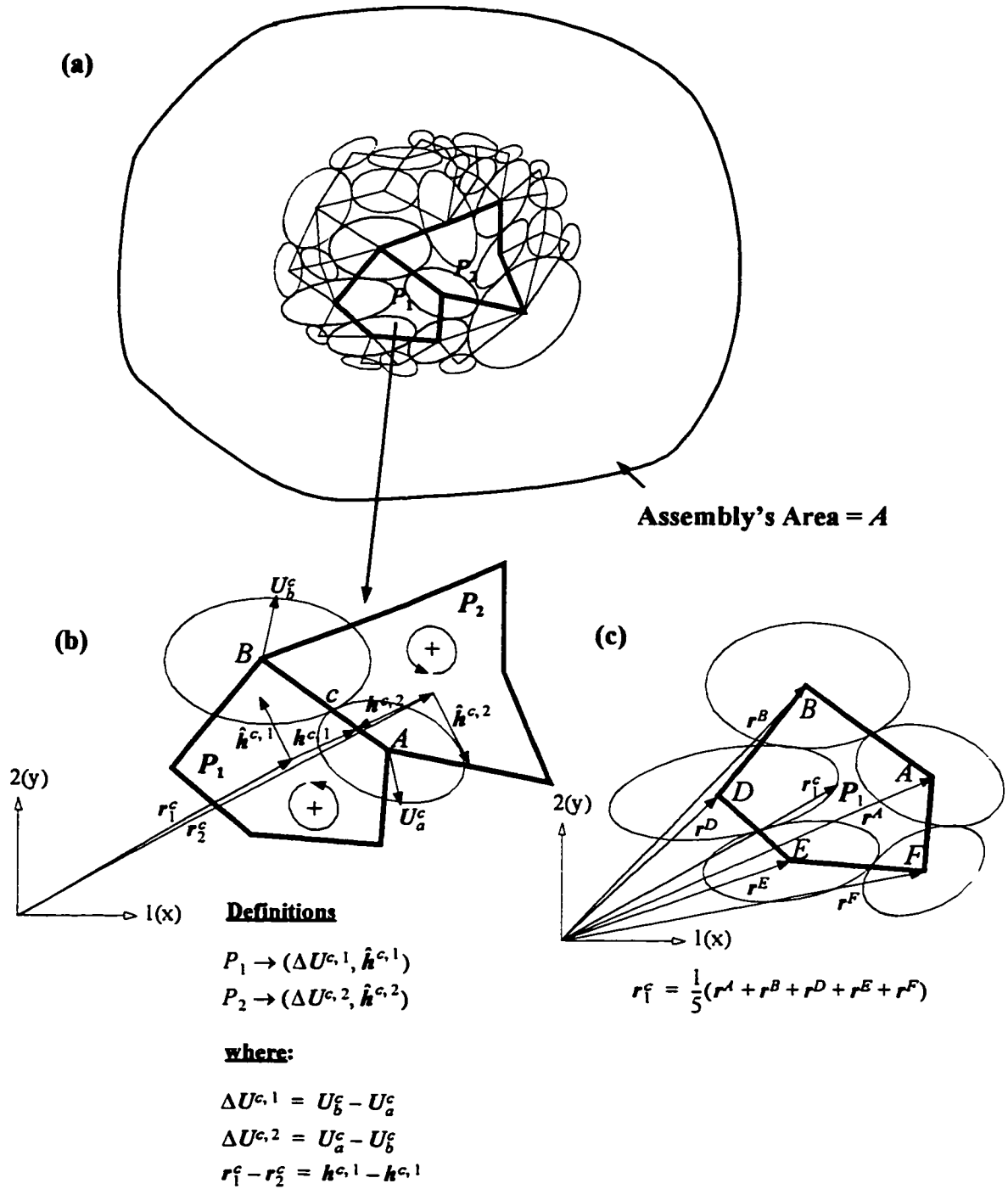


Figure 8-1 Elements of definition of the strain tensor for a plane granular system

CHAPTER VIII: CONCLUSIONS AND RECOMMENDATIONS

where V_i denote the components of the velocity vector at the contact point c . They are given by:

$$V_i = [\dot{x}_i^B + \varepsilon_{ijk}\omega_j^B(C_k - B_k)] - [\dot{x}_i^A + \varepsilon_{ijk}\omega_j^A(C_k - A_k)] \quad (8.14)$$

where A and B are the position vectors, and, \dot{x}^A and \dot{x}^B are the translation velocity vectors of the centroids of particles, A and B , respectively; ω_j^A and ω_j^B are the corresponding angular velocity vectors; C is the position vector of the contact point c ; and ε_{ijk} , is a third-rank permutation tensor used to express the cross product of spatial vectors.

The issue of partitioning a well-defined strain tensor for three-dimensional systems amongst various contributing deformational mechanisms will answer many questions about the interpretation of fourth anisotropy related terms in the approximation of spatial distributions of tangential contact forces for example and many more.

This subject is certainly a rich prospect for new ideas to further develop the micromechanical theories.

APPENDIX A: NEARLY-UNIFORM PARTITIONING OF THE ORIENTATION SPACE

A.1 Notation

The polar and azimuth angles relative to the three systems of Cartesian coordinates (xyz), (yzx) and (zxy), are denoted as follows:

Coordinate System	Polar Angle	Azimuth Angle
(xyz)	α_{yz}	β_x
(yzx)	α_{zx}	β_y
(zxy)	α_{xy}	β_z

A.3 Size of a Patch

284

$$\begin{cases} x_{node} = \cos \beta_x = \sin \alpha_{zx} \sin \beta_y & (a) \\ y_{node} = \cos \alpha_{yz} \sin \beta_x = \cos \beta_y & (b) \\ z_{node} = \sin \alpha_{yz} \sin \beta_x = \cos \alpha_{zx} \sin \beta_y & (c) \end{cases} \quad (A \bullet 1)$$

In the above system of equations, only two equations are independent. This is because the node (located on the unit sphere) must satisfy the sphere's generic equation $x_{node}^2 + y_{node}^2 + z_{node}^2 = 1$.

If the polar angles α_{yz} and α_{zx} are assumed to be known, then the system of equations (A• 1) need to be solved for β_x and β_y .

Multiplying equation (A• 1)(b) by $\cos \alpha_{zx}$, squaring the result, and adding it to the squared (A• 1)(c) equation, results in a new equation where the parameter β_x can be isolated as:

$$\sin \beta_x = \frac{\cos \alpha_{zx}}{\sqrt{\cos^2 \alpha_{zx} \cos^2 \alpha_{yz} + \sin^2 \alpha_{yz}}} \quad (A \bullet 2)$$

By substituting of the above equation into (A• 1)(b), the angle β_y is solved for as:

$$\cos \beta_y = \frac{\cos \alpha_{yz} \cos \alpha_{zx}}{\sqrt{\cos^2 \alpha_{zx} \cos^2 \alpha_{yz} + \sin^2 \alpha_{yz}}} \quad (A \bullet 3)$$

The Cartesian and spherical coordinates of the nodes are now fully determined.

A.3.1 Calculation of a Patch Area

The area of a patch (class amplitude) is calculated by the double integral of elementary areas in spherical coordinates as:

$$|\Delta n^z| = \int_{\alpha_{Lz}}^{\alpha_{Hz} + \Delta \alpha} \int_{\beta_f}^{\beta_f + \Delta \beta} \sin \beta_y d\beta_y d\alpha_{zx} = \int_{\alpha_{Lz}}^{\alpha_{Hz} + \Delta \alpha} \int_{\beta_f}^{\beta_f + \Delta \beta} \sin \beta_x d\beta_x d\alpha_{yz} \quad (A \bullet 4)$$

APPENDIX A: NEARLY-UNIFORM PARTITIONING OF THE ORIENTATION SPACE

Either expressions can be used (relative to (xyz) or (yzx), respectively). If the first integral is employed to calculate the class magnitude, then:

$$|\Delta n^g| = \int_{\alpha_x^g}^{\alpha_x^g + \Delta \alpha} (\cos \beta_y^g - \cos(\beta_y^g + \Delta \beta_y)) d\alpha_{xx} \quad (\text{A} \bullet 5)$$

By substituting of the expression of $\cos \beta_y$ in (A• 3) into the above equation, the class amplitude is calculated as:

$$|\Delta n^g| = J_{\alpha_x^g}(\alpha_{xx}^g, \alpha_{xx}^g + \Delta \alpha) - J_{\alpha_x^g + \Delta \alpha}(\alpha_{xx}^g, \alpha_{xx}^g + \Delta \alpha) \quad (\text{A} \bullet 6)$$

where:

$$J_\lambda(x_1, x_2) = \int_{x_1}^{x_2} \frac{\cos x \cos \lambda}{\sqrt{\cos^2 x \cos^2 \lambda + \sin^2 \lambda}} dx \quad (\text{A} \bullet 7)$$

The integral in (A• 7) can be calculated analytically and the result is:

$$J_\lambda(x_1, x_2) = \text{asin}(\cos \lambda \sin x_2) - \text{asin}(\cos \lambda \sin x_1) \quad (\text{A} \bullet 8)$$

A.4 Grouping Process

Assigning a unit vector to a parent class consists of two steps:

1. Identify the basic region containing the vector (among the 24 regions covering the unit sphere).
2. Determine the class containing the unit vector within the identified basic region.

Generally, the unit vector is specified in terms of its Cartesian coordinates in the default coordinate system $((x_m, y_m, z_n), \text{ for example})$.

A.4.1 Assignment into a Basic Region

In order to locate the basic region containing the unit vector, it is essential to label all regions differently. The labelling uses two indices:

1. One index, i_r , to characterize the pole to which the region is attached. The index, i_r , takes values from 1 to 3.
2. One index, i_c , to characterize the (1/8) of the unit sphere on which the region is located. The index i_c takes values from 1 to 8.

Hence, the total number of basic regions is $3 \times 8 = 24$.

A.4.1.1 Finding i_r

The index, i_r , characterizes the appropriate Cartesian coordinates to be used, or the pole associated with a particular region. It is determined as shown in the table below:

Inequality	Coordinate System	Index i_r
$x_n \geq \max(y_n, z_n)$	(xyz)	1
$y_n \geq \max(z_n, x_n)$	(yzx)	2
$z_n \geq \max(x_n, y_n)$	(zxy)	3

A.4.1.2 Finding i_c

Based on the value of i_r , the Cartesian components of the unit vector must be re-ordered to match the new coordinate system (given in the above table). Re-ordering is only required if $i_r \neq 1$. For example, if $i_r = 1$, then, i_c is determined as follows:

Inequalities	Index i_c	Inequalities	Index i_c
$x_n \geq 0, y_n \geq 0, z_n \geq 0$	1	$x_n \leq 0, y_n \geq 0, z_n \geq 0$	5
$x_n \geq 0, y_n \geq 0, z_n \leq 0$	2	$x_n \leq 0, y_n \geq 0, z_n \leq 0$	6
$x_n \geq 0, y_n \leq 0, z_n \geq 0$	3	$x_n \leq 0, y_n \leq 0, z_n \geq 0$	7
$x_n \geq 0, y_n \leq 0, z_n \leq 0$	4	$x_n \leq 0, y_n \leq 0, z_n \leq 0$	8

A.4.2 Assignment into a Patch (Class of Orientation)

Once the pair of indices (i_r, i_c) is determined, the basic region is identified and the assignment of the unit vector into its parent patch can be completed as follows:

1. The pair of polar angles (α_1^r, α_2^r) of the unit vector with respect to the appropriate spherical coordinate systems is calculated. The choice of which polar angles to calculate depends on the index i_r :

i_r	α_1	α_2
1	α_{xy}	α_{zx}
2	α_{yz}	α_{xy}
3	α_{yz}	α_{zx}

2. Determine the patch in which the pair (α_1^r, α_2^r) falls. This exercise is similar to assigning a contact normal vector in spherical coordinates.

APPENDIX B: INTERSECTION OF TWO ELLIPSOIDS

B.1 General Equation of Intersection of Two Ellipsoids

Since the characterization of the contact area will involve mainly ellipsoid A , it is convenient to express its generic equation in a parametric form written in its own frame of reference as:

$$\begin{cases} x = a \cos \theta \sin \phi \\ y = b \sin \theta \sin \phi \\ z = c \cos \phi \end{cases} \quad (\text{B} \cdot 1)$$

where $a \geq b \geq c$ are the ellipsoid principal radii, and, (θ, ϕ) , are the surface parameters. (θ, ϕ) are different from the polar and azimuth angles in spherical coordinates. They effectively degenerate to polar and azimuth angles for spheres only. The angle θ varies

from 0 to 2π , and the angle ϕ varies from 0 to π .

The equation of ellipsoid, B , is written in an algebraic form (relative to principal axes of ellipsoid, A) as:

$$\underline{X}Q_B\underline{X}^T = 0 \quad (\text{B} \bullet 2)$$

where Q_B is the discriminant matrix of ellipsoid B .

Hence, the intersection equation can be expressed locally (in ellipsoid A principal axes) as:

$$\begin{bmatrix} a \cos \theta \sin \phi & b \sin \theta \sin \phi & c \cos \phi & 1 \end{bmatrix} Q_B \begin{bmatrix} a \cos \theta \sin \phi \\ b \sin \theta \sin \phi \\ c \cos \phi \\ 1 \end{bmatrix} = 0 \quad (\text{B} \bullet 3)$$

B.2 Curve-to-Surface Equation

The general equation of intersection (B• 3) is quadratic with respect to the cosine and sine functions of θ and ϕ .

If one of the two variables can be set to a fixed value, for example, $(\theta = \text{const})$, then the intersection equation is only solved for ϕ . Geometrically, this corresponds to finding the intersection of the $(\theta = \text{const})$ -curve on the surface of the ellipsoid A (the curve joining all the points having $(\theta = \text{const})$ as their first parameter) and the surface of ellipsoid B . Thus, the two-variable surface-to-surface intersection equation is transformed to a single-variable, curve-to-surface intersection equation. Similarly, the value of ϕ can be set to be constant, and the resulting equation solved for θ .

B.3 Method of Solution

If θ is the varying parameter and ϕ is set to a fixed value, the (ϕ -curve)-surface equation is quadratic with respect to $\cos\theta$ and $\sin\theta$, with an expression that has a form similar to:

$$\begin{aligned} a_1 \cos^2\theta + a_2 \sin^2\theta + 2a_3 \cos\theta \sin\theta \\ + 2a_4 \cos\theta + 2a_5 \sin\theta + a_6 = 0 \end{aligned} \quad (\text{B} \bullet 4)$$

where a_i are constant coefficients depending on the geometry of ellipsoids A and B .

$\cos\theta$ and $\sin\theta$ are related to the single variable $w = \tan(\theta/2)$ as follows:

$$\begin{cases} \cos\theta = (1 - w^2)/(1 + w^2) \\ \sin\theta = 2w/(1 + w^2) \end{cases} \quad (\text{B} \bullet 5)$$

By substituting the above relationships into (B• 4) and rearranging, a fourth-degree algebraic equation is obtained. After solving for, w , the original parameter, θ , can be recovered from (B• 5).

APPENDIX C: CALCULATION OF INTEGRALS

$$\int_{\mathbf{n}} n_{i_1} n_{i_2} \dots n_{i_{2m}} d\mathbf{n}$$

Integrals over the unit sphere of the form, $\int_{\mathbf{n}} n_{i_1} n_{i_2} \dots n_{i_{2m}} d\mathbf{n}$, where n_{i_k} are arbitrary unit vectors, are often needed in tensor calculations. The Stress-Force-Fabric relationship (S-F-F) is one application where these integrals are required. These integrals can be expressed as sums and products of the Kronecker delta tensor δ_{ij} . However, a comprehensive general formula is impossible to write for an arbitrary order. Instead a procedure is shown that can be utilized to retrieve the formula once the order of the integral is known.

For convenience, the integrals are normalized to define tensorial quantities that can only assume integer values. These are defined as:

$$\beta_{i_1 i_2 \dots i_{2m}}^{(2m)} = \frac{(2m+1)!}{(2^m m!) 4\pi} \int_{\mathbf{n}} n_{i_1} n_{i_2} \dots n_{i_{2m}} d\mathbf{n} \quad (\text{C} \cdot 1)$$

APPENDIX C: CALCULATION OF INTEGRALS

The tensor $\beta_{i_1 i_2 \dots i_{2m}}^{(2m)}$ is directly related to the tensor of lower order $\beta_{i_1 i_2 \dots i_{2m-2}}^{(2m-2)}$. Hence, a sequence can be established that will bridge $\beta_{i_1 i_2 \dots i_{2m}}^{(2m)}$ with all successive lower orders until reaching the lowest order 2 for which the tensor is known $\beta_{ij}^{(2)} = \delta_{ij}$.

To illustrate the method, the case of the S-F-F relationship is considered where the following tensors are required:

$$\begin{aligned}\beta_{ij}^{(2)} &= \frac{3}{4\pi} \int_{\mathbf{n}} n_i n_j d\mathbf{n} \\ \beta_{ijkl}^{(4)} &= \frac{15}{4\pi} \int_{\mathbf{n}} n_i n_j n_k n_l d\mathbf{n} \\ \beta_{ijklpq}^{(6)} &= \frac{105}{4\pi} \int_{\mathbf{n}} n_i n_j n_k n_l n_p n_q d\mathbf{n} \\ \beta_{ijklpqrs}^{(8)} &= \frac{945}{4\pi} \int_{\mathbf{n}} n_i n_j n_k n_l n_p n_q n_r n_s d\mathbf{n}\end{aligned}\tag{C• 2}$$

The sequence is as follows:

$$\begin{aligned}\beta_{ij}^{(2)} &= \delta_{ij} \\ \beta_{ijkl}^{(4)} &= \delta_{ij} \beta_{kl}^{(2)} + \delta_{ik} \beta_{jl}^{(2)} + \delta_{il} \beta_{jk}^{(2)} \\ \beta_{ijklpq}^{(6)} &= \delta_{ij} \beta_{klpq}^{(4)} + \delta_{ik} \beta_{jlpq}^{(4)} + \delta_{il} \beta_{jkpq}^{(4)} + \delta_{ip} \beta_{jklq}^{(4)} + \delta_{iq} \beta_{jklp}^{(4)} \\ \beta_{ijklpqrs}^{(8)} &= \delta_{ij} \beta_{klpqrs}^{(6)} + \delta_{ik} \beta_{jlpqrs}^{(6)} + \delta_{il} \beta_{jkpqrs}^{(6)} + \delta_{ip} \beta_{jklqrs}^{(6)} \\ &\quad + \delta_{iq} \beta_{jklprs}^{(6)} + \delta_{ir} \beta_{jklpqz}^{(6)} + \delta_{is} \beta_{jklpqr}^{(6)}\end{aligned}\tag{C• 3}$$

To determine the expression of the 6th order tensor for example, two successive substitutions are needed. The final form of the tensor in terms of the Kronecker delta tensor can be written as follows:

APPENDIX C: CALCULATION OF INTEGRALS

$$\begin{aligned}
 \beta_{ijklpq}^{(6)} = & \delta_{ij}(\delta_{kl}\delta_{pq} + \delta_{kp}\delta_{lq} + \delta_{kq}\delta_{lp}) + \delta_{ik}(\delta_{jl}\delta_{pq} + \delta_{jp}\delta_{lq} + \delta_{jq}\delta_{lp}) \\
 & + \delta_{il}(\delta_{jk}\delta_{pq} + \delta_{jp}\delta_{kq} + \delta_{jq}\delta_{kp}) + \delta_{ip}(\delta_{jk}\delta_{lq} + \delta_{jl}\delta_{kq} + \delta_{jq}\delta_{kl}) \quad (\text{C}\cdot 4) \\
 & + \delta_{iq}(\delta_{jk}\delta_{lp} + \delta_{jl}\delta_{kp} + \delta_{jp}\delta_{kl})
 \end{aligned}$$

The same can be done with the eighth order tensor $\beta_{ijklpqrs}^{(8)}$, and any other higher order tensor.

REFERENCES

REFERENCES

- Aschenbrenner, B. C., (1956), A New Method of Expressing Particle Sphericity, *J. Sediment. Petrol.*, **26**, 15-31.
- Bardet, J.P., and Proubet, J. (1991), Adaptive Dynamic Relaxation for Statics of Granular Materials, *Computers and Structures*, **39**, 3/4, 221-229
- Bathurst, R.J. (1985), A Study of Stress and Anisotropy in Idealized Granular Assemblies, *Ph.D. Dissertation*, Department of Civil Engineering, Queen's University, Kingston, Ontario, 219 pp.
- Bathurst, R.J., and Rothenburg, L. (1988), Micromechanical Aspects of Isotropic Granular Assemblies with Linear Contact Interactions, *J. Appl. Mech.*, ASME, **55**, 3, 17-23
- Bathurst, R.J., and Rothenburg, L. (1990), Observation on Stress-Force-Fabric Relationships in Idealized Granular Materials, *Mechanics of Materials*, **9**, 1, 65-80.

REFERENCES

- Bathurst, R.J., and Rothenburg, L. (1992), Investigation of Anisotropic Assemblies of Plane Elliptical Particles, *Numerical Models in Geomechanics*, Pande & Pietruszczak (eds.), Balkema, Rotterdam, 47-54.
- Been, K., and Jefferies, M.G. (1985), A State Parameter for Sands, *Géotechnique*, **35**, 2, 99-112.
- Biarez, J., and Wiendieck, K. (1963), La Comparaison Qualitative Entre L'Anisotropie Mécanique et L'Anisotropie de Structure des Milieux Pulvérulents, *Comptes Rendus de L'Academie des Sciences*, 256, 1217-1220.
- Bishop, A. W. (1971), Shear Strength Parameters for Undisturbed and Remolded Soil Specimens, *Proc. Roscoe Memorial Symp.*, Cambridge University, 3-58
- Chantawarangul, K. (1993), Numerical Simulations of Three-Dimensional Granular Assemblies. *Ph.D. Dissertation*, Department of Civil Engineering, University of Waterloo Ontario, 219 pp.
- Christoffersen, J., Mehrabadi, M.M. and Nemat-Nasser, S. (1981), A Micromechanical Description of Granular Material Behaviour, *J. Appl. Mech.*, ASME, **48**, 339-344.
- Cundall, P.A. (1971), A Computer Model For Simulating Progressive, Large-Scale Movements in Blocky Rock Systems, *Proc. Symp. Soc. Rock Mech.*, Nancy, **2**, Paper 8, 12 pp.
- Cundall, P.A. (1978), *BALL - A Computer Program to Model Granular Media Using the Distinct Element Method*, Technical Note TN-LN-13, Advance Technology Group, Dames and Moore, London, 74 pp.
- Cundall, P.A. (1982) Adaptive Density-Scaling for Time-Explicit Calculations, *Proc. of*

REFERENCES

- IV International Conference on Numerical Methods in Geomechanics*, 1, 23-26
- Cundall, P.A. (1987), Distinct Element Models of Rock and Soil Structure, *Analytical and Computational Methods in Engineering Rock Mechanics*, E.T. Brown (eds.), Allen and Unwin, London, 129-163.
- Cundall, P.A. (1988), Computer Simulations of Dense Sphere Assemblies, *Micromechanics of Granular Materials*, M. Satake and J.T. Jenkins (eds.), Elsevier, Amsterdam, 113-123.
- Cundall, P.A. and Strack, O.D.L. (1979a), A Discrete Numerical Model for Granular Assemblies, *Géotechnique*, **29**, 1, 47-65.
- Cundall, P.A. and Strack, O.D.L. (1979b), The Development of Constitutive Laws for Soil Using the Discrete Element Method, *Proc. 3rd Int. Conf. Numerical Methods in Geomechanics*, Aachen, W. Witke (eds.), **1**, 289-298.
- Cundall, P.A. and Strack, O.D.L. (1979c), *The Discrete Element Method as a Tool for Research in Granular Media, Part II*, Report to National Science Foundation, Department of Civil and Mineral Engineering, University of Minnesota, Minneapolis, Minnesota, 204 pp.
- Cundall, P.A., Drescher, A. and Strack, O.D.L. (1982), Numerical Experiments on Granular Assemblies: Measurement and Observations, *Proc. IUTAM Conf. on Deformation and Failure of Granular Materials*, Delft, P.A. Vermeer and H.J. Luger (eds.), Balkema, Rotterdam, 355-370.
- Cundall, P.A. and Strack, O.D.L. (1983), Modeling of Microscopic Mechanisms in Granular Materials, *Mechanics of Granular Materials: New Model and Constitutive Re-*

REFERENCES

- lations*, J.T. Jenkins and M. Satake (eds.), Elsevier, Amsterdam, 137-149.
- Cundall, P.A., Jenkins, J.T and Ishibashi, I. (1989), Evolution of Elastic Moduli in a Deforming Granular Assembly, *Powders and Grains*, J. Biarez and R. Gourvès (eds.), Balkema, Rotterdam, 319-322.
- Dantu, P. (1957), Contribution à L'Etude Mécanique et Géométrique des Milieux Pulvérulents, *Proc. 4th Int. Conf. Soil Mech. Found. Eng.*, London, 1, 144-148.
- Dantu, P. (1968), Etude Statistique des Forces Intergranulaires dans un Milieu Pulvérulent, *Géotechnique*, **18**, 1, 50-55.
- De Josselin de Jong, G., and Verruijt, A. (1969), Etude Photo-Elastique d'un Empilement de Disques, *Cahiers du Groupe Français de Rhéologie*, **2**, 1, 73-86.
- Eliadorani, A.A. (1992), A Study of Steady-State Deformation of Granular Media by Numerical Simulation of Plane Elliptical Particles, *M.A.Sc. Thesis*, Department of Civil Engineering, University of Waterloo Ontario, 112 pp.
- Hart, R., Cundall, P.A. and Lemos, J. (1988), Formulation of a Three-Dimensional Distinct Element Model- Part II: Mechanical Calculations for Motion and Interaction of a System Composed of Many Polyhedral Blocks, *Int. J. Rock Mech. Min. Sci. & Geomech. Abstr.*, **25**, 3, 117-125.
- Home, M.R. (1965), The Behaviour of an Assembly of Rotund Rigid Cohesionless Particles, I and II, *Proc. Roy. Soc., London, Series A*, **286**, 62-97.
- Konishi, J., Oda, M. and Nemat-Nasser, S. (1982), Inherent Anisotropy and Shear Strength of Assembly of Oval Cross-Sectional Rods, *Deformation and Failure of Granular Materials*, P.A. Vermeer and H.J. Luger (eds.), Balkema Publishers,

REFERENCES

403-412.

- Konishi, J., Oda, M. and Nemat-Nasser, S. (1983), Induced Anisotropy in Assemblies of Oval Cross-Sectional Rods in Biaxial Compression, *Mechanics of Granular Materials: New Models and Constitutive Relations*, J.T. Jenkins and M. Satake, Elsevier Science Publishers B. V., 31-39.
- Krumbein, W. C. (1941), Measurement and Geological Significance of Shape and Roundness of Sedimentary Particles, *J. Sediment. Petrol.*, **11**, 2, 64-72.
- Kruyt, N.P. and Rothenburg, L. (1996) Micromechanical Definition of the Strain Tensor for Granular Materials, *J. Appl. Mech.*, **63**, 3, 706-711.
- Levin, J.Z. (1979), Mathematical Models for Determining the Intersections of Quadric Surfaces, *Computer Graphics and Image Processing*, **2**, 11, 73-87.
- Mehrabadi, M.M., Nemat-Nasser, S. and Oda, M. (1982), On Statistical Description of Stress and Fabric in Granular Materials, *Int. J. Num. Meth. Geomech.*, **6**, 95-108.
- Mirghasemi (1994), Numerical Simulation of Angular Particle Assemblies and Application to Rockfill Dams, *Ph.D. Dissertation*, Department of Civil Engineering, University of Waterloo Ontario, 178 pp.
- Mindlin, R.D. and Deresiewicz, H. (1953) Elastic Spheres in Contact Under Varying Oblique Forces, *J. Appl. Mech.*, ASME, **21**, 327-344.
- Oda, M. (1972) The Mechanism of Fabric Changes During Compressional Deformation of Sands, *Soils and Foundations*, **12**, 2, 1-18
- Oda, M. (1977), Co-ordination Number and Its Relation to Shear Strength of Granular Materials, *Soils and Foundations*, **17**, 2, 29-42.

REFERENCES

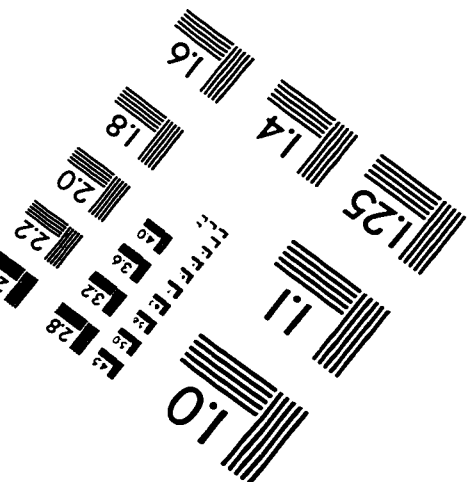
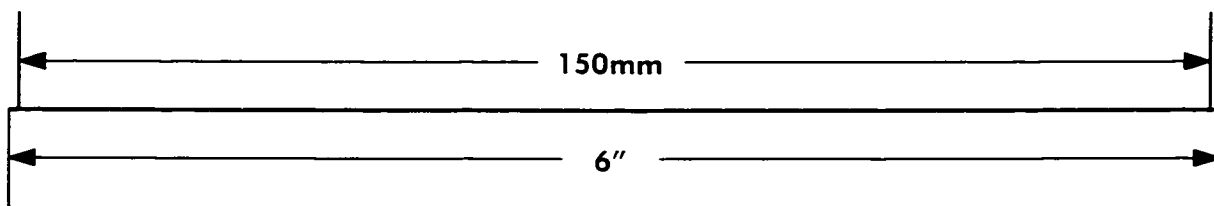
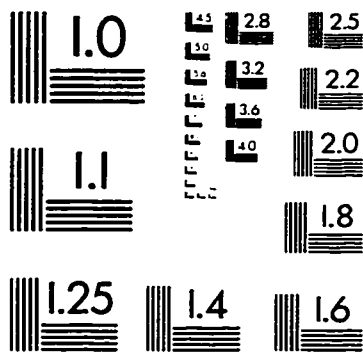
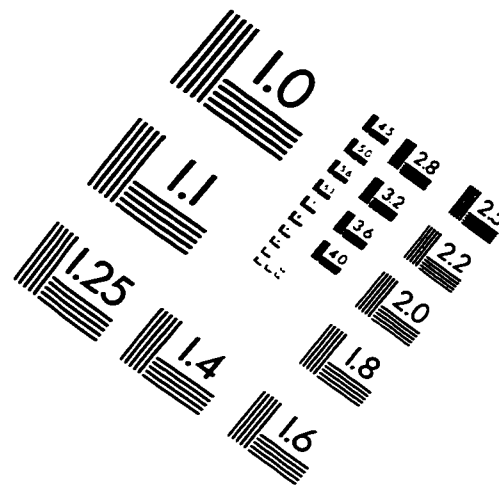
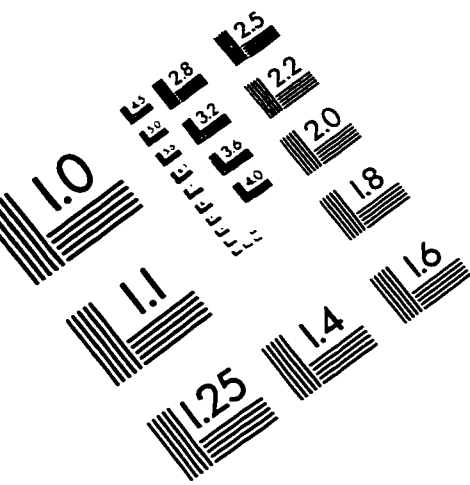
- Oda, M., Nemat-Nasser, S., and Konishi, J. (1983), Experimental Micromechanical Evaluation of The Strength of Granular Materials: Effects of Particle Rolling, *Mechanics of Granular Materials: New Models and Constitutive Relations*, J. T. Jenkins and M. Satake (eds.), Elsevier, Amsterdam, 21-30.
- Rothenburg, L. (1980), Micromechanics of Idealized Granular Systems, *Ph.D. Dissertation*, Department of Civil Engineering, Carleton University, Ottawa, Ontario, 332 pp.
- Rothenburg, L. and Selvadurai, A.P.S. (1981), A Micromechanical Definition of The Cauchy Stress Tensor for Particulate Media, *Proc. Int. Symp. Mechanical Behaviour of Structured Media*, Ottawa, A.P.S. Selvadurai (eds.), Part B, 469-486.
- Rothenburg, L. and Dusseault, M.B. (1987), *Application of a New Constitutive Model for Granular Materials to Oil Sands*, Progress Report to Alberta Oil Sands Technology and Research Authority, Department of Civil Engineering, University of Waterloo Ontario, 144 pp.
- Rothenburg, L. and Bathurst, R. J. (1989), Analytical Study of Induced Anisotropy in Idealized Granular Materials, *Géotechnique*, **39**, 4, 601-614.
- Rothenburg, L. and Bathurst, R.J. (1991), Numerical Simulation of Idealized Granular Assemblies with Plane Elliptical Particles, *Computers and Geotechnics*, **11**, 315-329.
- Rothenburg, L. and Bathurst, R.J. (1992), Micromechanical Features of Granular Assemblies with Planar Elliptical Particles, *Géotechnique*, **42**, 1, 79-95.
- Rothenburg, L. and Bathurst, R.J. (1993), Influence of Particle Eccentricity on Micromechanical Behavior of Granular Materials, *Mechanics of Materials*, **16**, 1-2, 141-

REFERENCES

152.

- Satake, M. (1978), Constitution of Mechanics of Granular Materials through the Graph Theory, *Proc. U.S.-Jap. Seminar on Continuum-Mechanical and Statistical Approaches in the Mechanics of Granular Materials*, Tokyo, 47-62.
- Smith, W.O., Foote, P.D., and Busang, P.F. (1929), Packing of Homogeneous Spheres, *Phys. Rev.*, **34**, 1271-1274.
- Strack, O.D.L. and Cundall, P.A. (1978), *The Discrete Element Method as a Tool for Research in Granular Media, Part I*, Report to National Science Foundation, Department of Civil and Mineral Engineering, University of Minnesota, Minneapolis, Minnesota, 97 pp.
- Strack, O.D.L. and Cundall, P.A. (1984), *Fundamental Studies of Fabric in Granular Materials*, Interim Report to National Science Foundation, Department of Civil and Mineral Engineering, University of Minnesota, Minneapolis, Minnesota, 53 pp.
- Thornton, C. and Barnes, D.J. (1986), Computer Simulated Deformation of Compact Granular Assemblies, *Acta Mechanica*, **64**, 1, 45-61.
- Ting, J.M., Khwaja, M., Meachum, L.R., and Rowell, J.D. (1993), An Ellipse-Based Discrete Element Model for Granular Materials, *Int. J. Num. Meth. Geomech*, **17**, 603-623
- Weber, J. (1966), Recherche Concernant les Contraintes Intergranulaires dans les Milieux Pulvérulents, *Bull. de Liaison des Ponts et Chaussées*, **20**,3, 1-3.20.
- Zhang, Y. and Cundall, P.A. (1986), Numerical Simulation of Slow Deformation, *Proc. 10th U.S. Nat. Cong. Appl. Mech.*, Austin, 347-349.

IMAGE EVALUATION TEST TARGET (QA-3)



APPLIED IMAGE, Inc.
1653 East Main Street
Rochester, NY 14609 USA
Phone: 716/482-0300
Fax: 716/288-5989

© 1993, Applied Image, Inc.. All Rights Reserved

